Probing ultracold ytterbium in optical lattices with resonant light: from coherent control to dissipative dynamics

Raphaël Bouganne

Thèse de doctorat de Sorbonne Université

préparée par Raphaël BOUGANNE

Interaction résonante entre un champ laser et un gaz d'atomes d'ytterbium ultrafroids sur réseau optique : du contrôle cohérent au régime dissipatif

---

Probing ultracold ytterbium in optical lattices with resonant light: from coherent control to dissipative dynamics

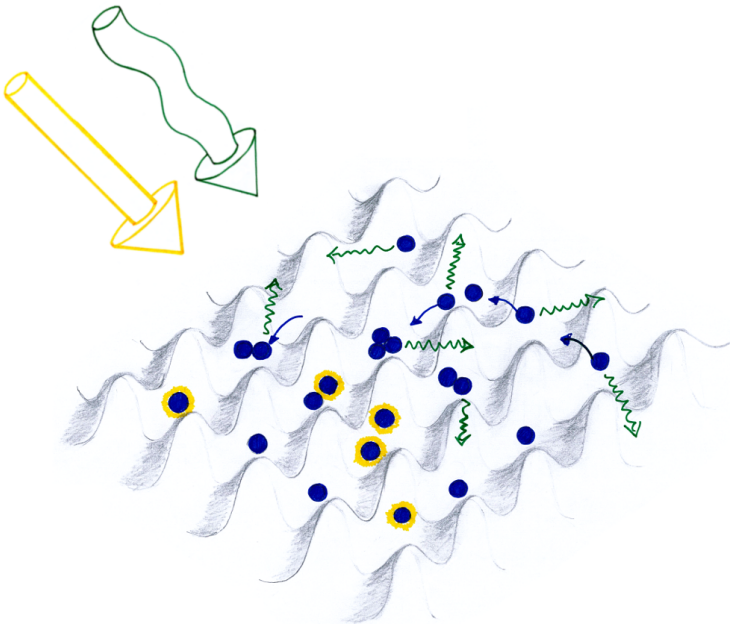

Soutenue le 24 septembre 2018 devant le jury composé de :

M. Leonardo FALLANI ..... Rapporteur
M. Laurent SANCHEZ-PALENCIA ..... Rapporteur
M. Tilman ESSLINGER ..... Examinateur
Mme Catherine SCHWOB ..... Examinatrice
M. Jérôme BEUGNON ..... Membre invité
M. Fabrice GERBIER ..... Directeur de thèse

Travail réalisé au laboratoire Kastler Brossel, au sein du Collège de France.

Abstract & Résumé

In this manuscript I present an experimental investigation of the dynamics of an ultracold gas of bosonic ytterbium loaded into optical lattices and exposed to resonant light. The interaction between atoms and light makes it possible to study the coherence properties of the gas. The resonant driving is performed on the relevant optical transitions featured by alkaline-earth-like atoms such as ytterbium. Specifically, I use the clock transition, which has no spontaneous emission, to coherently manipulate the internal degrees of freedom of the atoms. I also use the so-called intercombination transition, the spontaneous emission rate of which is tunable, to produce a controllable dissipation.

On the one hand, I demonstrate the coherent driving of the internal state of the atoms on the clock transition, the excited state of which is metastable and cannot spontaneously decay, thus preserving the coherence of the gas. The temporal internal dynamics in a deep lattice allows me to measure the collisional properties at low temperature for both clock states.

On the other hand, I use the spontaneously emitted photons of the intercombination transition excited level to induce a coupling to the external degrees of freedom of the atoms. I present the momentum diffusion of a superfluid excited on this transition. Strong interactions between atoms slow down the decoherence and lead to an anomalous sub-diffusive relaxation. A simple model comprising atomic motion, interactions and dissipation accounts for our observations. A theoretical study of the dissipative dynamics in optical lattices sheds light on complementary phenomena such as induced dipole-dipole interactions or collective effects in spontaneous emission.

Dans ce manuscrit je décris une série d'études expérimentales portant sur la dynamique d'un nuage d'atomes d'ytterbium bosonique dégénérés chargés dans un réseau optique et soumis à de la lumière résonante. L'interaction atome-lumière permet d'étudier les propriétés de cohérence quantique du gaz. Pour ces études j'utilise la structure électronique de l'ytterbium qui possède des transitions optiques bien adaptées, à savoir une transition d'horloge sans émission spontanée et une transition dite d'intercombinaison dont le taux d'émission spontanée est ajustable.

Dans un premier temps, je démontre la manipulation cohérente de l'état interne des atomes sur la transition d'horloge, dont l'état excité est métastable et ne peut pas émettre de photons spontanément, protégeant ainsi la cohérence du gaz. La dynamique temporelle de l'état interne d'atomes chargés dans un réseau optique profond permet de mesurer les propriétés collisionelles à basse température pour les états horloges de l'ytterbium.

Dans un second temps, j'utilise l'émission spontanée associée à la transition d'intercombinaison, ce qui permet un couplage aux degrés de liberté externes des atomes. Je présente l'étude de la diffusion en impulsion d'un superfluide excité sur cette transition. Les fortes interactions entre atomes conduisent à l'observation d'une décohérence ralentie aux temps longs et caractérisée par un régime sous-diffusif. Un modèle simple de type Bose-Hubbard incluant la dissipation permet de rendre compte de ces observations. Une étude théorique des effets à N-corps dans l'interaction atome-lumière vient en compléter l'analyse.

Cover picture designed with Marion Bouganne.

List of publications

This manuscript focuses mainly on two experimental investigations. The first one, where we probe the low-energy collision properties of ^{174}Yb with the clock transition, has already been published:

- R. Bouganne et al. (2017). *Clock spectroscopy of interacting bosons in deep optical lattices*. New Journal of Physics **19**.**11**, 113006.

The second one, where we study the momentum diffusion in an optical lattice for a degenerate gas subjected to spontaneous emission, is under preparation and should be submitted soon.

During the course of my thesis work, I also participated actively in the study of the non-linear dynamics of a Bose-Einstein condensate driven on the clock transition:

- M. Bosch Aguilera et al. (2018). *Non-linear relaxation of interacting bosons coherently driven on a narrow optical transition*. EPL (Europhysics Letters) **123**.**4**, 40004.

I was also involved in an experimental work on the topology of quasicrystals, where we probe topological invariants of Fibonacci chains with a diffraction experiment:

- A. Dareau et al. (2017). *Revealing the topology of quasicrystals with a diffraction experiment*. Physical Review Letters **119**.**21**, 215304.

Finally, in parallel to my teaching assignment at École polytechnique about holography, I developed a new laboratory course using digital micro-mirror devices. This new practical course is already in use, students learn Fourier optics and shape arbitrary light potentials in both the direct and Fourier imaging configurations.

Acknowledgments

Les lignes qui suivent sont là pour rendre hommage à celles et ceux qui ont contribué à la concrétisation de ce travail de thèse. En premier lieu je remercie Leonardo Fallani et Laurent Sanchez-Palencia d'avoir accepté de juger et critiquer mon travail. Je remercie également Tilman Esslinger et Catherine Schwob d'avoir participé à ma soutenance.

Ma première confrontation avec les condensats de Bose-Einstein s'est faite avec un reportage d'Arte : La conquête du froid absolu, que j'ai visionné à l'âge de 18 ans. Ce documentaire retrace l'histoire de la maîtrise du froid, et fait la part belle à l'observation de l'hélium superfluide et l'obtention de condensats de gaz mono-atomiques. J'y croisais des noms dont l'importance ne me serait révélée que bien plus tard : Daniel Kleppner, Eric Cornell ou encore Wolfgang Ketterle. La suite s'est déroulée quelques années après, sur les bancs de l'amphithéâtre Arago, en assistant aux cours enthousiasmants de Jean Dalibard, qui a su définitivement ancrer en moi le désir d'en apprendre plus au sujet de ces fameux condensats. L'art oratoire de Jean n'est plus à démontrer, et il fait parti de cette rare classe de chercheurs qui captivent et étonnent par leur capacité à rendre les concepts et phénomènes d'une clarté éblouissante. À bien des égards, ma présence au laboratoire Kastler Brossel fut-elle le résultat de cette aura qu'il 'émet'.

Malgré cela, intégrer une équipe de recherche sur les condensats n'a pas été une évidence. Dans un monde qui divinise les mots 'technologie' et 'innovation', la connaissance scientifique et sa recherche semblent parfois secondaires. À ma sortie d'école je me suis tourné vers une trajectoire qui peut surprendre, mais qui me semblait mêler service de l'État, expertise technologique et impact sociétal : j'ai intégré le corps de l'armement. Pour autant l'idée d'une thèse ne m'était pas étrangère et mon exil en Suisse pour terminer mon master, au cours duquel j'ai eu la chance d'étudier au sein du groupe de Tilman Esslinger, m'a amené à reconsidérer mon choix et tenter l'aventure de la recherche académique. Je ne suis pour autant pas parvenu à convaincre le corps de faire une thèse en son sein, et j'en ai donc pris congé. Ce bras de fer m'aura au moins amené à faire mon stage de master dans une belle entreprise : Muquans, où j'ai découvert une admirable symbiose dans un cadre de recherche et développement très pointu. Je garde un souvenir prégnant de cette courte période, et j'en remercie tous les employés de Muquans.

Je suis arrivé en mars 2015 au Collège de France, cette institution dont la réputation vous précède, pour y commencer une thèse sur la physique des atomes froids sur réseau. J'y ai rencontré deux hommes au caractère bien trempé, qui ont rempli leur rôle d'encadrant de thèse avec brio. Jérôme Beugnon et Fabrice Gerbier, deux personnalités bien différentes, ô combien complémentaires, et dont le dénominateur commun est une capacité d'écoute hors norme combinée avec un haut niveau d'intuition scientifique. Je vous remercie tous deux pour votre bienveillance et vos enseignements, et pour m'avoir permis de réaliser ce rêve d'enfant : jouer avec des condensats. Je souhaite aussi remercier ceux qui ont contribué à la construction de l'expérience ytterbium, dont j'ai eu l'honneur d'hériter. Matthias Scholl, dont la prononciation bien à lui des mots finissant en -il ou -ille me fait encore sourire; Quentin Beaufils, dont les ressemblances de caractère avec Fabrice sont troublantes; et Alexandre Dareau, à qui je souhaite une réussite très prochaine pour

un poste de chercheur. Je vous suis tous profondément reconnaissant. J'espère que les générations suivantes, Alexis Ghermaoui et les futurs thésards ytterbium, pourront réaliser de belles expériences et je leur souhaite le meilleur. Merci également à l'équipe pédagogique des TREX à l'École polytechnique, en particulier Guilhem Gallot et Mathias Kobylko, pour votre confiance dans la rénovation du Modal d'holographie. En plus d'être très instructif, ce fut un plaisir de développer le nouveau montage en toute autonomie.

Le bien-être au laboratoire pendant ces trois années ne provient pas d'une température de climatisation agréable en salle de manip', ni d'une clémence de nos lasers, mais bien des collègues avec qui j'ai travaillé. En premier lieu, Manel Bosch, la personne avec qui j'ai passé de nombreux mois penché sur une table optique à s'en faire mal au dos, ou assis devant Cicero à en attraper un rhume. Manel, merci pour ton agréable caractère, ta fidélité au travail et ta résilience face aux problèmes. Je ne t'ai jamais vu découragé, ni solitaire, mais enthousiaste et confiant. Merci pour ces journées de catharsis : le début du bon vide, le retour du MOT et du condensat et enfin l'observation du superfluide dans le réseau. Tu as été et restes un collègue idéal. Merci également à tous ceux qui ont partagé cette aventure à nos côtés pour des périodes plus courtes, par ordre d'apparition : Elisa Soave, Isabella Fritsche et Daniel Linnemann. Merci à tous les locataires du 2ème étage, stagiaires, thésards et permanents, avec qui les discussions sont souvent surprenantes. Merci au BCBP, aux GO du paper club, aux local helpers et aux catalogues Frankel. Merci aussi à Carmen Toderasc et Pascal Travers pour le soutien au Collège, à Antoine Heidmann et Thierry Lahaye pour leur suivi de ma thèse et leur sympathie. Merci à tous ceux qui ont aimé partager quelques moments rituels avec les ytterbium : les libanais, les p'tites pauses et les semaines UQUAM.

Pour finir, j'ai eu la chance d'être accompagné tout au long de ma vie par des figures exceptionnelles que je souhaite mentionner ici pour souligner l'importance qu'ils ont eu sur mon parcours, car comme le dit si bien Jules Michelet : « Le difficile n'est pas de monter, mais en montant de rester soi.» . Valentin Lecheval et Lucas Trouillard, qui les premiers m'ont accordé leur amitié, puis Paul Boisdron et Yosi Goasdoué, sources d'inspiration pour une vie entière, enfin Sarah Bekhada et Cédric Suhas, des esprits dont la force m'a longuement inspiré. Merci à vous d'avoir su m'accorder votre pleine confiance. D'autres personnes ont joué un rôle essentiel dans mon orientation académique, Pascal Lucazeau et Christophe Le Nagard mes professeurs d'histoire et de français au lycée et désormais amis, et enfin Christoph Kohstall et Sylvain de Léséleuc, tous deux doués d'une intelligence qui me dépasse et m'inspire. Je ne peux m'arrêter en si bon chemin, et je souhaite aussi remercier toutes les personnes qui ont joué un rôle fondamental dans mon bien-être, ma femme Marion, ma famille et mes amis.

« Qu'importe où nous allons, honnêtement. Je ne le cache pas. De moins en moins. Qu'importe ce qu'il y a au bout. Ce qui vaut, ce qui restera n'est pas le nombre de cols de haute altitude que nous passerons vivants. N'est pas l'emplacement où nous finirons par planter notre oriflamme, au milieu d'un champ de neige ou au sommet d'un dernier pic dont on ne pourra plus jamais redescendre. N'est plus de savoir combien de kilomètres en amont du drapeau de nos parents nous nous écroulerons! Je m'en fiche! Ce qui restera est une certaine qualité d'amitié, architecturée par l'estime. Et brodée des quelques rires, des quelques éclats de courage ou de génie qu'on aura su s'offrir les uns aux autres. Pour tout ça, les filles et les gars, je vous dis merci. Merci. »

A. Damasio, La Horde du contrevent.

Contents

Glossary

Constants and notations

Throughout the manuscript I use a number of physical constants:

- the speed of light in vacuum c,
- the Boltzmann constant k_{B},
- the vacuum permittivity ϵ_0,
- Planck's constant h,
- reduced Planck's constant $\hbar = h/(2\pi)$,
- the Bohr radius a_0,
- the Bohr magneton μ_{B}.

If not otherwise mentioned, t refers to the time variable and M to the atomic mass of ^{174}Yb. The square root of -1 is noted i, hermitian conjugate is noted h.c., $\delta_{i,j}$ is the Kronecker delta and $\delta^{(n)}$ is the Dirac delta distribution in dimension n. The Cauchy principal value of an integral is noted PV. Error bars are provided in parentheses and refer to the last relevant digit.

Acronyms

AEL Alkaline-earth-like,
AOM Acousto-optic modulator,
BEC Bose-Einstein condensate,
CCD Charge-coupled device,
DT Dipole trap,
EOM Electro-optic modulator,
MI Mott insulator,
MOT Magneto-optical trap,
PD Photo-diode,
PDH Pound-Drever-Hall,
PSD Power spectral density,
RAM Residual amplitude modulation.

0

Introduction

Atomic quantum gases exemplify a possible leitmotiv for natural sciences: *To render ourselves the lords and possessors of nature*, as the philosopher René Descartes expressed in his treaty on reason and the seek of truth in science (Descartes 1637). Indeed they represent one of the most controlled though elaborate systems found in physics laboratories and are now routinely realised in many places around the world. Quantum gases host a very rich variety of physical phenomena, they belong to this class of devices which are built from 'simple' building blocks, and that yet constitute complex interacting quantum systems with which one can explore the intriguing properties of quantum matter. The tremendous scientific progress of the last fifty years, supported by equally important technological advances, has made possible the realisation of many of such devices comprised of neutral atoms, ions, photons, electrons, or superconducting circuits among others (Georgescu et al. 2014). Many of these systems were initially studied for their own sake, but it has soon been realised that they can also be used to understand many more physical processes spanning a wide range of research topics.

The last decade of research with quantum gases has been focusing on the simulation of many-body problems. For instance, the analogy between interacting atomic gases in light potentials and electrons in solids is such that the former can be used to simulate the latter (Bloch 2005) and provide answers to fundamental challenges of solid-state physics. Implementation of Hubbard models (Greiner et al. 2002b), spin Hamiltonians (Struck et al. 2011) or disordered systems (Billy et al. 2008; Roati et al. 2008) were carried out with quantum gases. The general motivation stems from the high level of experimental control over quantum gases, which makes it possible to engineer and inspect models of condensed matter phenomena with greater ease. This analogy illustrates vividly the more general quantum simulation paradigm, the original idea of which being expressed in the words: *Let the computer itself be built of quantum mechanical elements which obey quantum mechanical laws* (Feynman 1982). The design of quantum simulators, which I referred to above as complex interacting quantum systems, is based on a bottom-up approach consisting in assembling elementary building blocks and coupling them together. Numerous implementations of quantum simulators are now achieved in laboratories. Neutral atoms can be trapped and addressed in optical lattices (Bloch et al. 2012) or optical tweezers (Weimer et al. 2010; Nogrette et al. 2014). Trapped ions constitute one of the most advanced platform for quantum computing (Blatt et al. 2012). Another promising platform for the development of quantum information processing is superconducting circuits (Devoret et al. 2013), which are particularly promising to foresee applications outside a physics laboratory. The range of problems that these systems can explore go from condensed-matter physics to quantum chaos or cosmology (Georgescu et al. 2014). Other tracks are being explored in parallel, even though they are not as developed as the previous ones. For example, the control of single spins in semiconductors (Hanson et al. 2008) is now extended to build arrays of quantum dots (Awschalom et al. 2013) or

nitrogen-vacancy centers (Childress et al. 2013). Finally, photons can also be manipulated and made to interact in photonic circuits (Aspuru-Guzik et al. 2012).

Many of these quantum simulators or quantum computers face the problem of decoherence (Zurek 2002; Haroche et al. 2006), i.e. the irreversible leak of information into an uncontrolled environment that blurs out quantum interference phenomena. Decoherence is a limiting factor for these experiments aiming at controlling many-body quantum systems for long times. However, the process by which quantum coherences spread out is a highly non-trivial problem and lacks complete theoretical description and understanding (Laloë 2001; Zurek 2002). More precisely, the question of how the coupling to an environment or inter-particle interactions affect the time evolution of quantum coherences is an ongoing though intense research topic (Zurek 2003; Choi et al. 2016; Kaufman et al. 2016). Such an interaction can happen in many different ways, e.g. coupling to the electro-magnetic field vacuum, losses in the system, finite temperature effects, collisions and more. The case of non-interacting particles has been addressed in the last twenty years and experiments aiming at exploring decoherence have been successfully performed with microwave cavities (Haroche et al. 2006; Haroche 2013) or ions (Myatt et al. 2000; Turchette et al. 2000; Wineland 2013). When systems are made up of many particles, the decoherence is usually expected to be hastened by interactions but in general the dynamics can be more sophisticated. Understanding the processes by which many-body systems interact with their surroundings is thus paramount. In that respect, an important feature of quantum gases is their good degree of isolation and thus protection from dissipative processes, in comparison with solid-state devices where dissipation channels are numerous. This makes it possible to engineer and control the degree of coupling to an external reservoir, which is a very appealing feature to study decoherence with quantum gases. The effect of light on the atomic motional degrees of freedom has been extensively studied in the framework of laser cooling (Wineland et al. 1979; Gordon et al. 1980; Chu 1998; Cohen-Tannoudji 1998; Phillips 1998), a process at the genesis of quantum gases. Ironically, one can also use spontaneous emission to study decoherence. Theoretical studies for many-body atomic systems (Milonni et al. 1974; Ellinger et al. 1994; Pichler et al. 2010) suggest that interactions can affect substantially the relaxation dynamics.

This thesis work has been conducted in this context and aims at understanding better the coherence properties of a quantum gas in optical lattices. The advent of quantum gases started in 1995 after the first observation of Bose-Einstein condensation in dilute atomic vapours (Anderson et al. 1995; Bradley et al. 1995; Davis et al. 1995), followed a few years later by the creation of degenerate Fermi gases (DeMarco et al. 1999; Schreck et al. 2001; Truscott et al. 2001). All this was achieved after two decades of intense efforts to manipulate the motion of atoms using light and magnetic fields (Hänsch et al. 1975; Wineland et al. 1979). Laser cooling and trapping techniques were developed to slow down atoms, making the most of spontaneous emission to extract entropy from the gas and lower its temperature. However the randomness of spontaneous emission provides a limit to the achievable temperatures, in the range of the microkelvin, which was still too high to observe quantum mechanical statistics on a macroscopic scale. The criterion for the observation of Bose-Einstein condensation is that the phase-space density $n\lambda_{\mathrm{T}}^3$ of the gas[1] exceeds a threshold on the order of one. At that time, phase-space densities around 10^{-5} were achieved using laser cooling. The decisive idea to cross the transition point relies on inter-particle interactions and is called evaporative cooling[2] (Hess 1986;

[1] n is the gas density and $\lambda_{\mathrm{T}} \propto 1/\sqrt{T}$ is the thermal wavelength with T the temperature of the gas.

[2] While this technique was first designed to cool down atomic hydrogen, condensation via evaporative

Masuhara et al. 1988). Essentially, the mechanism works as follows: Atomic collisions preferentially expel the most energetic atoms from the trap and simultaneously allow the remaining ones to thermalise. The mean energy of the system is then lowered, and so is its temperature. Facilitating the removal of the hottest atoms with a time-dependent ramp on the trap depth makes it possible to reach the regime of Bose-Einstein condensation. Nowadays, other routes are explored (or re-explored) and Bose-Einstein condensates have been realised without evaporative cooling (Stellmer et al. 2013; Hu et al. 2017).

The beauty of quantum gases lies in their exceptional physical properties. For instance, a Bose-Einstein condensate is a coherent, macroscopic matter wave, with which one can observe matter wave interferences (Andrews et al. 1997) or long-range phase coherence (Bloch et al. 2000). Another striking aspect of quantum gases is their superfluid behaviour, which made possible the observation of vortices (Matthews et al. 1999; Madison et al. 2000) and metastable currents (Ramanathan et al. 2011; Moulder et al. 2012). Furthermore, these systems offer great flexibility with the capacity to change their dimensionality, to mimic periodic potentials using optical lattices and to tune the inter-particle interactions using Fano-Feshbach resonances (Bloch et al. 2008). These features were central for the observation of a wealth of phenomena among which the superfluid-Mott insulator quantum phase transition with bosons (Greiner et al. 2002b), or the crossover between a Bose-Einstein condensate of weakly-bound molecules to a superfluid of Cooper pairs with fermions (Regal et al. 2004).

While quantum gases were originally achieved with alkali atoms, many other elements have been laser cooled and brought to quantum degeneracy [for instance ytterbium (Takasu et al. 2003)]. Among these, the family of alkaline-earth-like atoms helped to design a new generation of *optical atomic clocks*, owing to the very high quality factor of the ultranarrow optical transitions present in the low-lying energy structure of these atoms (Ludlow et al. 2015). Such clocks beat by many orders of magnitude the frequency standards based on a microwave transition of alkali atoms such as caesium or rubidium. Optical clocks already reach 10^{-18} fractional frequency precision or below. At this level, they should be capable of testing general relativity (Chou et al. 2010). While most of these clocks operate with thermal atoms, recent experiments have started to explore the degenerate regime, demonstrating 100 µHz precision in relative frequency measurement and showing new prospects for metrology (Marti et al. 2018). Another emergent but very active field is the study of dipolar quantum gases, which started with the condensation of chromium (Griesmaier et al. 2005) and gained a fresh impetus with the condensation of open-shell lanthanide species (Lu et al. 2011; Aikawa et al. 2012), which feature a high permanent magnetic moment. As an illustration, these dipolar quantum gases have recently allowed for the observation of a roton-like instability[3] (Chomaz et al. 2018) and quantum droplets[4] (Ferrier-Barbut et al. 2016).

Along the lines of what has been discussed so far, a more specific opportunity offered by quantum gases is the simulation of charged particles in strong magnetic fields. This is of particular interest to reach a regime where experiments with condensed matter samples are extremely challenging due to the high magnitude required for the magnetic field $\sim 1000\,\mathrm{T}$. The observation of quantized plateaus in the Hall conductance of a two-

cooling was first successful with alkali atoms.

[3]Such an instability, corresponding to an elementary excitation forming a minimum of energy at finite momentum, is reminiscent of the roton mode in ^{4}He.

[4]These droplets are a direct manifestation of quantum fluctuations, which imply corrections to the mean-field description and mechanically protect the otherwise unstable droplets.

dimensional gas of electrons is the integer quantum Hall effect (von Klitzing 1986). When inter-particle interactions come into play, additional plateaus located not at integer but at fractional values of the quantum of conductance also appear (Tsui et al. 1982; Laughlin 1983). In such a regime, strongly correlated phases of matter are predicted to form. Using quantum gases to simulate such systems requires to mimic the Lorentz force a charged particle feels in a magnetic field. This can be achieved using the Coriolis force on rapidly rotating quantum gases (Schweikhard et al. 2004). The Coriolis force $M\boldsymbol{\Omega} \times \boldsymbol{v}$, with $\boldsymbol{\Omega}$ the angular velocity vector and $\boldsymbol{v}$ the speed, has the same structure as the Lorentz force $e\boldsymbol{v} \times \boldsymbol{B}$, with e the electric charge and $\boldsymbol{B}$ the magnetic field. Another method consists in using the coherent coupling between atoms and a laser beam, where the exchange of photons can be tailored to induce momentum change orthogonal to the atomic motion. Many experiments have already explored the single-particle and mean-field regimes with this technique (Goldman et al. 2014), but beyond mean-field effects remain elusive to observation due to technical limitations inducing heating of the atomic sample. The experimental apparatus of this thesis work, based on the proposal in Gerbier et al. (2010), has been designed to overcome such limitations and reach a regime where bosonic counterparts of the quantum Hall states could be observable (Cooper et al. 2018).

In this manuscript I explain an original work carried out over the last three years in laboratoire Kastler Brossel at Collège de France. I present an experimental investigation of the dynamics of ultracold ytterbium gases loaded into optical lattices and subjected to a near-resonant laser light field. In that respect, two series of experiments have been performed. I first looked at the internal dynamics of atom pairs in the coherent driving regime using the 'clock' transition, the excited state of which is metastable. Then I studied the external dynamics of a superfluid in the dissipative regime using the 'intercombination' transition, with a controllable spontaneous emission rate. This investigation sheds light on the internal and external coherence properties of quantum gases in optical lattices.

The manuscript is arranged as follows:

Chapter 1 provides the background this thesis work relies on. Relevant attributes of alkaline-earth-like atoms are given with an emphasis on ytterbium. Then a reminder of the physics of ultracold atoms in optical lattices is presented. In a broader perspective, the intended purpose of the experiment is outlined.

Chapter 2 describes the experimental apparatus. It focuses on four major facets: the realisation of Bose-Einstein condensates, the detection method, the preparation of degenerate gases in optical lattices and the laser driving the clock transition.

Chapter 3 explains the optical 'clock' spectroscopy of interacting atoms in deep optical lattices. It shows how the coherent driving of atoms and atom pairs allows to characterise the population distribution in the system as well as measure all relevant scattering properties of the clock states.

Chapter 4 demonstrates anomalous momentum diffusion in a superfluid subjected to dissipation. The loss of coherence in the gas is shown to be drastically slowed down at long times. This behaviour is interpreted as a signature of strong inter-particle interactions and quantitatively reproduced with a model of continuous measurement.

Chapter 5 develops a theoretical framework to understand the observations of the preceding chapter. It shows why predictions from a single-particle master equation are not sufficient and elaborates preliminary evaluations of the many-body effects in light-matter interactions.

1

Ultracold alkaline-earth-like gases in optical lattices

Alkaline-earth-like (AEL) atoms refer to all atomic species which have complete internal shells and a complete outer s-shell with two electrons. This includes all alkaline-earth elements (Be, Mg, Ca, Sr, Ba and Ra), as well as those from the d-block (Zn, Cd and Hg) and from the f-block (Yb and No). This does not include He, which also has a complete outer s-shell, since the useful state for laser cooling and trapping is not the ground state but a metastable state[1]. So far only Be, Zn and No have not been laser cooled[2].

AEL atoms have recently attracted a lot of theoretical and experimental interest owing to their specific internal structure. Combining their features to the powerful platform provided by optical lattices (Bloch 2005) opens many avenues and prospects for fundamental research as well as possible long term applications. For instance, the ability to address distinctively two metastable states and manipulate them with different optical potentials, along with the presence of well-isolated spin degrees of freedom make AEL atoms a good platform for quantum information processing (Daley et al. 2008; Gorshkov et al. 2009). The optical 'clock' transition combined with a 'magic' wavelength made possible the construction of clocks with unprecedented precision (Bloom et al. 2014; Ludlow et al. 2015; Marti et al. 2018), making a redefinition of the SI second standards possible in the near future. The very high quality factor of these clock transitions is also key in the development of new ultra-narrow linewidth lasers (Bohnet et al. 2012; Norcia et al. 2018a). From the strong decoupling between nuclear spin and electronic angular momentum emerges a SU(N) symmetry suitable for simulating high-spin magnetism or impurity problems (Gorshkov et al. 2010; Martin et al. 2013; Cazalilla et al. 2014; Riegger et al. 2018). As a final example, AEL atoms are good candidates for simulating quantum Hall systems with their intriguing topological properties (Jaksch et al. 2003; Gerbier et al. 2010; Mancini et al. 2015; Livi et al. 2016; Cooper et al. 2018).

In this chapter I review the tools and theoretical concepts essential for our experiments and required in the later chapters to understand the measurements and analysis performed. I start by presenting the useful features of AEL atoms, among which the 'clock' transition and the 'magic' wavelength. Then I explain what optical lattices are, focusing on the celebrated many-body superfluid-Mott insulator phase transition. Combining AEL atoms and optical lattices, I finally describe the experimental implementation of artificial magnetic fields and charges for neutral atoms as envisioned in our experiment.

[1] The true ground state of He has transitions in the ultraviolet, a region of the electro-magnetic spectrum where no lasers are available, which makes it technically out of reach for radiative cooling. This feature is shared by all noble gases. The study of degenerate gases of metastable He* provides other very interesting opportunities though, such as single-atom detection, and we refer the reader to the review Vassen et al. (2012).

[2] Be and Zn ions have been laser cooled though.

1.1 Structure of AEL atoms

The distinctive features of AEL atoms mostly arise from their filled two-valence-electron shell (for ytterbium the electronic structure is $[\mathrm{Xe}]4f^{14}6s^2$). The two outer electrons can pair in a spin-singlet state (with total electronic spin $s = 0$) or spin-triplet states (with $s = 1$). Figure 1.1 shows a sketch of the low-lying states of an AEL atom.

In this section, I introduce the most prominent features of AEL atoms which attract attention for new research prospects: ultra-narrow 'clock' transitions associated to long-lived metastable states, state-dependent atom-light interactions and spin-independent interatomic collisions. I first show the electronic structure of AEL atoms with a focus on the narrow transitions. I then present the state-dependent electric polarisability for the clock states, with the existence of specific interesting wavelengths for trapping potentials. I finally discuss the decoupling between electronic spin degrees of freedom and the nuclear spin. Throughout the section, I provide numerical values for ytterbium atoms.

1.1.1 Energy levels

The low-energy physics of AEL atoms being determined mostly by the two outer electrons, we adopt the spectroscopic notation ${}^{2s+1}\mathrm{L}_J$ with s the total electronic spin, L the total electronic orbital momentum and $J = \mathrm{L} + s$ the total electronic angular momentum. The nuclear spin I is always zero for bosonic isotopes, and non-zero for fermionic isotopes.

The ground state is the spin-singlet state ${}^1\mathrm{S}_0$. It has zero total electronic angular momentum, which means no hyperfine structure and thus no possibility for sub-Doppler cooling mechanisms (Metcalf et al. 1999). The total angular momentum F is therefore given by the nuclear spin. Bosonic isotopes all have $F = 0$ and are thus insensitive to magnetic fields.

Neglecting spin-orbit coupling and the fine structure of the atom, the only dipole-allowed transitions from the ground state (from selection rules $\Delta\mathrm{L} = 1$ and $\Delta s = 0$) connect it to states in the spin-singlet manifold. The closest transition from the ground state is the ${}^1\mathrm{S}_0$–${}^1\mathrm{P}_1$ transition. Such a transition is broad (radiative linewidth of about $2\pi \times 30\,\mathrm{MHz}$ for ytterbium) and usually used for laser cooling and magneto-optical trapping. In the case of ytterbium, the transition is not exactly closed and the excited state can decay via relay states to metastable states of the spin-triplet manifold, limiting the loading of a magneto-optical trap to small atom number without repumping light (Honda et al. 1999).

Transitions linking the spin-singlet and spin-triplet manifolds are forbidden in the dipole approximation (Foot 2004). They become 'weakly' allowed because of perturbations to the atomic structure, for example due to spin-orbit coupling. This gives rise to the prominent features of narrow optical transitions. The so-called intercombination ${}^1\mathrm{S}_0$–${}^3\mathrm{P}_1$ transition is one of these weak transitions. The radiative linewidth of such a transition is narrower than the dipole-allowed transition (about $2\pi \times 200\,\mathrm{kHz}$ for ytterbium), and can be used for efficient Doppler cooling in magneto-optical traps down to low temperatures, on the order of $10\,\mu\mathrm{K}$ or below[3]. Interestingly, such a narrow intercombination line has been recently used in novel cooling schemes, for example to reach degeneracy with all-

[3]For the lightest AEL atoms (Mg and Ca) the radiative linewidth of the intercombination transition is much smaller and laser cooling requires other experimental schemes (Prudnikov et al. 2016; Mills et al. 2017).

optical cooling (Stellmer et al. 2013) or to allow efficient and fast cooling with small spontaneous emission rate (Norcia et al. 2018b).

The simpler electronic structure provided by AEL atoms, as compared to the hyperfine structure of alkali atoms, is attractive for exploring light scattering from atomic ensembles (Bromley et al. 2016). In particular the $J = 0 \to J = 1$ intercombination transition has been used to study the weak localisation regime in light scattering from a cold strontium cloud (Bidel et al. 2002), providing a much stronger signal than with rubidium (Labeyrie et al. 1999). In Chapter 4 we use the intercombination line to study momentum diffusion in a Bose-Hubbard gas.

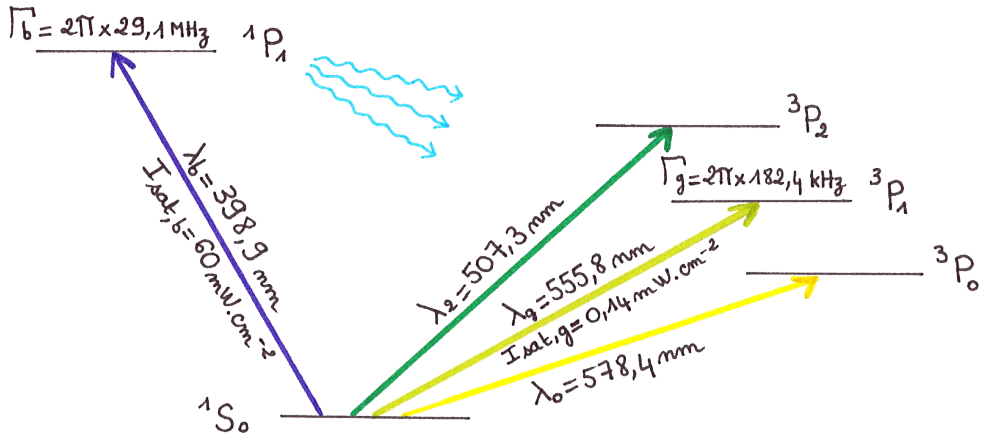

Figure 1.1: Sketch of the low-lying electronic structure of AEL atoms. The indicated values are given for the ytterbium atom. The cyan arrows denote the possible decay channels from the $^1P_1$ state. *Figure designed with Marion Bouganne.*

1.1.2 Clock transitions

The two remaining states $^3P_0$ and $^3P_2$ of the spin-triplet manifold are metastable, both transitions linking them to the ground state are forbidden by the selection rule $\Delta J = 1$. The ultranarrow magnetic quadrupole transition $^1S_0$–$^3P_2$ is usually not considered for a frequency standard because of the non-zero total electronic angular momentum $J = 2$ of the $^3P_2$ state[4], giving sensitivity to magnetic fields and to trapping light polarisation.

In the following I focus on the $^1S_0$–$^3P_0$ clock transition that we use in our experiment. This transition is doubly-forbidden because it does not conserve the electronic spin ($\Delta s \neq 0$) and violates the triangle selection rule ($J = 0 \to J = 0$ is forbidden). For fermions, hyperfine interactions mix the triplet states, and a small but finite dipole moment emerges (Porsev et al. 2004). This transition is already widely used in optical clocks due to its very high quality factor (Ludlow et al. 2015). For bosons the nuclear spin is zero and as a result there is no hyperfine coupling to open up the transition. A magnetic mixing technique, described below, can be used to overcome this. In Chapter 3, we use the clock transition to perform spectroscopy of ^{174}Yb atoms in deep optical lattices. Additionally, the long-lived excited $^3P_0$ state associated with this transition is now considered as a promising intermediate state for various experiments. For instance, a second clock transition can

[4]This is actually questionable (Yamaguchi et al. 2010), and has been recently discussed in Dzuba et al. (2018).

be reached from the $^3P_0$ state, allowing tests on possible variations of the fundamental constants (Safronova et al. 2018).

Furthermore, transitions in the infrared ($\lambda \sim 2\,\mu m$) accessible from the $^3P_0$ state, combined with a near ultra-violet 'magic' wavelength (see below), make it possible to reach a regime where the light-induced interaction length scale is much bigger than the mean inter-particle spacing (Olmos et al. 2013; Zhu et al. 2015). Such a scheme where the emitted photon wavelength is bigger than the inter-particle distance is also expected to exhibit non-trivial topological properties (Perczel et al. 2017).

$^1S_0$–$^3P_0$ transition for bosons

In order to allow single-photon excitation on the $^1S_0$–$^3P_0$ clock transition, Taichenachev et al. (2006) proposed to mix a controllable fraction of the $^3P_1$ state into the $^3P_0$ state with a static magnetic field $\boldsymbol{B} = B_0 \boldsymbol{e}_z$. Figure 1.2 shows a sketch of the concept.

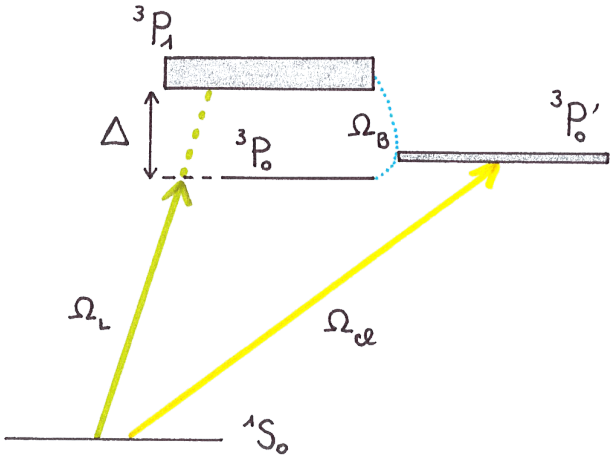

Figure 1.2: Sketch of the $^1S_0$–$^3P_0$ clock transition broadening. A static magnetic field mixes the $^3P_0$ and $^3P_1$ states and allows one-photon excitation. *Figure designed with Marion Bouganne.*

The coupling matrix element introduced by the magnetic field $\boldsymbol{B}$ is (Taichenachev et al. 2006)

$$\Omega_B = \frac{1}{\hbar} \langle {}^3P_0 | \, \hat{\boldsymbol{\mu}} \cdot \boldsymbol{B} \, | {}^3P_1 \rangle = \sqrt{\frac{2}{3}} \frac{\mu_B}{\hbar} B_0, \tag{1.1}$$

where $\hat{\boldsymbol{\mu}}$ is the magnetic-dipole operator. The eigenstates of the atomic and Zeeman Hamiltonian are given in first-order perturbation theory by (denoted with a $'$):

$$|{}^1S_0{}'\rangle \approx |{}^1S_0\rangle \,, \tag{1.2}$$

$$|{}^3P_0{}'\rangle \approx |{}^3P_0\rangle + \frac{\Omega_B}{\Delta} |{}^3P_1, m = 0\rangle \,, \tag{1.3}$$

where $\Delta \approx 2\pi \times 21\,\mathrm{THz}$ is the fine structure splitting between the triplet states $^3P_0$ and $^3P_1$. The expression for the perturbed states is justified when $|\Omega_B/\Delta| \ll 1$. The Rabi frequency for the transition is defined by

$$\hbar\Omega_{cl} = \langle {}^1S_0{}' | \, \hat{\boldsymbol{d}} \cdot \boldsymbol{E} \, | {}^3P_0{}' \rangle = \frac{\Omega_B}{\Delta} \langle {}^1S_0 | \, \hat{\boldsymbol{d}} \cdot \boldsymbol{E} \, | {}^3P_1, m = 0 \rangle \,, \tag{1.4}$$

where $\hat{\boldsymbol{d}}$ is the electric-dipole operator and $\boldsymbol{E}$ the electric field. We recognise the Rabi frequency for the $^1S_0$–$^3P_1$ transition $\hbar\Omega_L = \langle {}^1S_0| \hat{\boldsymbol{d}} \cdot \boldsymbol{E} |{}^3P_1, m = 0\rangle$. The transition only couples to the $m = 0$ state of $^3P_1$, and thus can only be excited by light linearly polarised along the magnetic field, which we assume from now on. We thus rewrite:

$$\Omega_{cl} = \frac{\Omega_B \Omega_L}{\Delta} = \alpha B_0 \sqrt{I_{cl}}, \tag{1.5}$$

where I_{cl} is the light intensity on the atom and α a constant given by:

$$\alpha = \sqrt{\frac{4\pi c^2 \Gamma_g \mu_B^2}{\hbar^3 \omega_g^3 \Delta^2}} \approx 2\pi \times 18.7\,\mathrm{mHz/G/(mW/cm^2)^{1/2}}. \tag{1.6}$$

Here ω_g and Γ_g are the frequency and radiative linewidth of the $^3P_1$ state, respectively.

The first experimental demonstration of this magnetically-induced transition is presented in Barber et al. (2006). For achievable magnetic fields and light intensities in our laboratory, typically $B_0 \approx 180\,\mathrm{G}$ and $I_{cl} = 2.5 \times 10^5\,\mathrm{mW\,cm^{-2}}$ (corresponding to 10 mW focused on 50 µm), we are able to achieve $\Omega_{cl} \approx 2\pi \times 1.7\,\mathrm{kHz}$.

Spontaneous emission rate

The small admixture of $^3P_1$ also implies a broadening of the forbidden clock transition, i.e. a finite lifetime for the excited clock state. The magnetically-induced radiative linewidth is given by[5]:

$$\Gamma_{cl} = \Gamma_g \frac{\Omega_B^2}{\Delta^2} \approx 2\pi \times 535\,\mathrm{pHz} \times \frac{B_0^2}{1\,\mathrm{G}^2}. \tag{1.7}$$

Spontaneous decay from the clock state can thus be safely neglected for reasonable magnetic fields around $B_0 \approx 180\,\mathrm{G}$. In Chapter 3, this absence of spontaneous emission is key for the achievement of coherent driving of the atomic gas. In that respect, an important ingredient to permit long interrogation times is to spatially trap the atoms. This is discussed in the following.

1.1.3 State-dependent optical potentials

The dispersive interaction between atoms and far-detuned light creates either attractive or repulsive conservative potentials: the optical dipole traps (Grimm et al. 2000). Optical dipole traps rely on the dispersive interaction between atom and light, which is described by the energetic potential, or light shift:

$$V(\boldsymbol{r}) = -\frac{1}{2\epsilon_0 c} \alpha(\lambda) I(\boldsymbol{r}), \tag{1.8}$$

where I is the light intensity and α the real part of the dynamic polarisability of the atom. Attractive dipole traps verify $V < 0$ ($\alpha > 0$) and are called 'red-detuned' traps whereas repulsive dipole traps verify $V > 0$ ($\alpha < 0$) and are called 'blue-detuned' traps. The value of α depends on the wavelength of the trapping light but also on the internal state of the atom. As such, optical trapping potentials can be different for the two clock states. Figure 1.3 shows the calculated real part of the dynamic polarisability for the clock states

[5] Power broadening is negligible for the experimentally achievable intensities.

of ytterbium [computation performed with data extracted from the calculation published in Dzuba et al. (2010)].

Among all possibilities, three are of interest for the trapping of both clock states.

- Wavelengths for which polarisabilities are equal are called *magic*. This happens for ytterbium at around $\lambda_m \approx 759.35\,\mathrm{nm}$ and was precisely measured in Barber et al. (2008). These wavelengths are of particular importance for avoiding differential light shifts between the clock states introduced by the trapping potential, and thus crucial for the operation of optical clocks (Ludlow et al. 2015).
- Wavelengths for which polarisabilities are equal in magnitude but opposite in sign are called *anti-magic*. This happens for ytterbium at around $\lambda_{am} \approx 617\,\mathrm{nm}$ and $\lambda_{am,2} \approx 1122\,\mathrm{nm}$. At these wavelengths one internal state is attracted by light while the other one is repelled. This is at the heart of state-dependent optical lattices where internal states are trapped in different regions of space (Gorshkov et al. 2009; Gerbier et al. 2010; Cooper 2011).
- Wavelengths for which polarisabilities are very different in magnitude. This happens for ytterbium for instance at around $\lambda_K \approx 987\,\mathrm{nm}$, where the polarisability in the metastable state vanishes. For lattices created at such wavelengths, in which internal states have very different spatial mobilities, implementations of the Kondo lattice model or other impurity models have been suggested (Gorshkov et al. 2010; Foss-Feig et al. 2010b; Foss-Feig et al. 2010a), and experiments have started to explore this regime (Riegger et al. 2018).

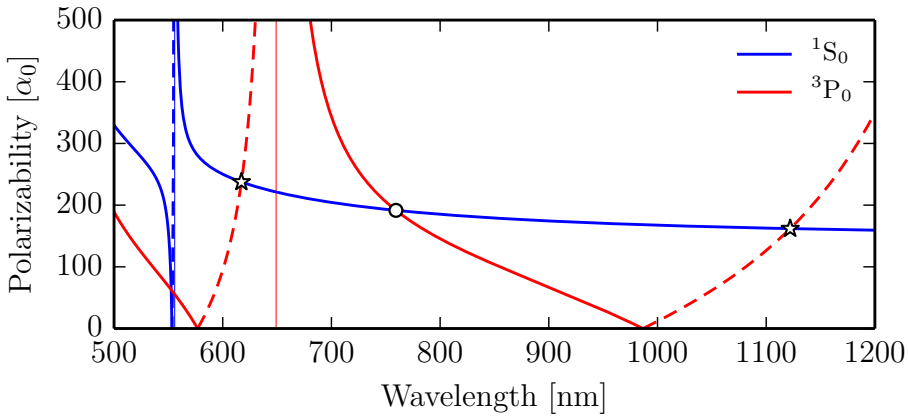

Figure 1.3: Absolute value of the real part of the dynamic polarisability for the $^1S_0$ ground state and $^3P_0$ metastable state of ytterbium, in units of the atomic polarisability $\alpha_0 = 4\pi\epsilon_0 a_0^3$. Solid lines denote positive values, whereas dashed lines denote negative values. The *magic* wavelength at $\lambda_m \approx 759.35\,\mathrm{nm}$ is indicated by a circle. *Anti-magic* wavelengths at $\lambda_{am} \approx 617\,\mathrm{nm}$ and $\lambda_{am,2} \approx 1122\,\mathrm{nm}$ are indicated by stars. Thin vertical lines indicate divergences due to transitions to excited states: around 555.8 nm for the $6s^2\,{}^1S_0$–$6s6p\,{}^3P_1$ transition and around 649.1 nm for the $6s6p\,{}^3P_0$–$6s7s\,{}^3S_1$ transition.

Optical dipole traps are usually realised using simple Gaussian laser beams. More advanced beam-shaping can be achieved using spatial light modulators and gives the ability to design light potentials at will. This has allowed recent developments such as optical micro-traps (Nogrette et al. 2014), uniform box potentials (Gaunt et al. 2013; Chomaz et al. 2015; Ville et al. 2017) or to address single atoms at a time (Zupancic et al. 2016; Barredo et al. 2016; Endres et al. 2016).

1.1.4 Protected spin degrees of freedom

An important feature of fermionic AEL atoms is the decoupling between electronic angular momentum and nuclear spin degrees of freedom. The absence of electronic angular momentum $J = 0$ in the ground $^1S_0$ and metastable $^3P_0$ states makes the nuclear spin degree of freedom I the only angular momentum degree of freedom, isolated inside the nucleus. The angular degree of freedom of the atom is thus decoupled from the dynamics happening at the electronic level. This is potentially interesting for quantum computing (Gorshkov et al. 2009) and precision metrology (Boyd et al. 2006).

Moreover, spin-changing collisions are expected to be suppressed and collisional properties between atoms in the clock states should be independent from the nuclear spin. This leads to a high SU($N = 2I + 1$) [SU stands for special unitary group] symmetry in the interaction potential for fermions (for example $I = 5/2$ for ^{173}Yb). The interaction parameters between atoms with different nuclear spins are in principle as numerous as the number of nuclear spin states. The description of interactions is thus drastically simplified in SU(N) symmetric systems for which the interaction parameters are all equal. Fermionic many-body systems with $N > 2$ are rare in nature, the case $N = 2$ (corresponding to an electron) being already well-studied, in particular using alkali atoms. AEL atoms offer numerous prospects since the nuclear spin of most fermionic isotopes is bigger than 1/2 (with I up to 9/2 for ^{87}Sr). This offers interesting perspectives in studying Fermi liquid instabilities or poorly understood condensed matter problems (Cazalilla et al. 2009; Gorshkov et al. 2010; Scazza et al. 2014; Cazalilla et al. 2014).

1.2 Optical lattices

While standing waves of light were first introduced as a mean to cool down atoms (Grynberg et al. 2001), they rapidly became an important tool to study degenerate quantum gases (Bloch 2005). Standing light wave conservative potentials are called *optical lattices*, in reference to the crystal-like spatial structure they provide. As such, ultracold degenerate quantum gases loaded in these periodic potentials are often considered as one of the most versatile tools to simulate condensed matter problems, for example by realising the celebrated Bose- and Fermi-Hubbard Hamiltonians (Lewenstein et al. 2007; Bloch et al. 2008). The first milestone in that respect was the observation of the superfluid-Mott insulator transition for bosons (Greiner et al. 2002b), followed a few years later by the identification of Mott-like phases for fermions (Jördens et al. 2008; Schneider et al. 2008). Many more experiments have been exploring the physics of degenerate quantum gases in optical lattices since then [see for example Gross et al. (2017)].

More recently, the advent of *quantum gas microscopy* (Bakr et al. 2010; Sherson et al. 2010; Cheuk et al. 2016a; Greif et al. 2016) allowed unprecedented control over lattice-based quantum gases. A quantum gas microscope is able to image a two-dimensional optical lattice with single-site resolution[6]. Important achievements with this approach have recently been carried out. For instance spatial spin correlations between neighbouring sites were accurately measured (Boll et al. 2016; Cheuk et al. 2016b; Parsons et al. 2016; Brown et al. 2017). The Fermi-Hubbard anti-ferromagnet with doping was realised

[6]Note that the light used for fluorescence measurement induces binary collisional losses (DePue et al. 1999), incidentally leaving zero or one atom in the sites depending on the initial parity of the occupation. This prevents from differentiating empty and doubly-occupied sites for example. Nevertheless, technical solutions have been found to bypass this problem (Preiss et al. 2015).

(Mazurenko et al. 2017). Also, many-body localisation in two-dimensions was studied by Choi et al. (2016).

In this section, I recall fundamental results about the physics of degenerate gases in optical lattices. Most of what is discussed here can be found in a more complete form in Ashcroft et al. (1976), Greiner (2003) and Bloch et al. (2008).

1.2.1 Optical lattice potentials

Optical lattices result from the interference of overlapping laser beams with near-equal wavelengths. Using the phase, frequency and wavevector orientation degrees of freedom, all possible Bravais lattice geometries can in principle be derived from a few laser beams (Grynberg et al. 2001). The most simple optical lattice is obtained by overlapping two counter-propagating laser beams with the same frequency. The resulting optical potential varies sinusoidally in space and is the building block for the simplest optical lattices in one-, two- and three-dimensions. In this thesis, we focus on the cubic lattice, obtained by superimposing three 1D optical lattices at right angles, with equal wavelength λ (wavevector $k = 2\pi/\lambda$). By choosing orthogonal polarisations, we ensure that the three 1D lattices do not interfere with each other. The potential experienced by the atoms is therefore well approximated by:

$$V_{\mathrm{OL}}(\boldsymbol{r}) = V_x(\boldsymbol{r}) \cos^2(kx) + V_y(\boldsymbol{r}) \cos^2(ky) + V_z(\boldsymbol{r}) \cos^2(kz)\,. \tag{1.9}$$

This creates a cubic optical lattice with spatial periodicity $d = \lambda/2$ in all three directions of space, with the lattice sites at the zeros of V_{OL}. The Gaussian envelope of the laser beams entails a Gaussian envelope on the optical lattice, resulting in slowly varying external trapping potentials $V_{\alpha=x,y,z}(\boldsymbol{r})$. The size of the atomic sample is usually much smaller than the waist of the laser beams creating the optical lattices so that the external trapping potentials vary almost quadratically with position $V_\alpha(\boldsymbol{r}) \propto r^2$. In turn the potential experienced by the atoms is captured by the simpler form:

$$V_{\mathrm{OL}}(\boldsymbol{r}) = V_{0,x} \cos^2(kx) + V_{0,y} \cos^2(ky) + V_{0,z} \cos^2(kz) + \frac{M}{2}\left(\Omega_x^2 x^2 + \Omega_y^2 y^2 + \Omega_z^2 z^2\right). \tag{1.10}$$

The maxima of the potential $V_{0,\alpha}$ in each direction of space are called the *lattice depths* and Ω_α are the external trapping frequencies associated with the quasi-quadratic potential induced by the Gaussian profiles of the laser beams. The natural energy scale is the *recoil energy* $E_{\mathrm{R}} = \hbar^2 k^2/(2M)$, which corresponds to the kinetic energy an atom would acquire by absorbing a photon from one of the laser beams constituting the optical lattices.

Band structure of a 1D lattice

The Hamiltonian for an atom in a 3D cubic lattice is separable in the spatial coordinates, so that it is sufficient to study the problem in one dimension and deduce the result for higher dimensions. In the following, we study the spectrum and eigenfunctions of an atom trapped in a uniform 1D optical lattice $V_{\mathrm{OL}}(x) = V_0 \cos^2(kx)$. According to Bloch's theorem (Ashcroft et al. 1976), the eigenvectors $|n, q\rangle$ (also called Bloch waves) are given by the product of a spatially periodic function (with the same period as the optical lattice) and of a plane wave with *quasimomentum* q. Due to the periodicity of the problem, it is sufficient to define q in the so-called first Brillouin zone $q \in]-\pi/d, \pi/d]$ (Ashcroft et al. 1976). At finite lattice depth, the eigenenergies of the system group in *energy bands*

separated by band gaps that grow with the lattice depth. These energy bands are labelled with an integer n starting from the lowest energy band, also called fundamental band. As the lattice depth is increased, the bands become flatter with a curvature increasing with the band index. Only bands with energies smaller than the lattice depth provide states trapped in the lattice potential (bound states).

Wannier basis

Bloch waves describe quantum states that are delocalised over the entire lattice, analogous to plane waves in the continuum. They are defined up to a constant global phase. For the upcoming discussion, it is convenient to set up a new basis of localised states: the Wannier basis. Wannier functions w_i^n (band n and site i) are constructed by Fourier transformation of the Bloch waves with respect to q (Wannier 1937):

$$w_j^n = \sqrt{\frac{d}{2\pi}} \int_{-\pi/d}^{\pi/d} \mathrm{d}q \; |n, q\rangle \, \mathrm{e}^{-\mathrm{i}jdq}. \tag{1.11}$$

All Wannier functions can be deduced from each other through a simple translation by a lattice vector:

$$w_j^n(x) = w_0^n(x - jd). \tag{1.12}$$

The Wannier functions depend on the choice of the global phase factor of the Bloch waves used to construct them. For a symmetric potential $V(-x) = V(x)$ with a local minimum at the origin, there exists for every energy band n a unique Wannier function w_0^n which is (Kohn 1959):

1. real-valued,
2. symmetric or anti-symmetric with respect to the origin,
3. and which falls off exponentially with the distance.

Very deep lattices: disconnected harmonic wells

While Wannier functions do not possess an analytical expression in general, the case of very deep lattice depth ($V_0 \gg E_\mathrm{R}$) provides an interesting limit. In such a case, the potential can be approximated by an array of disconnected harmonic potentials centred near the lattice sites in $x_i = id$ (see Figure 1.4a):

$$V_\mathrm{OL}(x \approx x_i) \underset{V_0 \gg E_\mathrm{R}}{\approx} \frac{M}{2} \omega_\mathrm{ho}^2 (x - x_i)^2, \tag{1.13}$$

with $\hbar\omega_\mathrm{ho} = 2\sqrt{V_0 E_\mathrm{R}}$. The bands are approximately flat and centred around the energies $E_n \approx \hbar\omega_\mathrm{ho}(n+1/2)$. The Wannier functions are well approximated by their corresponding harmonic oscillator wave functions. For instance, the fundamental band Wannier function is given by (see Figure 1.4b):

$$w_i^0(x) \underset{V_0 \gg E_\mathrm{R}}{\approx} \frac{1}{\pi^{1/4}\sqrt{\sigma_\mathrm{ho}}} \mathrm{e}^{-(x-x_i)^2/(2\sigma_\mathrm{ho}^2)}, \tag{1.14}$$

with $\sigma_\mathrm{ho} = \sqrt{\hbar/(M\omega_\mathrm{ho})}$.

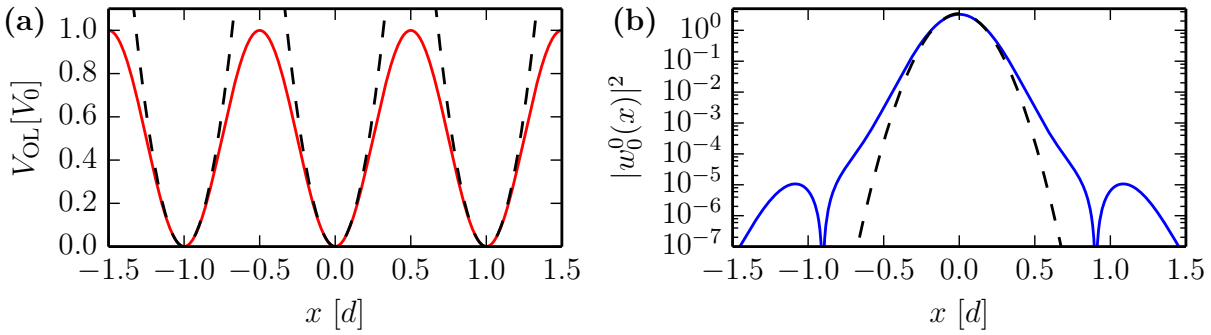

Figure 1.4: (a) Sketch of the sinusoidal optical lattice potential (solid line) and of the harmonic approximation near the bottom of each site (dashed lines). (b) Wannier wave function centred on the site $x_0 = 0$, in the fundamental band of a $V_0 = 15\,E_{\mathrm{R}}$ optical lattice (solid line), computed numerically from (1.11). Harmonic oscillator approximation from (1.14) (dashed line).

Higher dimensions

The extension to 2D or 3D is readily obtained from the previous discussion, owing to the separability of the Hamiltonian. The energies sum up and are labelled by the band index $\boldsymbol{n} = (n_x, n_y, n_z)$. The eigenvectors $|\boldsymbol{n}, \boldsymbol{q}\rangle$ are labelled by their quasimomentum $\boldsymbol{q}$ and constructed as the product of the 1D wave functions.

1.2.2 Bose-Hubbard Hamiltonian

We now turn to the description of interacting bosons in an optical lattice potential, for which we need the suitable formalism of second quantisation. We thus rewrite the non-interacting Hamiltonian $\hat{H}_0 = \hat{\boldsymbol{p}}^2/(2M) + V_{\mathrm{OL}}(\hat{\boldsymbol{r}})$, where $\hat{\boldsymbol{p}} = -\mathrm{i}\hbar\boldsymbol{\nabla}$ is the momentum operator, in the second quantised form:

$$\hat{H}_0 = \int \mathrm{d}^3 r\, \hat{\Psi}^\dagger(\boldsymbol{r}) \left\{ -\frac{\hbar^2}{2M}\nabla^2 + V_{\mathrm{OL}}(\boldsymbol{r}) \right\} \hat{\Psi}(\boldsymbol{r}), \tag{1.15}$$

where $\hat{\Psi}(\boldsymbol{r})$ is the field operator for a particle in $\boldsymbol{r}$. We expand this operator on the Wannier basis $\hat{\Psi}(\boldsymbol{r}) = \sum_{\boldsymbol{i},\boldsymbol{n}} w_{\boldsymbol{i}}^{\boldsymbol{n}}(\boldsymbol{r}) \hat{a}_{\boldsymbol{i}}^{\boldsymbol{n}}$ with $\hat{a}_{\boldsymbol{i}}^{\boldsymbol{n}}$ the annihilation operator on site $\boldsymbol{i}$ and band $\boldsymbol{n}$. Thus:

$$\hat{H}_0 = -\sum_{\boldsymbol{i},\boldsymbol{j},\boldsymbol{n}} J_{|\boldsymbol{i}-\boldsymbol{j}|}^{\boldsymbol{n}} \hat{a}_{\boldsymbol{i}}^{\boldsymbol{n}\dagger} \hat{a}_{\boldsymbol{j}}^{\boldsymbol{n}}, \tag{1.16}$$

$$J_{|\boldsymbol{i}-\boldsymbol{j}|}^{\boldsymbol{n}} = \int \mathrm{d}^3 r\, [w_{\boldsymbol{i}}^{\boldsymbol{n}}(\boldsymbol{r})]^* \left\{ -\frac{\hbar^2}{2M}\nabla^2 + V_{\mathrm{OL}}(\boldsymbol{r}) \right\} w_{\boldsymbol{j}}^{\boldsymbol{n}}(\boldsymbol{r}). \tag{1.17}$$

The quantity $J_{|\boldsymbol{i}-\boldsymbol{j}|}^{\boldsymbol{n}}$ can be interpreted as a matrix element quantifying the coherent tunnelling between the sites $\boldsymbol{i}$ and $\boldsymbol{j}$. The magnitude of this tunnelling energy increases with band index and decreases with site distance $|\boldsymbol{i} - \boldsymbol{j}|$.

Tight-binding limit and single-band approximation

For sufficiently high lattice depths, typically $V_{0,\alpha=x,y,z} \geq 5\,E_{\mathrm{R}}$, tunnelling energies to distant neighbours ($|\boldsymbol{i} - \boldsymbol{j}| > 1$) becomes negligible compared to nearest-neighbour tunnelling. One can therefore keep only the terms that couple sites to their nearest-neighbours

(tight-binding approximation). Moreover, in most experimentally relevant cases only the fundamental band is populated (single-band approximation). Under both assumptions, we can write:

$$\hat{H}_0 \approx -J \sum_{\langle \boldsymbol{i},\boldsymbol{j} \rangle} \hat{a}_{\boldsymbol{i}}^\dagger \hat{a}_{\boldsymbol{j}} + \text{h.c.}, \tag{1.18}$$

where we defined $J = J^{\mathbf{0}}_{|\boldsymbol{i}-\boldsymbol{j}|=1}$ and $\hat{a}_{\boldsymbol{i}} = \hat{a}^{\mathbf{0}}_{\boldsymbol{i}}$. The summation $\langle \cdot \rangle$ is performed on the nearest-neighbour pairs, each pair being counted once.

Interaction energy

We can now include interactions in the model (we restrict their description to low-energy s-wave terms). Under the single-band approximation, the Hamiltonian describing interactions is given by:

$$\hat{H}_{\text{int}} = \frac{1}{2} \sum_{\boldsymbol{i},\boldsymbol{j},\boldsymbol{k},\boldsymbol{l}} U_{\boldsymbol{ijkl}} \hat{a}_{\boldsymbol{i}}^\dagger \hat{a}_{\boldsymbol{j}}^\dagger \hat{a}_{\boldsymbol{k}} \hat{a}_{\boldsymbol{l}}, \tag{1.19}$$

$$U_{\boldsymbol{ijkl}} = g \int \mathrm{d}^3 r \, \left[w_{\boldsymbol{i}}^{\mathbf{0}}(\boldsymbol{r}) \right]^* \left[w_{\boldsymbol{j}}^{\mathbf{0}}(\boldsymbol{r}) \right]^* w_{\boldsymbol{k}}^{\mathbf{0}}(\boldsymbol{r}) w_{\boldsymbol{l}}^{\mathbf{0}}(\boldsymbol{r}), \tag{1.20}$$

with $g = 4\pi\hbar^2 a/M$ the s-wave coupling constant for low-temperature collisions captured by the scattering length a (Ketterle et al. 1999). Due to the localised nature of the Wannier functions, the prevailing term in the summation is purely local: $\boldsymbol{i} = \boldsymbol{j} = \boldsymbol{k} = \boldsymbol{l}$. Higher-order terms are at least two orders of magnitude smaller than the on-site interaction energy $U = U_{\mathbf{0000}}$, and we neglect them in the following. We can thus write:

$$\hat{H}_{\text{int}} \approx \frac{U}{2} \sum_{\boldsymbol{i}} \hat{a}_{\boldsymbol{i}}^\dagger \hat{a}_{\boldsymbol{i}}^\dagger \hat{a}_{\boldsymbol{i}} \hat{a}_{\boldsymbol{i}} = \frac{U}{2} \sum_{\boldsymbol{i}} \hat{n}_{\boldsymbol{i}} \left(\hat{n}_{\boldsymbol{i}} - 1 \right), \tag{1.21}$$

with $\hat{n}_{\boldsymbol{i}} = \hat{a}_{\boldsymbol{i}}^\dagger \hat{a}_{\boldsymbol{i}}$.

Bose-Hubbard Hamiltonian

This discussion leads us to the Bose-Hubbard Hamiltonian which describes interacting bosons in a uniform, single-band, tight-binding optical lattice (Fisher et al. 1989; Jaksch et al. 1998):

$$\hat{H}_{\text{BH}} = \hat{H}_0 + \hat{H}_{\text{int}} = -J \sum_{\langle \boldsymbol{i},\boldsymbol{j} \rangle} \left(\hat{a}_{\boldsymbol{i}}^\dagger \hat{a}_{\boldsymbol{j}} + \hat{a}_{\boldsymbol{j}}^\dagger \hat{a}_{\boldsymbol{i}} \right) + \frac{U}{2} \sum_{\boldsymbol{i}} \hat{n}_{\boldsymbol{i}} \left(\hat{n}_{\boldsymbol{i}} - 1 \right). \tag{1.22}$$

The ground state of this Hamiltonian undergoes a phase transition from a superfluid phase when $U \to 0$ to a Mott insulator phase when $J \to 0$ (Fisher et al. 1989; Jaksch et al. 1998; Greiner et al. 2002b; Zwerger 2003). The ratio U/J between the two relevant energy scales of the system governs the physics. As shown in Figure 1.5, U increases with lattice depth and J falls off exponentially with lattice depth, as a result the ratio U/J is easily spanned over orders of magnitude and the transition can be observed by changing only the lattice depth.

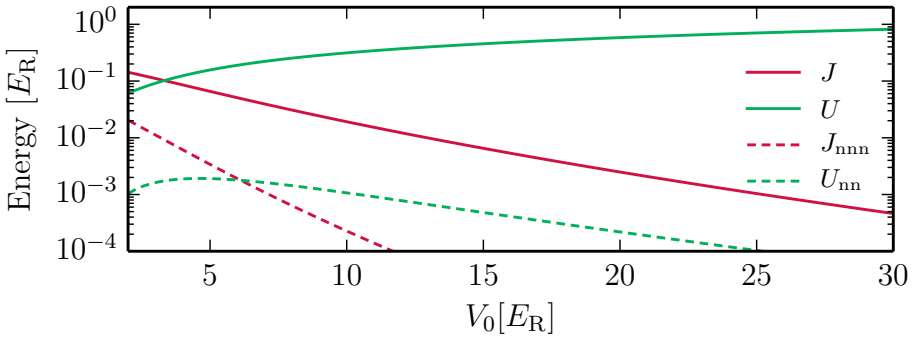

Figure 1.5: Bose-Hubbard parameters J and U versus lattice depth V_0 of an isotropic cubic lattice at $\lambda = 760\,\mathrm{nm}$, calculations are performed for ^{174}Yb. Next-nearest-neighbour tunnelling energy $J_{\mathrm{nnn}} = J^{\boldsymbol{n=0}}_{|\boldsymbol{i}-\boldsymbol{j}|=2}$ and nearest-neighbour interaction energy $U_{\mathrm{nn}} = U_{\mathbf{000}(1,0,0)}$ are shown for comparison.

1.2.3 Phase diagram

The Bose-Hubbard Hamiltonian is not analytically solvable in general, but its phase diagram has been extensively studied using quantum Monte Carlo simulations (Pollet 2012) or other numerical techniques. In particular, the phase boundary at the transition superfluid-Mott insulator is well known for one-, two- and three-dimensional cubic lattices with integer filling fractions $\bar{n} = N/N_{\mathrm{s}} = 1$ [N is the number of atoms and N_{s} the number of sites in the lattice] (Capogrosso-Sansone et al. 2007; Capogrosso-Sansone et al. 2008; Ejima et al. 2011). In the following I discuss the phase diagram of the Bose-Hubbard model (1.22) for a uniform system.

In the non-interacting limit $U \to 0$, the ground state is an ideal BEC where all atoms are in the $\boldsymbol{q} = \mathbf{0}$ Bloch state of the lowest band, well-described by a product of coherent states over the sites (Zwerger 2003):

$$|\Psi_{\mathrm{SF}}\rangle = \prod_{\boldsymbol{i}} |\alpha = \sqrt{\bar{n}}\rangle_{\boldsymbol{i}} \;\text{ with }\; |\alpha\rangle_{\boldsymbol{i}} = \mathrm{e}^{-|\alpha|^2/2} \sum_{n=0}^{\infty} \frac{\alpha^n}{\sqrt{n!}} |n\rangle_{\boldsymbol{i}} \,. \tag{1.23}$$

In the atomic limit $J \to 0$, the ground state is given by a product of Fock states over the sites (Zwerger 2003):

$$|\Psi_{\mathrm{MI}}\rangle = \prod_{\boldsymbol{i}} |\bar{n}\rangle_{\boldsymbol{i}} \,. \tag{1.24}$$

For arbitrary U/J there is no simple analytical expression for the ground state. Noting that in both aforementioned limits, the ground state is simply a product over all sites, an approximate method consists in postulating the existence of such a factorised state for every U/J:

$$|\Psi_{\mathrm{G}}\rangle = \prod_{\boldsymbol{i}} |\phi\rangle_{\boldsymbol{i}} \,, \tag{1.25}$$

$$|\phi\rangle_{\boldsymbol{i}} = \sum_{n=0}^{\infty} c(n) \, |n\rangle_{\boldsymbol{i}} \,. \tag{1.26}$$

This factorised ansatz [called *Gutzwiller* wave function (Rokhsar et al. 1991)] is exact in the two limits $U \to 0$ ($|\phi\rangle = |\alpha = \sqrt{\bar{n}}\rangle$) and $J \to 0$ ($|\phi\rangle = |\bar{n}\rangle$). The approximated ground

state is calculated using a variational method, minimising the free energy $\mathcal{G}$:

$$\mathcal{G} = \langle \Psi_{\mathrm{G}} | \hat{H}_{\mathrm{BH}} - \mu \sum_{\boldsymbol{i}} \hat{n}_{\boldsymbol{i}} | \Psi_{\mathrm{G}} \rangle , \tag{1.27}$$

where μ is the chemical potential, i.e. the energy required to add one particle to the system. For a uniform system this takes on the following expression:

$$\frac{\mathcal{G}}{N_{\mathrm{s}}} = -zJ|\bar{a}|^2 + \frac{U}{2}\langle \hat{n}^2 \rangle - \left(\mu + \frac{U}{2}\right)\bar{n}, \tag{1.28}$$

$$\bar{a} = \langle \phi | \hat{a} | \phi \rangle = \sum_{n=0}^{\infty} \sqrt{n+1} c^*(n) c(n+1), \tag{1.29}$$

$$\bar{n} = \langle \hat{n} \rangle = \sum_{n=0}^{\infty} n |c(n)|^2. \tag{1.30}$$

z is the number of nearest-neighbours, $\bar{n}$ is the filling fraction or mean number of atoms per lattice site. The expectation value of the annihilation operator $\bar{a} = \langle \phi | \hat{a} | \phi \rangle$ represents the superfluid order parameter and vanishes only for a Mott insulator state. $|\bar{a}|^2$ gives the condensate fraction. The solution of the numerical minimisation is given in Figure 1.6. The approximated phase boundaries for the superfluid-Mott insulator transitions are depicted with thick black lines.

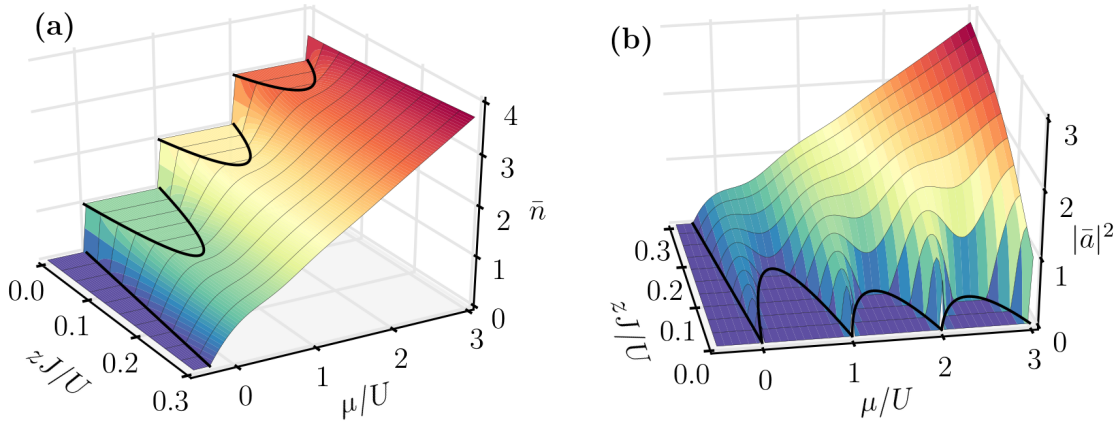

Figure 1.6: Bose-Hubbard phase diagram for an isotropic cubic lattice ($z = 6$). The phase boundaries at the superfluid-Mott insulator transition are depicted with thick black lines. (a) Filling fraction $\bar{n}$ on a lattice site versus chemical potential and ratio zJ/U. In the atomic limit $zJ/U \to 0$, we find a staircase with integer filling fractions. For increasing tunnelling energy, Mott plateaus with integer fillings are separated by increasing superfluid regions, until they completely disappear. (b) Superfluid order parameter $\bar{a}$ versus chemical potential and ratio zJ/U. $\bar{a}$ vanishes in the Mott insulating regions.

Density distribution for a non-uniform trapping potential

The external trapping potentials $V_{x,y,z}(\boldsymbol{r})$ provided by the Gaussian envelope of the lattice beams breaks the discrete translational symmetry. In this situation, band theory (and

the ensuing discussion) is strictly speaking not valid any longer. However, when the external confinement varies slowly on the scale of the lattice spacing d, the local density approximation holds and one can define a local chemical potential

$$\mu_{\mathrm{loc}}(\boldsymbol{r}) = \mu - V(\boldsymbol{r}), \tag{1.31}$$

given by the chemical potential of the whole gas with an offset set by the external trapping potential. The density profile of a gas trapped with an external potential is therefore given by $n(\boldsymbol{r}) = \bar{n}[zJ/U, \mu_{\mathrm{loc}}(\boldsymbol{r})]$. One can find the radial density profile by considering a straight line at a given zJ/U ratio in Figure 1.6a, starting from the chemical potential in the center of the cloud $\mu = \mu_0$, the density profile is given by the line which goes downhill towards $\mu = -zJ$ where the density vanishes. Such cuts through the phase diagram are shown in Figure 1.7 for various energy ratios $U/(zJ)$.

In typical experiments, the external trapping potential is well approximated by a harmonic potential varying as κr^2 [see 1.10]. In the atomic limit $J \to 0$, the Mott insulator phase $\bar{n} \in \mathbb{N}$ atoms per site is reached when $\mu_{\mathrm{loc}} = U\bar{n}$. This corresponds to the radii

$$r_{\bar{n}} = \sqrt{\frac{U}{\kappa}}\sqrt{\frac{\mu_0}{U} - \bar{n}} \text{ with } \bar{n} \in \mathbb{N}. \tag{1.32}$$

Mott phases with given integer filling fraction $\bar{n}$ are also called *Mott shells*, due to the shell-like spatial structure of the Mott plateau in two- and three-dimensions.

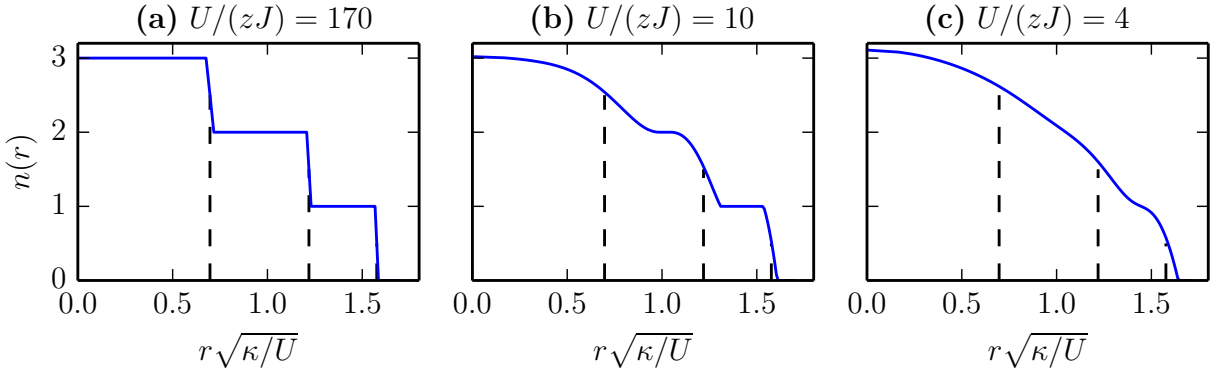

Figure 1.7: Radial density profiles for an isotropic cubic lattice ($z = 6$), the chemical potential is fixed to $\mu_0 = 2.5\,U$. (a) Mott insulator regime with $U/(zJ) = 170$. The integer filling plateaus are well defined. (b) Intermediate regime with $U/(zJ) = 10$, the plateau with $\bar{n} = 1$ is still well defined but the plateau with $\bar{n} = 2$ is gone. (c) Superfluid regime with $U/(zJ) = 4$. In all plots, the vertical dashed lines indicate the expected radii $r_{\bar{n}}$ for $\bar{n} = 1, 2, 3$.

1.2.4 Correlations for many-body systems

The various observables of interest in a many-body system can all be expressed in terms of correlation functions. Usually only few-body correlation functions are considered. For example, the one-body density matrix

$$\hat{\rho}^{(1)}(\boldsymbol{r}, \boldsymbol{r}') = \langle \hat{\Psi}^\dagger(\boldsymbol{r})\hat{\Psi}(\boldsymbol{r}')\rangle\,, \tag{1.33}$$

describes spatial phase correlations. The atomic density can be retrieved with $n(\boldsymbol{r}) = \hat{\rho}^{(1)}(\boldsymbol{r}, \boldsymbol{r})$. For a Bose-Einstein condensate we get $\hat{\rho}^{(1)}(\boldsymbol{r}, \boldsymbol{r}') \approx N|\phi_0|^2$, where N is the number of particles in the condensate and ϕ_0 is the wave function of the condensate. As such, Bose-Einstein condensates possess infinite long-range phase correlations. In optical lattices, the superfluid phase possess long-range phase correlations but in the Mott insulator phase $\hat{\rho}^{(1)}(\boldsymbol{r}, \boldsymbol{r}')$ decays exponentially. Quantum coherence is however not absent but hidden in second-order correlations: density-density correlations. See for example the experiments in Fölling et al. (2005) with bosons or Rom et al. (2006) with fermions.

Higher-order density matrices $\hat{\rho}^{(i)}$ (with i up to N for N particles) can be constructed using $2i$ field operators in normal order:

$$\hat{\rho}^{(i)}(\boldsymbol{r}_1, \cdots, \boldsymbol{r}_{2i}) = \langle \hat{\Psi}^\dagger(\boldsymbol{r}_1) \cdots \hat{\Psi}^\dagger(\boldsymbol{r}_i) \hat{\Psi}(\boldsymbol{r}_{i+1}) \cdots \hat{\Psi}(\boldsymbol{r}_{2i}) \rangle \,. \tag{1.34}$$

In optical lattices, where the field operators can be expanded in the Wannier Basis $\hat{\Psi}(\boldsymbol{r}) = \sum_{\boldsymbol{i},\boldsymbol{n}} w_{\boldsymbol{i}}^{\boldsymbol{n}}(\boldsymbol{r}) \hat{a}_{\boldsymbol{i}}^{\boldsymbol{n}}$, spatial correlations between sites are given by the correlators:

$$\mathcal{C}_{\boldsymbol{i}_1, \cdots, \boldsymbol{i}_k}^{\boldsymbol{n}_1, \cdots, \boldsymbol{n}_k} = \langle \hat{a}_{\boldsymbol{i}_1}^{\boldsymbol{n}_1 \dagger} \cdots \hat{a}_{\boldsymbol{i}_k}^{\boldsymbol{n}_k} \rangle \,. \tag{1.35}$$

Such correlators can be directly measured with quantum gas microscopes (Boll et al. 2016; Cheuk et al. 2016b; Parsons et al. 2016; Brown et al. 2017).

In practice, the one-body density matrix can be evaluated using momentum distributions measured in time-of-flight experiments (Bloch et al. 2008). As long as interactions do not perturb the expansion of the atoms (Pedri et al. 2001; Gerbier et al. 2007), the momentum distribution is proportional to the Fourier transform of the one-body density matrix. Other methods use interferences (Andrews et al. 1997) or Bragg spectroscopy (Stenger et al. 1999).

Density-density correlations can be revealed through noise correlations on momentum distributions (Fölling et al. 2005; Rom et al. 2006). Third-order correlation was measured using metastable He* (Hodgman et al. 2011). Second- and third-order correlations have an effect on loss rates (Burt et al. 1997; Kinoshita et al. 2005). Higher-order correlations are difficult to measure in experiments (Bloch et al. 2008; Schweigler et al. 2017). However, one-body spatial correlations are usually the first to decay when a many-body system is subject to a loss of coherence. Therefore, in general, spatial coherence of a many-body system is well captured by the first- and/or second-order density matrices.

1.3 Towards artificial gauge fields

Combining both previously described ingredients, AEL atoms and optical lattices, opens fruitful and vast opportunities for research. Among all these opportunities, we are interested in the possibility to simulate artificial magnetic fields and charges for neutral atoms with laser light (Dalibard et al. 2011; Goldman et al. 2014). Under suitably tailored laser light fields combined with the proper atomic structure, atomic motion becomes analogous to the motion of a charged particle in a magnetic field. The main ingredient to realise these artificial gauge fields is a geometric phase: the Berry phase, which is the analogous of the Aharonov-Bohm phase for charged particles. A handful of experimental techniques have already been proposed [see Goldman et al. (2016) and Aidelsburger (2018) for a review], some of them already realised in laboratories. For instance with state-dressing (Lin et al. 2009), super-lattices (Atala et al. 2013; Aidelsburger et al. 2015), shaken lattices

(Jotzu et al. 2014; Fläschner et al. 2016) or synthetic dimensions (Mancini et al. 2015; Stuhl et al. 2015).

In this section, I describe a specific implementation using laser-induced tunnelling in optical lattices. Following a proposal in Jaksch et al. (2003), the idea is to engineer a state-dependent optical lattice in which motion is induced and controlled by laser light. The net force exerted by the laser can be made orthogonal to the induced motion, thereby mimicking the Lorentz force. The experimental scheme has been adapted to alkaline-earth-like atoms in Gerbier et al. (2010) and I present it here.

1.3.1 Gauge potential and geometric phase

We consider here a particle with mass M and charge e, moving in space under a magnetic field $\boldsymbol{B}(\hat{\boldsymbol{r}})$. The quantum-mechanical description of the dynamics (which would be given by the Lorentz force $\boldsymbol{F} = e\boldsymbol{v} \times \boldsymbol{B}$ in the classical case, with $\boldsymbol{v} = \langle \hat{\boldsymbol{r}} \rangle$ the speed of the particle) is given by the Hamiltonian:

$$\hat{H} = \frac{[\hat{\boldsymbol{p}} - e\boldsymbol{A}(\hat{\boldsymbol{r}})]^2}{2M}, \tag{1.36}$$

where $\hat{\boldsymbol{r}}$ and $\hat{\boldsymbol{p}} = -\mathrm{i}\hbar\boldsymbol{\nabla}$ are the position and momentum operators. The vector potential $\boldsymbol{A}$ is associated to the magnetic field $\boldsymbol{B}$:

$$\boldsymbol{\nabla} \times \boldsymbol{A}(\hat{\boldsymbol{r}}) = \boldsymbol{B}(\hat{\boldsymbol{r}}). \tag{1.37}$$

As such $\boldsymbol{A}$ is only defined up to a gauge transformation.

In the following we consider a static magnetic field in the vertical direction $\boldsymbol{B} = B\boldsymbol{e}_z$. The energy spectrum of the system is given by equally spaced energy levels called Landau levels (Landau 1930):

$$E_n = \hbar\omega_\mathrm{c}\left(n + \frac{1}{2}\right) \text{ with } \omega_\mathrm{c} = \frac{eB}{M}, \tag{1.38}$$

where ω_c is the cyclotron frequency of the particle in the magnetic field B. A length scale emerges from this problem, called the magnetic length:

$$\ell_\mathrm{B} = \sqrt{\frac{\hbar}{eB}}, \tag{1.39}$$

which corresponds to the smallest cyclotron orbit of the particle.

The degeneracy $\mathcal{D}$ of the Landau levels is macroscopic and roughly given by the number of cyclotron orbits fitting in the sample area $\mathcal{S}$:

$$\mathcal{D} = \frac{\mathcal{S}}{2\pi\ell_\mathrm{B}^2} = \frac{\Phi}{\Phi_0}, \tag{1.40}$$

with $\Phi = B\mathcal{S}$ the magnetic flux through the sample and $\Phi_0 = h/e$ the flux quantum.

Aharonov-Bohm phase

Here we switch to a semi-classical description, where the motion of the particle is not quantised any more. The Lagrangian of a free particle in a magnetic field is $L(\boldsymbol{r}, \boldsymbol{v}) =$

$M\boldsymbol{v}^2/2+e\boldsymbol{v}\cdot\boldsymbol{A}$. When the particle moves during an infinitesimal time $\mathrm{d}t$, its wave function acquires a phase given by the action along its path $\delta\boldsymbol{r}$ divided by $\hbar$:

$$\delta\phi = \frac{1}{\hbar}L(\boldsymbol{r},\boldsymbol{v},t)\mathrm{d}t = \frac{M}{2\hbar}\boldsymbol{v}^2\mathrm{d}t + \frac{e}{\hbar}\boldsymbol{A}\cdot\delta\boldsymbol{r}. \tag{1.41}$$

The first term is usually referred to as the dynamical phase and depends on how the particle moves (here its speed). The second term defines a purely geometric phase. If the particle moves around a closed loop in space $\mathcal{C}$, besides the dynamical phase it acquires a phase ϕ_{AB}, the Aharonov-Bohm phase (Aharonov et al. 1959), given by:

$$\phi_{\mathrm{AB}} = \frac{e}{\hbar}\oint_{\mathcal{C}}\boldsymbol{A}(\boldsymbol{r})\cdot\mathrm{d}\boldsymbol{r} = \frac{e}{\hbar}\int_{\mathcal{S}}\boldsymbol{B}(\boldsymbol{r})\cdot\mathrm{d}\boldsymbol{S} = 2\pi\frac{\Phi}{\Phi_0}, \tag{1.42}$$

where we used the Stokes theorem to define the integral over the surface $\mathcal{S}$ defined by the closed contour $\mathcal{C}$. The Aharonov-Bohm phase is a purely geometric quantity and is gauge-independent: $\boldsymbol{A}\to\boldsymbol{A}+\boldsymbol{\nabla}f$ will not change the value of the phase ϕ_{AB}.

Landau gauge

Among all possible gauge choices for $\boldsymbol{A}$, a simple choice is the Landau gauge, defined as:

$$\boldsymbol{A}(\boldsymbol{r}) = -By\boldsymbol{e}_x. \tag{1.43}$$

This gauge breaks the rotational symmetry around the z-direction. This is a suitable gauge for the description of gauge fields in an optical lattice, where the rotational symmetry is broken anyway.

1.3.2 Realising the Harper Hamiltonian

We are interested in realising artificial magnetic fields for atoms in optical lattices, for which the continuum description given so far is not adequate. Nevertheless, the previous description for the dynamics of a charged particle in the continuum can be mapped to a discretised space using the Peierls substitution (Peierls 1933). It consists in allowing tunnelling matrix elements between nearest-neighbours of a tight-binding lattice to be complex. The phase acquired on hopping should thus be related to the Aharonov-Bohm phase in order to describe the same dynamics in the continuum limit of vanishing lattice spacing. The phase of the tunnelling matrix element between nearest-neighbour sites $\boldsymbol{i}$ and $\boldsymbol{j}$ is given by:

$$\phi(\boldsymbol{i}\to\boldsymbol{j}) = \frac{e}{\hbar}\int_{\boldsymbol{r}_{\boldsymbol{i}}}^{\boldsymbol{r}_{\boldsymbol{j}}}\boldsymbol{A}(\boldsymbol{r})\cdot\mathrm{d}\boldsymbol{r}. \tag{1.44}$$

The tight-binding Hamiltonian including these modified tunnelling matrix elements is called Harper Hamiltonian and reads:

$$\hat{H}_{\mathrm{Harper}} = -J\sum_{\langle\boldsymbol{i},\boldsymbol{j}\rangle}\mathrm{e}^{\mathrm{i}\phi(\boldsymbol{i}\to\boldsymbol{j})}\hat{a}_{\boldsymbol{j}}^{\dagger}\hat{a}_{\boldsymbol{i}}. \tag{1.45}$$

We now consider a two-dimensional square lattice in the xy-plane, with period d and sites labelled by indices (m,n), as sketched in Figure 1.8. In the Landau gauge we have:

$$\phi[(m,n)\to(m+1,n)] = -\frac{e}{\hbar}Bd^2n, \tag{1.46}$$

$$\phi[(m,n)\to(m,n+1)] = 0, \tag{1.47}$$

so that the Harper Hamiltonian becomes:

$$\hat{H}_{\text{Harper}} = -J \sum_{m,n} \mathrm{e}^{-\mathrm{i}\chi n} \hat{a}^\dagger_{m+1,n} \hat{a}_{m,n} + \hat{a}^\dagger_{m,n+1} \hat{a}_{m,n} + \text{h.c.}, \tag{1.48}$$

$$\chi = \frac{eBd^2}{\hbar} = \left(\frac{d}{\ell_{\text{B}}}\right)^2 = 2\pi \frac{\Phi}{\Phi_0}. \tag{1.49}$$

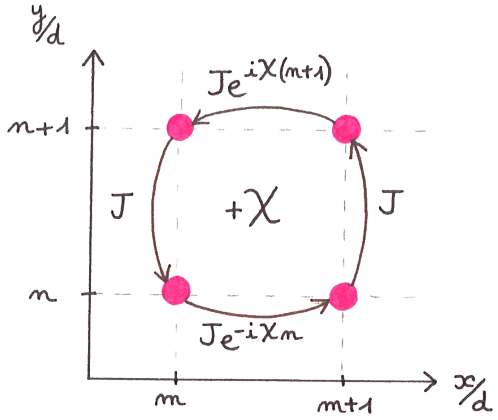

Figure 1.8: Illustration of the Harper Hamiltonian. When a particle performs a counter-clockwise closed loop around a square cell of the lattice it acquires the phase $+\chi$. *Figure designed with Marion Bouganne.*

When the particle performs a counter-clockwise closed loop around a square cell of the lattice (see Figure 1.8), it acquires the phase $+\chi$, the equivalent of the Aharonov-Bohm phase in the continuum. Useful magnetic field values thus make χ vary between 0 and 2π, or equivalently the magnetic flux through a unit cell $\Phi = Bd^2$ varies between 0 and 1 flux quantum. In a semi-classical picture, this can be understood as the regime of cyclotron orbit radii ℓ_{B} as small as the size of a unit cell, below which the discrete nature of the lattice makes it irrelevant.

Topology

The band structure of the Harper Hamiltonian possesses a distinctive feature related to the complex-valued tunnelling coefficients: it is *topological*. This was first understood by Thouless et al. (1982) in the frame of the quantum Hall effect, they calculated the Hall conductivity of a band insulator of non-interacting electrons in a Harper lattice. They showed that when the Fermi energy lies in a gap, the Hall conductivity σ_{H} divided by the conductance quantum e^2/h is a sum of integers:

$$\sigma_{\text{H}} = \frac{e^2}{h} \sum_n \mathcal{C}_n, \tag{1.50}$$

where the sum runs over the filled bands n. The integer $\mathcal{C}_n$ is the so-called Chern number, a topological invariant which characterises the band n. The fact that Chern numbers can only take integer values provides a certain *robustness* of the band structure properties under perturbations. The Chern number associated to a band can change if and only if a gap separating it from another one closes. Such robustness is at the heart of many

systems, including quantum Hall systems, which are referred to as 'topological insulators' (Hasan et al. 2010; Qi et al. 2011; Bernevig et al. 2013).

An important concept deeply connected to topology is the *bulk-edge* correspondence, which arises when considering finite size samples. In such a case robust states appear in the gap between two topological bands, these states are called *edge states* due to their spatial localisation on the boundaries of the sample. We provide an illustration of this in the next paragraph. For a good introduction to the topic we refer the reader to the discussion in Livi (2018), or for more in-depth information to a recent review concerning topology with ultracold atoms (Cooper et al. 2018).

1.3.3 Energy spectrum and edge states in the rational case

In general, the translational symmetry of the lattice problem is lost due to the complex phase of the tunnelling coefficients. A periodicity is however recovered when the flux ratio $\chi/(2\pi) = \Phi/\Phi_0$ is a rational $\chi/(2\pi) = p'/p$. In that case, the Harper Hamiltonian in the Landau gauge (1.48) becomes periodic along y with an elongated period pd. The new unit cell of the lattice, called the *magnetic cell*, now contains p sites, which provides p energy bands in the spectrum.

Energy spectrum

Diagonalising the Harper Hamiltonian leads to the iconic Hofstadter butterfly (Hofstadter 1976), which is shown in Figure 1.9.

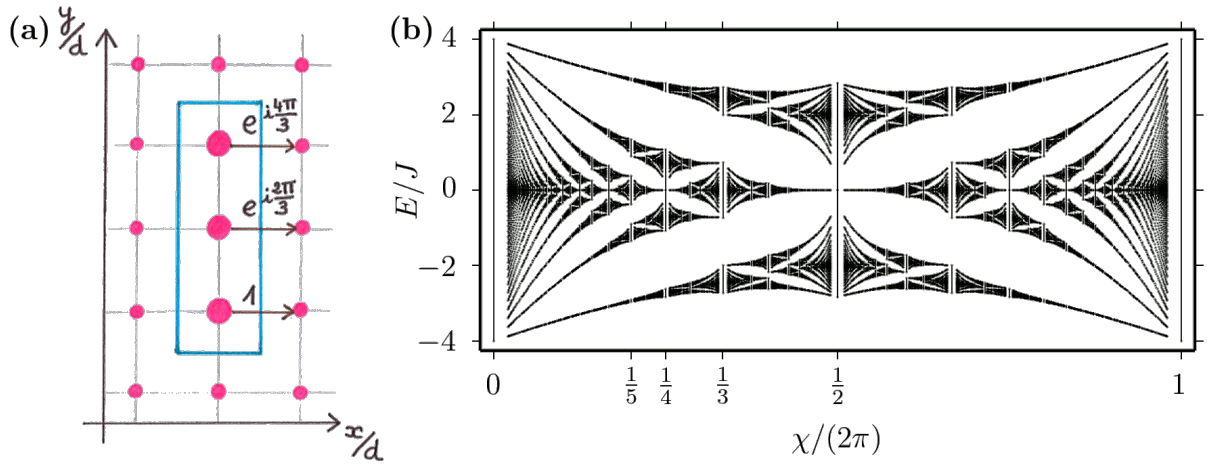

Figure 1.9: (a) Example of a unit cell of the Harper Hamiltonian in the Landau gauge for the flux $\chi/(2\pi) = 1/3$. (b) Hofstadter butterfly: energy spectrum of the Harper Hamiltonian, calculated for rational values of the flux ratio $\chi/(2\pi) = p'/p$ between 0 and 1, with p and p' integers smaller than 50. Simple rational values in $1/p$ clearly show p different bands. *Figure designed with Marion Bouganne.*

The numerical computation of the energy spectrum is performed using Bloch's theorem on the magnetic lattice, whose first Brillouin zone is $]-\pi/d, +\pi/d] \times]-\pi/(pd), +\pi/(pd)]$. We find the energy spectrum by diagonalising the p-dimensional Hamiltonian for each

quasimomentum $\boldsymbol{q}$ (Bernevig et al. 2013):

$$\hat{H}_p(\boldsymbol{q}) = -J \begin{bmatrix} 2c_0 & 1 & 0 & 0 & \mathrm{e}^{\mathrm{i}pdq_y} \\ 1 & \ddots & 1 & \ddots & 0 \\ 0 & 1 & 2c_n & 1 & 0 \\ 0 & \ddots & 1 & \ddots & 1 \\ \mathrm{e}^{-\mathrm{i}pdq_y} & 0 & 0 & 1 & 2c_{p-1} \end{bmatrix} \quad \text{with } c_n = \cos\left(dq_x + \chi n\right). \tag{1.51}$$

The matrix elements of $\hat{H}_p(\boldsymbol{q})$ can be understood in terms of the real space nearest-neighbour couplings:

- Couplings between sites inside the magnetic cell are given by J, those are situated in $\hat{H}_p(\boldsymbol{q})$ on the secondary diagonals.
- Couplings between two magnetic cells in the vertical direction link both extremities of magnetic cells and are given by $J\mathrm{e}^{\mathrm{i}pd\boldsymbol{e}_y\cdot\boldsymbol{q}}$, situated in the corners of $\hat{H}_p(\boldsymbol{q})$.
- Couplings between two magnetic cells in the horizontal direction link similar sites and are therefore situated on the principal diagonal of $\hat{H}_p(\boldsymbol{q})$, the n-th site in the magnetic cell is coupled to similar sites with a complex tunnelling and hence $2c_n = \mathrm{e}^{\mathrm{i}(d\boldsymbol{e}_x\cdot\boldsymbol{q}+2\pi np'/p)} + \mathrm{e}^{-\mathrm{i}(d\boldsymbol{e}_x\cdot\boldsymbol{q}+2\pi np'/p)}$.

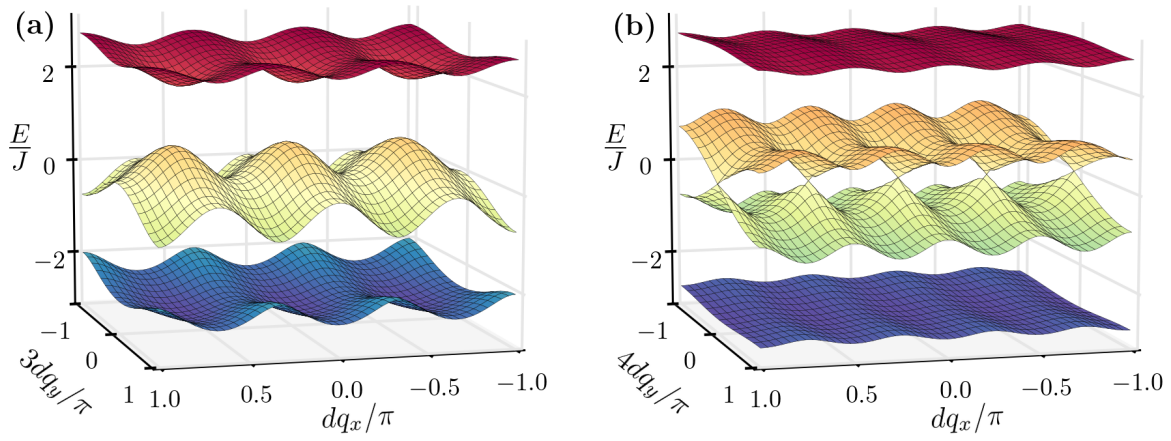

Figure 1.10: Energy bands for the Harper Hamiltonian in the Landau gauge: (a) $\chi/(2\pi) = 1/3$ with 3 bands, (b) $\chi/(2\pi) = 1/4$ with 4 bands.

The energy bands of $\hat{H}_p$ are shown for two specific values of the magnetic flux in Figure 1.10. The p bands are separated by gaps. The Hofstadter butterfly in Figure 1.9 is obtained by collapsing the energy bands on a vertical line.

Edge states

The previous discussion relied on Bloch's theorem, which assumes infinite periodic systems. What happens if we break translational symmetry by imposing open boundary conditions? This can be looked at by considering periodic boundary conditions along x and open boundary conditions along y. The momentum space diagonalisation of the Harper Hamiltonian can be done along the x direction only. The resulting Hamiltonian

for a system with N_s sites along the y direction is thus:

$$\hat{H}_{N_s}(q) = -J \begin{bmatrix} 2c_0 & 1 & 0 & \cdots & 0 \\ 1 & \ddots & 1 & \ddots & \vdots \\ 0 & 1 & 2c_n & 1 & 0 \\ \vdots & \ddots & 1 & \ddots & 1 \\ 0 & \cdots & 0 & 1 & 2c_{N_s-1} \end{bmatrix} \text{ with } c_n = \cos(dq + \chi n). \tag{1.52}$$

The energy spectrum of $\hat{H}_{N_s}$ is shown in Figure 1.11a for $\chi/(2\pi) = 1/3$ and $N_s = 40$. The black energy bands are the *bulk* levels and correspond to the infinite situation considered in the last paragraph. The Chern numbers associated to these bands are +1, -2 and +1, in ascending order (Thouless et al. 1982). The intermediate levels appear because of the open boundary conditions and cross the gaps. These levels provide *edge* states as seen in Figure 1.11b-c, where we plot the spatial probability distribution $|\psi|^2$ of the eigenvectors corresponding to the energy levels indicated by dashed lines in Figure 1.11a. The 'Hall conductivity' of the states is related to the sum of the Chern numbers of the lower bands. This is highlighted with the color code red/blue, with which we see that the quasi-momenta associated to each side of the sample are inverted with respect to the band gap (the lower band gap has a 'Hall conductivity' $\propto +1$, the upper band gap has a 'Hall conductivity' $\propto +1 - 2 = -1$).

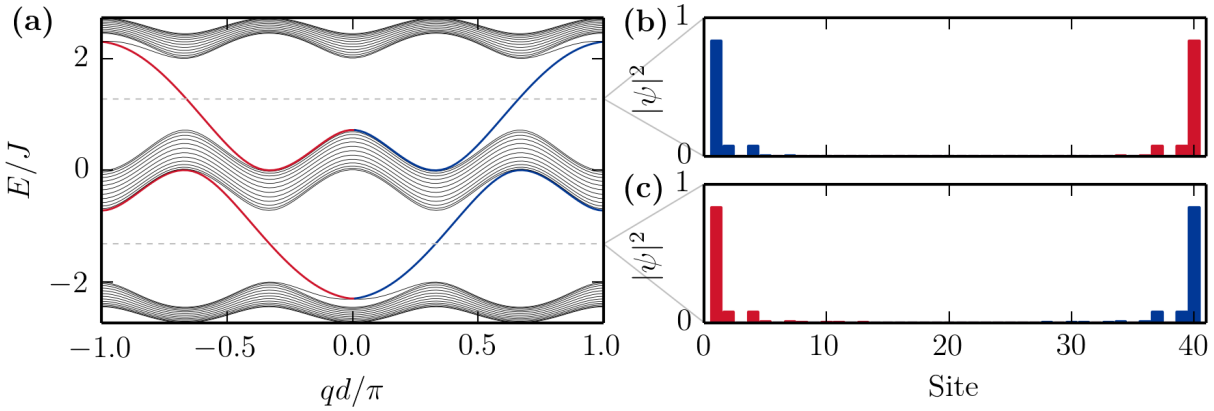

Figure 1.11: Edge states in the Harper Hamiltonian for $\chi/(2\pi) = 1/3$. (a) Energy spectrum of the Harper Hamiltonian in the Landau gauge for open boundary conditions in one direction ($N_s = 40$). (b) Spatial probability distribution $|\psi|^2$ of the eigenvectors corresponding to the energy $E \approx 1.3\,J$ and $q \approx \pm 0.67\,\pi/d$. (c) Spatial probability distribution $|\psi|^2$ of the eigenvectors corresponding to the energy $E \approx -1.3\,J$ and $q \approx \pm 0.33\,\pi/d$.

1.3.4 Many-body physics with orbital magnetism

So far our discussion has been restricted to single-particle effects, which already exhibit very rich possibilities for exploration with quantum gases (Goldman et al. 2014; Cooper et al. 2018). Understanding the influence of interactions in systems subject to orbital magnetism is the crux for many condensed matter problems. The fundamental process by which an interacting system remains in the ground state under the influence of orbital magnetism is the nucleation of vortices (Bloch et al. 2008). This was experimentally demonstrated with rapidly rotating Bose-Einstein condensates (Madison et al.

2000; Schweikhard et al. 2004), for which the Coriolis force mimics the role of the Lorentz force. In the weakly interacting regime, the nucleated vortices all carry a unit charge and repel each other. In the continuum, the vortices arrange in a triangular structure called Abrikosov lattice, which can be modified using additional potentials such as optical lattices that pin the vortices (Tung et al. 2006).

This description of the ground state in terms of vortex lattices is well suited in the limit of weak interactions, where the number of vortices is small compared to the number of atoms. In that case a mean-field approach is expected to hold. When interactions get stronger, and the number of vortices exceeds the number of atoms, the vortex lattice is predicted to melt and undergo a phase transition to incompressible phases with strong inter-particle correlations (Cooper 2008). Numerous strongly correlated phases of matter are predicted in that context (Bloch et al. 2008). An iconic example is the Laughlin states, which are predicted to be the ground states of the Harper Hamiltonian with inter-particle interactions. These states are at the heart of the fractional quantum Hall effect.

The experimental realisation of these incompressible phases is of paramount importance and within reach of experiments[7] (Cooper et al. 2018). As already mentioned, fractional quantum Hall states for bosons could be explored for the first time. Additionally, anyonic excitations or non-Abelian phases are predicted.

1.3.5 Experimental limitations

Most experimental realisations of artificial gauge fields using ultracold atomic systems are limited by heating mechanisms that prevent the observation of the aforementioned ground states. Here I briefly review the current experimental limitations, and conclude about the chances offered by our experimental solution.

In the case of rotating atomic gases, going beyond the mean-field regime prescribes drastic experimental conditions on the external trapping potential, which are extremely challenging to realise in practice and if not fulfilled could lead to heating (Bloch et al. 2008; Cooper 2008).

In the case of shaken lattices or time-dependent super-lattices, the time modulation of the optical potential combined with inter-atomic collisions induces band transfers and heating, which has precluded the observation of many-body effects[8] (Bilitewski et al. 2015).

Finally, the implementations using Raman transitions with alkali atoms suffer from relatively high spontaneous emission rates associated to the fine structure of the energy levels (Lin et al. 2009; Wang et al. 2012; Aidelsburger et al. 2015). This has prevented the stabilisation of vortices in the Abrikosov lattice for example (Lin et al. 2009).

These heating limitations can be bypassed by considering implementations with the narrow lines of lanthanides (Dreon 2017; Cooper et al. 2018) or AEL atoms (Gerbier et al. 2010), for which the spontaneous emission rates are negligible.

1.3.6 Implementation with ytterbium atoms

A direct implementation of the Harper Hamiltonian is possible using the clock states of AEL atoms in state-dependent optical lattices. While the initial proposal was given in

[7] Note that a first result combining orbital magnetism with two-body interactions has been published recently (Tai et al. 2017), but the system consists of two particles.

[8] See also the discussion in the thesis of Alexandre Dareau (2015).

Jaksch et al. (2003) for alkali atoms, here I describe the extension of Gerbier et al. (2010) to AEL atoms which we plan to implement on the experiment. Throughout this section, I label the clock states $g \equiv {}^1\mathrm{S}_0$ and $e \equiv {}^3\mathrm{P}_0$.

State-dependent lattice

The essential ingredient of the Harper Hamiltonian are the complex tunnelling terms, which provide a non-zero phase when hopping around a unit cell of the lattice. In the Landau gauge, for instance, the complex tunnelling terms all lie in one spatial direction while in the orthogonal one the tunnelling is regular. Complex tunnelling coefficients can be obtained by imprinting a tailored laser phase on the wave function of the atom. The building block is thus a pair of sites which can trap g atoms on one side and e atoms on the other side (see Figure 1.12a). Tunnelling between the two sites can be induced using a resonant photon which transfers the atom from one state to the other. Let us consider such a pair of sites oriented in the x-direction, separated by d_x. The effective tunnelling rate inside the pair is given by:

$$J_{g\to e} = (J_{e\to g})^* = \frac{\hbar\Omega_{\mathrm{cl}}}{2} \mathrm{e}^{\mathrm{i}\boldsymbol{k}_{\mathrm{cl}}\cdot\boldsymbol{R}} \int \mathrm{d}^2 r\, w_e^0(\boldsymbol{r} - d_x\boldsymbol{e}_x/2)\mathrm{e}^{\mathrm{i}\boldsymbol{k}_{\mathrm{cl}}\cdot\boldsymbol{r}} w_g^0(\boldsymbol{r} + d_x\boldsymbol{e}_x/2), \tag{1.53}$$

where Ω_{cl}, $\boldsymbol{k}_{\mathrm{cl}}$ are the Rabi frequency and wavevector of the resonant photon and $\boldsymbol{R}$ is the central position of the site pair. The Wannier functions in the fundamental band have been chosen real and even, so that the integral in (1.53) is real, but the tunnelling coefficient remains complex due to the phase term evaluated in the center of the site pair.

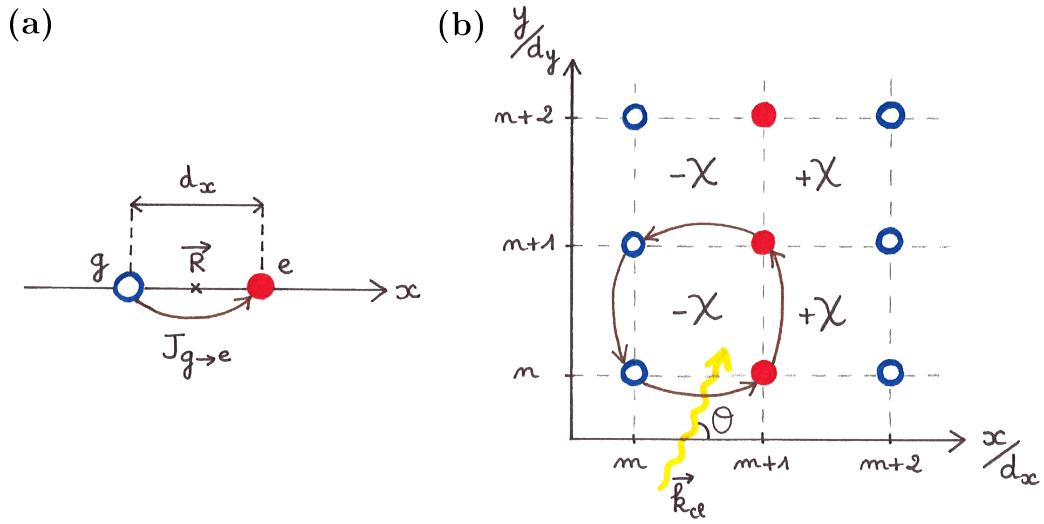

Figure 1.12: (a) Pair of g-e sites, the building block of the state-dependent lattice. (b) State-dependent lattice, with a staggered flux along the x-direction. *Figure designed with Marion Bouganne.*

We can now extend this to create a two-dimensional state-dependent optical lattice, which consists in staggered columns of g and e trapping sites (see Figure 1.12). The optical lattice in the y-direction has a period d_y with regular nearest-neighbour tunnelling. The optical lattice in the x-direction has a period $2d_x$ and tunnelling between nearest-neighbours follows the previous description. We label the site positions by the integers

(m, n), with the choice of g sites on even m. The Peierls phases are:

$$\phi[(m,n) \to (m+1,n)] = (-1)^m k_{\mathrm{cl}} \left[\left(m + \frac{1}{2} \right) d_x \cos\theta + n d_y \sin\theta \right], \tag{1.54}$$

$$\phi[(m,n) \to (m,n+1)] = 0, \tag{1.55}$$

where θ is the angle between $\boldsymbol{k}_{\mathrm{cl}}$ and the x-axis (see Figure 1.12). The total phase accumulated around a closed counter-clockwise square loop encompassing four closest sites is:

$$\chi_{\mathrm{loop}} = \phi[(m,n) \to (m+1,n)] - \phi[(m,n+1) \to (m+1,n+1)] \tag{1.56}$$

$$= (-1)^{m+1} k_{\mathrm{cl}} d_y \sin\theta. \tag{1.57}$$

This accumulated phase is a geometric phase, similar to the Aharonov-Bohm phase, and corresponds to a magnetic flux piercing through the lattice, as shown in Section 1.3.2. However, the flux is homogeneous in the y-direction but staggered in the x-direction. Achievable positive fluxes are:

$$\frac{\chi}{2\pi} = \frac{|\chi_{\mathrm{loop}}|}{2\pi} = \frac{k_{\mathrm{cl}} d_y}{2\pi} \sin\theta = \frac{d_y}{\lambda_{\mathrm{cl}}} \sin\theta, \tag{1.58}$$

which ranges from 0 to $d_y/\lambda_{\mathrm{cl}}$, adjustable with the angle θ. Before discussing how to rectify the flux to make it homogeneous in both directions, let us discuss the actual implementation with ytterbium.

Two-color lattice

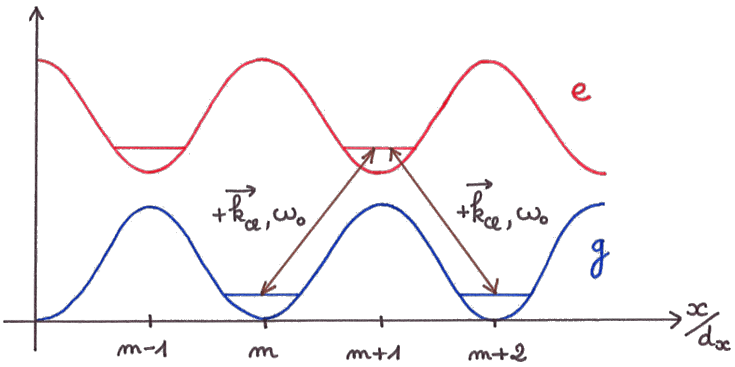

Figure 1.13: Illustration of the two-color lattice in the anti-magic direction. Both links $g \to e$ and $e \to g$ are addressed with the same laser beam with frequency ω_0 and wavevector $\boldsymbol{k}_{\mathrm{cl}}$, leading to the staggered flux configuration of Figure 1.12. *Figure designed with Marion Bouganne.*

Three building blocks are required to generate the previously described scheme:

1. a trapping potential for confining atomic motion in two dimensions,
2. a one-dimensional optical lattice trapping g and e atoms similarly in one direction,
3. a one-dimensional optical lattice trapping g and e atoms separately in the other direction.

The first building block can be realised using a light sheet at the magic wavelength, which freezes the vertical motion of the atoms irrespective of their internal state. We plan to use one anti-node of a one-dimensional optical lattice at the magic wavelength λ_{m} propagating vertically. The experimental difficulty lies in the loading of a unique anti-node from a Bose-Einstein condensate. The second building block can be realised using a one-dimensional lattice at the magic wavelength λ_{m} propagating along the y-direction. The lattice period is $d_y = \lambda_{\mathrm{m}}/2$. The third building block can be realised using a one-dimensional lattice at the anti-magic wavelength λ_{am} propagating along the x-direction (see Figure 1.13). The lattice period is $2d_x = \lambda_{\mathrm{am}}/2$.

The achievable fluxes with this configuration are:

$$\frac{\chi}{2\pi} = \frac{\lambda_{\mathrm{m}}}{2\lambda_{\mathrm{cl}}} \sin\theta \approx 0.65 \sin\theta, \tag{1.59}$$

which allows in principle to scan all relevant values of the flux from 0 to 1/2 by tuning the angle θ.

Validity conditions The Harper Hamiltonian with staggered flux is implemented if the tight-binding and single-band approximations hold.

The single-band approximation holds if the laser induces negligible inter-band transitions. This requires that the Rabi frequency of the coupling is small compared to the band gap between the fundamental and the first excited band of the lattice:

$$\hbar\Omega_{\mathrm{cl}} \ll \Delta_{\mathrm{gap}}. \tag{1.60}$$

Figure 1.14b shows the band gap Δ_{gap} in units of the recoil energy $E_{\mathrm{R,am}} \approx h \times 3\,\mathrm{kHz}$. The condition (1.60) is largely fulfilled for reasonable Rabi frequencies $\Omega_{\mathrm{cl}} \sim 2\pi \times 1\,\mathrm{kHz}$.

The tight-binding approximation can be satisfied easily in the y-direction by considering lattice depths $\gtrsim 5\,E_{\mathrm{R}}$, which restricts tunnelling to the nearest-neighbour terms. In the x-direction, the tight-binding approximation holds if the laser-induced tunnelling between g and e sites prevails over the natural tunnelling terms between two consecutive g or e sites. The condition reads:

$$|J_{g\to e}| \gg J_{g\to g}, J_{e\to e}, \tag{1.61}$$

where $J_{g\to g}$, $J_{e\to e}$ are the natural tunnelling amplitudes along the x-direction. In Figure 1.14a we compare these tunnelling amplitudes. For lattice depths $\gtrsim 20\,E_{\mathrm{R,am}}$, the condition (1.61) is fulfilled.

Super-lattice: flux rectification

The simple scheme presented in the last paragraph creates a staggered magnetic flux in the x-direction of the lattice. This allows to realise the Harper Hamiltonian (1.48) for only two specific values of the flux $\chi/(2\pi) = 0$ or $\chi/(2\pi) = 1/2$ (π is equivalent to $-\pi$). For arbitrary values of the flux $\chi/(2\pi)$ one needs to rectify the flux and make it homogeneous.

The underlying idea behind the flux rectification is to use two different laser beams to address the two tunnelling events $g \to e$ and $e \to g$. By making the two laser beams counter-propagating, the second tunnelling event acquires a minus sign with respect to the first one ($\theta \to \theta + \pi$), thereby compensating for the sign change due to the internal state inversion.

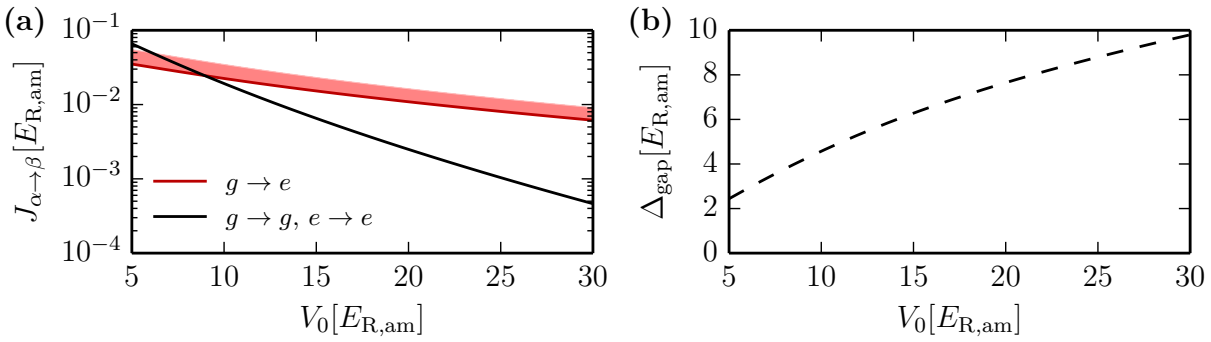

Figure 1.14: (a) Comparison between laser-induced tunnelling $J_{g\to e}$ and natural tunnellings $J_{g\to g}$ and $J_{e\to e}$ for a typical Rabi frequency $\Omega_{\mathrm{cl}} = 2\pi \times 1\,\mathrm{kHz}$. The red shaded area represents the possible values taken by $J_{g\to e}$ when varying the flux $\chi/(2\pi)$ from 0 to 1/2. (b) Band gap Δ_{gap} between the fundamental and the first excited band of the lattice.

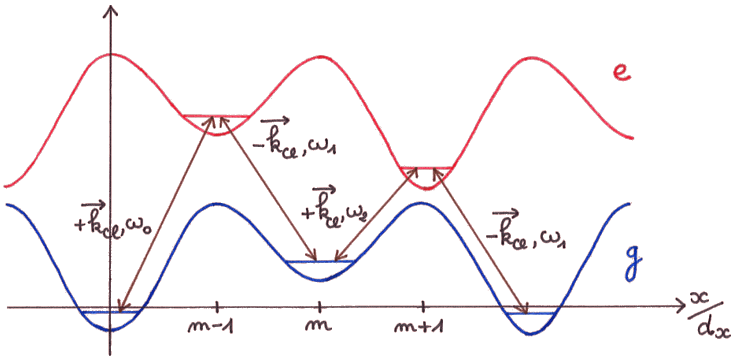

Figure 1.15: Illustration of the rectified two-color lattice in the anti-magic direction, where an optical super-lattice shifts every other sites leading to a doubled periodicity of 4 sites. Links $g \to e$ and $e \to g$ are now addressed with two different laser beams: the first and third links are addressed with two beams with wavevectors $+\boldsymbol{k}_{\mathrm{cl}}$ and frequencies ω_0 or ω_2, the second and fourth links are addressed with a single beam with wavevector $-\boldsymbol{k}_{\mathrm{cl}}$ and frequency ω_1. This leads to a uniform flux configuration. *Figure designed with Marion Bouganne.*

In order to spectrally separate the tunnelling events, and address them with different frequencies, Gerbier et al. (2010) proposed to superimpose along the x-direction an additional optical lattice with a spatial period λ_{am}, equal to twice the spatial period of the main anti-magic lattice[9,10] (see Figure 1.15). By choosing the depth of the super-lattice smaller than the main anti-magic lattice one, the trapping potential remains unchanged for the two internal states but the degeneracy of the transition frequencies is lifted. The unit cell of the lattice is doubled, and one needs to consider four consecutive sites along the x-direction, associated to four different transition frequencies. This scheme thus requires a priori two counter-propagating laser beams with four different frequencies. A careful choice of the relative phase between the anti-magic lattice and the super-lattice

[9]In the actual implementation, the anti-magic lattice laser is derived by second-harmonic generation in a non-linear crystal, as a result the super-lattice wavelength is readily at hand.

[10]A similar implementation has been realised with alkali atoms, the tunnelling being restored by Raman transitions (Aidelsburger et al. 2015).

allows to reduce the number of frequencies to three [see the exhaustive discussion in the thesis of Matthias Scholl (2014)], this situation is sketched in Figure 1.15.

Validity conditions The flux rectification introduces an energy shift Δ_{mod} between successive sites. This additional modulation helps to further suppress natural tunnelling, but must remain small compared to Δ_{gap} in order to prevent resonant tunnelling between bands. This new condition reads:

$$\hbar\Omega_{\mathrm{cl}} \ll \Delta_{\mathrm{mod}} \ll \Delta_{\mathrm{gap}}. \tag{1.62}$$

For an anti-magic lattice depth $\sim 10\,E_{\mathrm{R,am}}$ and a super-lattice modulation $\Delta_{\mathrm{mod}} \approx 3\,E_{\mathrm{R,am}}$, the previous condition is fulfilled [see the benchmark values given in the thesis of Alexandre Dareau (2015)].

Other technical issues regarding the experimental implementation of the Harper Hamiltonian must be contemplated:

- inelastic collisions involving the metastable state e which lead to losses and heating,
- the Gaussian profile of the lattice laser beams, which entail spatially varying detuning between sites that can reduce the laser-induced tunnelling along x or the natural tunnelling along y,
- and the required power level and stability for the lattice lasers to reach the interesting regime of the Harper Hamiltonian.

These points have been addressed extensively in the thesis of Matthias Scholl (2014), where the selected technical solutions are also described in details.

1.4 Summary

In this chapter, I have outlined the context of this thesis work and covered the essential material required to understand the content of later chapters. Firstly, I introduced the specific features of AEL atoms arising from their electronic structure. The pair of valence electrons provide narrow transitions with interesting state-dependent polarisabilities. These features make AEL atoms advantageous for the exploration of various fundamental research prospects, ranging from quantum information processing to many-body physics. Secondly, I recalled the framework of ultracold atoms in optical lattices, with an emphasis on the Bose-Hubbard Hamiltonian and the superfluid-Mott insulator transition. I stressed how one can measure many-body correlations as a way to characterise the system. I finally presented the experimental perspective when combining AEL atoms with optical lattices, namely the realisation of artificial gauge fields for neutral atoms. I indicated why this is crucial for the exploration of strongly correlated phases of matter in a magnetic field and explained the envisioned implementation in our laboratory.

2

Experimental apparatus

The importance of laboratory development can be hidden behind scientific achievements; yet, a significant piece of work lies in the careful construction and daily maintenance of the experimental apparatus. This delicate machinery which provides beautiful observations still occasionally undergoes imponderables of experimental science. In this chapter I summarise the status of the apparatus used for the experiments described in the remainder of the manuscript, and survey its main characteristics and properties. A sketch of the vacuum system and laser beams shone on the atoms is given in Figure 2.1.

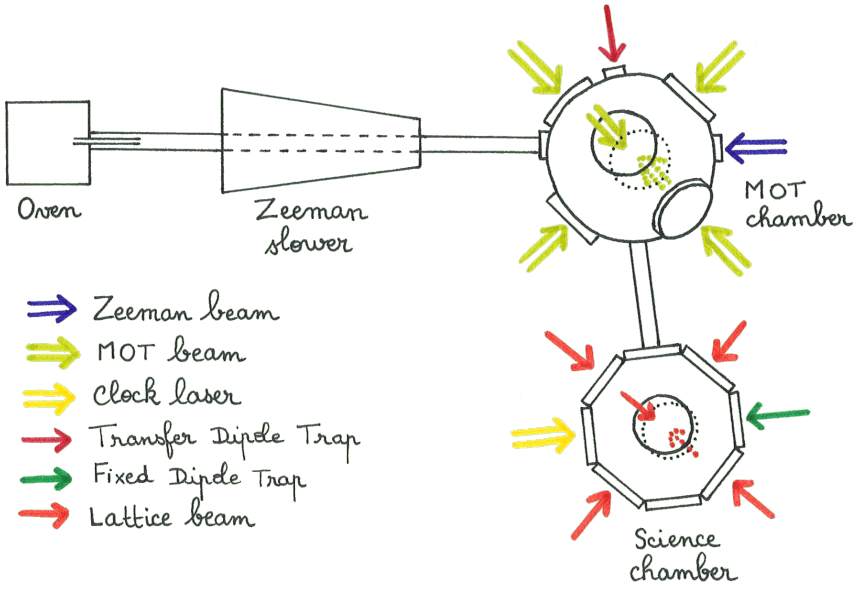

Figure 2.1: Sketch of the vacuum system and laser beams. During an experimental sequence, atoms go from left to right, from the oven to the science chamber. They travel less than two meters in fifteen seconds, but their temperature drops down by ten orders of magnitude. Magneto-optical trapping happens in the MOT chamber, and evaporation leading to condensation occurs in the science chamber. *Figure designed with Marion Bouganne.*

First, I present how we realise Bose-Einstein condensation of ^{174}Yb in an optical trap. Secondly, I describe our detection method, based on absorption imaging, which allows to probe selectively both clock states. Thirdly, I report on the successful loading of a quantum degenerate gas in a three-dimensional optical lattice. Finally, I characterise the laser used to drive the $^1S_0$–$^3P_0$ clock transition of ytterbium.

2.1 Bose-Einstein condensation of ^{174}Yb in a crossed optical dipole trap

In this section I describe how we experimentally realise the Bose-Einstein condensation of ^{174}Yb. Condensation is the starting point of almost all the studies presented in this manuscript. Hence a reliable and stable production of Bose-Einstein condensates (BEC) is paramount. This is achieved through several cooling stages. We first decelerate an atomic beam in a Zeeman slower, operating on the $^1S_0$–$^1P_1$ transition. The slowed-down atoms are then captured and cooled in a magneto-optical trap (MOT), operating on the intercombination $^1S_0$–$^3P_1$ transition. Cooled atoms are then loaded into a far-off resonant dipole trap and subsequently transported by moving the focus of the laser beam into a neighbouring vacuum chamber. There, a second orthogonal laser intersects the first and creates a high-density cloud of atoms in the crossing region. The last step, evaporative cooling, is performed by lowering the power of the dipole traps to reach Bose-Einstein condensation. The experiment, depicted in Figure 2.1, consists of four main parts: the oven, the Zeeman slower, the MOT chamber and the science chamber. More details about the content of this section are given in the theses of Matthias Scholl (2014) and Alexandre Dareau (2015).

2.1.1 Atomic flux generation

Atomic beam

Cold atomic samples are very fragile, and specially sensitive to collisions with the background gas. The lifetime of the samples is greatly reduced if these collisions are too numerous. Preventing such a detrimental effect over the duration of experiments (a few seconds to one minute) requires to work in the so-called ultra-high vacuum (UHV) regime, around or below 10^{-11} mbar. In order to achieve such extremely low pressures, the vacuum enclosure of the experiment is continuously pumped with various ion and non-evaporable getter pumps.

Ytterbium is loaded into an oven in small lumps of metal of about 1 mm^3. The melting point of ytterbium is 824 °C at the standard pressure. The temperature required to produce a high enough vapour pressure to provide sufficient atomic flux is around 500 °C, well below the melting point. At this temperature, the pressure in the vicinity of the oven reaches about 3×10^{-8} mbar. The resulting ytterbium vapour is collimated by a narrow tube at the oven output, providing an atomic flux with a divergence of around 10 mrad. This is the starting point of the experiment. A succession of two differential pumping stages are used to protect the MOT and science chambers from ytterbium contamination and bring down the pressure to around 10^{-10} mbar in the MOT chamber and less than 10^{-11} mbar in the science chamber.

Zeeman slower

The hot atomic beam exiting the oven tube goes through a Zeeman slower, where it is decelerated by a counter-propagating laser beam at $\lambda_b \approx 399$ nm. The design and operation of our Zeeman slower is thoroughly described in the thesis of Alexandre Dareau (2015), the essence of which lies in the radiation pressure exerted by a resonant light beam (Metcalf et al. 1999). Briefly, the laser beam frequency is set close to resonance with the

$^1S_0$–$^1P_1$ transition of ytterbium at 399 nm. A magnetic field gradient shifts the Zeeman sublevels in order to compensate for the varying Doppler shift along the atoms' path and to keep the atoms near resonance with the laser beam. The Zeeman beam is focused so that its divergence matches the calculated divergence of the atomic beam.

The laser used to drive the imaging transition is based on the frequency doubling technique. The fundamental wavelength at 798 nm is derived from a commercial tapered amplifier[1] delivering about 2 W of infrared light. This light is frequency doubled in a non-linear ppKTP[2] crystal of 1 cm length. In order to enhance the output power, the crystal is placed inside a bow-tie cavity. The achieved output power is around 200 mW, which is far from the ideal situation, owing to the occurrence of blue-induced infrared absorption (Tjörnhammar et al. 2015), but still sufficient for our experimental purposes.

Frequency locking

The frequency reference for the laser operating on the imaging transition is obtained via modulation transfer spectroscopy on a hollow cathode lamp. Previously, a standard saturated absorption spectroscopy was performed on the same lamp, but the error signal offset was drifting, shifting away the lock frequency from its set-point. These deviations imposed a regular re-optimisation of the laser frequency for the Zeeman slower, which was detrimental for a proper day-to-day performance of the experiment.

We implemented a modulation transfer spectroscopy set-up because it is much less sensitive to perturbing offset signals than standard saturated absorption spectroscopy (Shirley 1982; Camy et al. 1982). The principle of operation is the following one. Two counter-propagating beams (a pump and a probe) overlap inside the hollow cathode lamp. The pump beam is frequency modulated with an electro-optic modulator (EOM). Both beams interact with the ytterbium atomic vapour inside the lamp and create a non-linear polarisation in the medium. Four-wave mixing processes then yield a modulation sideband in the probe beam itself. This sideband can be detected and demodulated to provide an error signal free of undesired offsets.

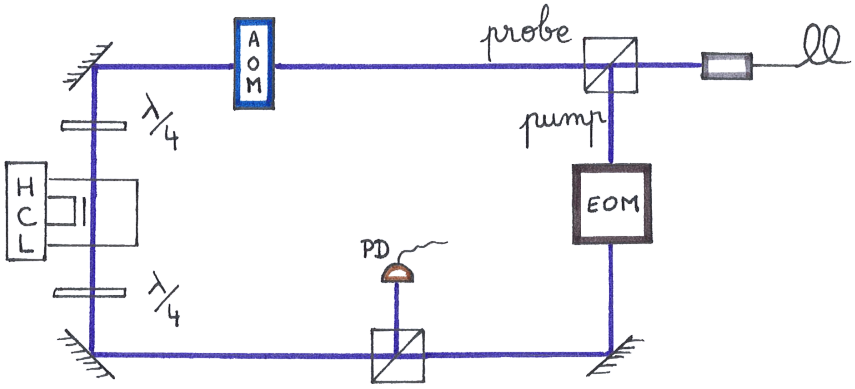

Figure 2.2: Optical set-up for the modulation transfer spectroscopy on a hollow cathode lamp (HCL) of ytterbium. *Figure designed with Marion Bouganne.*

The optical set-up is depicted in Figure 2.2. About 10 mW of blue light drawn from the output of the doubling cavity are split into a pump beam of 8 mW and a probe beam of

[1] TA-Pro, Toptica.

[2] Periodically poled potassium titanyl phosphate, Raicol crystals.

2 mW. The pump beam goes through an EOM modulated at 20.8 MHz. The probe beam is frequency shifted in an acousto-optic modulator (AOM) by 80 MHz. The two beams are sent counter-propagating in the hollow cathode lamp, with circular polarisations, and the probe beam is subsequently detected with a photodiode (PD). A lock-in amplifier then performs the demodulation. The resulting error signal has a signal-to-noise ratio of about 10 and no long-term drift of the offset.

2.1.2 Magneto-optical trapping

MOT operation

Slow atoms coming from the Zeeman slower then reach the MOT chamber, where they get trapped using the intercombination transition at $\lambda_g \approx 556\,\text{nm}$. A detailed presentation of the MOT is done in the thesis of Matthias Scholl (2014). Briefly, a magneto-optical trap is the combination of optical molasses and a quadrupole magnetic field. The optical molasses, created by three orthogonal counter propagating laser beams with circular polarisation, slow down the atoms via Doppler cooling. The quadrupole magnetic field adds a position dependence on the effective cooling force, resulting in a net confinement of the atoms at the center of the quadrupole.

An important feature of a MOT operating on the intercombination transition ($\Gamma_g = 2\pi \times 182\,\text{kHz}$) is a very low Doppler temperature

$$T_D = \frac{\hbar\Gamma_g}{2k_B} \approx 4.4\,\mu\text{K}, \tag{2.1}$$

which is sufficiently small to achieve efficient direct loading into an optical dipole trap. This is important for bosonic isotopes of ytterbium, which are difficult to cool below the Doppler limit (Maruyama et al. 2003). Indeed, in contrast with alkali atoms or fermionic ytterbium, the absence of ground state internal structure prevents sub-Doppler cooling mechanisms (Metcalf et al. 1999),

The laser used to drive the intercombination transition of ytterbium is based again on frequency doubling. The fundamental wavelength at 1112 nm is derived from a commercial fiber laser[3] delivering about 2.5 W of infrared light. This light is frequency doubled in a non-linear ppSLT[4] crystal of 2 cm length. In order to enhance the output power, the crystal is placed inside a bow-tie cavity. The achieved output power is around 900 mW.

The frequency reference for the intercombination transition is obtained via standard saturated absorption spectroscopy on a molecular iodine cell. Details about this spectroscopy device, the frequency lock and the MOT optimisation procedures are given in the thesis of Alexandre Dareau (2015).

Loading the MOT with atoms

The MOT loading can be understood as the competition between two processes. On the one hand, slowed down atoms constantly come from the Zeeman slower to enter the MOT. On the other hand, depletion mechanisms (for example one-body losses, resonant light absorption from the Zeeman beam or excited state collisions) empty the MOT. Assuming

[3] Orange One, Menlo Systems.
[4] Periodically poled stoichiometric lithium tantalate, Covesion.

constant loading characterised by a rate R and a one-body loss rate κ, the differential equation describing the evolution of the atom number N in the MOT is:

$$\frac{\mathrm{d}N}{\mathrm{d}t} = R - \kappa N, \tag{2.2}$$

the solution of which is $N(t) = (1 - \mathrm{e}^{-\kappa t})R/\kappa$. We typically load 10^8 atoms in the MOT with a loading rate $R \approx 10^7\,\mathrm{s}^{-1}$ and a one-body lifetime $\kappa^{-1} \approx 30\,\mathrm{s}$ (extracted from loading curves as in Figure 2.4). A further cooling step is then performed (Scholl 2014), and the achieved final temperature is around 50 µK. Colder temperatures (down to about 10 µK) can be achieved but the final temperature was chosen to maximise the atom number transferred to the optical dipole trap.

2.1.3 Condensation by evaporation

Dipole trap loading and transport

Atoms in the MOT are transferred into a far-off resonant optical dipole trap by superimposing the MOT center on the focus of a high-intensity laser beam, that I label *transfer dipole trap* (TDT) in the remainder. The latter is derived from the output of a fiber laser[5] at $\lambda_{\mathrm{TDT}} \approx 1070\,\mathrm{nm}$. The measured power impinging on the atoms is $P_0 \approx 45\,\mathrm{W}$ focused to a calibrated waist[6] $w_0 \approx 40\,\mu\mathrm{m}$. The focus of the dipole trap is moveable for subsequent transport of the atoms. The dipole trap depth is given by

$$U_0 = \frac{1}{\epsilon_0 c}\alpha_g(\lambda_{\mathrm{TDT}})\frac{P_0}{\pi w_0^2} \approx k_{\mathrm{B}} \times 660\,\mu\mathrm{K}, \tag{2.3}$$

where α_g is the ground state polarisability (Grimm et al. 2000), which is $164\,\alpha_0$ at 1070 nm ($\alpha_0 = 4\pi\epsilon_0 a_0^3$ is the atomic unit of polarisability). This depth, about ten times higher than the MOT temperature, is sufficient for efficient trapping.

We measured the axial trap frequency $\omega_{\mathrm{ax}} = \sqrt{2U_0\lambda_{\mathrm{TDT}}^2/(M\pi^2 w_0^4)}$ and the radial trap frequency $\omega_{\mathrm{rad}} = \sqrt{4U_0/(Mw_0^2)}$ using the atomic cloud response to an external perturbation. The large difference between ω_{ax} and ω_{rad} requires two different measurement methods. First, displacing the focus of the laser beam along its direction of propagation induces oscillations of the center-of-mass of the cloud in the harmonic potential along the axial direction of the trap. Second, parametric excitations induced by modulating the dipole trap power cause atom losses at twice the radial trapping frequency, and also possibly at integer sub-harmonics (Friebel et al. 1998). Both measurements are presented in Figure 2.3. A damped oscillation fit on the center-of-mass movement gives $\omega_{\mathrm{ax}} = 2\pi \times 8.0(1)\,\mathrm{Hz}$. A fit by two equidistant Gaussian functions on the parametric excitation resonances gives $\omega_{\mathrm{rad}} = 2\pi \times 1.42(1)\,\mathrm{kHz}$. The small value of ω_{ax} prescribes the method of center-of-mass oscillations because parametric excitations are not easily performed at such low frequencies. In the kilo-hertz regime, cloud oscillation measurement becomes inaccurate due to the finite imaging time resolution, and parametric excitations are more precise.

If we assume a total power $P_0 \approx 45\,\mathrm{W}$, then the radial frequency measurement gives a value to the waist $w_0 \approx 40\,\mu\mathrm{m}$, which coincides with our independent calibration with a CCD[7] camera. The calculated axial trapping frequency $\omega_{\mathrm{ax}} \approx 2\pi \times 8.5\,\mathrm{Hz}$ also coincides

[5] YLR-50-LP-AC-Y12, IPG Photonics.
[6] $1/\mathrm{e}^2$ diameter.
[7] Charge-Coupled Device.

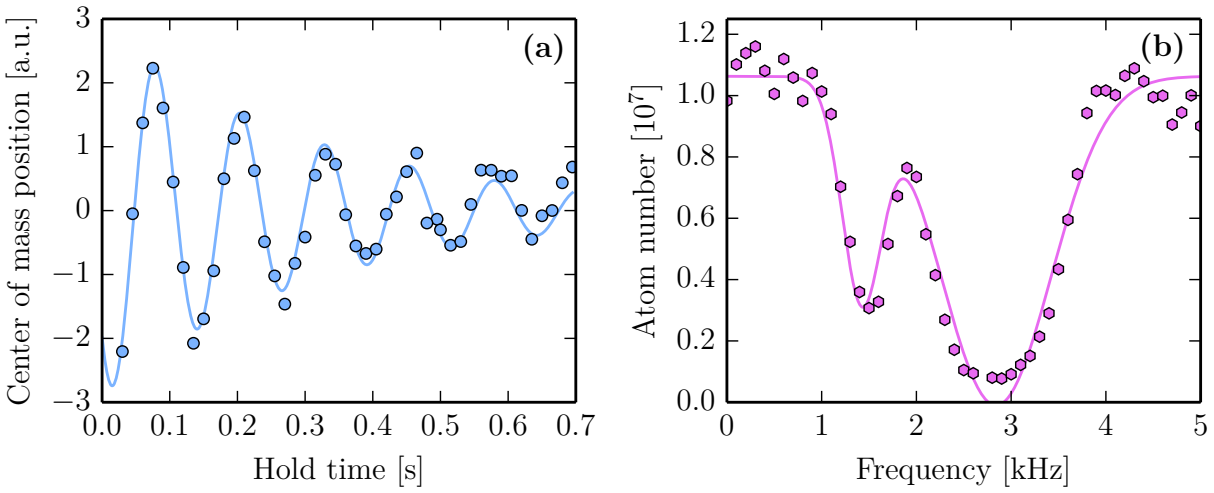

Figure 2.3: Measurement of the transfer dipole trap frequencies. Solid lines are fits to the data (see text). (a) Center-of-mass oscillations give $\omega_{\mathrm{ax}} = 2\pi \times 8.0(1)\,\mathrm{Hz}$. (b) Parametric excitation resonances lead to $\omega_{\mathrm{rad}} = 2\pi \times 1.42(1)\,\mathrm{kHz}$.

with the measured value. Using a time-of-flight expansion of the cloud, we measured the temperature of the cloud

$$T = 40(5)\,\mu\mathrm{K}. \tag{2.4}$$

This justifies the harmonic approximation (implicit when speaking of trap frequencies) for the trap since the condition $R_{\mathrm{th}} \ll w_0$ (R_{th} being the cloud size), or equivalently $k_{\mathrm{B}}T \ll U_0$, is well satisfied.

After optimisation of the loading parameters, we transfer slightly less than 10^7 atoms into the dipole trap (see Figure 2.4a), which corresponds to an efficiency of about 10 %. Such a low transfer efficiency is typical and expected for our parameters (Kuppens et al. 2000). It could be enhanced by changing the geometry of the dipole trap, for example by increasing its waist. This would lead to a less confined cloud, and potentially create problems for the subsequent transport and evaporation. Here we actually saturate the dipole trap in atom number, which is an advantage since it suppresses shot-to-shot atom number fluctuations present in the MOT. An experimental image in Figure 2.4b shows atoms trapped in the dipole trap, and the remaining untrapped atoms from the MOT falling underneath.

Crossed dipole trap and evaporation

Good optical access is crucial to realise optical lattices and artificial gauge fields, as described in Section 1.3. It would be difficult to combine all the laser beams in all the required directions in the MOT chamber directly. Instead, we chose to move the atoms to a science chamber[8] where the optical access is much better.

Atoms are transported over 20 cm in 1 s. This is performed by displacing the focus of the laser beam using a retro-reflecting corner cube mounted on a translation stage. Details on this step can be found in the thesis of Matthias Scholl (2014). After transport, almost 80 % of the atoms are still in the trap. We intersect the focus of the TDT with a second, orthogonal and horizontal dipole trap, labelled *fixed dipole trap* (FDT), with

[8] Spherical octagon, Kimball.

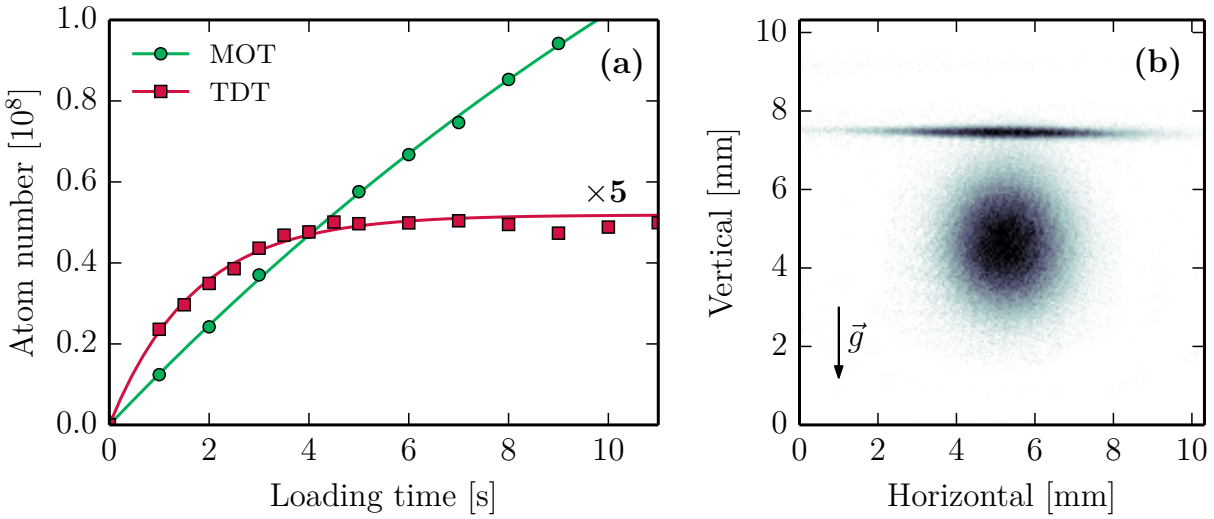

Figure 2.4: (a) Loading curves for the magneto-optical trap and transfer dipole trap. Solid lines are fit to the data using (2.2), loading rates for the MOT and TDT are respectively $10^7\,\mathrm{s}^{-1}$ and $3\times10^6\,\mathrm{s}^{-1}$. Saturation of the dipole trap loading is manifest. (b) Picture of trapped atoms in the dipole trap after a 1 ms time-of-flight expansion, and falling untrapped atoms underneath. Gravity points to the bottom of the picture.

initial power of about 1 W and focused to a waist of 16 µm. In the intersecting region of the crossed dipole traps, the attractive force is much stronger than in the first dipole trap alone, leading to a much higher atomic density. The light used to create the second trap is derived from a commercial source[9] at 532 nm.

Forced evaporative cooling is performed by ramping down the dipole traps power. As the power is lowered, the phase-space density of atoms in the crossing region increases, see Figure 2.5 for an illustration. The power ramp on the FDT is performed controlling the radio-frequency amplitude of an AOM in the path. Since the required final power is about 1 % of its initial value, it is controlled with a standard feedback loop on the AOM driver, with the laser power measured on a standard photodiode. Ramping down the TDT power is more involved for two reasons. First, the high power levels (~ 50 W) incited us not to use an AOM because of possible thermal drifts (Fröhlich et al. 2007). Instead, we can tune the output laser power by changing the laser pump power with an analog input. This leads us to the second difficulty; when the pump power is reduced to less than 10 % of its maximal value, the laser stops operating properly and output light consists mostly of amplified spontaneous emission from the fiber. The required dynamic range for power control (about 1000) is too large to directly implement the loop on the analog input of the laser. Instead, we use a feed-forward signal sent to a rotating waveplate combined with a Glan-Taylor prism that perform the biggest part of the power reduction. The output laser power is then regulated around this feed-forward ramp with the analog input. In this way the pump power of the laser never drops below the lasing threshold. More details on this servo-loop can be found in the thesis of Matthias Scholl (2014).

At the end of the 4 s long evaporation ramp, phase-space density has crossed the condensation threshold. We obtain a Bose-Einstein condensate of typically 6 to 8×10^4 atoms, with no discernible thermal fraction. Typical shot-to-shot fluctuations of the atom

[9] Verdi V-6, Coherent.

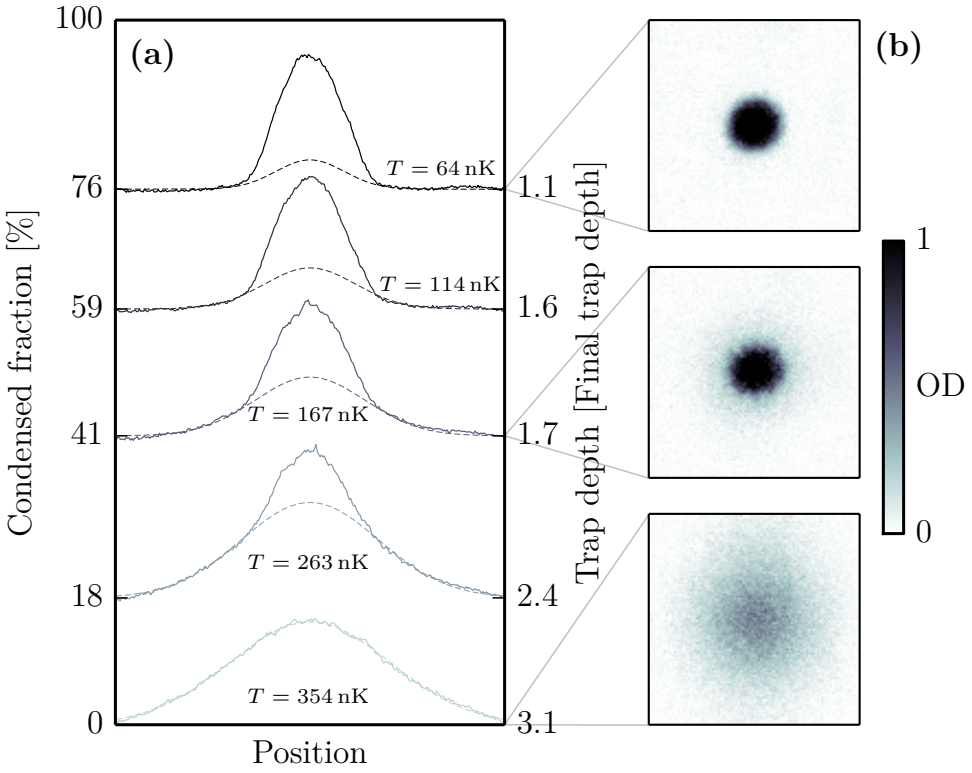

Figure 2.5: Cloud profiles after time-of-flight expansion during evaporation. As the crossed dipole trap power is lowered, evaporation leads to condensation (emergence of a peak in the momentum distribution). (a) Integrated profiles of the atomic cloud versus condensed fraction. The dashed line indicates the remaining thermal fraction, which provides a value for the temperature of the cloud. (b) Pictures of atomic clouds.

number are on the order of 5 %. The trap frequencies of the crossed dipole trap at the end of the evaporation ramps were measured using collective mode oscillations of a BEC: $\{\omega_x, \omega_y, \omega_z\} = 2\pi \times \{60\,\mathrm{Hz}, 230\,\mathrm{Hz}, 260\,\mathrm{Hz}\}$, and $\bar{\omega} = (\omega_x\omega_y\omega_z)^{1/3} = 2\pi \times 153\,\mathrm{Hz}$. This gives a length $a_\mathrm{ho} = \sqrt{\hbar/(M\bar{\omega})} \approx 600\,\mathrm{nm}$ for the harmonic oscillator. With $N_\mathrm{at} = 6 \times 10^4$ atoms, the chemical potential is $\mu = 0.5\hbar\bar{\omega}(15N_\mathrm{at}a/a_\mathrm{ho})^{2/5} \approx h \times 2.8\,\mathrm{kHz}$. The scattering length a describes low-energy s-wave scattering between two atoms, and has been measured in Kitagawa et al. (2008) and Borkowski et al. (2017): $a = 105\,a_0$ with a_0 the Bohr radius. When neglecting the contribution of kinetic energy, the spatial distribution of trapped condensates is an equilibrium between repulsive inter-atomic interactions and the trapping potential. This so-called Thomas-Fermi regime is legitimate when the interaction energy dominates (Ketterle et al. 1999): $\mu \gg \hbar\omega_{x,y,z}$. Thomas-Fermi cloud radii $R_i = \sqrt{2\mu/(M\omega_i^2)}$ are $\{R_x, R_y, R_z\} = \{9.5\,\mu\mathrm{m}, 2.5\,\mu\mathrm{m}, 2.2\,\mu\mathrm{m}\}$ and the central density in the harmonic trap is $n_0 = 15N_\mathrm{at}/(8\pi R_x R_y R_z) = 7.0 \times 10^{14}\,\mathrm{cm}^{-3}$. At these density levels, three-body recombination starts to become important. When three atoms collide, two of them can form a molecule and the binding energy is converted into kinetic energy that expels both the molecule and the third atom out of the trap. The typical time scale for such recombinations is roughly given by $1/(n_0^2 L_3) \approx 0.3\,\mathrm{s}$ with $L_3 \approx 7 \times 10^{-30}\,\mathrm{cm}^6\,\mathrm{s}^{-1}$ (Fukuhara et al. 2009). This sets strong limitations on the achievable total atom number in an optical trap but also on the lifetime of the BEC.

A crucial point to perform efficient evaporation ramps and proper atom number sta-

bility is the alignment of the dipole traps. This alignment, on a micro-meter scale, is very sensitive to temperature variations and day-to-day operation of the experiment. The TDT is derived from the output of a fiber laser and the propagation path to the atoms is larger than two meters, with a lever arm from the last mirror of about half a meter. If we include the fact that the retro-reflecting corner cube is mounted on a moving translation stage, we understand that the focus position is likely to move over time. The FDT comes from the output of a fiber clamped close to the science chamber, and is therefore not as sensitive as the TDT. In order to solve the issue of foci misalignment, we installed a position monitoring and feedback loop for the laser foci position[10]. The foci are both imaged on two separate position sensitive photo-detectors which provide an error signal to motorised mirror mounts. These mounts then correct the position of the foci to a fixed point in space. In practice, this servo loop is mainly turned off and switched on twice a day on average to correct slow, presumably thermal, drifts.

2.2 Detection and optical imaging

In this section I describe an essential tool to measure atomic samples, namely absorption imaging. This technique relies on the resonant absorption of photons by the atoms and is the only detection tool that we use to probe them (Ketterle et al. 1999). The original idea is fairly simple, a large and resonant beam of light is cast on the atoms, and subsequently recorded on a CCD camera. The atoms absorb part of the incoming light and thus leave a shadow in the beam. This shadow carries information about the atomic density integrated along the line of sight. I first present the theory and the experimental implementation for the ground $^1S_0$ atoms. I then explain how we are able to image also the metastable excited $^3P_0$ state. Finally, I describe an algorithm used to enhance the quality of the images, leading to better information about the atomic distribution.

2.2.1 Absorption imaging

Theoretical background

Absorption imaging is performed on the $^1S_0$–$^1P_1$ transition with angular frequency $\omega_b = 2\pi c/\lambda_b$ and width $\Gamma_b = 2\pi \times 29\,\mathrm{MHz}$. Although it would also be possible to use the intercombination transition, we did not implement it so far. The imaging transition is a simple $J = 0$ to $J = 1$ transition with large Γ_b, allowing for efficient cycling. Cooperative events in light absorption or emission and multiple scattering effects can be neglected when the gas density n is sufficiently small, $n[\lambda_b/(2\pi)]^3 \ll 1$ (Labeyrie et al. 2003; Araújo et al. 2016). While this condition typically does not hold for in-situ BEC ($n_0[\lambda_b/(2\pi)]^3 \sim 1$), it becomes well-fulfilled for time-of-flight expansions of a few milliseconds where the density is reduced by orders of magnitude. The density of atoms in the cloud is related to the light intensity absorption through the Beer-Lambert law, at resonance it reads

$$\frac{\mathrm{d}I}{\mathrm{d}z} = -n\sigma_0 \frac{I}{1 + I/I_{\mathrm{sat},0}}, \tag{2.5}$$

where $\sigma_0 = 3\lambda_b^2/2\pi$ is the resonant absorption cross section, I the light intensity, z the coordinate along the direction of propagation of the laser beam and $I_{\mathrm{sat},0} = \hbar\Gamma_b\omega_b^3/(12\pi c^2)$

[10] Aligna 4D, TEM Messtechnik.

the saturation intensity of the transition. After integration, it gives the optical depth $\mathrm{OD} = \sigma_0 \int n \mathrm{d}z$, which can be formulated as

$$\mathrm{OD} = -\ln\left(\frac{I_\mathrm{f}}{I_\mathrm{i}}\right) + \frac{I_\mathrm{i} - I_\mathrm{f}}{I_{\mathrm{sat},0}}, \tag{2.6}$$

where I_f (resp. I_i) is the light intensity in a plane after (resp. before) the atomic cloud. For low-intensity absorption imaging ($I \ll I_{\mathrm{sat},0}$), this reduces to the standard formula for the optical density $\mathrm{OD}|_{I \ll I_{\mathrm{sat},0}} = -\ln(I_\mathrm{f}/I_\mathrm{i})$.

Absorption imaging in the laboratory

The intensities I_i and I_f are actually recorded on the same CCD camera, positioned after the atomic cloud in the laser beam path. A first image is taken with the atoms, giving I_f. This image destroys the sample, and after a few milliseconds of free fall, the atoms are not in the camera field of view any longer. A second image is then taken, giving I_i. In practice, various effects need to be taken into account in order to measure faithfully the optical depth of the cloud and compute the atomic density.

First, for a generic atomic species, the laser beam might not perfectly address the atomic transition, because of polarisation imperfections, resonance detuning, structure of the ground and excited states or magnetic field fluctuations. In this respect, the case of bosonic ytterbium is relatively simple. The absence of hyperfine structure in the ground state (in contrast with fermionic isotopes or alkali atoms) makes the $^1\mathrm{S}_0$–$^1\mathrm{P}_1$ transition a $J = 0 \to J = 1$ transition for which all Clebsch-Gordan coefficients are equal to 1. Additionally, the transition is broad, so that magnetic field fluctuations are negligible in practice. Therefore, as long as polarisation is well-controlled and the frequency of light set to resonance, one can use (2.6) with confidence.

Second, the optical set-up needs to be characterised in order to relate accurately the count levels of the camera to the light intensity at the atomic position. The parameters that enter in the proportionality factor are: photon losses on the path β, quantum efficiency of the detector q_e, bit depth of the analog-to-digital conversion 2^d, magnification of the optical set-up m, pixel size p_s and pulse duration t_p. In the recorded images (with bit resolution 2^r), a pixel level N_level is related to the intensity in the atomic plane I by

$$N_\mathrm{level} = \frac{2^{r-d} q_\mathrm{e} \beta p_\mathrm{s}^2 t_\mathrm{p}}{\hbar \omega_\mathrm{b} m^2} I. \tag{2.7}$$

On the one hand, in the limit of low-intensity ($I \ll I_{\mathrm{sat},0}$), the optical density can be computed with only a ratio of measured intensities, directly accessible from the images. On the other hand, if the second term of (2.6) can not be neglected, one must calibrate the coefficient N_level/I. The coefficient $\beta \sim 1$ can be estimated with power measurements, we assume it be 1. The magnification m needs to be calibrated (see the following paragraph) and all other coefficients are in principle accessible from camera specifications.

Calibration of the magnification

An important quantity to calibrate is the magnification m of the optical imaging set-up. It gives access to the atomic density from the measurement of the optical depth. This calibration is often impossible to do via purely optical means since the object plane lies inside a vacuum chamber. Fortunately, the atoms provide a way to measure it, with

various alternatives. A first option is to use the dependency of the Thomas-Fermi radius of a BEC on the total atom number, but the weak scaling ($\propto N^{1/5}$) does not provide much accuracy. If the camera line of sight is not along gravity, one can use the free fall of the atomic cloud to measure the magnification. This option can be done with condensates but also with thermal clouds and provides a good calibration. Both options are, however, not as convenient as the following one.

The simplest to interpret and probably most accurate technique of calibration uses the matter-wave diffraction of a condensate on an optical grating (light standing wave). The diffracted atomic wavepackets have a velocity related to the wavevector of the light forming the grating. One can measure accurately the wavepackets spacing after a time-of-flight propagation and deduce the magnification based on an accurate knowledge of the properties of the optical grating. We used this option in the experiment to calibrate our imaging system. Specific details about such diffraction patterns is given in Section 2.3.2, but we can draw here a simple argument based on wave-particle duality.

The diffraction of light with wavelength λ_0 on a diffraction grating with slit spacing d gives diffraction peaks at angles $\sin\theta = n\lambda_0/d$, where n is an integer. After a propagation distance $L = ct$ from the grating, the diffraction orders are separated by the distance

$$\Delta x = L\sin\theta = \frac{c\lambda_0}{d}t. \tag{2.8}$$

The diffraction of an atom by an optical grating should behave similarly if we interchange the roles of matter and light. We assume the atom to be a plane matter wave, to which we assign a wavelength equal to its de Broglie wavelength $\lambda_0 \mapsto \lambda_{\mathrm{dB}} = h/(Mv)$, where v is the atomic mean velocity. The slit spacing of the optical grating is $d \mapsto \lambda/2$, where λ is the light wavelength. After propagation on a distance $L = vt$, the diffraction orders are separated by

$$\Delta x = \frac{v\lambda_{\mathrm{dB}}}{\lambda/2}t = 2\frac{\hbar k}{M}t, \tag{2.9}$$

where $k = 2\pi/\lambda$ is the light wavenumber. Relative uncertainties on t and $m\Delta x$ are better than 10^{-3} and relative uncertainties on k and M are negligible. We conclude that the magnification can be measured up to three significant digits.

2.2.2 A repumping laser for the clock state

So far I described how we can image the ground state of ytterbium using absorption imaging on a broad and closed transition. Such a transition does not exist for the metastable clock state. Still, we can measure excited atoms with a two-step procedure. First, we repump them to the ground state with an auxiliary laser, and then we image them with the $^1\mathrm{S}_0$–$^1\mathrm{P}_1$ transition as described above.

Principle of operation

The metastable excited state can be repumped with the $^3\mathrm{P}_0$–$5\mathrm{d}6\mathrm{s}\,^3\mathrm{D}_1$ transition at $\lambda_\mathrm{r} \approx 1389\,\mathrm{nm}$ (see Figure 2.6), with width $\Gamma_\mathrm{r} = 2\pi \times 430\,\mathrm{kHz}$ (Bowers et al. 1996). The upper $5\mathrm{d}6\mathrm{s}\,^3\mathrm{D}_1$ state decays to the $^3\mathrm{P}_J$ states ($J = 0$, 1 and 2). Atoms in the $^3\mathrm{P}_1$ state decay back to the ground state by emitting a photon at 556 nm. The $^3\mathrm{P}_2$ state is a metastable state (Yamaguchi et al. 2010). However, the branching ratio from the $5\mathrm{d}6\mathrm{s}\,^3\mathrm{D}_1$ state

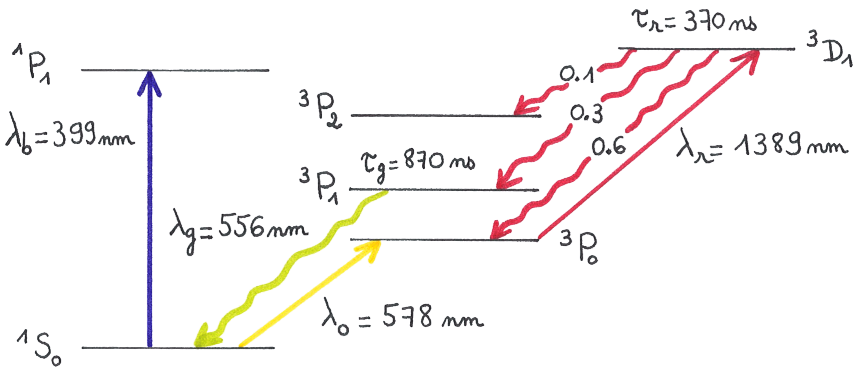

Figure 2.6: Relevant energy levels and transitions for the repumping from the metastable $^3P_0$ state to the ground state. *Figure designed with Marion Bouganne.*

is small (Porsev et al. 1999). Therefore, cycling on $^3P_0$–5d6s $^3D_1$ transition leads to a repumping efficiency η_e from $^3P_0$ to $^1S_0$ close to unity.

Strictly speaking, this repumping transition may also be used to perform direct absorption imaging, with the drawback of not being a closed transition, and at the expense of using a camera sensitive to infrared light. Having only one detection system for both ground and metastable states is easier to operate. Also, the $^3P_0$–6s7s $^3S_1$ transition can also be used as a repumper to the ground state (Scazza 2015), but this option requires two different lasers to operate properly since the branching ratio to the metastable $^3P_2$ state is important.

Experimental implementation

The source used to drive the repumping $^3P_0$–5d6s $^3D_1$ transition is a commercial laser diode[11] with an output power around 20 mW. We illuminate the atoms with a 5 mW collimated beam of about 500 µm waist. For a two-level atom this would lead to a broadening of the transition by saturation to a width of about 100 MHz. In practice, the line is also broadened by excitation time (repumped atoms do not participate in the dynamics any longer) and we observe efficient repumping on a frequency span of about 1 GHz, coinciding with the prediction of optical Bloch equation calculations, as shown in Figure 2.7.

We carefully stabilised the temperature of the diode such that its frequency drift over a day would not be larger than the broadened transition width, thus a frequency lock was not needed. After locating the resonance with the atoms, we only had to keep the laser running around this frequency with a precision accessible by a wavelength meter. The one we have in the laboratory only works in the visible to near infrared spectrum[12], which prevents direct measurement on the laser output. Therefore we chose to frequency double the light at 1389 nm to bridge the gap to the sensitive span of the meter[13].

The repumping efficiency η_e from the metastable state to the ground state was measured to be around 80 % for a 500 µs-long pulse, as shown in Figure 2.7. During such

[11] NEL Laser Diode, NTT Electronics.
[12] WS5, High Finesse.
[13] Details about the actual optical set-up and temperature stabilisation is given in the thesis of Manel Bosch Aguilera (2019).

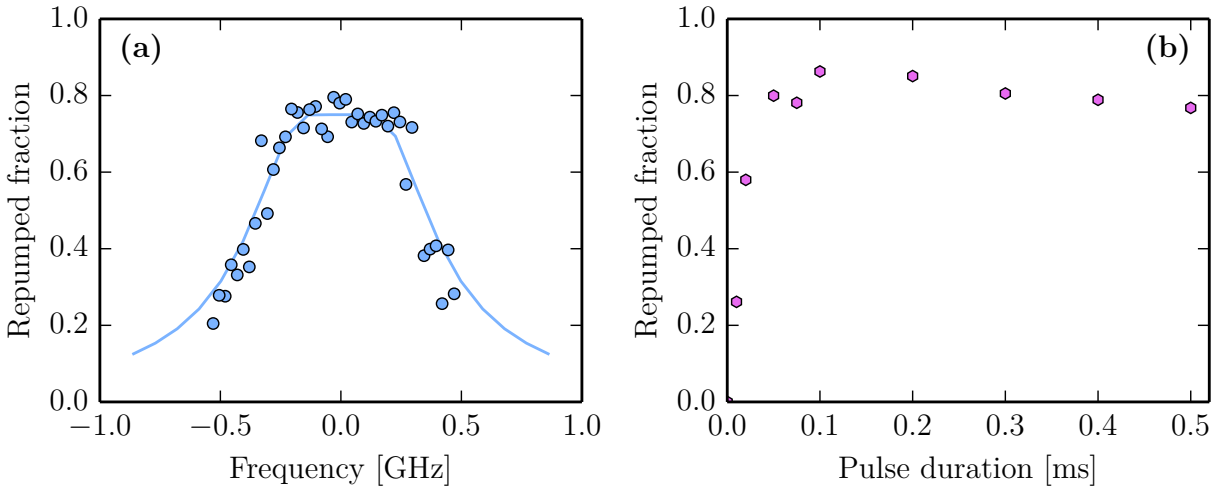

Figure 2.7: Characterisation of the repumping laser. (a) Spectrum of the repumping transition with 500 µs-long pulses, the solid line is a calculation using optical Bloch equations for the 5-level system shown in Figure 2.6. (b) Efficiency of the repumping versus pulse duration.

a pulse, atoms in the ground state are far off-resonant and hardly affected by the light. This allows us to measure the total population in the ground and metastable states.

In order to selectively address the metastable excited atoms, we apply a removal pulse of light on the imaging transition to remove all ground state atoms prior to repumping. With a few µW focused on 40 µm, we are able to get rid of all ground state atoms in 5 µs.

2.2.3 Improving the quality of the images

Limitations on absorption imaging

Absorption imaging parameters must be restricted if one wants to faithfully measure the density distribution of atoms and not only the total atom number. Indeed, absorption imaging can induce substantial modification of the atomic density and velocity distributions through photon recoil. Here I would like to stress some limitations on the number of absorbed photons by the atomic sample.

First, absorbed photons modify the longitudinal speed of the atoms and induce a Doppler shift that should remain smaller than the width of the imaging transition. I call N_{abs} the number of photons absorbed by an atom during an image. Then the Doppler shift is roughly $\Delta\omega \approx N_{\mathrm{abs}}\hbar k_{\mathrm{b}}^2/M$. We want $\Delta\omega \lesssim \Gamma_{\mathrm{b}}$ which means

$$N_{\mathrm{abs}} \lesssim \frac{M\Gamma_{\mathrm{b}}}{\hbar k_{\mathrm{b}}^2} \approx 2100. \tag{2.10}$$

With optical depths on the order of 1, this means about $N_{\mathrm{inc}} \approx 10^3$ incident photons ($N_{\mathrm{abs}}/N_{\mathrm{inc}} \approx 1 - \mathrm{e}^{-\mathrm{OD}}$). Second, spontaneously emitted photons lead to momentum diffusion in the transverse plane (Metcalf et al. 1999). This momentum spread $\Delta p \approx \hbar k_{\mathrm{b}}\sqrt{N_{\mathrm{abs}}/3}$ must induce a displacement during the image time t_{p} smaller than the pixel size p_{s}

$$N_{\mathrm{abs}} \leq \left(\frac{\sqrt{3}Mp_{\mathrm{s}}}{\hbar k_{\mathrm{b}} t_{\mathrm{p}}}\right)^2 \approx 600, \tag{2.11}$$

with $t_p = 25\,\mu s$ and $p_s = 2\,\mu m$. This is the same order of magnitude as before. With typical imaging beam waists of about 1.5 mm, and magnification between 2 and 5, this limits the saturation parameter of the imaging beams to a value slightly bigger than 1. All images taken for this thesis work were obtained with saturation parameters of 1 or less.

A final limitation on the quality of the images is the dead time between the two images taken by the camera. In our experiment, the dead time is about 150 ms, limited by the image transfer from the camera to the computer. This makes the optical depth computation very sensitive to intensity variations during the dead time. In order to get rid of artefacts coming from these fluctuations (background shift or fringes), I implemented a post-treatment algorithm of our images, as described below.

Best-reference picture algorithm

Two images are recorded in a sequence, an image S with atoms and a reference image R without atoms. The reproducibility of the intensity pattern shone on the atoms for S and R is crucial in order to determine faithfully the optical depth. Any intensity fluctuation between the two images in a sequence results in an artificial optical depth. Many technical reasons can create those intensity fluctuations: fluctuation of laser power or polarisation, fluctuation of AOM diffraction efficiency or mechanical vibrations. The dead time between the two images must therefore be reduced to the minimum. While global intensity fluctuations are quite easy to get rid of by simply subtracting a background value on the optical depth, fringes or speckle patterns are very detrimental and not straightforward to remove. This is where the best-reference picture algorithm comes into play.

The basic idea is to construct a best-reference picture Q by linear combination of a set of reference pictures in such a way that S and Q are identical in a region with no atoms (Ockeloen-Korppi et al. 2010; Frapolli 2017). The main assumption is that the background signal of S in the region with atoms is also identical to Q. We decompose Q on the R images set

$$Q = \sum_j c_j R_j, \tag{2.12}$$

where the sum typically runs over 50 images. We want to minimise the quantity $\sum_{\mathbf{x}}(S_{\mathbf{x}} - Q_{\mathbf{x}})^2$, where the sum runs over all the pixels $\mathbf{x}$ for which there is no atomic signal. Setting partial derivatives with respect to the c_j to zero, we get a linear system of equations, for all j:

$$\sum_k c_k b_{jk} = \sum_{\mathbf{x}} R_{j,\mathbf{x}} S_{\mathbf{x}} = a_j, \tag{2.13}$$

where $b_{ij} = \sum_{\mathbf{x}} R_{i,\mathbf{x}} R_{j,\mathbf{x}}$. $B = (b_{ij})$ is a square matrix, $A = (a_k)$ and $C = (c_k)$ are column vectors. In order to solve the linear system $A = BC$, we split B using the (LU) decomposition: we can always write $B = PLU$ where P is a permutation matrix, L a lower triangular matrix and U an upper triangular matrix. We then compute C using a two-step linear solver, first we solve $LD = P^{-1}A$ in order to find $D = UC$. Then we solve $UC = D$ in order to find C.

Linear algebra packages allow for the fast computation of the (LU) decomposition and solving of linear systems with triangular matrices. For a given set of images, the (LU) decomposition of B can be calculated once, and C is then calculated for each image S. This is an efficient post-processing algorithm that allows to enhance the quality of the images. A quantitative study of the performance of the algorithm can be found

in Appendix A.1. In this thesis, I applied the algorithm to all images concerning the decoherence study of a superfluid in Chapter 4. In Chapter 3, we are only interested in integrated atom numbers for which the algorithm is not necessary.

2.3 Quantum gas of ytterbium in 2D optical lattices

In this section I report on the experimental achievement of quantum degeneracy in two-dimensional (2D) optical lattices (see Section 1.2 for some theoretical background). This is performed by adiabatic loading of a BEC into three-dimensional optical lattices. The detrimental effect of gravity prescribes a specific loading sequence that I describe in detail. It leads to the realisation of a stack of 2D optical lattices. I then present the characterisation of the trapping potential created by the lattice beams, both the on-site lattice depth and the external harmonic confinement. As a benchmark of our system, the achievement of the quantum phase transition from a superfluid to a Mott insulator is shown. Finally, I describe a collapse and revival experiment that allows for a direct calibration of the on-site interaction strength.

2.3.1 Loading sequence

The laser source used to create the optical lattices is a Ti:Sapphire laser[14] operating at the magic wavelength $\lambda_m \approx 759.35\,\text{nm}$, and pumped by a 16 W commercial 532 nm laser source[15]. We split the 4 W output of the laser into three different paths. Each of them goes through an AOM for power regulation and frequency shifting. The outgoing beams are sent through optical fibers to the experiment and focused in the science chamber where they intersect at right angles. In addition to the frequency shifts provided by the AOMs[16], polarisations are orthogonal to each other in order to minimise mutual interferences. After passing through the chamber, each beam is collimated by a lens and retro-reflected by a mirror. The overlapping forward- and retro-beams create a standing wave. Optical lattice beam waists in the chamber can be found in Table 2.1.

Adiabatic transfer into optical lattices

Before discussing our actual transfer sequence, I want to stress the relevant adiabaticity timescales prescribed by the loading into optical lattices, where atomic confinement near a lattice site is much stronger than in dipole traps. The lattice beams must be ramped up slowly enough to ensure that the gas remains close to the many-body ground state. A necessary condition is that the transfer must not induce inter-band transitions. If this is achieved and the atoms occupy the lowest band, the loading must not create density excitations in the gas.

The first criterion is the adiabaticity with respect to the band structure of the lattice. It can be grasped in a single-particle picture by considering the general adiabatic criterion applied to one particle in a one-dimensional lattice. For vanishing lattice depth V_0, we assume that the condensate occupies the fundamental band of the lattice ($n = 0$) with close-to-zero quasi-momentum ($q \approx 0$). The relevant adiabaticity criterion is given in

[14] SolsTiS, M Squared.

[15] Finesse, Laser Quantum.

[16] The frequency difference between the beams must be much larger than all energy scales in the system, typically we set the difference to few MHz, such that any residual interference averages out.

Ben Dahan et al. (1996), for sufficiently shallow lattices and quasi-momenta far from the Brillouin zone edges, it reads

$$\left|\frac{1}{E_\mathrm{R}}\frac{\partial V_0}{\partial t}\right| \ll 32\sqrt{2}\frac{E_\mathrm{R}}{\hbar} \approx 5.6\times 10^5\,\mathrm{s}^{-1}, \tag{2.14}$$

with $E_\mathrm{R} \approx h \times 1973\,\mathrm{Hz}$. Adiabaticity is therefore easily fulfilled with ramps in the millisecond regime.

The second criterion is the adiabaticity with respect to the density distribution of the cloud. Power ramps must be slow enough to ensure reshaping of the atomic distribution keeping a constant chemical potential. Three relevant energy scales describe the physics in optical lattices:

1. the tunnelling energy J,
2. the on-site interaction energy U,
3. the external harmonic confinement frequency Ω.

When increasing the lattice depth, U and Ω increase slowly, whereas J falls off exponentially. For a weakly interacting system forming a condensate, the adiabaticity criterion roughly quantifies the ability for the atomic distribution to match the instantaneous equilibrium Thomas-Fermi distribution through tunnelling. If the ramps are too fast, atoms do not have time to redistribute spatially, which leads to an increase of entropy and to heating of the atomic sample. Following Gericke et al. (2007), a criterion can be given as

$$\mathcal{A} = \max\frac{\hbar|\dot{J}|}{J^2} \ll 1. \tag{2.15}$$

We use the actual experimental ramps to compute $\mathcal{A}$ (as seen in Figure 2.8) and find that the critical value for which this parameter gets smaller than unity happens for ramps longer than 80 ms, close to our experimental optimisation time.

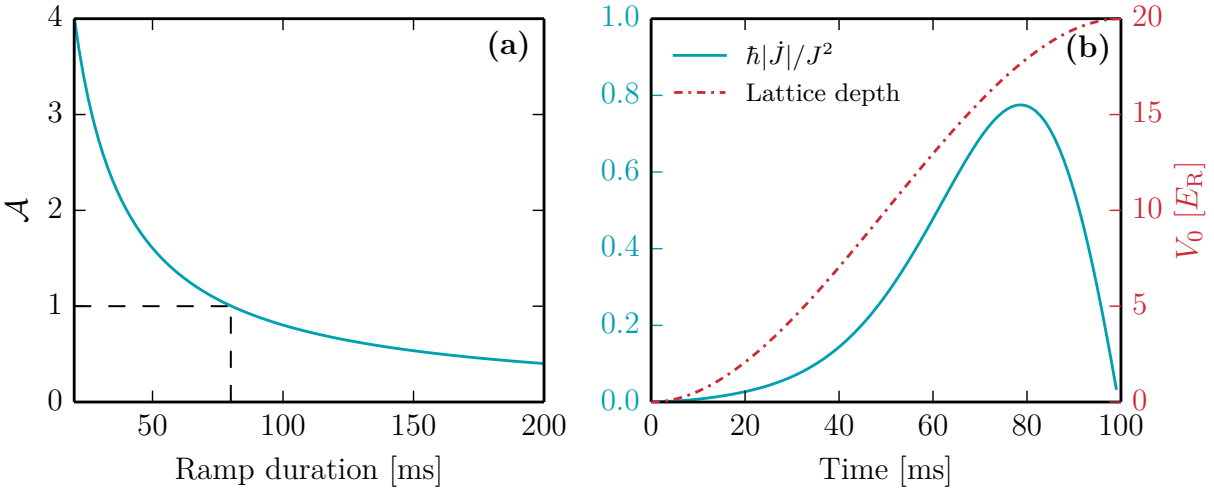

Figure 2.8: Adiabatic criterion for lattice loading up to 20 E_R. (a) Value of the parameter $\mathcal{A}$ with respect to ramp duration. The critical value $\mathcal{A}_\mathrm{c} = 1$ is reached for a ramp duration of 80 ms. (b) Time evolution of $\hbar|\dot{J}|/J^2$ during a 100 ms ramp (solid line). The dashed line shows the lattice depth ramp profile.

Importance of gravity

In our situation, realising an adiabatic transfer of the condensate from the crossed dipole trap to the three-dimensional optical lattices becomes delicate because of gravity. Indeed, gravity tilts the trapping potential in the vertical direction, reducing potential depth and displacing the minimum of the potential felt by the atoms. This displacement, called *sag* is $\Delta z \approx 4\,\mu\text{m}$ in the optical dipole trap whereas in the external harmonic potential of the optical lattice it would be $\Delta z \approx 230\,\mu\text{m}$. During the transfer this can induce motion in the vertical direction (Morsch et al. 2006) and possibly undesired heating or atom loss. Gravity could in principle be compensated for. While magnetic trapping is impossible for bosonic ytterbium, the dipole force of a beam with linearly varying intensity could be used. This solution requires rather high power[17] and was not pursued. We chose instead to adapt the loading sequence to account for this.

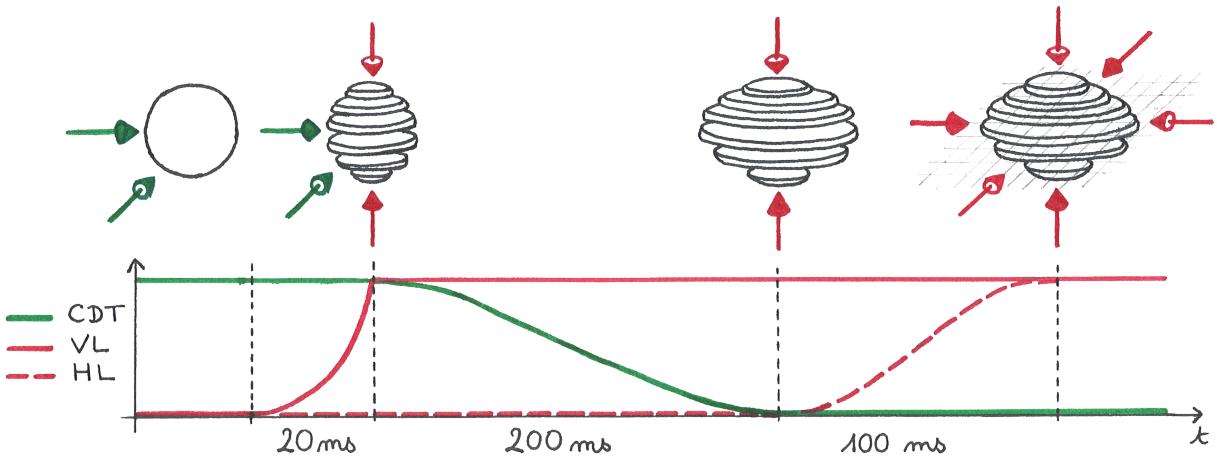

Figure 2.9: Time sequence for loading the optical lattices. A deep vertical lattice is first ramped-up in 20 ms. Then the crossed dipole trap is smoothly extinguished in 200 ms to let atoms redistribute in the planes. Finally, horizontal lattices are adiabatically turned on in 100 ms. *Figure designed with Marion Bouganne.*

Our loading sequence is made of three steps, which are summarised in Figure 2.9,

1. a fast ramp-up of the vertical lattice (VL) to its maximum depth,
2. a slow extinction of the crossed optical dipole trap (CDT),
3. an adiabatic increase of the horizontal lattices (HL).

The first step is a 20 ms exponential ramp of the vertical lattice, superimposed on the crossed dipole trap. It essentially freezes vertical motion and prevents detrimental effects from gravity. It is however long enough to avoid inter-band transitions. In a second step we smoothly ramp down the crossed optical trap potential in 200 ms, allowing atoms to expand horizontally. This creates a stack of two-dimensional condensates in the vertical lattice potential. This step has the additional benefit to lower the density, which mitigates the rate of three-body recombination processes. In a final step, we adiabatically ramp up the horizontal lattices in 100 ms to their final values.

[17] With the side of a Gaussian beam at λ_m focused to 70 µm, 1 W is required.

2.3.2 Optical lattice characterisation

The loading sequence used in the experiment creates a stack of independent 2D Bose-Hubbard lattices. In order to describe quantitatively our system we characterised the optical lattice beams using collective mode oscillations of a condensate and Kapitza-Dirac diffraction.

External trap frequencies

The external trap frequencies originate from the Gaussian shape of the optical lattice laser beams [see (1.10) in Section 1.2]. We characterised them by recording collective mode oscillations of a condensate in a crossed dipole trap as was described in Section 2.1.3. In order to hold atoms against gravity, we had to use either the TDT or the FDT along with the lattice beams. Therefore calibrations were done in crossed dipole traps formed by one forward lattice beam along with either the TDT or the FDT. Data are consolidated in Table 2.1.

Lattice depth calibration

An efficient tool to calibrate lattice depths is Kapitza-Dirac diffraction, namely matter-wave diffraction by an optical grating. This phenomenon is named after Kapitza and Dirac who first proposed in Kapitza et al. (1933) to reflect electrons from a standing wave of light. The first observation of matter-diffraction by light was performed with a beam of sodium atoms in Gould et al. (1986), and the observation with electrons was only demonstrated in Freimund et al. (2001).

Kapitza-Dirac diffraction on a BEC consists in pulsing an optical lattice on the condensate for a given duration, and observing the momentum distribution after a time-of-flight expansion. The condensate is modelled as a plane matter wave with zero momentum (and therefore zero quasi-momentum). The sudden illumination by an optical lattice projects this plane wave in the Bloch wave basis, where each Bloch component evolves during the exposition time. Besides, because of quasi-momentum conservation, these components all have zero quasi-momentum but different band indices. The sudden suppression of the lattice then 'projects' back the wave function on the set of plane waves. Again quasi-momentum is conserved and the decomposition only contains terms with integer multiples of $2\hbar\boldsymbol{k}$, where $\boldsymbol{k}$ is the wavevector associated with the light creating the optical lattice. This can also be viewed as a virtual process of photon absorption from one light beam and stimulated emission in the opposite beam, leading to the momentum difference $2\hbar\boldsymbol{k}$. It also coincides with the simple wave-particle picture from Section 2.2.1.

The non-trivial evolution for the populations of the diffraction orders can be computed numerically, and only depends on the lattice depth V_0 (Gadway et al. 2009). A fit of the experimental data then yields an accurate value for the lattice depth. An example of such a calibration is shown in Figure 2.10. Data for our actual lattice implementation are given in Table 2.1.

2.3.3 Superfluid to Mott insulator quantum phase transition

A typical benchmark experiment for the successful loading of an optical lattice with a degenerate quantum gas is the observation of the superfluid to Mott insulator transition. A Mott insulator originally describes a condensed matter material which exhibits collective

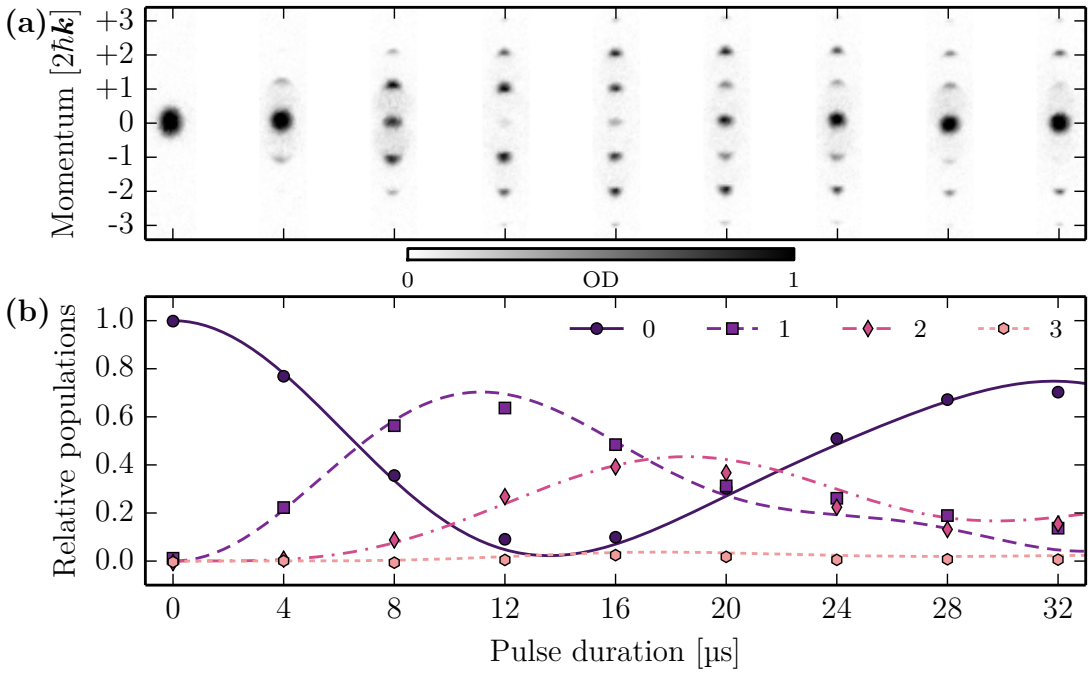

Figure 2.10: Calibration of the lattice depth via Kapitza-Dirac diffraction. (a) Pictures after a time-of-flight expansion with respect to the pulse duration. Diffracted orders are separated in momentum by integer numbers of $2\hbar\boldsymbol{k}$. (b) Relative populations of the diffracted orders versus pulse duration. Lines are a fit to the data using a numerical integration of the Schrödinger equation yielding $V_0 = 28.5(2)\,E_\mathrm{R}$.

	x-axis	y-axis	z-axis
AOM frequency shift [MHz]	+80	-80	+110
Maximum power [mW]	410	400	610
Trap frequency Ω [$2\pi \times$ Hz]	42	38	33
Waist w [µm]	115	125	150
Typical lattice depth V_0 [E_R]	24	25	27

Table 2.1: Trap frequencies and depths for the optical lattice beams.

localisation of its would-be conducting electrons due to their Coulomb repulsion. In other words, in such a material, Coulomb interactions favour the localisation of the electrons, in competition with their kinetic energy, which tends to delocalise them to create a Fermi sea. The Bose-Hubbard Hamiltonian for cold atoms in optical lattices reproduces the same physics. The electrons and their spin are replaced by spin-less bosons, with an arbitrary on-site filling number. The competition between kinetic energy and on-site interactions leads to a quantum phase transition. It was first proposed for cold atomic systems in Jaksch et al. (1998) and observed in Greiner et al. (2002b). An insightful review of this experiment is done in Zwerger (2003).

With our system we realise two-dimensional systems which can be described by the following 2D Bose-Hubbard Hamiltonian

$$\hat{H} = -\sum_{\langle i,j\rangle_\perp} J_\perp(\hat{a}_i^\dagger \hat{a}_j + \hat{a}_j^\dagger \hat{a}_i) + \sum_{i_\perp} \frac{U}{2}\hat{n}_i\,(\hat{n}_i - 1) + \sum_{i_\perp} \frac{M}{2}(\Omega_x^2 x_i^2 + \Omega_y^2 y_i^2)\hat{n}_i. \tag{2.16}$$

The notation $i_\perp$ refers to all lattice sites at positions $\boldsymbol{\rho}_i = (x_i, y_i)$ in a plane, and $\langle i, j\rangle_\perp$ denotes nearest-neighbour pairs. In-plane tunnelling is captured by the kinetic energy $J_\perp$. Tunnelling along the gravity direction between adjacent systems is neglected. The on-site energy U is given by

$$U = \frac{4\pi\hbar^2 a}{M} \int \mathrm{d}z \mathrm{d}^2\rho \left| w_z(z) w_\perp(\boldsymbol{\rho} - \boldsymbol{\rho}_i) \right|^4, \tag{2.17}$$

where $\boldsymbol{\rho}$ denotes a two-dimensional vector in the $x-y$ plane and where w_z (respectively $w_\perp$) are the Wannier functions for the vertical (resp. horizontal) lattice potential, in the fundamental band.

The superfluid to Mott insulator transition in two dimensions was observed with ultracold gases in Spielman et al. (2007). At zero-temperature, these systems are well understood (Bloch et al. 2008; Jiménez-García et al. 2010). For uniform systems with integer filling fraction, Monte-Carlo simulations predict zero-temperature phase transition critical values $(U/J_\perp)_\mathrm{c}$ given in Table 2.2 (Capogrosso-Sansone et al. 2008; Teichmann et al. 2009). The corresponding horizontal lattice depths are also indicated. In the following, N designates the total atom number, N_s the number of occupied lattice sites and $\bar{n} = N/N_\mathrm{s}$ the average filling fraction, or average number of atoms per lattice site.

	$\bar{n} = 1$	$\bar{n} = 2$	$\bar{n} = 3$
$(U/J_\perp)_\mathrm{c}$	16.9	28.7	40.4
$V_{0,x} = V_{0,y}$ $[E_\mathrm{R}]$	9.1	10.9	12.2

Table 2.2: Critical value for the Mott transition in uniform 2D systems with integer filling fraction. We also indicate the corresponding horizontal lattice depths for our parameters.

On the one hand, for shallow lattices where $U/J_\perp \ll 1$, the kinetic energy term in (2.16) dominates and the ground-state energy is minimised for a delocalised wave function over the entire lattice. In the case of a homogeneous system and for vanishing U, the many-body state can be described by a factorised ansatz (see Section 1.2.3),

$$|\Psi_\mathrm{SF}\rangle \propto \left(\sum_{i_\perp} \hat{a}^\dagger_{i_\perp} \right)^N |0\rangle. \tag{2.18}$$

The system is in a superfluid phase where all atoms are in the $\boldsymbol{q} = 0$ Bloch wave in the lowest band. Long-range phase coherence extends across the whole lattice, the spatial correlation function is non-zero $\langle \hat{a}^\dagger_i \hat{a}_j \rangle = \bar{n}$, for all i, j. This is detectable in time-of-flight, where momentum distribution exhibits sharp diffraction peaks.

On the other hand, for deep lattices where $J_\perp/U \ll 1$, the interaction term dominates in (2.16) and one expects atoms to be localised on the lattice sites. In the homogeneous case with integer filling fraction and for vanishing $J_\perp$, the many-body state can be described by a product of local Fock states (see Section 1.2.3),

$$|\Psi_\mathrm{MI}\rangle \propto \prod_{i_\perp} \left(\hat{a}^\dagger_{i_\perp} \right)^{\bar{n}} |0\rangle. \tag{2.19}$$

Atom number fluctuations on a site are suppressed, long-range phase coherence is lost at the benefit of strong occupation number correlations. In time-of-flight this can be revealed

through noise correlations (Bloch et al. 2008; Spielman et al. 2007) in the momentum distribution. The third term in (2.16) is caused by the smooth harmonic trap provided by the Gaussian envelope of the lattice beams. This external trapping potential leads to the characteristic *wedding cake* density profiles for Mott insulator phases, i.e. density plateaus with integer filling fraction, the denser plateau occurring near the center of the trap [see Section 1.2.3 and Bloch et al. (2008)].

A signature of the transition is the loss of long-range order in the one-particle density matrix $\rho^{(1)}(\boldsymbol{r}, \boldsymbol{r})$, the Fourier transform of which can be captured to a good approximation by time-of-flight expansion of the cloud [see Gerbier et al. (2008) for a discussion of the limitations]. Figure 2.11 shows pictures of the atomic distribution after a 20 ms time-of-flight, and the visibility of the resulting interference pattern. The visibility is calculated following the procedure of Gerbier et al. (2005), and vanishes while crossing the transition. Still, this is strictly speaking not a proof of the superfluid to Mott insulator transition. One would need in principle to probe the incompressibility of the Mott state, observe the density plateaus, or measure the gap opening in the band structure. We checked that the loss of coherence was not caused by heating of the atomic sample using a short ramp back in the superfluid regime (linear ramp of about 10 ms duration), and observed the reappearance of the sharp peaks.

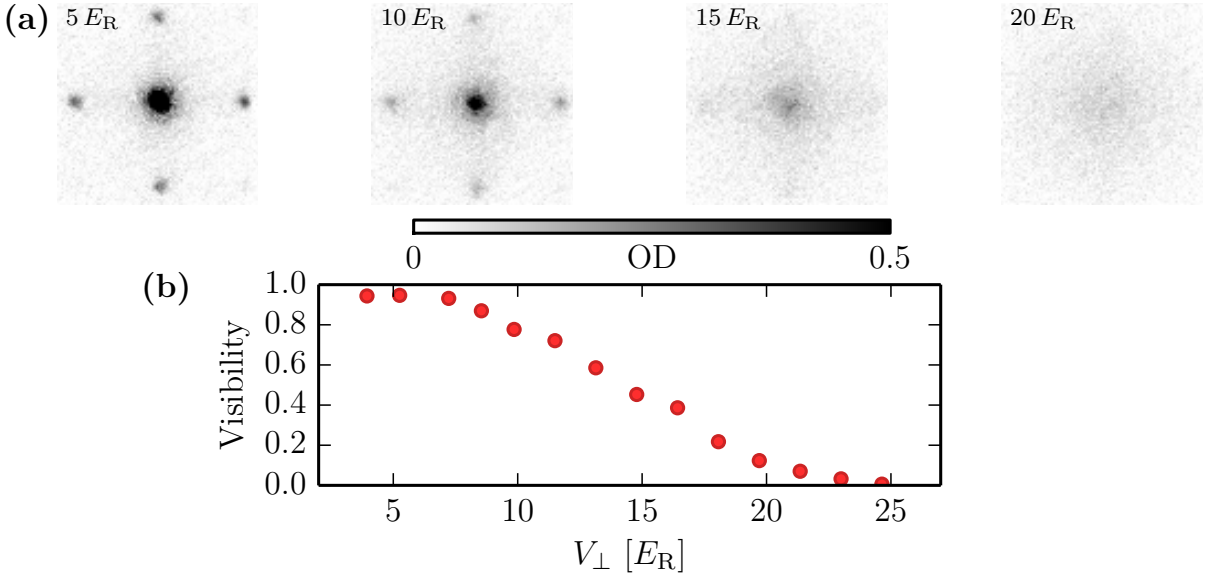

Figure 2.11: Superfluid to Mott insulator transition in 2D Bose-Hubbard systems. The loss of long-range phase coherence is visible in time-of-flight expansion of the cloud. The transition occurs at depths compatible with theoretical predictions from Capogrosso-Sansone et al. (2008) and Teichmann et al. (2009).

2.3.4 Collapse and revival

As a further characterisation of the system, one can measure the on-site interaction energy U using a collapse and revival experiment. This was first realised in Greiner et al. (2002a).

The quantum gas is prepared in the superfluid phase in a shallow lattice and suddenly quenched to a depth where tunnelling is negligible. This essentially freezes the on-site

atom number distribution. After some evolution time in the deep lattices, a time-of-flight expansion is performed to reveal the momentum distribution. Due to the non-linear dependence of the interaction energy on the atom number, the diffraction pattern in time-of-flight shows a beautiful collapse and revival behaviour.

The exact description of a superfluid state given in (2.18) corresponds to the projection of a coherent state product on the subspace with fixed atom number. In the limit of large N, where atom number fluctuations are negligible, we can approximate (2.18) by a product of coherent states $|\alpha_i\rangle$ (Bloch et al. 2008). Besides, in the limit of deep lattices, the system essentially reduces to a collection of decoupled sites, where the prevailing term in (2.16) is the interaction Hamiltonian $U\hat{n}(\hat{n}-1)/2$. The Fock states $|n\rangle$ are eigenstates of this interaction Hamiltonian with energies $Un(n-1)/2$. The time evolution of a coherent state after the quench is then easily calculated

$$|\alpha\rangle(t) = \mathrm{e}^{-|\alpha|^2/2} \sum_n \frac{\alpha^n}{\sqrt{n!}} \mathrm{e}^{-\mathrm{i}Un(n-1)t/(2\hbar)} |n\rangle. \tag{2.20}$$

At $t = 0$, the system is in a coherent state. The non-linear dependence of the phase factors in the Fock basis rapidly leads to destructive interferences, and the visibility vanishes. Nonetheless, at integer multiples of the revival time h/U, the phases all get equal modulo 2π, and the coherent state is recovered along with good visibility. These collapses and revivals can be observed in time-of-flight where the visibility of the diffraction pattern is proportional to the superfluid order parameter $\langle \hat{a} \rangle$. Using (2.20) one can write,

$$\langle \hat{a} \rangle^2 = \bar{n} \exp\left\{ \bar{n} \left[\cos\left(\frac{Ut}{\hbar} \right) - 1 \right] \right\}. \tag{2.21}$$

The time evolution of (2.21) exhibits collapses and revivals with periodicity h/U. The collapse time depends on the average filling, and thus on the atom number distribution on a lattice site (Greiner 2003).

In a non-uniform system, like in the experiment, the revival frequency is solely given by U, which can be taken uniform over the lattice within good approximation. However, the revivals are washed out by the inhomogeneous dephasing due to the external harmonic confinement (Will et al. 2010), and by deviations from the approximation by a coherent state (2.20) due to interactions or finite temperature (Greiner et al. 2002a). Data are shown in Figure 2.12, the solid line is a fit using equidistant Gaussian functions. This allows for a precise determination of the on-site interaction energy $U = h \times 1475(25)\,\mathrm{Hz}$.

2.4 A laser to address the clock transition

In this section I describe the essential tool to probe the $^1\mathrm{S}_0$–$^3\mathrm{P}_0$ transition of ytterbium, namely the clock laser operating at 578 nm. This laser is fundamental for inducing coherent tunnelling in the two-state lattices (see Section 1.3), thereby realising the artificial gauge fields scheme. The required laser coherence time should then be at least on the order of a tunnelling time [an estimation in the thesis of Matthias Scholl (2014) gives about 10 ms]. Typical laser linewidth should then be on the order of few tens of hertz to one hundred hertz. This condition can be relaxed if the Rabi frequency of the driving is much bigger than the laser linewidth, which can be done in the experiment. With this in mind,

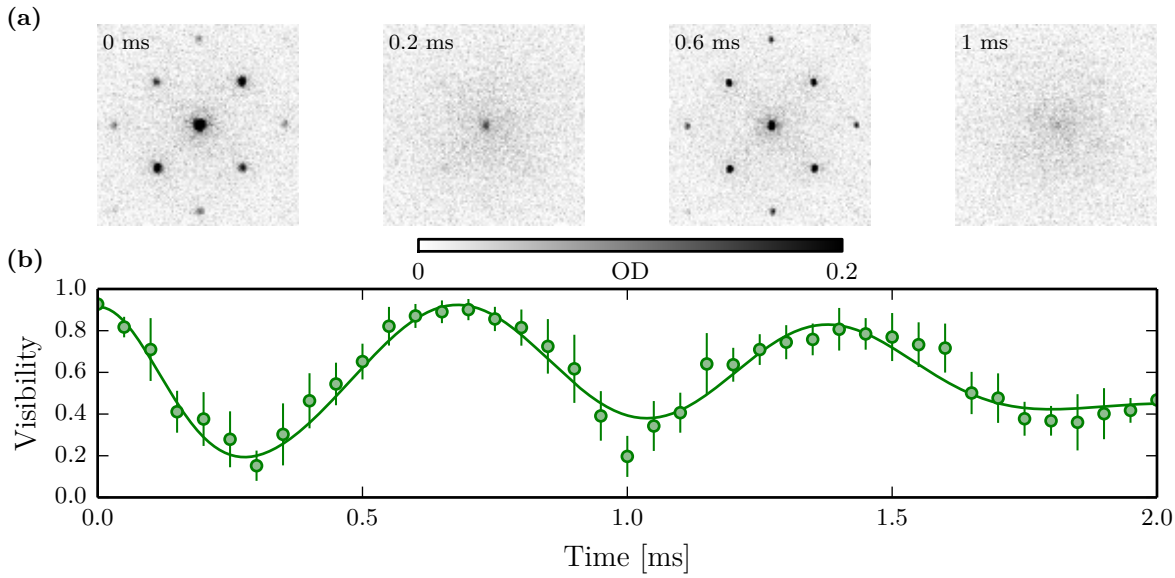

Figure 2.12: Collapses and revivals of a condensate in optical lattices. (a) Experimental images of the interference pattern at different hold times after quenching the horizontal lattices. (b) Visibility of the interference pattern undergoing collapse and revival dynamics. The period of the revivals is given by the on-site interaction energy U. The solid line is a phenomenological fit using a sum of equidistant Gaussian functions giving $U = h \times 1475(25)\,\mathrm{Hz}$. Lattice depths are $V_{0,x} = V_{0,y} \approx 26\,E_\mathrm{R}$ and $V_{0,z} \approx 27\,E_\mathrm{R}$. *Figure reproduced from Bouganne et al. (2017).*

I shall omit many details on the exact technical implementation[18] but stress the performance of the laser in terms of frequency stability. After presenting the frequency chain used to derive a stable output to the atoms, I present a characterisation of the frequency lock. Then I detail important features regarding the stability of the laser frequency with respect to temperature.

2.4.1 Frequency chain

The clock laser operating at $\lambda_0 \approx 578\,\mathrm{nm}$, results from the frequency sum of two infrared laser sources at 1030 nm[19] and 1319 nm[20]. Sum-frequency generation is realised in a nonlinear ppLN[21] crystal of 2 cm length. We get around 70 mW of yellow light after a single pass in the crystal. This light goes through a first AOM used for intensity and frequency locking, then couples into an optical fiber reaching the experimental table. As described in Figure 2.13, the out-going light is split into two arms. The first arm goes to the science chamber through a second AOM used to control the frequency seen by the atoms. The second arm is fiber-coupled and sent to an ultra-stable cavity where the laser frequency is locked via Pound-Drever-Hall modulation. Phase-noise cancellation is performed on this arm using a third AOM and a Michelson interferometer with a fast photodiode[22].

[18] The interested reader can find them in the thesis of Alexandre Dareau (2015).
[19] 5 W Amplified fiber laser, Koheras Boostik Y10, NKT Photonics.
[20] 0.5 W Nd:Yag laser, Mephisto, Coherent.
[21] Periodically poled lithium niobate, Coherent.
[22] FPD310-FV, Menlo Systems.

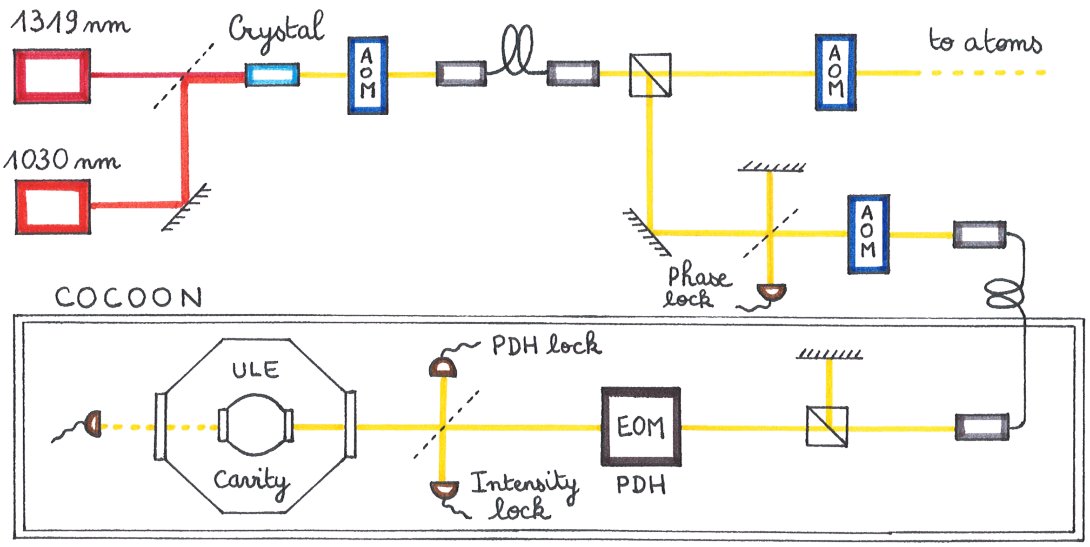

Figure 2.13: Frequency chain of the clock laser. *Figure designed with Marion Bouganne.*

The cavity is used as a stable relative frequency reference. It is a 50 mm long plano-concave Fabry-Perot cavity with very high reflectivity mirrors, separated by a spherical ultra-low expansion (ULE) glass body[23]. Dareau et al. (2015) measured the free spectral range $\Delta_{\mathrm{FSR}} = 2\pi \times 3\,144\,366(2)\,\mathrm{kHz}$, and the finesse $\mathcal{F} \approx 257\,000$. The cavity peak width is therefore $\Delta\omega_{\mathrm{cav}} = \Delta_{\mathrm{FSR}}/\mathcal{F} \approx 2\pi \times 12\,\mathrm{kHz}$, which permits efficient frequency locking. Nevertheless, the absolute frequency of the cavity is slowly drifting with time because of the cavity length evolution. Indeed, the ageing of the ULE glass leads to a slow shrinkage of the cavity spacer (Dubé et al. 2009). An absolute frequency reference is therefore essential to find the atomic resonance. In this respect, the absolute frequency of the cavity can be measured against a molecular iodine reference, this is described in detail in the thesis of Alexandre Dareau (2015). This comparison provides a frequency calibration with a typical accuracy of 40 kHz, sufficient to find the atomic resonance with the laser.

In order to minimise all perturbations from the environment on the reference cavity, the latter is carefully isolated in a *cocoon*. The cavity is mounted inside a thermal shield whose temperature is regulated with a Peltier cooler. Both are assembled inside a vacuum chamber at around 10^{-8} mbar, efficiently reducing thermal and acoustic noise[24]. A vibration isolation platform[25] supports the vacuum chamber and the surrounding optics. This platform sits inside a wooden box, itself placed inside an soundproof box[26]. All these insulating layers stabilise the absolute frequency to a few tens of kilo-hertz over a few days. The equilibrium temperature of the opto-mechanical system is largely decoupled from room temperature (the relaxing time is about 3 days), but the residual coupling has a measurable impact on the kilo-hertz scale. Indeed, as discussed at the end of this section, the air temperature around the platform and vacuum chamber has an effect on the cavity length. We therefore stabilise it with a chill plate cooled by circulating water from a thermo-regulated chiller[27]. Moreover, the plate helps to remove heat generated by

[23] ATF-6301, Advanced Thin Films.
[24] Stable Laser Systems.
[25] Nano-K 50 BM-10, Minus K Technology.
[26] Custom-made, Keoda.
[27] ThermoCube, SSCS.

electrically powered components inside the box.

2.4.2 Pound-Drever-Hall lock

The quality of the frequency lock on the reference cavity determines the short-term spectrum of the clock laser. The Pound-Drever-Hall (PDH) method (Drever et al. 1983; Black 2000) provides a very sensitive error signal on the cavity frequency. It uses the intensity reflection from the optical cavity input mirror. This reflection is a coherent superposition between the directly reflected field on the input mirror and the leaking intra-cavity field, which vanishes on resonance, allowing a fast response to phase fluctuations of the laser field. The input field is modulated with an EOM at 4 MHz, a frequency much larger than the cavity resonance width, in such a way that the resulting sidebands are totally reflected. The reflection from the cavity is sent on a photodiode and the beatnote between the sidebands and the reflected carrier is demodulated with a commercial servo control[28] to yield the error signal with a slope

$$p_{\mathrm{PDH}} = 4\pi \frac{\Delta V}{\Delta \omega_{\mathrm{cav}}} \approx 1\,\mathrm{mV\,Hz^{-1}} \text{ with } \Delta V \approx 6\,\mathrm{V}. \tag{2.22}$$

The error signal is fed back to the laser system in two ways. First the servo output goes to a frequency synthesiser that drives the first AOM frequency and corrects the fast fluctuations. Second, the servo output is further integrated to derive a slow signal fed to the 1319 nm laser piezo, this allows to regulate the long term drifts of the laser frequency.

We characterised the behaviour of the frequency lock by measuring the power spectral density (PSD) of the error signal. This error signal is an in-loop quantity and therefore does not reflect directly the PSD of the laser itself. It only tells how tight the lock responds. We measured the detector noise (no light impinging on the PDH photodiode, and servo off), the amplitude noise (light impinging on the PDH photodiode, servo off), and the error signal noise (light impinging on the PDH photodiode, servo on). Measurements were done using both the AC and DC error monitor outputs of the servo box. Frequencies from 1 Hz to 10 kHz were acquired using the DC error output with a digital oscilloscope[29] (15 measurements of 1 s duration at 909 kS). Frequencies from 10 kHz to 1 MHz were acquired using the AC error output with a spectrum analyser[30] (spectra averaged over 15 realisations, resolution bandwidth of 1 kHz). Results are presented in Figure 2.14.

In what follows I discuss the results by giving the root-mean square (RMS) deviation of the signals. It is calculated taking the square-root of the integral of the PSD from zero to a cut-off frequency that we choose to be 100 kHz. This is a very conservative choice because atoms are not sensitive to fluctuations over such a wide frequency range. First, the detector noise floor (blue line) is low enough to ensure no direct contribution to the laser linewidth broadening (RMS gives about 1 Hz). Out of lock (red line), the dominant contribution of the noise lies under 1 kHz, above which the signal reaches the detector noise floor. The action of the lock is dramatic (black line), the noise is completely removed under 10 kHz, above which a typical noise bump is observed. This bump should not contribute significantly to the laser linewidth [see the discussion in the thesis of Alexandre Dareau (2015)]. As seen by the black curve going under the blue curve, the lock re-injects part of the detector noise into the loop, but this contribution is also negligible. This type of

[28] D2-125, Vescent Photonics.
[29] PicoScope 4262, Pico Technology.
[30] MS2830A, Anritsu.

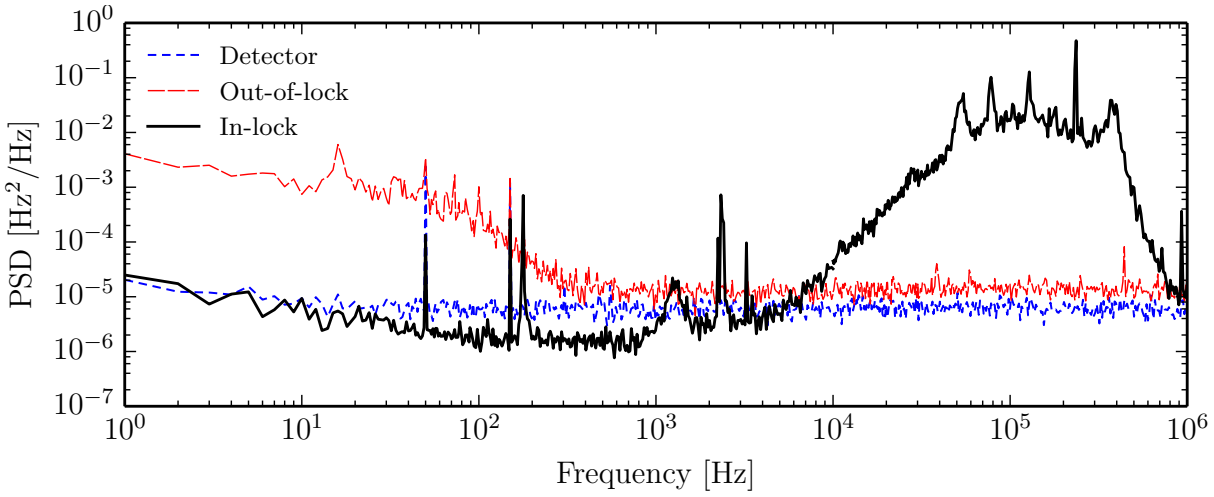

Figure 2.14: Power spectral densities of the error signal for the PDH lock.

noise curve is similar to what was observed in the optical clocks community (Westergaard 2010). The RMS of the locked error signal is about 36 Hz. Altogether, the PDH lock seems to work nicely with no significant contribution to frequency broadening. In order to faithfully describe the laser frequency noise, one would need to compare it with an independent but similar source, which we do not have at hand.

At longer time scales, residual amplitude modulation (RAM) of the light impinging on the cavity can introduce offset fluctuations of the PDH error signal. This can degrade the laser frequency stability. When the signal impinging on the PDH photodiode has amplitude modulation, it creates oscillating interferences with the sidebands and can give rise to noise modulated at the PDH modulation frequency. This noise would hence be demodulated by the servo box and introduce a fluctuating offset of the error signal. This fluctuating offset is fed back to the laser but does not originate from actual frequency fluctuations present in the light going to the atoms. We did two types of measurements: a short-term measurement of the intensity modulation of the light at 4 MHz, and a long-term measurement of the offset fluctuations of the error signal.

1. The former is done by measuring the light intensity modulation at 4 MHz on a photodiode with servo on. We used the intensity lock photodiode signal for that purpose. We measured 0.016 % of RAM on this photodiode, which results in frequency fluctuations of about 2 Hz.
2. The latter is done by measuring the DC error output offset with servo off. This is realised using a digital oscilloscope and a low-pass filter (160 Hz). Again, frequency fluctuations are about 3 Hz.

2.4.3 Zero-crossing point

The frequency reference is given by the cavity, and the short-term linewidth of the laser is inherited from the frequency lock on the cavity. Therefore the absolute frequency of the cavity must not fluctuate beyond the linewidth achieved by the lock. The main source of cavity frequency fluctuations is cavity length modifications from mechanical vibrations and thermal expansion or contraction. The impact of the latter can be minimised using the so-called zero-crossing point of the ULE glass. At a specific temperature T_{ZC}, the thermal

expansion coefficient of the cavity vanishes. Therefore, at T_{ZC} the cavity length is minimal (Legero et al. 2010), and the frequency maximal. Setting the cavity temperature close to this point ensures a reduced sensitivity to temperature variations.

We systematically compared the laser frequency with the iodine reference while tuning the cavity temperature set-point. Results are consolidated in Figure 2.15. A striking observation is the hysteresis in the temperature loop, which might come from mechanical constraints on the cavity itself. The two branches are fitted using parabolas and yield a mean zero-crossing temperature $T_{\mathrm{ZC}} = 4.13(2)\,^{\circ}\mathrm{C}$, with a curvature $\kappa = 2\pi \times 350(20)\,\mathrm{kHz\,K^{-2}}$.

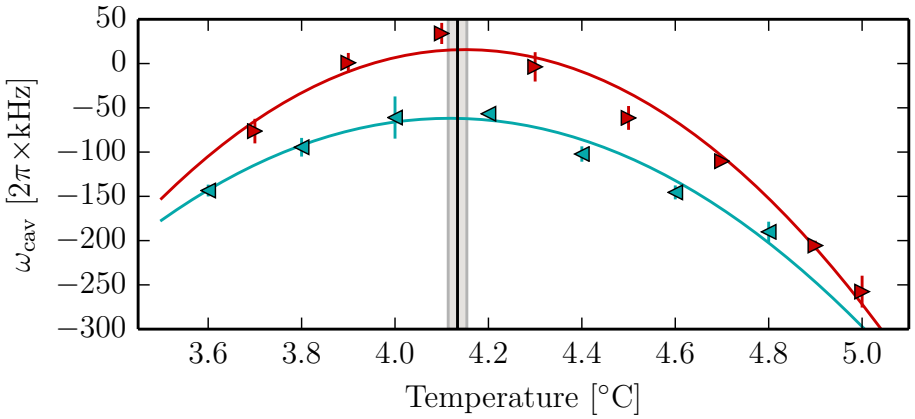

Figure 2.15: Zero-crossing point of the reference cavity. Set-point temperature was changed following the direction indicated by the markers.

Measurements performed on the cavity temperature servo loop indicate frequency fluctuations of about a few hertz. Still, the temperature of the cavity itself is not sufficient to achieve long-term frequency stability, as described in what follows.

2.4.4 Temperature stabilisation

Time-of-flight spectroscopy on the clock transition (Dareau et al. 2015) provides frequency calibration at the kilohertz precision. Using this technique, we monitored the absolute frequency of the cavity ω_{cav} with time as well as the ambient temperature T in the soundproof box. Results are presented in Figure 2.16. Temperature data points result from an average over one hour.

Frequency measurements show a clear correlation with the ambient temperature even though the temperature of the cavity itself was maintained constant throughout the days. A simple empirical model can account for such a behaviour. We assume that both the instantaneous cavity frequency and its ageing slope have a linear dependence on the ambient temperature. The cavity resonance then reads

$$\omega_{\mathrm{cav}}(t) = \omega_{\mathrm{cav}}(0) + p_{\mathrm{inst}}\,[T(t) - T(0)] + p_{\mathrm{age}} \int_0^t \mathrm{d}t'\; [T(t') - T_{\mathrm{age}}]\,. \tag{2.23}$$

A fit of this phenomenological model to the data gives a rather good prediction of the absolute cavity frequency with parameters $p_{\mathrm{inst}} \approx 2\pi \times 43.5\,\mathrm{kHz\,K^{-1}}$, $p_{\mathrm{age}} \approx 2\pi \times 0.432\,\mathrm{kHz\,K^{-1}\,day^{-1}}$ and $T_{\mathrm{age}} \approx 35.0\,^{\circ}\mathrm{C}$. A similar fit without the ageing term is much less accurate. Note that this crude model does not describe well frequency variations over

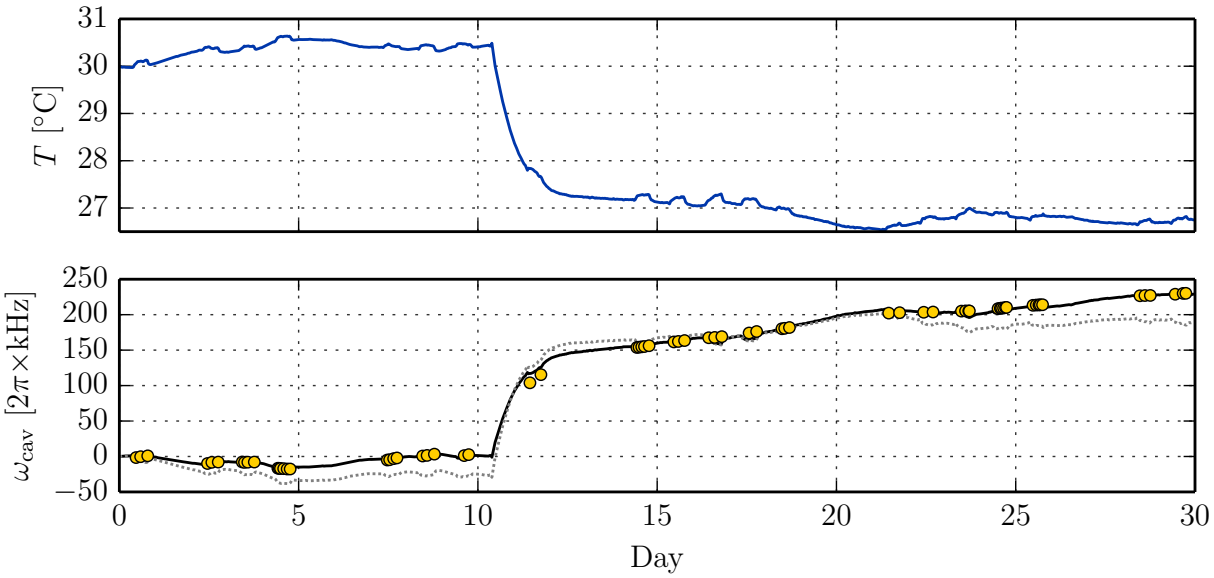

Figure 2.16: Correlation between the absolute cavity frequency ω_{cav} and the ambient temperature T in the soundproof box over 30 days. Frequency is measured with time-of-flight spectroscopy of a BEC (Dareau et al. 2015), yellow circles. The solid line shows a fit using the empirical model (2.23) and the grey line is a fit without the ageing term. During day 10, the temperature set-point of the chiller was lowered by 3 degrees.

times longer than about a month. Also, the ageing parameters are purely phenomenological, and one should not conclude from their specific values that the ageing of the cavity would vanish at 35.0 °C.

Ambient temperature impacts can be mitigated using an efficient temperature stabilisation of the surrounding air. So far, this stabilisation is performed with a chill plate cooled by circulating water from a thermo-regulated chiller. We achieve a constant temperature of about 26.7 °C, with variations of less than 0.1 °C over a day, leading to a stable ageing slope of about 3.6 kHz day^{-1}. Nevertheless, long-term fluctuations of the temperature still happen because the chiller is coupled to the room temperature of the laboratory. A possible solution would use a Peltier cooler to finely regulate the air in the soundproof box. A neat design needs to be found to evacuate the heat produced by these coolers (Cappellini et al. 2015).

2.5 Summary

In this chapter, I have presented the experimental platform used to study atom-light interactions in ultracold atomic ensembles. This apparatus has been used to perform the measurements presented in later chapters. Firstly, I presented how we achieve Bose-Einstein condensation of bosonic ^{174}Yb in an optical dipole trap. Secondly, I detailed the detection method used throughout this thesis work to probe the atoms, namely optical imaging through resonant absorption. Thirdly, I explained how we prepare degenerate quantum gases in two-dimensional optical lattices, realising the Bose-Hubbard Hamiltonian. Finally, I described the important experimental tool used to coherently manipulate the atoms: the laser for the clock transition.

3

Optical spectroscopy of degenerate bosons in deep optical lattices

Manipulation of atomic external degrees of freedom can be realised with internal transitions. For example, Raman transitions between two hyperfine states was used to selectively address a narrow velocity class of sodium atoms (Kasevich et al. 1991). Doppler-free two-photon optical spectroscopy was crucial to observe Bose-Einstein condensation of spin-polarised atomic hydrogen (Killian et al. 1998; Fried et al. 1998). Optical Bragg spectroscopy on a Bose-Einstein condensate was devised to measure the dynamic structure factor with sub-recoil resolution (Stenger et al. 1999; Zambelli et al. 2000).

Coherent control on the internal degrees of freedom of ^{174}Yb can be performed using the $^1\mathrm{S}_0$–$^3\mathrm{P}_0$ clock transition. The recoil associated with the photon absorption, necessary to reach the metastable state, couples the internal degrees of freedom with the external ones through the Doppler effect. We performed spectroscopy on the clock transition in a bulk BEC, where this Doppler effect is not negligible. A detailed study of this investigation is given in the thesis of Manel Bosch Aguilera (2019). Briefly, the interplay between Doppler effect and inelastic interactions (related to collisional losses) gives rise to a beautiful and non-trivial time evolution of the system. This leads to the observation of a non-linear relaxation dynamics, which can be understood as the evolution of two classical fields (one for each clock state ensembles) coupled by atom-light interaction as well as elastic and inelastic interactions (Bosch Aguilera et al. 2018).

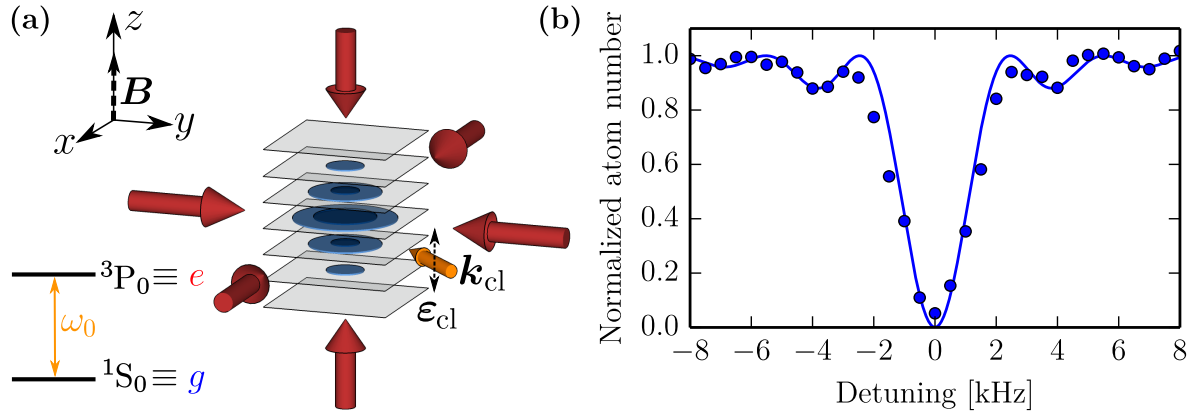

Figure 3.1: (a) Sketch of the experiment and of the level scheme of the clock transition. The clock laser wavevector $\boldsymbol{k}_{\mathrm{cl}}$ lies in the horizontal plane at 45° with respect to the lattice axes. The polarisation $\boldsymbol{\varepsilon}_{\mathrm{cl}}$ is set along the vertical direction parallel to the applied magnetic field $\boldsymbol{B}$. (b) Excitation spectrum in a deep lattice of depth $\sim 25\,E_{\mathrm{R}}$. The Rabi frequency is $\Omega \approx 2\pi \times 1450\,\mathrm{Hz}$ and the clock pulse time is $t = \pi/\Omega \approx 350\,\mu\mathrm{s}$. The solid line is the excitation probability for a single atom from (3.7).

When the external confinement of the atoms is much stronger than the recoil energy associated with the photon absorption, the internal dynamics decouples from the external ones and recoil is suppressed: this is the Lamb-Dicke effect (Ludlow et al. 2011). In this chapter, I report on high-resolution optical spectroscopy of interacting bosonic ^{174}Yb atoms in deep optical lattices, where this decoupling is effective. We prepare an array of Fock states with one or two atoms per site using the superfluid-Mott insulator transition (as presented in Section 2.3.3). The final lattice depth is high enough to neglect tunnelling between sites. The resulting array of singly- and doubly-occupied isolated sites is probed using the $^1S_0$–$^3P_0$ clock transition (see Figure 3.1). Atoms in singly-occupied sites undergo long-lived Rabi oscillations, whereas atoms in doubly-occupied sites are strongly affected by interatomic interactions. By measuring inelastic decay rates and energy shifts in these latter sites we obtain all relevant collisional parameters involving both clock states, which were previously unknown. Similar measurements were independently performed at LENS in parallel (Franchi et al. 2017).

Firstly, I present the optical setup and a characterisation of the atom-light interaction in optical lattices at the single-particle level. Secondly, I analyse the temporal evolution of Rabi oscillations for Mott insulator (MI) phases with varying total atom number. This analysis also provides a characterisation of the Mott shell populations. Finally, I present the measurements of the doubly-occupied site lifetime and energy shift due to interactions. Throughout this chapter, I label the clock states $g \equiv {}^1S_0$ and $e \equiv {}^3P_0$.

3.1 Quasi-adiabatic preparation of Mott insulator phases

In Section 2.3.1 I presented the loading procedure of a degenerate quantum gas of ^{174}Yb in a 3D magic optical lattice. Due to the external confinement provided by the Gaussian shape of the lattice laser beams, the atomic density is inhomogeneous. In this section, I model the loading procedure to predict the density distribution in the *atomic limit*, where the lattice depth is high enough to neglect tunnelling. The preparation of MI phases consists in three steps:

1. fast ramp-up of the vertical lattice to its maximum depth,
2. slow extinction of the crossed optical dipole trap,
3. adiabatic increase of the horizontal lattices up to their maximal depth.

We model the first phase of this loading sequence using a sudden approximation, hence the name quasi-adiabatic. The initial atomic distribution for a BEC in the crossed optical dipole trap is projected on a periodic potential of period $d = \lambda_m/2$ much smaller than the initial Thomas-Fermi half-length L of the BEC. For a BEC in the Thomas-Fermi regime (Dalfovo et al. 1999), this results in a distribution

$$N_{i_z} \approx \frac{15 N_{at} d}{16 L} \left[1 - \left(\frac{i_z d}{L}\right)^2\right]^2 \Theta\left[1 - (i_z d/L)^2\right], \tag{3.1}$$

for the number of atoms in each plane of the vertical lattice at the altitude $z = i_z d$ (the integers i_z label the planes), with Θ the Heaviside function. At the end of the first step, the system is a stack of $2L/d$ planes, with each plane forming a quasi-2D BEC with N_{i_z} atoms.

From there, the second and third steps are assumed adiabatic. Using the distribution N_{i_z}, we assume a zero entropy sample in each plane, determined as the ground state of the 2D Bose-Hubbard model with N_{i_z} atoms, in the so-called atomic limit,

$$\hat{H}_{i_z} = \sum_{i_\perp} \frac{U_{gg}}{2} \hat{n}_i \left(\hat{n}_i - 1\right) + \frac{M}{2}(\Omega_x^2 x_i^2 + \Omega_y^2 y_i^2)\hat{n}_i, \tag{3.2}$$

which is the same as (1.22) where we have neglected tunnelling ($J_\perp \approx 0$) due to the high values of the final horizontal lattice depth. The notation $i_\perp$ refers to all lattice sites at positions $\boldsymbol{\rho}_i = (x_i, y_i)$ in the plane at altitude $z = i_z d$. Unless mentioned otherwise, all experiments described in this chapter are performed with final lattice depths $\{V_{0,x}, V_{0,y}, V_{0,z}\} = \{24(0.5), 25(0.5), 27(0.5)\} E_\mathrm{R}$. The corresponding external trapping frequencies are $\{\Omega_x, \Omega_y, \Omega_z\} = 2\pi \times \{42, 38, 33\}$Hz.

Introducing a chemical potential $\mu \geq 0$, the spatial structure in the local density approximation and the atomic limit is given by

$$n(\boldsymbol{\rho}_i) = \mathrm{Int}\left[\frac{\mu - \frac{M}{2}(\Omega_x^2 x_i^2 + \Omega_y^2 y_i^2)}{U_{gg}}\right] + 1, \tag{3.3}$$

where $\mathrm{Int}(x)$ denotes the integer part of x. For finite temperatures and/or tunnelling (still small compared to U_{gg}), the overall density profile remains similar but with smoother edges than predicted by (3.3) (Zwerger 2003). We compute n in each plane i_z by finding the proper chemical potential μ which gives the correct atom number in the plane N_{i_z}.

The relative weight of the shell with $\overline{n}$ atoms can be characterised by its population $N_{\overline{n}}$ normalised to the total atom number N_at,

$$\mathcal{N}_{\overline{n}} = \frac{N_{\overline{n}}}{N_\mathrm{at}}. \tag{3.4}$$

Figure 3.2 shows the weights $\mathcal{N}_{\overline{n}}$ for total atom numbers up to 9×10^4, calculated from (3.3). The chemical potential is determined self-consistently to match the total atom number. For sufficiently small atom number, we predict a MI phase with only singly-occupied sites. For higher atom numbers, filling fractions of two and three are also populated.

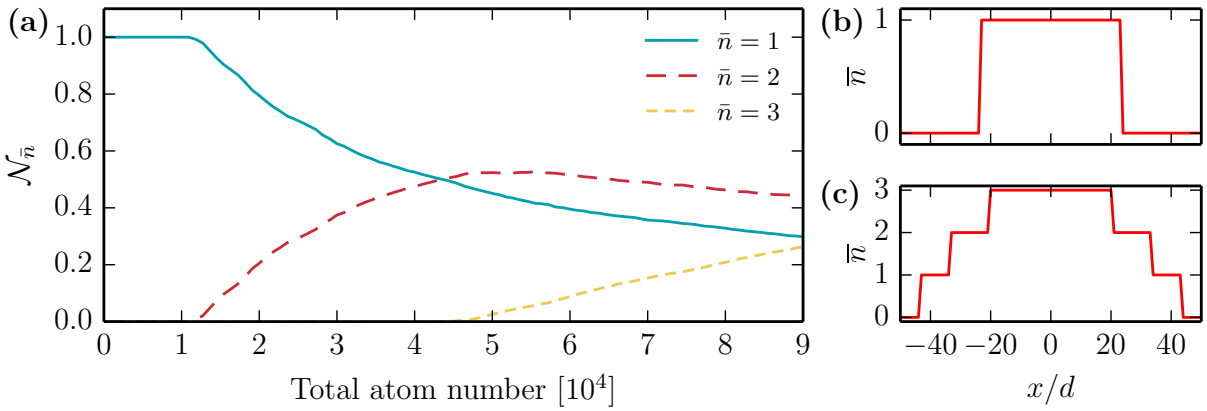

Figure 3.2: (a) Evolution of the Mott shell relative populations $\mathcal{N}_{\overline{n}}$ versus total atom number. Radial density profile $n(x, 0, 0)$ for (b) $N_\mathrm{at} = 8 \times 10^3$, (c) $N_\mathrm{at} = 8 \times 10^4$.

3.2 Single-particle spectra in optical lattices

According to the previous model, we can prepare a MI phase with only singly-occupied sites. This collection of isolated atoms can then be coherently excited on the clock transition using a resonant laser beam. In this section, I give an overview of the experimental set-up used to perform this coherent driving. I start by presenting the optical configuration and the achievable Rabi frequencies. I then show single-particle spectra for various driving frequencies, which allows to validate the calibration of the laser beam parameters. I finally discuss the spectroscopy of the band structure of the optical lattice, which is revealed by the observation of motional sidebands (Ludlow et al. 2011).

3.2.1 Coherent driving on the clock transition

As sketched in Figure 3.1a, a laser beam resonant on the $g \rightarrow e$ transition at $\lambda_0 = 2\pi c/\omega_0 \approx 578.4\,\mathrm{nm}$ is sent on the atoms. The laser beam propagates in the horizontal plane along the $\boldsymbol{e}_x + \boldsymbol{e}_y$ direction at 45° with respect to the horizontal lattice axes. The beam is linearly polarised along the vertical direction $\boldsymbol{e}_z$ and focused on the atoms with a waist $w_{\mathrm{cl}} \approx 70\,\mu\mathrm{m}$[1]. With the optical setup described in Section 2.4.1 we can send up to $P_{\mathrm{cl}} \approx 18\,\mathrm{mW}$ of resonant light on the atoms. The clock laser detuning δ from the atomic resonance ω_0 is $\delta = \omega_{\mathrm{cl}} - \omega_0$.

Effective coupling strength

We use a static magnetic field $\boldsymbol{B} = B_0 \boldsymbol{e}_z$ with $B_0 \approx 182\,\mathrm{G}$ to enable the doubly-forbidden electric dipole transition, as described in Section 1.1.2. The effective coupling strength on the internal degrees of freedom is given by (Barber et al. 2006; Taichenachev et al. 2006):

$$\Omega_{\mathrm{cl}} = \alpha B_0 \sqrt{I_{\mathrm{cl}}}, \tag{3.5}$$

where $I_{\mathrm{cl}} = 2P_{\mathrm{cl}}/(\pi w_{\mathrm{cl}}^2)$ is the intensity of the clock laser light on the atoms and $\alpha \approx 18.7\,\mathrm{mHz/G/(mW/cm^2)^{1/2}}$. With the maximum available power this results in an achievable coupling strength $\Omega_{\mathrm{cl}}^{(\mathrm{max})} \approx 2\pi \times 1600\,\mathrm{Hz}$.

Motional degrees of freedom

The excitation by the clock laser is performed on atoms loaded in optical lattices, the transition is thus $|g, \boldsymbol{n} = \boldsymbol{0}, \boldsymbol{q}\rangle \rightarrow |e, \boldsymbol{n} = \boldsymbol{0}, \boldsymbol{q} + \boldsymbol{k}_{\mathrm{L}}\rangle$[2]. The complete transition rate from the ground to the excited state is modified by the overlap between the motional states (Ludlow et al. 2015):

$$\Omega = \langle w_\perp^0 | \mathrm{e}^{\mathrm{i}\boldsymbol{k}_{\mathrm{cl}}\cdot\hat{\boldsymbol{R}}} | w_\perp^0 \rangle \, \Omega_{\mathrm{cl}}, \tag{3.6}$$

where $w_\perp^0$ denotes the Wannier function in the fundamental band of the horizontal directions of the lattice. At $V_\perp = 24\,E_{\mathrm{R}}$ the overlap factor between the Wannier states is $\langle w_\perp^0 | \mathrm{e}^{\mathrm{i}\boldsymbol{k}_{\mathrm{cl}}\cdot\hat{\boldsymbol{R}}} | w_\perp^0 \rangle \approx 0.92$. The transition rate is therefore limited to $\Omega^{(\mathrm{max})} \approx 2\pi \times 1500\,\mathrm{Hz}$. In the following and in Figure 3.1 the rate Ω is called Rabi frequency.

[1] The waist is measured with a CCD camera outside the vacuum chamber.

[2] In the atomic limit, all quasi-momentum states are populated with equal probability and the quasi-momentum notation becomes irrelevant.

3.2.2 Spectra in deep lattices

For an isolated two-level atom without spontaneous emission, the excitation probability after a time t under a driving of strength Ω and detuning δ is given by (Foot 2004):

$$P_e(\delta) = \frac{\Omega^2}{\Omega^2 + \delta^2} \sin^2\left(\frac{\sqrt{\Omega^2 + \delta^2}}{2} t\right). \tag{3.7}$$

The sinc^2 lineshape in (3.7) corresponds to the Fourier transform of the square-shaped light pulse and has a full-width at half-maximum (FWHM) $\approx 0.8\Omega/\pi$.

We prepare a MI with unit filling fraction [$N_{\mathrm{at}} \approx 8 \times 10^3$, see Section 3.1] and probe it with the clock laser beam. We measure P_e as a function of the laser detuning δ by counting the number of excited state atoms e after a light pulse of duration $t = \pi/\Omega$, with Ω the calculated Rabi frequency for a given laser power P_{cl} computed from (3.6). Figure 3.3a-c shows experimental spectra for three different Rabi frequencies. The lineshape is well reproduced for high enough Rabi frequencies (as in Figure 3.3b-c). For Rabi frequencies around $\Omega \approx 2\pi \times 100\,\mathrm{Hz}$ or smaller, the lineshape is distorted (as in Figure 3.3a). This point is further addressed in Section 3.4. Figure 3.3d shows the fitted FWHM using (3.7) with Ω as a free parameter. Best-fit parameters are close to the expected values $\approx 0.8\Omega/\pi$. This validates the calibration of the Rabi frequency from the measured waist w_{cl} and laser power P_{cl}.

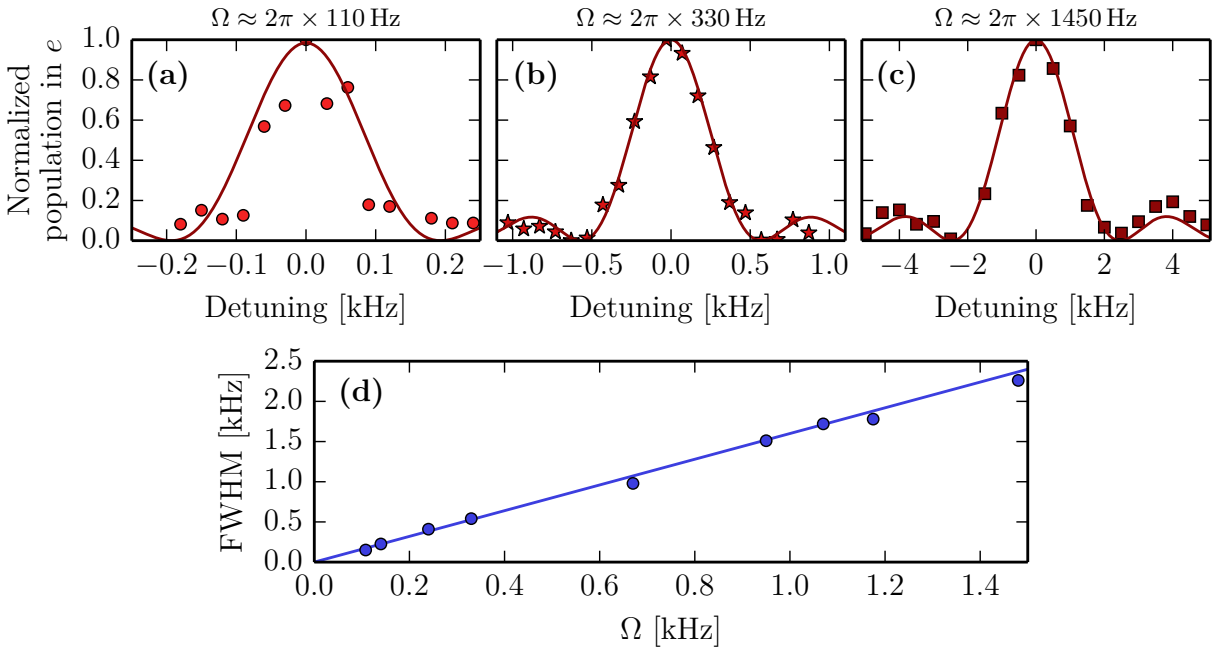

Figure 3.3: (a)-(c) Excitation spectra on ground state atoms for Rabi frequencies $\Omega/(2\pi) = 110\,\mathrm{Hz}$, $330\,\mathrm{Hz}$ and $1450\,\mathrm{Hz}$. The vertical lattice depth is $V_{0,z} \approx 27\,E_{\mathrm{R}}$ and the horizontal lattice depth is $V_{\perp} \approx 24\,E_{\mathrm{R}}$. The solid line is the theoretical excitation probability (3.7) for a single atom. (d) Full-width at half-maximum of the measured spectra with respect to Ω. The solid line is the expectation $\approx 0.8\Omega/\pi$ from our calibrations.

3.2.3 Band spectroscopy

The clock transition is a powerful tool to characterise the energy levels in the system using spectroscopy. For instance, it can be used to probe the band structure arising from the optical lattice. In this section only, we also probe the system at shallow horizontal lattice depths. As described in Section 2.3, we prepare a degenerate cloud of atoms in the fundamental band of a stack of two-dimensional optical lattices. The vertical lattice depth is set to $V_{0,z} = 27\,E_\mathrm{R}$. The horizontal lattice depths are set equal within a few percent and tuned to three different values $V_\perp = 6.5\,E_\mathrm{R}$, $14\,E_\mathrm{R}$ and $28\,E_\mathrm{R}$. The laser Rabi frequency is set to $\Omega \approx 2\pi \times 1450\,\mathrm{Hz}$. We illuminate the atoms with a pulse of clock laser light of duration $t \approx 350\,\mu\mathrm{s}$, corresponding to a π-pulse for a single atom. We measure the number of atoms in the ground state by absorption imaging after a time-of-flight expansion of 10 ms. Figure 3.4a shows the resulting spectra when varying the laser detuning with respect to the atomic transition.

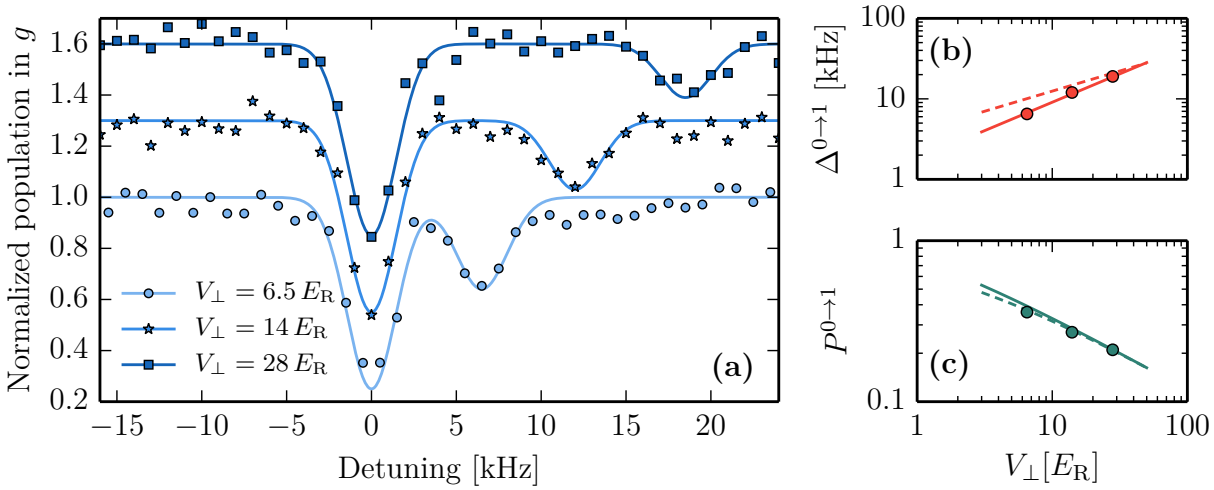

Figure 3.4: (a) Excitation spectra on ground state atoms at various horizontal lattice depth $V_\perp$. The vertical lattice depth is $V_{0,z} \approx 27\,E_\mathrm{R}$. The second peak on the blue side of the central resonance corresponds to the excitation of an atom to the excited state and to the first excited band of the lattice. The solid line is a fit by the sum of two Gaussian functions. The curves at $V_\perp = 14\,E_\mathrm{R}$ and $28\,E_\mathrm{R}$ are shifted vertically by 0.3 and 0.6, respectively, for clarity. The Rabi frequency is $\Omega \approx 2\pi \times 1450\,\mathrm{Hz}$. (b) Position of the excited band peak versus lattice depth. The solid line is the theoretical prediction given by (3.8) and the dashed line is the prediction for a harmonic oscillator. (c) Amplitude of the excited band peak versus lattice depth. The solid line is the theoretical prediction given by (3.9) and the dashed line is the prediction for a harmonic oscillator.

The main peak at zero detuning corresponds to the transition $|g, \boldsymbol{n} = \boldsymbol{0}\rangle \to |e, \boldsymbol{n} = \boldsymbol{0}\rangle$. The observed blue-detuned sidebands at positive detuning correspond to the transitions $|g, \boldsymbol{n} = \boldsymbol{0}\rangle \to |e, \boldsymbol{n} = (1,0,0)\rangle$ and $|g, \boldsymbol{n} = \boldsymbol{0}\rangle \to |e, \boldsymbol{n} = (0,1,0)\rangle$ where the excited atom has acquired one quanta of motion in one of the horizontal directions of the lattice. As the coupling laser propagates in the horizontal direction, higher motional levels in the vertical direction are not excited. In principle, one would expect two sidebands corresponding to each horizontal degrees of freedom, but the choice of almost equal horizontal lattice depths makes the sidebands indistinguishable with our resolution. In the following we therefore drop the 3D notation and keep only one motional degree of freedom. We prepare g atoms

in the fundamental band, hence the symmetrical sidebands to the red side of the central peak corresponding to the transition $|g, n = 1\rangle \rightarrow |e, n = 0\rangle$ are not observed.

We extract the position and amplitude of the sidebands from a fit to the data by a sum of two Gaussian functions. In the following I show how the position and amplitude evolve with respect to the horizontal lattice depth.

Sideband position

The frequency gap $\Delta^{0\rightarrow1}$ between the central peak and the motional sideband, measured as the separation between the centres of the two Gaussian functions, is plotted in Figure 3.4b. The gap increases with the lattice depth with a slope around 0.7 in logarithmic scale. The excitation laser wavevector $\boldsymbol{k}_{\mathrm{cl}}$ is oriented along $\boldsymbol{e}_x + \boldsymbol{e}_y$ and as such the lowest excitation corresponds to the promotion of an atom to the first excited band of the lattice either along the $\boldsymbol{e}_x$ or the $\boldsymbol{e}_y$ direction. The absorption of a laser photon therefore induces a shift in quasi-momentum equal to $\Delta q = k_{\mathrm{cl}}/\sqrt{2}$. The sideband position is given by the energy difference between the states $|n = 0, q\rangle$ to $|n = 1, q + \Delta q\rangle$. For small lattice depths $V_\perp \leq 11\, E_{\mathrm{R}}$, where the system is in the superfluid phase, all atoms are in the $q = 0$ Bloch wave in the lowest band. For higher lattice depths and in the Mott insulator regime, the ground and first excited bands are flat enough so that quasi-momentum is not relevant any more. The frequency gap is thus well captured for arbitrary lattice depth by:

$$\hbar\Delta^{0\rightarrow1} = E(n = 1, \Delta q) - E(n = 0, 0). \tag{3.8}$$

The prediction (3.8) is plotted as a solid line in Figure 3.4b and matches the data very well.

In the deep lattice limit ($V_\perp \gg 100\, E_{\mathrm{R}}$), where the energy bands are close to the energy levels of the harmonic oscillator, the band gap between fundamental and first excited band is given by $\Delta^{0\rightarrow1} \approx 2\sqrt{V_\perp E_{\mathrm{R}}}$ (see Section 1.2). This prediction agrees only roughly with the observed values, which stems for the relatively low values of the lattice depths that we explored.

Sideband amplitude

The amplitude $P^{0\rightarrow1}$ of the motional sideband, measured as the amplitude of the Gaussian function for the sideband, is plotted in Figure 3.4c. The amplitude decreases with the lattice depth with a slope around -0.5 in logarithmic scale. At resonance with the motional sideband, the clock laser induces Rabi oscillations between the states $|g, n = 0\rangle$ and $|e, n = 1\rangle$. The Rabi frequency associated with this transition is $\Omega' = \eta\Omega_{\mathrm{cl}}$ where $\eta = \langle w_\perp^1 | \mathrm{e}^{\mathrm{i}\boldsymbol{k}_{\mathrm{cl}}\cdot\hat{\boldsymbol{R}}} | w_\perp^0 \rangle$ describes the motional overlap between the involved states ($w_\perp^1$ denotes the Wannier function in the first excited band). The excitation probability is therefore given by (Ludlow et al. 2015):

$$P^{0\rightarrow1} = \sin^2\left(\frac{\Omega' t}{2}\right). \tag{3.9}$$

The prediction (3.9), plotted as a solid line in Figure 3.4c, and agrees very well with the data.

In the deep lattice limit ($V_\perp \gg 100\, E_{\mathrm{R}}$), η is roughly equal to $k_{\mathrm{cl}}\sigma_\perp$ where $\sigma_\perp \propto V_\perp^{-1/4}$ is the spatial extension of the Wannier function. Since η is smaller than one, we have $P^{0\rightarrow1} \approx \eta^2(\Omega_{\mathrm{cl}} t/2)^2$ at short times and we get a scaling $P^{0\rightarrow1} \propto V_\perp^{-1/2}$, similar to what is measured experimentally.

3.3 Rabi oscillations in deep lattices

In this section, I present the experimental observation of Rabi oscillations between the clock states in deep lattices. I first discuss the case of Rabi oscillations for a MI phase with unit filling fraction, which discards the effect of interactions. Secondly, I present Rabi oscillations for MI phases with filling fractions of one and two. In the latter case, the temporal dynamics at early times differ strongly from the single-particle expectation. An analysis of this temporal evolution, compatible with a calculation based on our loading model described in Section 3.1, allows us to measure the Mott shell populations.

3.3.1 Single-particle Rabi oscillations

For atoms confined in singly-occupied isolated sites, the time evolution under the driving by the clock laser consists of textbook Rabi oscillations between g and e (Foot 2004), described by the Hamiltonian

$$\hat{H}_{\text{eff}}^{(\bar{n}=1)} = \begin{bmatrix} 0 & \frac{\hbar\Omega}{2} \\ \frac{\hbar\Omega}{2} & -\hbar\delta \end{bmatrix}, \tag{3.10}$$

with δ the laser detuning and Ω the Rabi frequency, as introduced before. We start from a sample in the ground state and switch on the coupling laser. The atomic populations then oscillate between g and e at the frequency $\sqrt{\Omega^2 + \delta^2}$, according to (3.7).

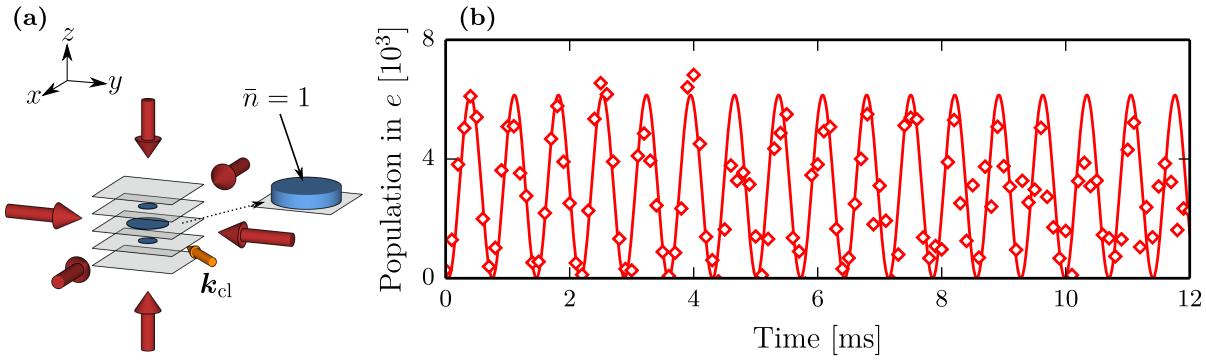

Figure 3.5: Single-particle Rabi oscillations. The coupling by the clock laser is turned on at time $t = 0$. (a) Sketch of the experiment, the atomic sample is a MI phase with unit filling fraction ($N_{\text{at}} \approx 8 \times 10^3$). (b) Coherent driving on the clock transition with Rabi frequency $\Omega \approx 2\pi \times 1400\,\text{Hz}$ and zero detuning, measuring the number of excited state atoms. We observe long-lived oscillations up to 10 ms before the contrast diminishes. The solid line is a sinusoidal fit to the data. *Figure adapted from Bouganne et al. (2017).*

Figure 3.5 shows Rabi oscillations for a MI phase with unit filling fraction ($N_{\text{at}} \approx 8 \times 10^3$). We observe long-lived Rabi oscillations with full contrast up to 10 ms. However, dephasing seems to blur the oscillations for times $\gtrsim 8\,\text{ms}$.

3.3.2 Rabi oscillations for higher filling fraction

We now perform the same experimental procedure on a system with a larger atom number ($N_{\text{at}} \approx 8 \times 10^4$). Figure 3.6 presents the experimental result.

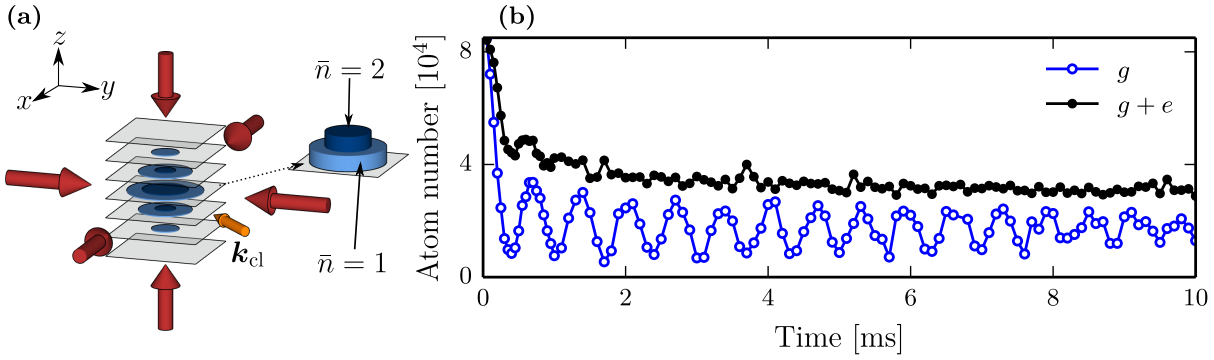

Figure 3.6: Rabi oscillations for high atom number. The driving by the clock laser is turned on at time $t = 0$. (a) Sketch of the experiment, the atomic sample consists of MI phases with filling fractions of one and two ($N_{\mathrm{at}} \approx 8 \times 10^4$). (b) Coherent driving on the clock transition with Rabi frequency $\Omega \approx 2\pi \times 1450\,\mathrm{Hz}$ and zero detuning. Closed (respectively open) symbols represent the remaining total atom number (resp. the population in the ground state g). We observe an initial decay at early times followed by long-lived oscillations. *Figure adapted from Bouganne et al. (2017).*

The temporal dynamics at early times differ strongly from the Rabi oscillations expected for isolated atoms, as presented in Section 3.3.1. In the limit of disconnected sites, we can attribute the early decay to the depletion of multi-occupied sites due to inelastic decay via principal quantum number changing collisions (Traverso et al. 2009), leaving only singly-occupied sites after $\sim 1\,\mathrm{ms}$. The long-time asymptote of the total population thus reflects the initial fraction $\mathcal{N}_{\bar{n}=1}$ of atoms in singly-occupied sites.

Determination of Mott shell populations

Figure 3.7 shows the measured values of the asymptotic value of the total population for various total initial atom numbers[3]. For the parameters of our experiment, there are typically $2L/d \approx 10$ occupied planes, with occupation numbers in a deep MI phase ranging from $\bar{n} = 1$ to $\bar{n} = 3$. For the lowest atom numbers explored in this chapter [$N_{\mathrm{at}} \approx 8 \times 10^3$], we find only a plateau with $\bar{n} = 1$, in agreement with Figure 3.5. For the largest atom numbers [$N_{\mathrm{at}} \approx 8 \times 10^4$], we find plateaus with normalised populations $\mathcal{N}_{\bar{n}=\{1,2,3\}} = \{0.25, 0.39, 0.36\}$. The prediction of this loading model for the normalised population $\mathcal{N}_{\bar{n}=1}$, shown in Figure 3.7 as a dashed line, agrees with the measured values only for low atom numbers $N_{\mathrm{at}} \lesssim 4 \times 10^4$.

We attribute the marked difference for higher atom numbers to three-body inelastic processes. We estimate a lifetime $\tau_{3\mathrm{B}}$ for triply-occupied sites using the three-body rate constant $L_{3\mathrm{B}} \approx 7 \times 10^{-30}\,\mathrm{cm}^6\,\mathrm{s}^{-1}$ measured in Fukuhara et al. (2009):

$$\tau_{3\mathrm{B}} \approx \frac{1}{6 L_{3\mathrm{B}} \int \mathrm{d}^3 r |w_0^0(\boldsymbol{r})|^6} \approx 100\,\mathrm{ms}, \tag{3.11}$$

where w_0^0 is the Wannier function in the fundamental band of the lattice and the factor 6 accounts for the occupation factor $n(n-1)(n-2)$ on a lattice site with $n = 3$. The lifetime is comparable to the loading time in the horizontal lattice. We extend the model

[3]For this experiment, the FDT was left on at its smallest value during the lattice loading, leading to a slightly higher external confinement $\{\Omega_x, \Omega_y\} \approx 2\pi \times \{47, 47\}$Hz than given previously.

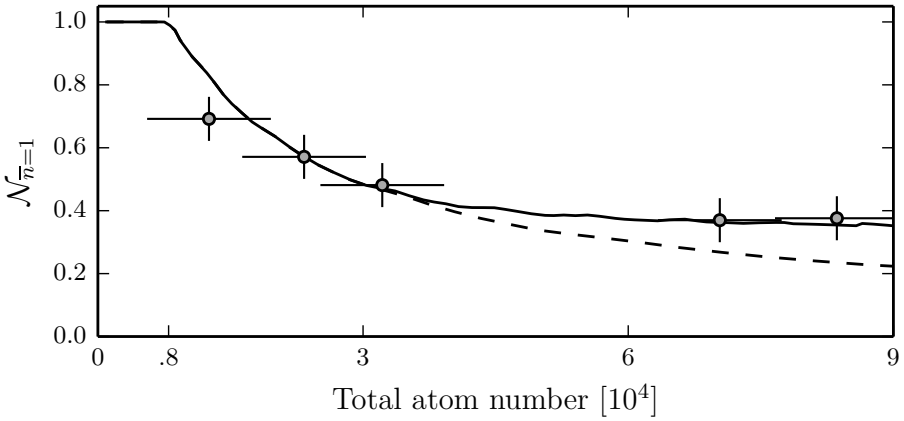

Figure 3.7: Normalised population $\mathcal{N}_{\overline{n}=1}$ in the shell with unit filling fraction as a function of total initial atom number in the lattice. Open symbols show the measurements using the asymptotic value of the total population after many Rabi oscillations as presented in Figure 3.6b. The dashed line is the prediction from our loading model without three-body losses. The solid line accounts phenomenologically for three-body recombination processes which prevent sites with triple occupancy. *Figure adapted from Bouganne et al. (2017).*

of Section 3.1 in a simple way, by assuming that triply-occupied sites decay during the loading, and that adiabatic loading only prepares singly- and doubly-occupied sites (the model predicts negligible population of sites with occupancy $\overline{n} > 3$, and we neglect them in our discussion, see Figure 3.2). For the largest atom numbers [$N_{\mathrm{at}} \approx 8 \times 10^4$], the normalised populations become $\mathcal{N}_{\overline{n}=\{1,2,3\}} = \{0.36, 0.64, 0\}$. The prediction of this lossy loading model, shown in Figure 3.7 as a solid line, agrees well with the measured values and suggests that the in-trap density distribution is close to the predicted one. However, the approximation of complete decay of triply-occupied sites is probably not very accurate. This could also point towards the fact that the lattice loading is not adiabatic for high atom numbers.

3.4 Sources of dephasing

In Figure 3.3a, the agreement between the expected and the measured spectrum is fair but not as good as for higher Rabi frequencies. Actually, for Rabi frequencies smaller than 100 Hz, the FWHM of the spectra stays constant around 150 Hz and the shape is very deformed with substantial shot-to-shot variations. This could be explained by shot-to-shot fluctuations of the clock laser frequency with a standard deviation around 100 Hz. Moreover, Rabi oscillations at high atom numbers presented in Figure 3.6b exhibit loss of contrast after $\sim$ 6 ms whereas in the low atom number case presented in Figure 3.5 such a loss was not observed. In this section, I present possible dephasing mechanisms to explain our observations.

3.4.1 Magic wavelength deviation

If the wavelength of the laser creating the optical lattice is not set to the exact magic wavelength $\lambda_{\mathrm{m}} \approx 759.353\,74(7)$ nm (Barber et al. 2008) the differential light shift between the clock states created by the optical potential causes a frequency shift of the atomic

resonance across the atomic cloud. The laser detuning becomes inhomogeneous over the cloud and this leads to a broadening of the resonance. Barber et al. (2008) measured the slope of the differential polarisability $\Delta\alpha = \alpha_g - \alpha_e$ around the magic wavelength:

$$\left.\frac{\mathrm{d}\Delta\alpha}{\mathrm{d}\lambda}\right|_{\lambda_\mathrm{m}} = 11.4\,\mathrm{Hz}\,{E_\mathrm{R}}^{-1}\,\mathrm{nm}^{-1}. \tag{3.12}$$

We use a parabolic approximation for the Gaussian profile of the lattice beams, which gives a differential laser intensity between the center of the cloud and its edge

$$\Delta I = 2I_\mathrm{cl}R^2/w_\mathrm{latt}^2, \tag{3.13}$$

where R is the cloud radius. We estimate $R \approx 16\,\mu\mathrm{m}$ for the highest atom number $N_\mathrm{at} \approx 8\times10^4$ explored in this experiment using our loading model (see Section 3.1). $w_\mathrm{latt} \approx 130\,\mu\mathrm{m}$ is the mean waist of the lattice beams.

For the highest powers explored in this experiment, the total optical potential on the atoms is $75\,E_\mathrm{R}$. A rough estimation of the clock transition shift over the cloud given by a mismatch of 0.1 nm on the magic wavelength is:

$$\Delta\omega_0 \approx 2\pi \times 2.6\,\mathrm{Hz}. \tag{3.14}$$

In the experiment we take care to keep the lattice wavelength within $\pm0.01\,\mathrm{nm}$ of the magic wavelength using a commercial wavelength meter[4]. The effect of wavelength deviation from the magic wavelength can therefore be neglected in the present work.

3.4.2 Frequency or intensity fluctuations

Fluctuations in the laser frequency or intensity can result in an effective damping of the Rabi oscillations over time. The time scale t_fluc associated with these fluctuations shall be compared with the experiment duration $t \sim 1\,\mathrm{ms}$. On the one hand, if $t_\mathrm{fluc} \ll t$, fluctuations average the signal within each realisation. This leads to the observation of Rabi oscillations with a decaying contrast over time. On the other hand, if $t_\mathrm{fluc} \gtrsim t$, fluctuations translate in a random detuning or Rabi frequency constant during an experiment but randomly changing from shot to shot. In that case, it generally leads to a loss of contrast. When frequency fluctuations are much smaller than the Rabi frequency, it only leads to the observation of Rabi oscillations with full contrast but randomised phase.

Such fluctuations can be modelled in a simplified way by a Gaussian noise on either the detuning or the Rabi frequency. There is no a priori fundamental reason why noise on the frequency or Rabi frequency should be Gaussian, but analytical results can be obtained easily. We thus consider two separate Gaussian noises, with root-mean-square widths γ_det for the detuning and γ_amp for the Rabi frequency. One can analytically calculate the average excitation probability $\overline{P_e}$ after a time t in both cases.

Intensity fluctuations The average excitation probability at zero detuning is given by

$$\overline{P_e}\big|_{\delta=0}(t) = \frac{1}{2}\left[1 - \cos(\Omega t)\mathrm{e}^{-\gamma_\mathrm{amp}^2 t^2/2}\right]. \tag{3.15}$$

[4] WS5, High Finesse.

A fit to the data in Figure 3.5b using this expression yields $\gamma_{\mathrm{amp}} = 2\pi \times 12\,\mathrm{Hz}$. This Rabi frequency noise is related to the laser intensity noise by

$$\gamma_{\mathrm{amp}} = \delta\Omega = \frac{\Omega}{2}\frac{\delta I_{\mathrm{cl}}}{I_{\mathrm{cl}}}, \tag{3.16}$$

which gives a relative laser intensity noise $\delta I_{\mathrm{cl}}/I_{\mathrm{cl}} \approx 2\,\%$. Monitoring the laser intensity with a photodiode shows that actual intensity fluctuations are below 1 % and cannot fully explain the observed dephasing.

Frequency fluctuations The average excitation probability at fixed Rabi frequency is

$$\overline{P_e}\big|_{\Omega}(t) = \frac{1}{2}\left\{1 - \frac{\cos\left[\Omega t + \tan^{-1}(\gamma_{\mathrm{det}}^2 t/\Omega)\right]}{\left[1 + (\gamma_{\mathrm{det}}^2 t/\Omega)^2\right]^{1/4}}\right\} + \frac{\gamma_{\mathrm{det}}^2}{2\Omega^2}\left\{\frac{\cos\left[\Omega t + 3\tan^{-1}(\gamma_{\mathrm{det}}^2 t/\Omega)\right]}{\left[1 + (\gamma_{\mathrm{det}}^2 t/\Omega)^2\right]^{3/4}} - 1\right\}. \tag{3.17}$$

A fit to the data in Figure 3.5b using this expression yields $\gamma_{\mathrm{det}} = 2\pi \times 150\,\mathrm{Hz}$. This is compatible with the narrowest spectra observed in the experiment (see Section 3.2.2).

3.4.3 Inhomogeneous broadening

A remarkable feature of the Rabi oscillations at high atom number shown in Figure 3.6b is their dephasing time $\sim 6\,\mathrm{ms}$, significantly shorter than for the oscillations at small atom number presented in Figure 3.5b. This can be understood as a consequence of inhomogeneous broadening due to the Gaussian profile of the clock laser beam. The cloud size increases with total atom number in such a way that inhomogeneous broadening is more pronounced as atom number increases.

The Gaussian profile of the clock laser beam entails a non-uniform Rabi frequency, but also induces a position-dependent differential light shift (Barber et al. 2008), leading to a non-uniform detuning. Inhomogeneities cause a dephasing over time between atoms in the center and atoms at the edge of the cloud, and thus to an apparent damping when averaging over the whole cloud. We use our loading model to calculate the cloud radii: $R \approx 8.9\,\mu\mathrm{m}$ for $N_{\mathrm{at}} \approx 8 \times 10^3$ and $R \approx 16\,\mu\mathrm{m}$ for $N_{\mathrm{at}} \approx 8 \times 10^4$.

Non-uniform Rabi frequency Using a parabolic approximation for the Gaussian profile of the coupling beam, the Rabi frequency at the edge of the cloud is $\Omega' = \Omega(1 - R^2/w_{\mathrm{cl}}^2)$. We estimate a dephasing time $\tau_{\mathrm{amp}} = 1/|\Omega - \Omega'| \approx w_{\mathrm{cl}}^2/(\Omega R^2)$. We find $\tau_{\mathrm{amp}} \approx 7\,\mathrm{ms}$ for $N_{\mathrm{at}} \approx 8 \times 10^3$ and $\tau_{\mathrm{amp}} \approx 2\,\mathrm{ms}$ for $N_{\mathrm{at}} \approx 8 \times 10^4$. These crudely estimated dephasing times $\tau_{\mathrm{amp}} \propto 1/R^2$ give a lower limit since the dephasing rate is certainly lower than the value given here. They are compatible with our observations in both cases.

Non-uniform detuning Using a parabolic approximation for the Gaussian profile of the coupling beam, the differential light shift between the center and the edge of the cloud is $\hbar\Delta\omega_0 = [\alpha_g(\lambda_0) - \alpha_e(\lambda_0)]I_{\mathrm{cl}}R^2/(\epsilon_0 c w_{\mathrm{cl}}^2)$. The Rabi frequency at the edge of the cloud is therefore $\Omega'' = \sqrt{\Omega^2 + \Delta\omega_0^2}$. We estimate a dephasing time $\tau_{\mathrm{det}} = 1/|\Omega - \Omega''|$. We find $\tau_{\mathrm{det}} \approx 45\,\mathrm{ms}$ for $N_{\mathrm{at}} \approx 8 \times 10^3$ and $\tau_{\mathrm{det}} \approx 5\,\mathrm{ms}$ for $N_{\mathrm{at}} \approx 8 \times 10^4$. These crudely estimated dephasing times $\tau_{\mathrm{det}} \propto 1/R^4$ give a lower limit for the actual ones. The calculated values indicate that non-uniform detuning is not sufficient to account for our observations.

Beam alignment Note that a misalignment of the clock laser beam with respect to the atomic cloud is very detrimental as the inhomogeneity easily gets much bigger than what is estimated here. In particular, the parabolic expansion does not hold any more but a linear expansion would be more reliable. However, such a misalignment also leads to a reduction in the maximum achievable Rabi frequency, and is therefore easily detectable experimentally. We can rule it out for the measurements presented here.

3.4.4 Conclusion

We finally conclude that the observed dephasing of the Rabi oscillations in Figure 3.6b is probably mostly caused by an inhomogeneous Rabi frequency over the cloud, which is much less pronounced for small atom number, compatible with almost no decay in Figure 3.5b. For coupling times $t \gtrsim 10\,\mathrm{ms}$ and at small atom numbers, Rabi oscillations seem to keep full contrast but with a randomised phase. Along with the observation of deformed spectra at low Rabi frequencies, this points towards shot-to-shot frequency fluctuations of the clock laser. A further study of the laser frequency fluctuations using Ramsey fringes is presented in the thesis of Manel Bosch Aguilera (2019). While we do not have experimental evidence yet, fluctuations of the resonance frequency of the reference cavity is a possible cause (see Section 2.4). In particular, the strong correlation between the ambient temperature and the resonance frequency suggests that thermal effects might play an important role.

3.5 Interacting atoms driven on the clock transition

So far I have mainly discussed single-particle phenomena. However, the dynamics of doubly-occupied sites, as shown in Figure 3.6b, are very different. In this section I study the behaviour of atoms in doubly-occupied sites under the driving by the clock laser. Interatomic interactions strongly modify the dynamics expected for isolated atoms. After presenting a microscopic model used to analyse singly- and doubly-occupied sites evolving under the driving by the clock laser, I present the measurements of the scattering parameters involving both clock states. First, inelastic interactions lead to atom losses characterised by rates $\gamma_{\alpha\beta}$. Second, elastic interactions lead to energy shifts of the on-site interaction strength $U_{\alpha\beta}$. These parameters depend on the internal state of the atoms present on a same site $\alpha, \beta = g, e$. Two atoms in the ground state are stable against losses, $\gamma_{gg} = 0$, and we calibrated the energy shift due to contact interaction $U_{gg} = h \times 1475(25)\,\mathrm{Hz}$ by a collapse and revival experiment (see Section 2.3.4). We thus need to determine the unknown quantities γ_{eg}, γ_{ee}, U_{eg} and U_{ee}. Most of the material in this section is reproduced from Bouganne et al. (2017).

3.5.1 Model

The dynamics of doubly-occupied sites driven by the clock laser differs from singly-occupied sites in several aspects. First, due to bosonic enhancement, the coupling strength is $\sqrt{2}$ times higher for double than for single occupancy. Second, the three possible symmetric states $|gg\rangle$, $|eg\rangle$ and $|ee\rangle$ have in general different interaction energies, characterised by Hubbard parameters U_{gg}, U_{eg} and U_{ee}. Finally, the states $|eg\rangle$ and $|ee\rangle$ are prone to inelastic losses. We model this inelastic process by adding an imaginary term $-\mathrm{i}\hbar\gamma_{e\alpha}/2$ to

the Hamiltonian, with $\alpha = e, g$. This results in a dynamics captured by a non-hermitian effective Hamiltonian

$$\hat{H}_{\text{eff}}^{(\overline{n}=2)} = \begin{bmatrix} 0 & \frac{\hbar\Omega}{\sqrt{2}} & 0 \\ \frac{\hbar\Omega}{\sqrt{2}} & U_{eg} - U_{gg} - \mathrm{i}\frac{\hbar\gamma_{eg}}{2} - \hbar\delta & \frac{\hbar\Omega}{\sqrt{2}} \\ 0 & \frac{\hbar\Omega}{\sqrt{2}} & U_{ee} - U_{gg} - \mathrm{i}\frac{\hbar\gamma_{ee}}{2} - 2\hbar\delta \end{bmatrix}, \tag{3.18}$$

in the $\{|gg\rangle, |eg\rangle, |ee\rangle\}$ basis.

We numerically solve the generalised Schrödinger equation using the effective Hamiltonian (3.18) with initial condition $|\psi^{(2)}\rangle = |gg\rangle$. We also solve the Schrödinger equation for singly-occupied sites using the Hamiltonian (3.10) with initial condition $|\psi^{(1)}\rangle = |g\rangle$. We extract from the solutions the transition probabilities denoted $P_\alpha^{(1)} = |\langle\alpha|\psi^{(1)}\rangle|^2$ with $\alpha = g, e$ and $P_\beta^{(2)} = |\langle\beta|\psi^{(2)}\rangle|^2$ with $\beta = gg, eg, ee$. We then sum the contributions of singly- and doubly-occupied sites to obtain the average populations $\overline{N}_g$ and $\overline{N}_e$:

$$\frac{\overline{N}_g}{N_{\text{at}}} = \mathcal{N}_{\overline{n}=1} P_g^{(1)} + \mathcal{N}_{\overline{n}=2}\left(P_{gg}^{(2)} + \frac{1}{2}P_{eg}^{(2)}\right), \tag{3.19}$$

$$\frac{\overline{N}_e}{\eta_e N_{\text{at}}} = \mathcal{N}_{\overline{n}=1} P_e^{(1)} + \mathcal{N}_{\overline{n}=2}\left(P_{ee}^{(2)} + \frac{1}{2}P_{eg}^{(2)}\right). \tag{3.20}$$

3.5.2 Lifetime of doubly-occupied sites: two-body decay rates

Here I present a series of experiments measuring the inelastic loss rates γ_{ee} and γ_{eg} from lifetime measurements of samples containing doubly-occupied sites.

Excited-excited pairs

We first investigate the part of e-e inelastic collisions: two atoms in the excited state collide and are expelled from the trap. This loss dynamics is described by (Syassen et al. 2008; García-Ripoll et al. 2009):

$$\frac{\mathrm{d}\langle\hat{\Psi}_e^\dagger\hat{\Psi}_e\rangle}{\mathrm{d}t} = -\beta_{ee}\langle\hat{\Psi}_e^\dagger\hat{\Psi}_e^\dagger\hat{\Psi}_e\hat{\Psi}_e\rangle. \tag{3.21}$$

We write the field operator on the Wannier basis $\hat{\Psi}_e(\boldsymbol{r}) = w_0^0(\boldsymbol{r})\hat{e}$, with $\hat{e}$ the annihilation operator for an atom in the excited state, and thus

$$\langle\hat{\Psi}_e^\dagger\hat{\Psi}_e\rangle = \int \mathrm{d}^3r|w_0^0(\boldsymbol{r})|^2\langle\hat{e}^\dagger\hat{e}\rangle = \langle\hat{e}^\dagger\hat{e}\rangle = \langle\hat{n}_e\rangle, \tag{3.22}$$

$$\langle\hat{\Psi}_e^\dagger\hat{\Psi}_e^\dagger\hat{\Psi}_e\hat{\Psi}_e\rangle = \int \mathrm{d}^3r|w_0^0(\boldsymbol{r})|^4\langle\hat{e}^\dagger\hat{e}^\dagger\hat{e}\hat{e}\rangle = \int \mathrm{d}^3r|w_0^0(\boldsymbol{r})|^4\langle\hat{n}_e(\hat{n}_e-1)\rangle. \tag{3.23}$$

Here we recognise the integral of the fourth power of the Wannier function, which is proportional to U_{gg} [see (2.17)]. We define

$$\gamma_{ee} = \beta_{ee}\frac{U_{gg}M}{4\pi\hbar^2 a_{gg}}, \tag{3.24}$$

and thus

$$\frac{\mathrm{d}\langle\hat{n}_e\rangle}{\mathrm{d}t} = -\gamma_{ee}\langle\hat{n}_e(\hat{n}_e-1)\rangle\,. \tag{3.25}$$

The occupation probability $P_{ee}^{(2)}(t)$ for two atoms in the excited state thus evolves as:

$$\frac{\mathrm{d}P_{ee}^{(2)}}{\mathrm{d}t} = -\gamma_{ee}P_{ee}^{(2)}(t). \tag{3.26}$$

Singly-occupied sites do not decay, but doubly-occupied sites decay exponentially with a rate γ_{ee}.

State preparation The procedure to measure the loss rate γ_{ee} is presented in Figure 3.8. We first apply a clock laser pulse of area $\Omega t \approx \pi$ [$\Omega \approx 2\pi \times 1450\,\mathrm{Hz}$] in order to obtain a substantial population of $|ee\rangle$. Then we get rid of the ground state atoms with a removal pulse on the $^1\mathrm{S}_0$–$^1\mathrm{P}_1$ transition (see Section 2.2.1). We are then left with a collection of singly- and doubly-occupied sites where all atoms are in the excited state e.

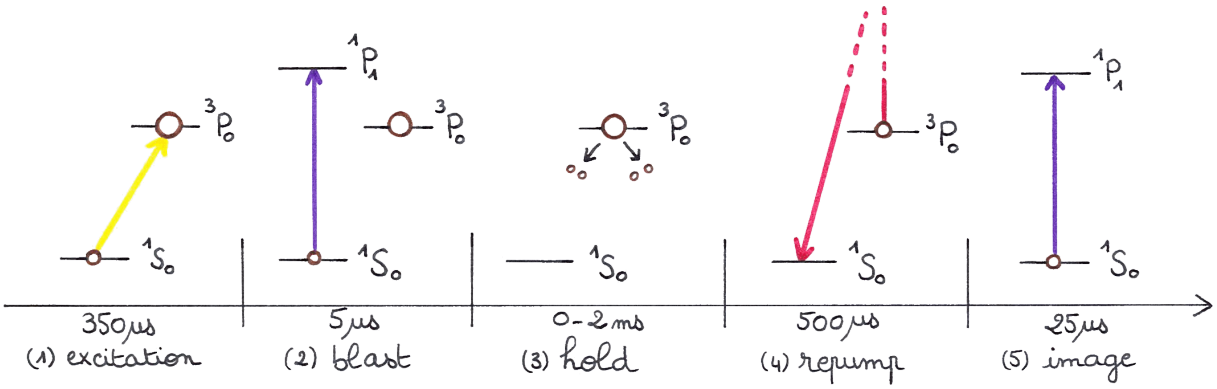

Figure 3.8: Time sequence used to measure the excited-excited loss rate γ_{ee}. *Figure designed with Marion Bouganne.*

After a variable hold time t, we measure the population in the excited state which evolves as

$$\frac{\overline{N}_e(t)}{\eta_e N_{\mathrm{at}}} = \mathcal{N}_{\bar{n}=1}P_e^{(1)}(0) + \mathcal{N}_{\bar{n}=2}P_{ee}^{(2)}(0)\mathrm{e}^{-\gamma_{ee}t}. \tag{3.27}$$

Figure 3.9 shows the measured lifetime of this sample. We detect a fast exponential decay at short times which we interpret as the consequence of inelastic e-e collisions. For longer times, we observe a plateau corresponding to the remaining e atoms in singly-occupied sites. The exponential decay rate is a direct measurement of $\gamma_{ee} = 9300(100)\,\mathrm{s}^{-1}$, which gives $\beta_{ee} = 2.5(1)\times10^{-11}\,\mathrm{cm}^3\,\mathrm{s}^{-1}$.

Ground-excited pairs

We now look at the part of e-g inelastic collisions: an atom in the excited state collides with an atom in the ground state and both are expelled from the trap. This loss dynamics is described by:

$$\frac{\mathrm{d}\left(\langle\hat{\Psi}_e^\dagger\hat{\Psi}_e\rangle + \langle\hat{\Psi}_g^\dagger\hat{\Psi}_g\rangle\right)}{\mathrm{d}t} = -2\beta_{eg}\langle\hat{\Psi}_e^\dagger\hat{\Psi}_g^\dagger\hat{\Psi}_e\hat{\Psi}_g\rangle\,, \tag{3.28}$$

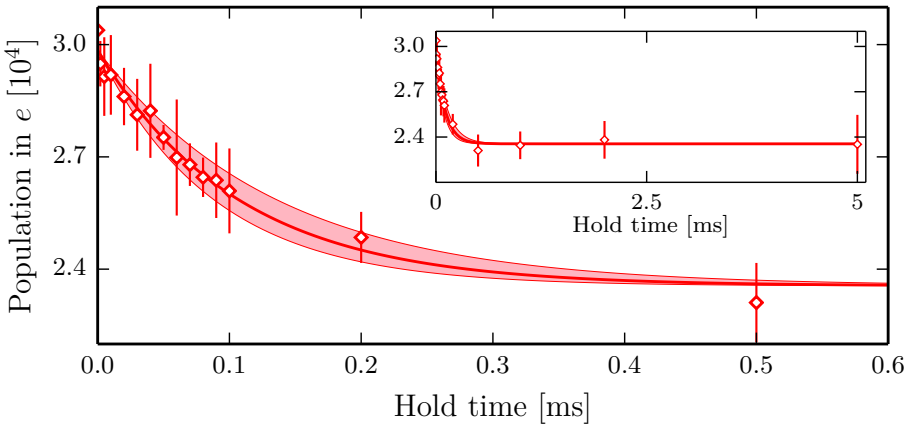

Figure 3.9: Lifetime measurement for a sample with only atoms in e. Doubly-occupied sites decay exponentially through inelastic collisions. The inset shows the plateau of remaining singly-occupied sites for longer times. The solid line is an exponential fit to the data, with the shaded area reflecting 68 % confidence interval. *Figure adapted from Bouganne et al. (2017).*

which implies [with $\gamma_{eg} = \beta_{eg} M U_{gg}/(4\pi\hbar^2 a_{gg})$]

$$\frac{\mathrm{d}\left(\langle \hat{n}_e \rangle + \langle \hat{n}_g \rangle\right)}{\mathrm{d}t} = -2\gamma_{eg} \langle \hat{n}_e \hat{n}_g \rangle \,. \tag{3.29}$$

The occupation probability $P_{eg}^{(2)}(t)$ for one atom in the ground state and one atom in the excited state thus evolves as

$$\frac{\mathrm{d}P_{eg}^{(2)}}{\mathrm{d}t} = -\gamma_{eg} P_{eg}^{(2)}(t). \tag{3.30}$$

State preparation The procedure to measure the loss rate γ_{eg} is presented in Figure 3.10. We apply a clock laser pulse of area $\Omega t \approx \pi/2$ [$\Omega \approx 2\pi \times 1450\,\mathrm{Hz}$] in order to obtain a substantial population of $|eg\rangle$.

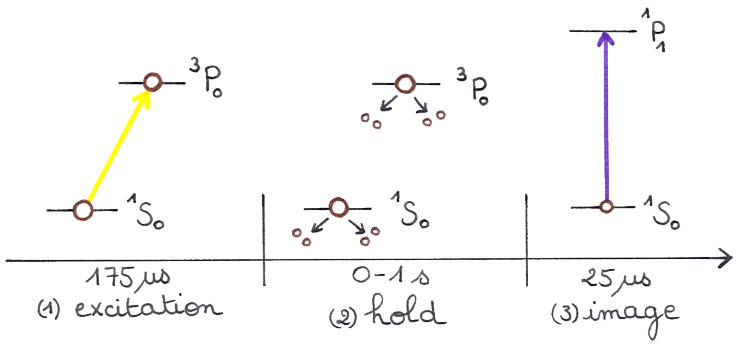

Figure 3.10: Time sequence used to measure the excited-ground loss rate γ_{eg}. *Figure designed with Marion Bouganne.*

After a variable hold time we measure the population of ground state atoms which evolves as

$$\frac{\overline{N}_g(t)}{N_{\mathrm{at}}} = \mathcal{N}_{\overline{n}=1} P_g^{(1)}(0) + \mathcal{N}_{\overline{n}=2} P_{gg}^{(2)}(0) + \mathcal{N}_{\overline{n}=2} \frac{P_{eg}^{(2)}(0)}{2} \mathrm{e}^{-\gamma_{eg} t}. \tag{3.31}$$

Figure 3.11 shows the measured lifetime of this sample. We detect almost no decay up to 1 s, a time after which coherent tunnelling can start to play a role. An exponential fit to the data, with a rate γ as the only free parameter, yields $\gamma \approx 0.5\,\mathrm{s}^{-1}$. We measure a similar lifetime for atoms in g in the absence of the clock laser excitation. Hence the measured damping rate γ only provides an upper bound for γ_{eg}, and thus $\beta_{eg} \leq 10^{-15}\,\mathrm{cm}^3\,\mathrm{s}^{-1}$.

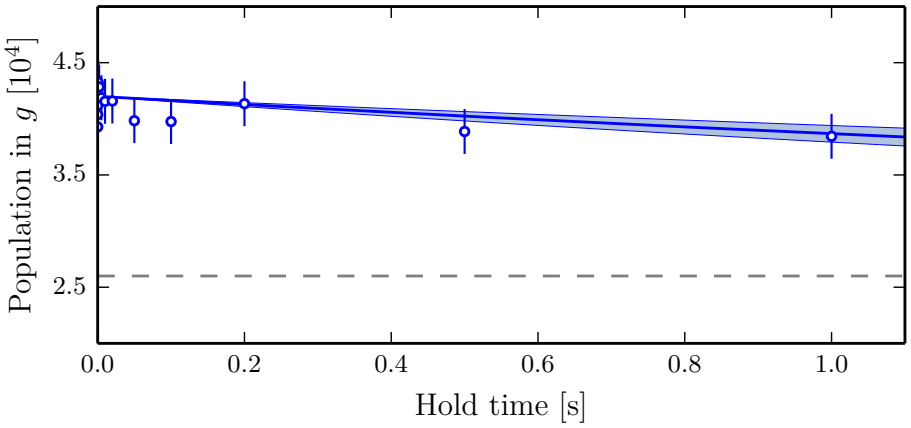

Figure 3.11: Absence of inelastic collisions involving g and e. The dashed line shows the asymptote expected for a complete decay of e-g pairs. The solid line is an exponential fit to the data, with the shaded area reflecting 68 % confidence interval. *Figure adapted from Bouganne et al. (2017).*

3.5.3 Spectroscopy of elastic interactions: scattering lengths

Having characterised inelastic collisions, I now show experiments measuring the elastic energy shifts U_{eg} and U_{ee}. To this end, we perform spectroscopic experiments probing doubly-occupied sites.

Ground-excited pairs

The determination of the ground-excited energy shift U_{eg} is best performed in a perturbative limit, where the pulse area and the population of $|ee\rangle$ remain small. In that case, the evolution of $|\psi^{(2)}\rangle$ reduces to that of a two-level system resonant for

$$\hbar\delta = U_{eg} - U_{gg}. \tag{3.32}$$

Such a resonance can be resolved provided that the Rabi frequency of the driving is smaller than the shift $(U_{eg} - U_{gg})/\hbar$ from the zero-detuning resonance of singly-occupied sites. This is shown illustratively in Figure 3.12a.

Excited-excited pairs

In order to extract the interaction strength U_{ee}, one could in principle use a two-photon resonance directly linking $|gg\rangle$ and $|ee\rangle$. This requires a weak enough Rabi frequency $\Omega \ll \Delta$ and $\delta' \ll \Delta$, where $\hbar\Delta = U_{eg} - (U_{ee} + U_{gg})/2$ is an interaction shift and where $\delta' = \delta - (U_{ee} - U_{gg})/(2\hbar)$ is the two-photon detuning. Under these conditions, the intermediate state $|eg\rangle$ can be adiabatically eliminated, and the dynamics reduces to that of an effective

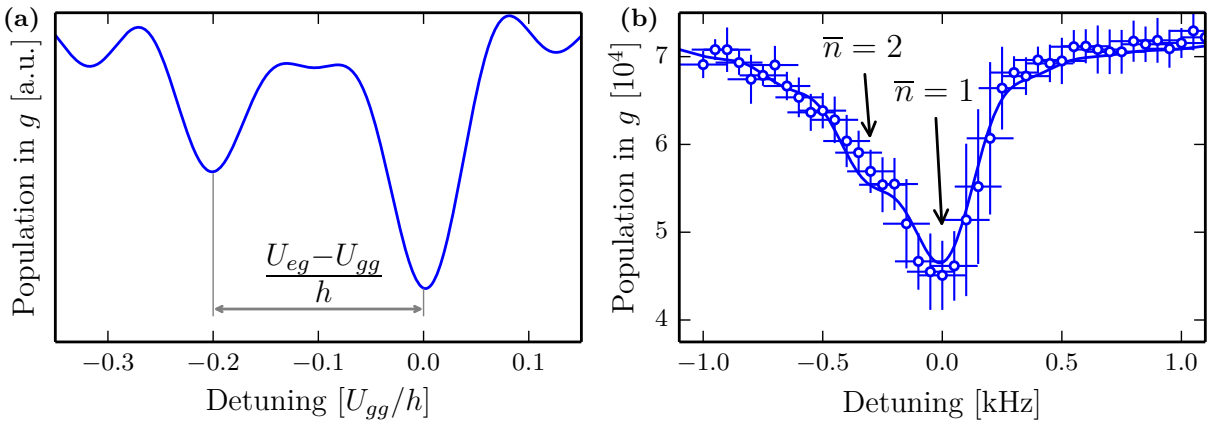

Figure 3.12: Determination of U_{eg}. (a) Illustration of the method. The number of atoms in g is plotted with respect to the detuning δ of the clock laser, with a pulse area $\Omega t = \pi$. Singly-occupied sites are excited on the single-atom resonance at $\delta = 0$. Interactions shift the resonance for doubly-occupied sites to $(U_{eg} - U_{gg})/\hbar$. This interaction sideband can be resolved for a sufficiently weak Rabi frequency $\Omega \lesssim |U_{eg} - U_{gg}|/\hbar$. For illustrative purposes, $\Omega = 2\pi \times 70\,\mathrm{Hz}$ and $U_{eg} = 0.8\,U_{gg}$ in this plot. (b) Experimental determination of U_{eg} with $\Omega t \approx \pi$. The shoulder near $\delta = -2\pi \times 300\,\mathrm{Hz}$ indicates the excitation of doubly-occupied sites. *Figure adapted from Bouganne et al. (2017).*

two-level system. The difference $(U_{ee} - U_{gg})/2$ can therefore be directly measured from the location of the two-photon resonance. Practically, this idealised experiment is difficult to perform for weak coupling due to the strong loss rate γ_{ee}, which gives a substantial width to the two-photon resonance.

In order to circumvent this issue, we perform the experiment at a larger Rabi frequency, and make use of the losses by measuring the total population after a clock pulse of area $\Omega t = 2\pi$. The *background signal* from singly-occupied sites is minimised near resonance, whereas doubly-occupied sites show a pronounced feature due to $e - e$ losses located at

$$\hbar\delta \approx \frac{U_{ee} - U_{gg}}{2}. \tag{3.33}$$

This is shown illustratively in Figure 3.13a. Even for large Rabi frequencies, we find that the loss spectral feature in the total signal is only weakly affected by the intermediate $|eg\rangle$ state (inset of Figure 3.13a).

The experimental results are presented in Figures 3.12b and 3.13b. Data are re-centred so that $\delta = 0$ corresponds to the single-atom resonance. The measurement of U_{eg} (Figure 3.12b) is done with a weak Rabi frequency $\Omega^{\mathrm{weak}} \approx 2\pi \times 150\,\mathrm{Hz}$ and displays a shoulder near $\delta \approx -2\pi \times 300\,\mathrm{Hz}$. This corresponds to the signal from doubly occupied sites. On the other hand, the measurement of U_{ee} (Figure 3.13b), performed at strong Rabi frequency $\Omega^{\mathrm{strong}} \approx 2\pi \times 1500\,\mathrm{Hz}$, shows a loss peak almost coincident with $\delta \approx 2\pi \times 0\,\mathrm{Hz}$, or equivalently $U_{ee} \approx U_{gg}$.

Fit procedure

To extract quantitative values, we fit the prediction of the model from Section 3.5.1 to the experimental spectra (solid and dashed lines in Figures 3.12b and 3.13b). We fix the normalised populations $\mathcal{N}_{\overline{n}=1,2}$, the loss rates γ_{ee}, γ_{eg} and the initial atom number N_{at} to

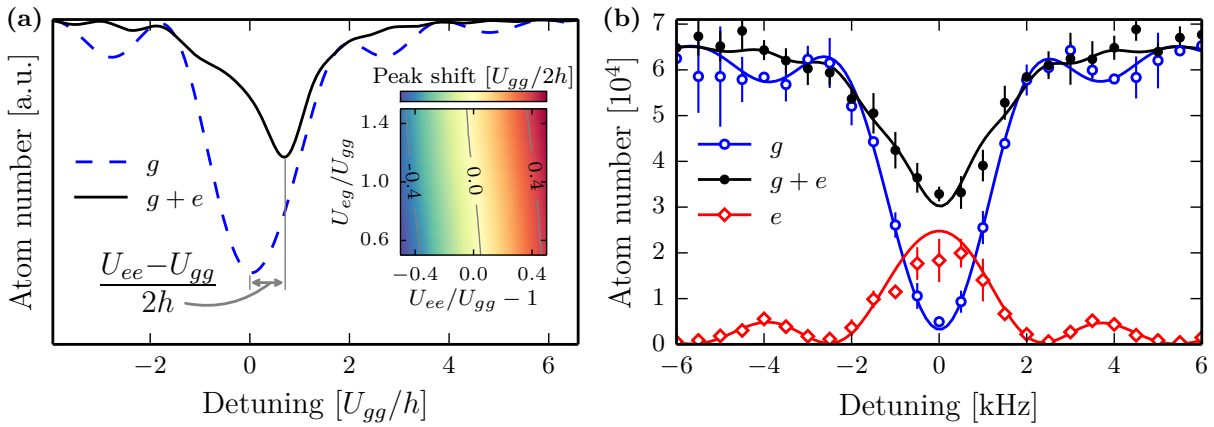

Figure 3.13: Determination of U_{ee}. (a) Illustration of the method. For strong Rabi frequencies and pulse area $\Omega t = 2\pi$, the total population of doubly occupied sites has decreased due to inelastic losses (black solid line). This loss resonance is shifted with respect to the single-atom resonance (dashed blue line, pulse area $\Omega t = \pi$) by $(U_{ee} - U_{gg})/(2\hbar)$, with weak dependence on U_{eg} (see inset). For illustrative purposes, $\Omega = 2\pi \times 1500\,\mathrm{Hz}$ and $U_{ee} = 2.5\,U_{gg}$ in this plot. (b) Experimental determination of U_{ee}. The open symbols show the population in g (circles) and e (diamonds) for the reference measurement with $\Omega t \approx \pi$ locating the single-atom resonance. The closed ones correspond to the total population for the loss measurement with $\Omega t \approx 2\pi$. The loss curve is almost centred on the single-atom resonance. *Figure adapted from Bouganne et al. (2017).*

their measured values and leave the Rabi frequencies Ω^{weak}, Ω^{strong}, the interaction energies U_{ee}, U_{eg} and the repumping efficiency η_e as free parameters. The repumping efficiency η_e from the metastable $^3\mathrm{P}_0$ state (see Section 2.2.2) is assumed to be independent from the filling fraction for simplicity. The prediction of the model has been further convolved with a Gaussian function to account phenomenologically for single-particle damping (see the discussion in Section 3.4), taking the root-mean-square width σ of the Gaussian as an extra free parameter.

We obtain $\Omega^{\mathrm{weak}} = 2\pi \times 145(13)\,\mathrm{Hz}$, $\Omega^{\mathrm{strong}} = 2\pi \times 1470(70)\,\mathrm{Hz}$ and $\eta_e = 68(6)\,\%$, consistent with our calibrations. The width of the convolving Gaussian $\sigma = 100(40)\,\mathrm{Hz}$, is consistent with the narrowest spectrum we could observe, as discussed in Section 3.3.1. Finally we extract

$$U_{ee} - U_{gg} = h \times -40(340)\,\mathrm{Hz}, \tag{3.34}$$
$$U_{eg} - U_{gg} = h \times -270(120)\,\mathrm{Hz}, \tag{3.35}$$

in agreement with the qualitative discussion above. The error bars represent statistical 68 % confidence intervals on the optimal values of U_{eg} and U_{ee}, obtained by the bootstrap method (Bohm et al. 2010). This method consists in constructing *virtual* data sets using the residuals of the best fit performed on the actual data set. Virtual data sets are constructed by adding the randomly shuffled residuals to the actual data. A bootstrap re-sampling set is the best fit parameters set obtained from these virtual sets. Figure 3.14 shows the histograms of 1000 bootstrap re-sampling sets. We find histograms centered on the best-fitted values on the actual data set, their widths give the experimental error in the determination of the parameters.

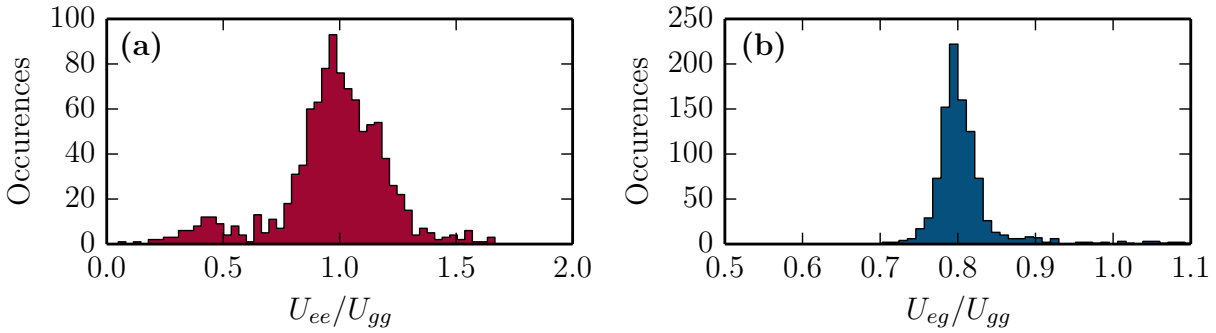

Figure 3.14: Determination of errors bars on the energy shifts (a) U_{ee} and (b) U_{eg}, given as the standard deviation on the histograms. The histograms are constructed by the bootstrap method [see text and Bohm et al. (2010)].

3.5.4 Collisional parameters

From the previous measurements we are able to extract all relevant collisional parameters involving both clock states. For this we use our calibration of the on-site interaction energy in the ground state $U_{gg} = h \times 1475(25)\,\mathrm{Hz}$. The ratio of the elastic interaction energies U_{eg} and U_{ee} to U_{gg} is equal to the ratio of the respective scattering lengths, thus

$$a_{eg} - a_{gg} = -19(11)\,a_0, \tag{3.36}$$
$$a_{ee} - a_{gg} = -3(25)\,a_0. \tag{3.37}$$

The error bars represent statistical 68 % confidence intervals and do not take into account possible systematic errors.

	Bouganne et al. (2017)	Franchi et al. (2017)
a_{eg} $[a_0]$	86(11)	94.7(16)
a_{ee} $[a_0]$	102(25)	126.7(23)
β_{eg} $[\mathrm{cm^3\,s^{-1}}]$	$\leq 10^{-15}$	$\leq 10^{-14}$
β_{ee} $[\mathrm{cm^3\,s^{-1}}]$	$2.5(1) \times 10^{-11}$	$1.3(7) \times 10^{-11}$

Table 3.1: Comparison between intra- and inter-state scattering lengths and two-body loss rates as published in Bouganne et al. (2017) and Franchi et al. (2017).

Combining our measurements with the measurement of the scattering length in the ground state $a_{gg} = 105\,a_0$ (Kitagawa et al. 2008; Borkowski et al. 2017), we obtain the scattering lengths a_{eg} and a_{ee}. We also give an upper bound for β_{eg} and the value of β_{ee}. We compare in Table 3.1 our measurements to very similar and independent ones performed at LENS in Florence (Franchi et al. 2017). The measured scattering lengths agree within the error bars. Still, the determination of the scattering lengths is more precise in Franchi et al. (2017) owing to their ability to resolve better the interaction peak [the linewidth and frequency jitter of their laser was characterised to be smaller than 50 Hz (Cappellini et al. 2015)]. The inelastic loss rate in the excited state are however slightly different, our measurement providing a smaller uncertainty. Franchi et al. (2017) could not reach the range of Rabi frequencies required to substantially populate the state $|ee\rangle$ and performed the measurement in a 1D lattice, with a substantial fraction of thermal

atoms. Moreover, the analysis of the temporal evolution of the atom number required a more complex modelling, potentially leading to systematic errors.

We thus find all scattering lengths involving the clock states of ^{174}Yb equal within 20 %. This is somewhat surprising and these observations differ markedly from the fermionic ^{173}Yb isotope, where the equivalent scattering lengths have been found quite different from one another (Cappellini et al. 2014; Scazza et al. 2014) [for example $a_{ee} \approx 1.5 a_{gg}$ and $a_{eg}^{+} \approx 15 a_{gg}$]. The inelastic loss rates are compatible with previous measurements on the fermionic ^{171}Yb and ^{173}Yb isotopes (Ludlow et al. 2011; Scazza et al. 2014) or bosonic ^{88}Sr (Traverso et al. 2009).

3.6 Conclusion

In this chapter, I have demonstrated coherent control on the clock transition of degenerate atoms loaded in optical lattices. This coherent control can be used to probe the band structure of the lattice, to prepare coherent superpositions of the clock states or to measure the relative populations of the Mott insulator phases with unit and double filling fractions. For sufficiently high lattice depths, such Mott phases can be considered as a collection of independent singly- and doubly-occupied sites, whose dynamics are simple to understand and analyse. In that respect I showed the measurement of the previously unknown scattering lengths and two-body loss rate coefficients involving the clock state of the bosonic ^{174}Yb isotope, published in Bouganne et al. (2017). Similar measurements were independently performed at LENS in parallel (Franchi et al. 2017).

The inelastic loss rate between two atoms in the excited state is substantial and constitutes a threat to experiments where such collisions can happen. Several solutions exist to get around this effect. First, in the case of bosons, one can finely tailor the external trapping potential of the optical lattice to be able to prepare only a Mott phase with unit occupancy, even for large atom numbers, thereby preventing inelastic losses to happen. This also works naturally with a polarised gas of fermions, where double occupancies are suppressed by the Pauli principle (Jördens et al. 2008; Campbell et al. 2017). Secondly, one could use an *interaction blockade*, where transitions to the states $|eg\rangle$ and $|ee\rangle$ are always off-resonant and thus inefficient. The near-equality of the intra- and inter-state scattering lengths for ^{174}Yb restricts this method to very low Rabi frequencies. However this should be usable for the fermionic ^{173}Yb isotope where the shifts are large. Finally, the large value of the inelastic loss rate suggests that a *quantum Zeno* suppression of losses (Syassen et al. 2008; Barontini et al. 2013; Zhu et al. 2014; Sponselee et al. 2018) could occur in our system. Strong losses project the system to a lossless subspace, in a similar way as repeated measurements freezes the evolution of a system. For a suitable initial state and weak enough coupling, an adiabatic preparation of a state belonging to the lossless subspace should be possible.

4

Anomalous momentum diffusion in an open Bose-Hubbard gas

So far I have shown that the driving of internal states can be made coherent when the motional degrees of freedom are unaffected as in deep optical lattices (Bouganne et al. 2017). The observed long coherence times between the clock states stems from the use of the ultra-narrow transition linking them, relying on the absence of spontaneous emission in the excited state. Even in these experiments we could observe various dephasing mechanisms, either technical (laser frequency fluctuations, spatial inhomogeneities of the coupling...) or more fundamental (inelastic losses in the metastable state, atomic motion...). When the motional degrees of freedom come into play, as in a bulk BEC (Bosch Aguilera et al. 2018), the dynamics enrich but spatial coherence remains. Coherence can however disappear due to various dissipative processes, as realised in quantum gases by atom losses or spontaneous emission for example. The information carried by the expelled particles or by the spontaneously emitted photon is lost, interrupting the coherent dynamics.

A simple but illuminating example of how quantum information is lost through the coupling to an environment is the 'standard model' of quantum optics, i.e. a two-level atom coupled to an electro-magnetic field. See for instance the lectures of Claude Cohen-Tannoudji (1989), where the density matrix[1] helps to describe the spatial coherences of the atom in a bath of photons. In this work, the use of a master equation with quantum jump operators[1] was crucial to describe the decoherence processes (Haroche et al. 2006). However, when systems are made up of many particles, the decoherence dynamics is generally expected to be hastened by interactions. This corresponds for example to interaction broadening in spectroscopy.

Recent experiments with quantum gases have shown that the dynamics are strongly altered and that interactions are generally not degrading coherence. Light scattering was used to inhibit coherent tunnelling in an optical lattice (Patil et al. 2015), the spontaneously emitted photon acting as a measurement device. Also, the robustness of localised many-body states subjected to dissipation and thermalisation was studied (Lüschen et al. 2017). One-body losses were realised using an electron beam aiming at a Bose-Einstein condensate, with which a suppression of atom losses was observed (Barontini et al. 2013). A delay of the Mott insulator melting with dissipation was investigated (Tomita et al. 2017) using two-body losses from photo-association resonances. Interestingly, dissipation induced by collisional losses can help to prepare highly-correlated states, as was performed with cold molecular gases in a 1D optical lattice (Syassen et al. 2008) or in the Fermi-Hubbard model (Sponselee et al. 2018).

[1] See also Appendix B.1 for a reminder of this concept.

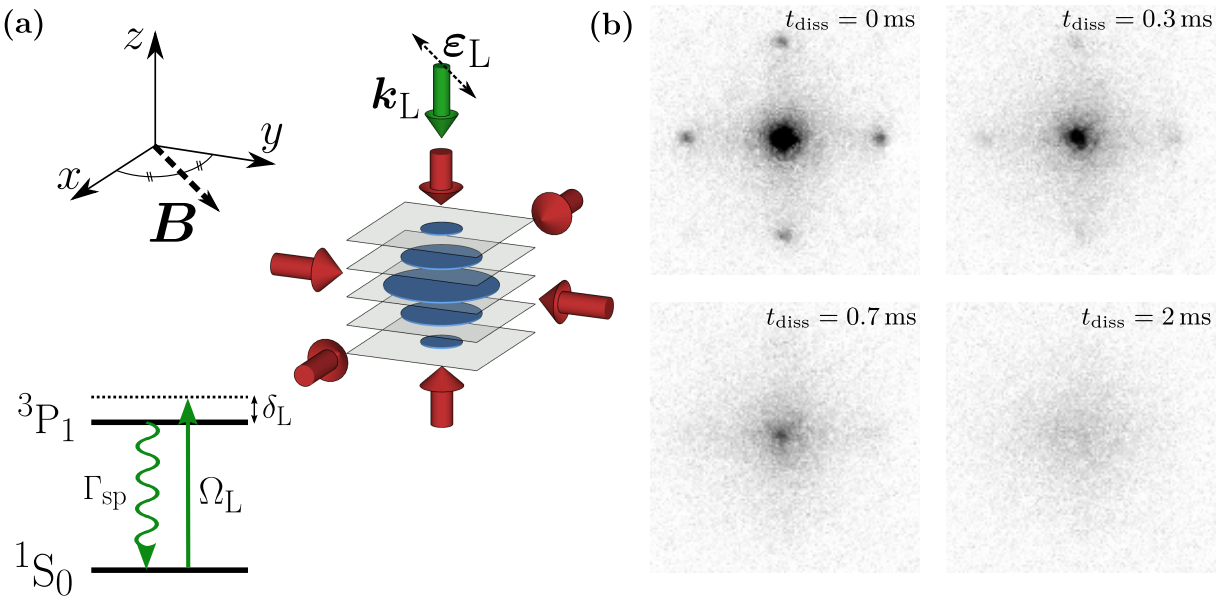

Figure 4.1: Dissipation in a superfluid. (a) Sketch of the experiment and of the level scheme of the intercombination transition. The red arrows denote optical lattice beams, the green arrow denotes the dissipation laser beam with wavevector $\boldsymbol{k}_L$ propagating vertically with a polarisation $\boldsymbol{\varepsilon}_L$ parallel to the applied magnetic field $\boldsymbol{B}$ along the $x+y$ direction. The dissipation laser drives the intercombination transition with Rabi frequency Ω_L, detuning δ_L and spontaneous emission rate Γ_{sp}. (b) Absorption images taken after 20 ms expansion for various dissipation times t_{diss}, the line of sight is vertical. In this experiment the parameters are $V_\perp = 8.8\,E_R$, $\Gamma_{sp} = 250\,s^{-1}$, $\delta_L = +15\Gamma_g$ and $\Omega_L = 2\pi \times 81\,kHz$.

In this chapter, I present an experimental study of the decoherence dynamics of a superfluid under dissipation, as sketched in Figure 4.1. The dissipation is caused by spontaneous emission events, which destroy the spatial coherence naturally present in the initial superfluid state. However, the dynamics at long times is changed in a rather surprising way: interactions *slow down* decoherence. The interplay between dissipation and inter-atomic interactions leads to an unconventional relaxation dynamics that I investigate both experimentally and theoretically.

First, I recall fundamental results about the effect of spontaneous emission on spatial coherences for a single particle. Secondly, I present the experimental observation of a drastic slowdown in the relaxation of a superfluid. Thirdly, I detail a model for the dissipation in optical lattices which I use to shed light on the slowdown behaviour. I finally present two complementary analysis of this relaxation dynamics.

4.1 Dissipation with spontaneous emission for a single atom

In this section I introduce the context to describe the dissipative dynamics of an atom continuously excited by a laser but decaying back to its ground state by spontaneous emission. I first consider the spontaneous decay of an atom in free space, and show how spatial coherences are destroyed down to a size set by the photon wavelength. Then I turn to the case of many successive photon scattering events, close to what happens

for an atom continuously excited by a resonant laser field. I show the importance of momentum diffusion and how it is related to the destruction of spatial coherences. The relaxation dynamics due to spontaneous emission is shown to be exponential in time. Furthermore, the momentum and position distributions undergo Brownian motion and display a standard diffusive behaviour, i.e. the variance of the distribution increases linearly with time. This section introduces the main elements required to understand the remainder of the chapter, but is not meant to cover the topic in a comprehensive way.

4.1.1 Spontaneous emission and momentum diffusion in free space

Quantum description of spontaneous emission

The description of spontaneous emission requires us to consider a Markovian environment surrounding the atom, i.e. the vacuum of photons. In other words, we consider a system {atom} coupled to an environment {the electro-magnetic field} taken in its vacuum state, which constitutes a memory-less *reservoir* or *bath*. The denomination Markovian or memory-less is equivalent to saying that the relaxation time of the environment is much shorter than the relaxation time of the system. This separation of time scales is a very good approximation for atomic systems and is called Born-Markov, or short memory time approximation. It allows to trace out the environment numerous and unobserved degrees of freedom, and to only look at what happens to the system of interest.

We first consider an atom in free space, the internal structure of which is described by two levels a and b: $|a\rangle$ is the ground state with zero energy and $|b\rangle$ is the excited state with radiative linewidth Γ and energy $\hbar\omega_0$. The atomic density matrix is written $\hat{\rho}$. In the remainder of this thesis, I call populations the diagonal elements of $\hat{\rho}$ and coherences the off-diagonal elements of $\hat{\rho}$. The dynamics of the system is generally described by a master equation written in the Lindblad form[2] (Haroche et al. 2006)

$$\frac{\partial\hat{\rho}}{\partial t}=\frac{1}{\mathrm{i}\hbar}\left[\hat{H},\hat{\rho}\right]+\Gamma\int_{\mathcal{S}^1}\mathrm{d}^2u\,N(\boldsymbol{u})\left\{\hat{C}(\boldsymbol{u})\hat{\rho}\hat{C}^\dagger(\boldsymbol{u})-\frac{1}{2}\hat{C}^\dagger(\boldsymbol{u})\hat{C}(\boldsymbol{u})\hat{\rho}-\frac{1}{2}\hat{\rho}\hat{C}^\dagger(\boldsymbol{u})\hat{C}(\boldsymbol{u})\right\}, \tag{4.1}$$

where $\hat{H}$ is the Hamiltonian describing the unitary evolution of the system and $\hat{C}$ quantum jump operators. In the case of spontaneous emission we choose $\hat{C}(\boldsymbol{u})=\mathrm{e}^{-\mathrm{i}k_0\boldsymbol{u}\cdot\hat{\boldsymbol{R}}}\,|a\rangle\langle b|$ (Dalibard et al. 1985; Marte et al. 1993) which describes the decay of the atom from b to a by spontaneous emission of a photon with wavenumber $k_0=\omega_0/c$ and direction given by the unit vector $\boldsymbol{u}$. $\hat{\boldsymbol{R}}$ is the position operator and $N(\boldsymbol{u})$ is a directional factor that weighs the spontaneous emission direction $\boldsymbol{u}$ over the unit sphere $\mathcal{S}^1$. We take this equation as a starting point for the discussion, it will be justified later in Chapter 5.

The atom is initially in the excited state with well-defined momentum $\boldsymbol{p}=\boldsymbol{0}$. The probability density to find the atom at a given position is uniform in space. The initial spatial coherences are infinitely long-range in the excited state and zero in the ground state: $\rho^b_{\boldsymbol{r}',\boldsymbol{r}''}(0)=\langle b,\boldsymbol{r}'|\,\hat{\rho}(0)\,|b,\boldsymbol{r}''\rangle\sim 1$ and $\rho^a_{\boldsymbol{r}',\boldsymbol{r}''}(0)=\langle a,\boldsymbol{r}'|\,\hat{\rho}(0)\,|a,\boldsymbol{r}''\rangle=0$. The master equation (4.1) allows one to derive the time evolution of the spatial coherence $\rho^a_{\boldsymbol{r}',\boldsymbol{r}''}(t)$. We have

$$\frac{\partial\rho^a_{\boldsymbol{r}',\boldsymbol{r}''}}{\partial t}=\Gamma\int\mathrm{d}^2u\,N(\boldsymbol{u})\mathrm{e}^{\mathrm{i}k_0\boldsymbol{u}\cdot(\boldsymbol{r}''-\boldsymbol{r}')}\rho^b_{\boldsymbol{r}',\boldsymbol{r}''}. \tag{4.2}$$

[2] See Appendix B.1 for a reminder of the derivation of this equation.

We consider an isotropic directional factor for simplicity $N(\boldsymbol{u}) = 1/(4\pi)$ so that

$$\int \mathrm{d}^2 u\, N(\boldsymbol{u}) \mathrm{e}^{\mathrm{i}k_0 \boldsymbol{u}\cdot(\boldsymbol{r}''-\boldsymbol{r}')} = \frac{\sin\left(k_0|\boldsymbol{r}''-\boldsymbol{r}'|\right)}{k_0|\boldsymbol{r}''-\boldsymbol{r}'|}, \tag{4.3}$$

and

$$\frac{\partial \rho^a_{\boldsymbol{r}',\boldsymbol{r}''}}{\partial t} = \Gamma \frac{\sin\left(k_0|\boldsymbol{r}''-\boldsymbol{r}'|\right)}{k_0|\boldsymbol{r}''-\boldsymbol{r}'|} \rho^b_{\boldsymbol{r}',\boldsymbol{r}''}. \tag{4.4}$$

After a time $t \gg \Gamma^{-1}$ the atom has decayed to the level a with high probability. The growth of spatial coherences in the ground state is limited to a spatial extension set by the cardinal sine function in (4.4), which is a peaked function around $|\boldsymbol{r}''-\boldsymbol{r}'| = 0$ with a spatial extension $\sim \lambda_0 = 2\pi/k_0$. This shows that a spontaneous emission event destroys infinitely-long range spatial coherences, shrinking them down to a length set by the wavelength of the emitted photon.

Photon scattering and random walk

The previous treatment of spontaneous emission applies to the average over many realisations of single spontaneous emission events. It can be extended to the situation where the atom experiences many successive photon recoils through absorption-spontaneous emission cycles. Experimentally, this is performed with a resonant laser field continuously exciting the atom from the ground to the excited state. Due to the inherent randomness of spontaneous emission in free space, the atom performs a random walk in momentum space with steps $\hbar(\boldsymbol{k}_\mathrm{L} - k_0\boldsymbol{u})$, with $\boldsymbol{k}_\mathrm{L}$ the laser wavevector and $\boldsymbol{u}$ a random direction prescribed by a directional factor $N(\boldsymbol{u})$. This momentum diffusion is characterised by a diffusion coefficient D that describes the rate of increase of the momentum variance Δp^2 (Cohen-Tannoudji 1989). In one dimension it reads

$$\Delta p^2 = 2Dt. \tag{4.5}$$

Interestingly, the momentum distribution $\mathcal{P}$ and the spatial coherences are intimately linked. We define a global spatial coherence function $\mathcal{F}$

$$\mathcal{F}(u) = \int_{-\infty}^{+\infty} \mathrm{d}x\, \langle x + u/2|\, \hat{\rho}\, |x - u/2\rangle\,, \tag{4.6}$$

which is the sum of the spatial coherences between all points separated by a distance u. $\mathcal{F}$ is the Fourier transform of the momentum distribution $\mathcal{P}$, and its width gives the *coherence length* $\ell_\mathrm{c} \sim \hbar/\Delta p$ of the system (Cohen-Tannoudji 1989). A broadening of the momentum distribution is therefore equivalent to a reduction of the coherence length. Hence the scattering of photons, which leads to momentum diffusion through spontaneous emission, destroys spatial coherences.

Moreover, the time evolution of spatial coherences is given by (Cohen-Tannoudji 1989)

$$\frac{\partial}{\partial t} \langle \boldsymbol{r}'|\, \hat{\rho}\, |\boldsymbol{r}''\rangle = -\frac{D}{3\hbar^2} |\boldsymbol{r}''-\boldsymbol{r}'|^2 \langle \boldsymbol{r}'|\, \hat{\rho}\, |\boldsymbol{r}''\rangle\,. \tag{4.7}$$

The relaxation dynamics of spatial coherences on a distance r is therefore exponential with a rate proportional to the diffusion coefficient D and the square of the distance r^2. The same behaviour applies to coherent superpositions of spatially separated wave-packets undergoing spontaneous emission (Cohen-Tannoudji 1989).

Continuous limit of many events

The randomness of spontaneous emission is key to understanding the principle of laser cooling. A resonant beam exerts a net force (the radiation pressure force) on the atom proportional to the rate of spontaneous emission times $\hbar k_0$. With two resonant counter-propagating beams, the net force vanishes but the velocity dependence of the detuning (Doppler effect) creates a friction force that can slow down the atom. This force is characterised by a friction coefficient γ describing the rate of change of the atom average momentum $\langle p \rangle$

$$\frac{\partial \langle p \rangle}{\partial t} = -\gamma \langle p \rangle. \tag{4.8}$$

Momentum diffusion corresponds to the fluctuations of the friction force around the average value $-\gamma\langle p \rangle$. The equilibrium between friction and diffusion prescribes a limit to the achievable temperatures in the system, $k_{\mathrm{B}} T_{\mathrm{eq}} = D/\gamma$. This relation was first discovered by Einstein in his study of the Brownian motion (Einstein 1905; Einstein 1917). For Doppler cooling, this limit evaluates to $k_{\mathrm{B}} T_{\mathrm{D}} = \hbar\Gamma/2$ (Cohen-Tannoudji et al. 1992; Metcalf et al. 1999).

In the limit of many spontaneous emission processes, the dynamics of the momentum distribution $\mathcal{P}$ follows a Fokker-Planck equation (Cohen-Tannoudji 1989), which describes Brownian motion. In one dimension it reads

$$\left(\frac{\partial}{\partial t} - \gamma \frac{\partial}{\partial p} p \right) \mathcal{P}(p,t) = D \frac{\partial^2}{\partial p^2} \mathcal{P}(p,t). \tag{4.9}$$

In this case the 'heavy' Brownian particle is the atom and the 'light' particles are the photons. This type of equation can be solved analytically (Cohen-Tannoudji 1989) and one can show that at long times, both momentum and position distribution variances broaden linearly with time

$$\Delta p^2 = 2Dt \text{ and } \Delta x^2 = 2\frac{D}{M^2\gamma^2} t. \tag{4.10}$$

In conclusion, dissipation induced by many spontaneous emission events has three important consequences:

1. it destroys spatial coherences with an exponential time dependence, the rate of which is proportional to the diffusion coefficient and to the square of the distance [see (4.7)],
2. it localises spatial coherences on a scale set by the wavelength of the emitted photon [see (4.4)], the relaxation time of which decreases with dissipation strength Γ,
3. it freezes the motion of the atom [see (4.10)], with a relaxation time increasing with dissipation strength Γ.

4.1.2 Resonant scattering and momentum diffusion in an optical lattice

Momentum diffusion for an atom trapped in an optical lattice is not much different from the free space case considered in Section 4.1.1. This point is further addressed in the next chapter (see Section 5.2.1) and I summarise here the main results:

1. The time evolution of the variance of the position distribution Δx^2 shows a crossover between a ballistic expansion at short times, characterised by a quadratic dependence with time, and a Brownian diffusion for time $t \gtrsim \Gamma_{\mathrm{sp}}^{-1}$, characterised by a linear dependence with time (Γ_{sp} is the rate of spontaneous emission events). The ballistic expansion stems from coherent tunnelling between nearest-neighbour sites while Brownian diffusion is caused by spontaneous emission, as described in Section 4.1.1, which dominates the long time evolution.
2. Spatial coherences are destroyed exponentially with time, as seen in the decay of the coherence length of the system.
3. The fraction of atoms at zero quasi-momentum decreases exponentially with time.
4. Finally, spontaneous emission can induce inter-band transitions.

The remainder of this chapter shows how inter-atomic interactions modify the previous statements (valid for a single atom) and lead to the observation of anomalous sub-diffusion. This is explored both experimentally and theoretically.

4.2 Dramatic change in the relaxation of a superfluid under dissipation

We now turn to the case of many interacting particles trapped in an optical lattice. Interactions are essential to understand the dynamics at play, and they can modify substantially what was stated for the single-particle case. In this section, I present an experimental study of the relaxation dynamics for a superfluid submitted to dissipation by spontaneous emission. The system of interest is a degenerate gas of ^{174}Yb adiabatically loaded in a 2D optical lattice, close to the ground state of a 2D Bose-Hubbard system, as already discussed in Section 2.3. Dissipation is induced using a near-resonant laser beam that triggers spontaneous emission. As mentioned in the previous section, spontaneous emission destroys the long-range coherence initially present in the many-body system. However, the dynamics at long times are observed to be very different from the exponential relaxation expected in the single-particle case. In this section I address the question of how the system evolves under dissipation. After depicting the experimental procedure used to look at the relaxation dynamics, I present the observation of a dramatic change in the relaxation from an exponential to an algebraic decay. In a preliminary analysis, the dependences of this decay on the lattice depth and the dissipation rate are shown.

4.2.1 Experimental procedure

The experiment starts with a BEC of about 7×10^4 ytterbium atoms with no discernible thermal fraction, adiabatically loaded into 2D optical lattices at the magic wavelength λ_{m} with variable depth $V_\perp$ (this procedure is described in Section 2.3). The dissipation laser beam is sent in the vertical direction $\boldsymbol{e}_z$, along with the vertical lattice. As before, we set the vertical lattice depth to $V_{0,z} \approx 27\, E_{\mathrm{R}}$. Horizontal lattice beams propagate along $\boldsymbol{e}_x$ and $\boldsymbol{e}_y$, and we set their depth equal to $V_\perp$, which can vary in the range 3.5–13 E_{R}. The corresponding relevant Bose-Hubbard parameters are indicated in Table 4.1.

After the preparation of 2D Bose-Hubbard systems, we turn on dissipation by illuminating the atoms with the near-resonant laser for a given duration t_{diss}. Atoms are then released from the optical lattices and expand for 20 ms before an absorption image

Horizontal lattice depth $V_\perp$ $[E_\mathrm{R}]$	3.5	13
On-site interaction strength U $[h \times \mathrm{Hz}]$	410	980
In-plane tunnelling energy $J_\perp$ $[h \times \mathrm{Hz}]$	190	20
Ratio $U/J_\perp$	2.1	50

Table 4.1: Bose-Hubbard parameters for the extremal values of the horizontal lattice depth $V_\perp$ explored in this section.

is taken. A sketch of the experimental system is depicted in Figure 4.1a, absorption images after various dissipation times are shown in Figure 4.1b. We clearly see the loss of coherence by the disappearance of the interference peaks in time-of-flight.

Dissipation laser

Dissipation is induced by a laser beam with a frequency close to the inter-combination transition at $\lambda_\mathrm{g} \approx 556\,\mathrm{nm}$. The frequency detuning is fixed to $\delta_\mathrm{L} = \omega_\mathrm{L} - \omega_\mathrm{g} = +15\Gamma_\mathrm{g}$, where ω_L is the laser angular frequency. The laser polarisation is linear and parallel to the applied magnetic field $[\boldsymbol{\varepsilon}_\mathrm{L} = (\boldsymbol{e}_x + \boldsymbol{e}_y)/\sqrt{2}]$ and with it being so we excite the π-transition from $|J = 0, m = 0\rangle_{\boldsymbol{\varepsilon}_\mathrm{L}}$ to $|J = 1, m = 0\rangle_{\boldsymbol{\varepsilon}_\mathrm{L}}$ (see Figure 4.1a). The beam propagates vertically, with a waist $w_\mathrm{L} \approx 1\,\mathrm{mm}$ and a maximum power around 1 mW. We call Ω_L the resonant Rabi frequency of the atom-laser interaction. For a laser power P and intensity $I = 2P/(\pi w_\mathrm{L}^2)$ we have

$$\Omega_\mathrm{L} = \Gamma_\mathrm{g}\sqrt{\frac{I}{2I_\mathrm{sat}}} \approx 2\pi \times 2.77\,\mathrm{MHz} \times \sqrt{\frac{P}{1\,\mathrm{mW}}}. \tag{4.11}$$

Here $I_\mathrm{sat} = \hbar\Gamma_\mathrm{g}\omega_\mathrm{g}^3/(12\pi c^2) = 0.14\,\mathrm{mW\,cm^{-2}}$ is the saturation intensity of the inter-combination transition. We calibrated the Rabi frequency in the experiment using Rabi oscillations on a BEC. The rate of spontaneous emission Γ_sp can be estimated from the steady-state solution of the optical Bloch equations,

$$\Gamma_\mathrm{sp} = \frac{\Gamma_\mathrm{g}}{2}\frac{s}{1+s} \text{ with } s = \frac{\Omega_\mathrm{L}^2/2}{\delta_\mathrm{L}^2 + \Gamma_\mathrm{g}^2/4}. \tag{4.12}$$

The saturation parameter s is 0.5 for a power $P = 1\,\mathrm{mW}$. Experimentally, the power P is controlled by the radio-frequency driving amplitude of an AOM in the laser beam path. In most experiments described in this chapter, the saturation parameter is much smaller than one, and the spontaneous emission rate is proportional to the laser power

$$\Gamma_\mathrm{sp} \underset{s\ll 1}{\approx} 2\pi \times 46.2\,\mathrm{Hz} \times \frac{P}{1\,\mu\mathrm{W}}. \tag{4.13}$$

With our experimental parameters we are able to scan Γ_sp over four orders of magnitude from $10\,\mathrm{s^{-1}}$ to $10^5\,\mathrm{s^{-1}}$ ($\hbar\Gamma_\mathrm{sp}/U$ ranges from 10^{-2} to 10^2).

4.2.2 Crossover from exponential to algebraic decay

From the absorption images of the cloud taken after time-of-flight expansion (see Figure 4.1b), we can extract various quantities. The total atom number N_at is obtained from the

full $N_{\mathrm{pix}} \times N_{\mathrm{pix}} = 400 \times 400$ pixels squared region centred on zero momentum. This region of interest spans 4 Brillouin zones in reciprocal space[3]. A simple observable that captures the coherence properties of the atomic sample is the fraction of atoms at zero momentum $\mathcal{P}_{k=0}$. We compute it by counting the total atom number N_{peak} in a small central square region of 25×25 pixels, and calculate $\mathcal{P}_{k=0} = N_{\mathrm{peak}}/N_{\mathrm{at}}$.

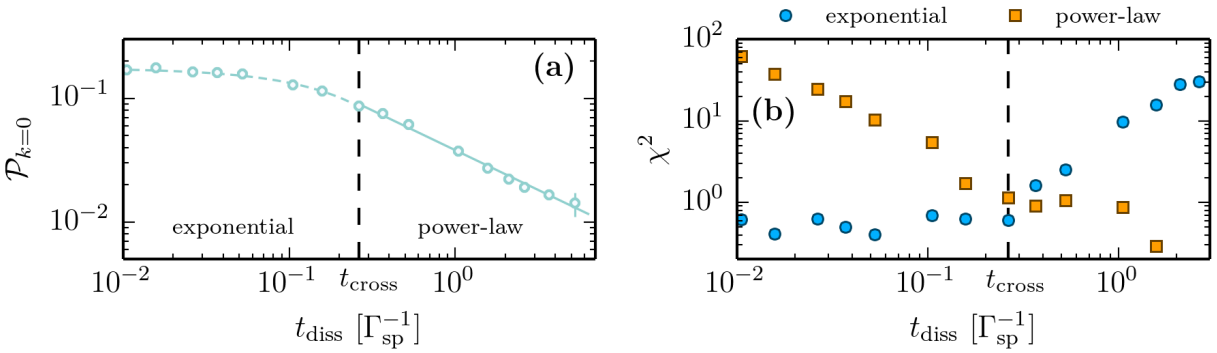

Figure 4.2: (a) Time evolution of the fraction of atoms at zero momentum $\mathcal{P}_{k=0}$, the lines are fits using (4.14) with parameters $G \approx 0.18$, $\gamma \approx 2.7$, $A \approx 0.038$ and $\alpha \approx 0.6$.(b) Determination of the crossover time t_{cross}. χ^2 values for the exponential (circles) and power-law (squares) fits. The crossover time, shown with the vertical dashed lines, is chosen as the minimum of the total χ^2 value. The experimental parameters for this experiment are $V_\perp = 3.5\, E_{\mathrm{R}}$ and $\Gamma_{\mathrm{sp}} = 520\,\mathrm{s}^{-1}$.

A typical experimental result is given in Figure 4.2a. The time evolution of the population at zero-momentum shows a drastic change, initially as a fast initial decay up to times $\sim 0.15\,\Gamma_{\mathrm{sp}}^{-1}$, and as a slower decay afterwards. The logarithmic scale on both axes of Figure 4.2a indicates that the slow decay follows a power-law.

Fitting model

In order to describe quantitatively our observations, we call t_{cross} the crossover time between the two regimes: fast exponential decay for early times and algebraic decay for longer times. For each data set, we perform a fit using an exponential function for $t_{\mathrm{diss}} \leq t_{\mathrm{cross}}$ and a power-law for $t_{\mathrm{diss}} > t_{\mathrm{cross}}$,

$$\mathcal{P}_{k=0}(t_{\mathrm{diss}}) = \begin{cases} G\mathrm{e}^{-\gamma\Gamma_{\mathrm{sp}} t_{\mathrm{diss}}} & \text{for } t_{\mathrm{diss}} \leq t_{\mathrm{cross}}, \\ A(\Gamma_{\mathrm{sp}} t_{\mathrm{diss}})^{-\alpha} & \text{for } t_{\mathrm{diss}} > t_{\mathrm{cross}}. \end{cases} \tag{4.14}$$

From this fit we extract a global χ^2 as the sum of the χ^2 values in the exponential and in the power-law windows normalised to the number of degrees of freedom[4]. We choose t_{cross} to minimise the global χ^2 and find typically $t_{\mathrm{cross}} \approx 0.15\,\Gamma_{\mathrm{sp}}^{-1}$. See Figure 4.2b for an illustrative determination of the crossover time.

[3] One pixel represents a square of 1.2 µm size. The first Brillouin zone has a width of $2k_{\mathrm{m}} = 4\pi/\lambda_{\mathrm{m}}$, corresponding to 120 µm for a time-of-flight of 20 ms.

[4] The number of degrees of freedom is meant in the statistical sense, it is equal to the number of data points minus the number of fitting parameters.

Choice of observable

The choice of $\mathcal{P}_{k=0}$ to characterise the coherence of the atomic sample can be motivated from a simple model of the density distribution after a time-of-flight expansion. In the single-band approximation, and assuming that interactions do not perturb the expansion (Gerbier et al. 2008), the density distribution after time-of-flight can be written as the product of two terms $n_{\mathrm{tof}}(\boldsymbol{k}) \simeq \mathcal{S}_0(\boldsymbol{k})\mathcal{W}_0(\boldsymbol{k})$. $\mathcal{W}_0$ is a smooth envelope function given by the Fourier transform of the on-site Wannier function in the fundamental band. $\mathcal{S}_0$ is a structure factor, given by the Fourier transform of the first-order correlation function $\mathcal{C}(i,j) = \langle \hat{a}_i^\dagger \hat{a}_j \rangle$ (omitting the band index $n = 0$ for clarity). We therefore have

$$\mathcal{P}_{k=0} = \frac{\mathcal{W}_0(0)}{N_{\mathrm{at}}} \sum_{i,j} \langle \hat{a}_i^\dagger \hat{a}_j \rangle. \tag{4.15}$$

The time evolution of $\mathcal{P}_{k=0}$ therefore characterises the evolution of the spatial coherences $\langle \hat{a}_i^\dagger \hat{a}_j \rangle$ in the sample. Other observables such as the visibility of the interference pattern or the cloud radius could also capture the evolution of coherence of the atomic sample. We have considered them but they both exhibit the same qualitative behaviour as $\mathcal{P}_{k=0}$, hence I do not show them in the manuscript.

4.2.3 Dependence on horizontal lattice depth

In a first series of experiment, we varied the horizontal lattice depth $V_\perp$ from $3.5\,E_{\mathrm{R}}$ to $13\,E_{\mathrm{R}}$ for a fixed spontaneous emission rate $\Gamma_{\mathrm{sp}} = 520\,\mathrm{s}^{-1}$. The time evolution of $\mathcal{P}_{k=0}$ is plotted in Figure 4.3. The presence of two regimes in the decay is very clear. Fitting by an exponential at the beginning can be discussed, because we mostly see the initial linear behaviour, but the crossover to an algebraic regime with power-law decay is manifest. For all lattice depths, the product $\Gamma_{\mathrm{sp}} t_{\mathrm{cross}}$ is roughly 0.1 without any obvious dependence on the lattice depth. The decrease in the initial value of $\mathcal{P}_{k=0}$ with increasing $V_\perp$ is purely caused by the broadening of the momentum distribution when approaching the Mott-insulating regime (the transition occurs around $V_\perp \approx 11\,E_{\mathrm{R}}$). The fitting parameters are shown in Figure 4.4.

1. In Figure 4.4a, we observe that the algebraic decay exponent α decreases with lattice depth. The amplitude of the power-law behaves similarly, as shown in Figure 4.4b. The algebraic depletion of the $k = 0$ component of the cloud seems therefore controlled mainly by U and/or $J_\perp$.
2. In Figure 4.4c, the normalised exponential decay rate γ is higher than one. Besides, the normalised decay rate seems to converge to unity as lattice depth increases. The amplitude is also reduced as lattice depth is increased.

We conclude that increasing the lattice depth slows down the relaxation dynamics, both in the exponential and the algebraic regimes. We also performed the same measurements with $\Gamma_{\mathrm{sp}} = 73\,\mathrm{s}^{-1}$ and $\Gamma_{\mathrm{sp}} = 2200\,\mathrm{s}^{-1}$, but results are essentially the same and are not shown here for clarity.

4.2.4 Dependence on dissipation rate

In a second series of experiment, we varied the spontaneous emission rate by changing the dissipation laser power, fixing the horizontal lattice depth to $V_\perp = 3.5 E_{\mathrm{R}}$ ($U/J_\perp \approx 2$).

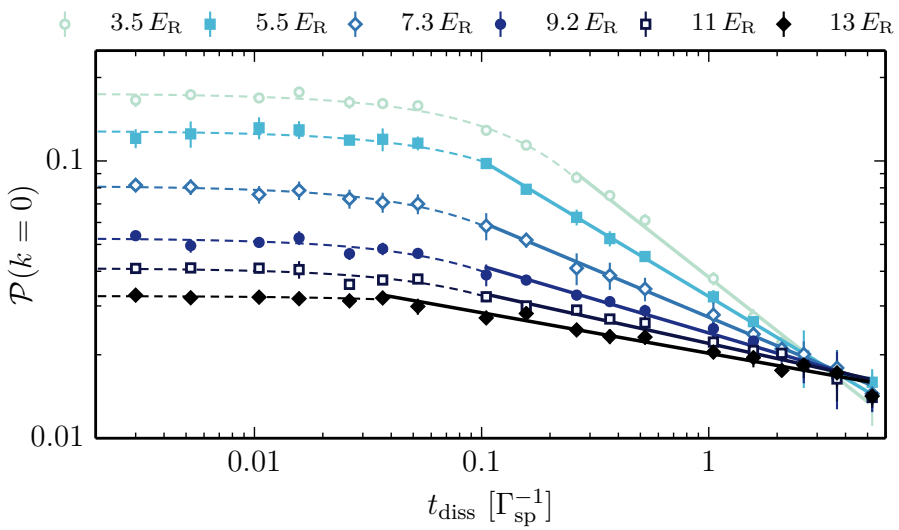

Figure 4.3: Time evolution of the fraction of atoms at zero momentum $\mathcal{P}_{k=0}$ under dissipation with varying $V_\perp$ and fixed $\Gamma_{sp} = 520\,s^{-1}$. Dashed lines are exponential fits, solid lines are algebraic fits, according to (4.14).

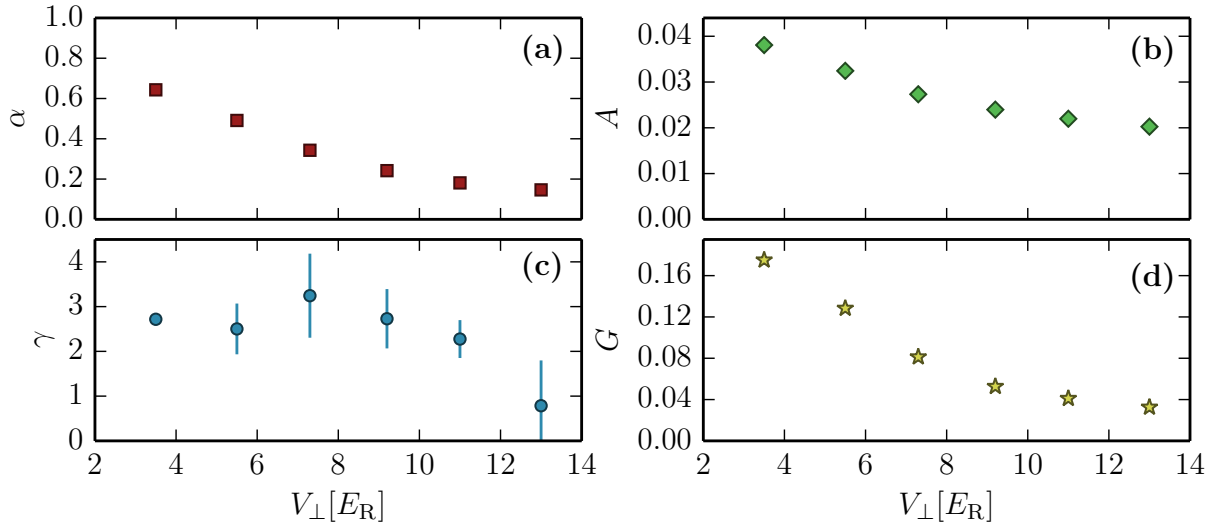

Figure 4.4: Fitted parameters on the dissipative time evolution of $\mathcal{P}_{k=0}$ for varying $V_\perp$ and fixed $\Gamma_{sp} = 520\,s^{-1}$. α and A are respectively the exponent and the amplitude characterising the evolution of $\mathcal{P}_{k=0}$ in the algebraic regime. γ and G are respectively the normalised decay rate and the amplitude for $\mathcal{P}_{k=0}$ in the exponential regime.

The time evolution of $\mathcal{P}_{k=0}$ under dissipation is plotted in Figure 4.5. The presence of two regimes in the decay is again very clear. For all spontaneous emission rates, the product $\Gamma_{sp}t_{cross}$ is roughly 0.2 without any obvious dependence on the spontaneous emission rate. The rightmost data points show the behaviour of $\mathcal{P}_{k=0}$ without dissipation, a decay is observed after 100 ms, probably due to heating from laser intensity fluctuations of the lattice beams or three-body losses. This demonstrates that decay at shorter times can be attributed to the dissipation laser. The fit parameters are shown in Figure 4.6.

1. In Figure 4.6a, the algebraic decay exponent α is almost constant around 0.7 and

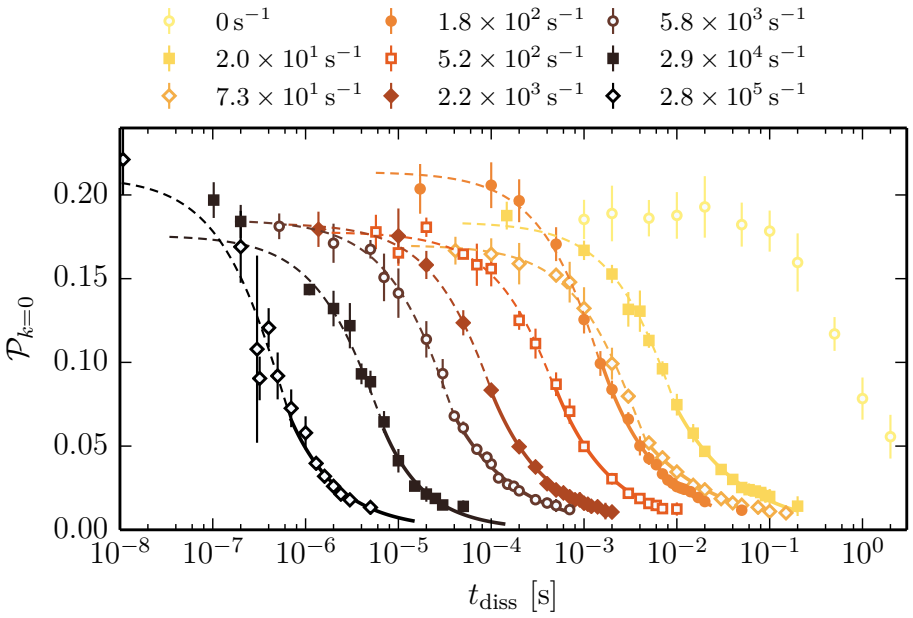

Figure 4.5: Time evolution of the fraction of atoms at zero momentum $\mathcal{P}_{k=0}$ with varying Γ_{sp} and fixed $V_\perp = 3.5\,E_{\mathrm{R}}$. Dashed lines are exponential fits, solid lines are algebraic fits, according to (4.14). The rightmost points correspond to the bare lattice heating with no resonant light.

slightly increases towards 1 as dissipation gets dominant over U and $J_\perp$. This confirms our previous conjecture that the algebraic depletion of the $k = 0$ component of the cloud is controlled mostly by the Bose-Hubbard parameters U and/or $J_\perp$. A similar behaviour is observed for the amplitude, as seen in Figure 4.6b.

2. In Figure 4.6c, we see that the normalised exponential decay rate γ is again higher than one and we observe a peculiar behaviour with respect to the spontaneous emission rate, with a minimum corresponding to $\hbar\Gamma_{\mathrm{sp}}/U \approx 0.1$. The amplitude of the initial exponential decay is however almost constant (Figure 4.6d).

4.2.5 Atom losses

The dissipation induced by the near-resonant laser not only destroys spatial coherences, it also induces atom losses in the system. Figure 4.7 shows a typical time evolution of the total atom number during dissipation. In order to characterise these losses, we fit the time evolution of the total atom number N_{at} using an *ad hoc* function,

$$N_{\mathrm{at}}(t_{\mathrm{diss}}) = \frac{N_0}{1 + (\Gamma_{\mathrm{sp}} t_{\mathrm{diss}}/B)^\beta}. \tag{4.16}$$

This function provides an asymptotic exponent β for the decay. The coefficient B is a normalised lifetime. The fit function captures well the dynamics, as shown in Figure 4.7.

The fit parameters for the experiments described in the last two sections, (Sections 4.2.3 and 4.2.4) are shown in Figure 4.8. The asymptotic exponent β decreases slightly with lattice depth (Figure 4.8a), however no clear correlation is observed with the spontaneous emission rate (Figure 4.8c). The lifetime B decreases with the lattice depth (Figure

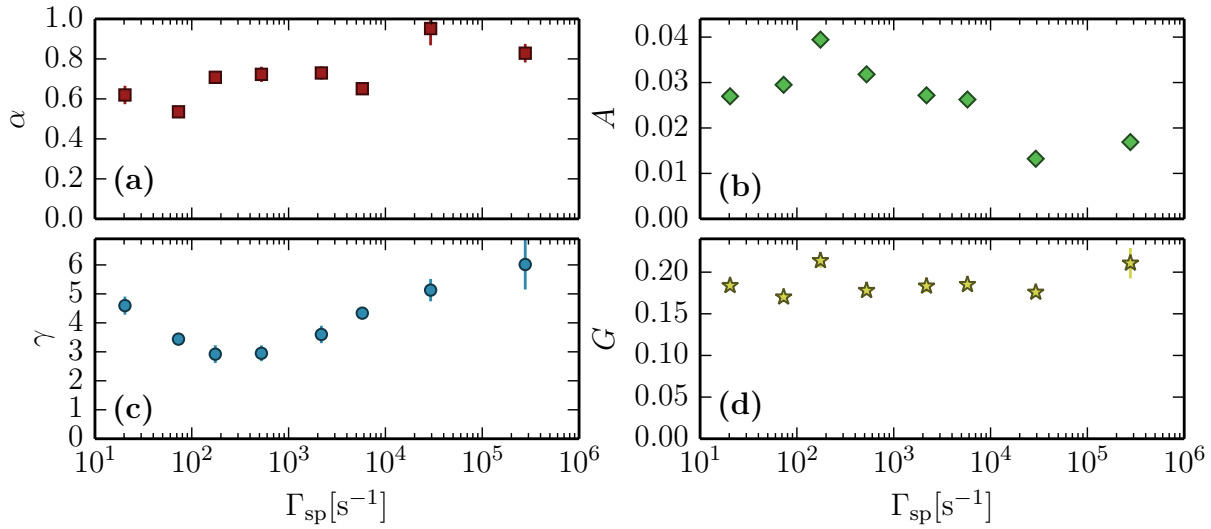

Figure 4.6: Fitted parameters on the time evolution of $\mathcal{P}_{k=0}$ for varying Γ_{sp} and fixed $V_\perp = 3.5\,E_{\mathrm{R}}$. α and A are respectively the exponent and the amplitude characterising the evolution of $\mathcal{P}_{k=0}$ in the algebraic regime. γ and G are respectively the normalised decay rate and the amplitude for $\mathcal{P}_{k=0}$ in the exponential regime.

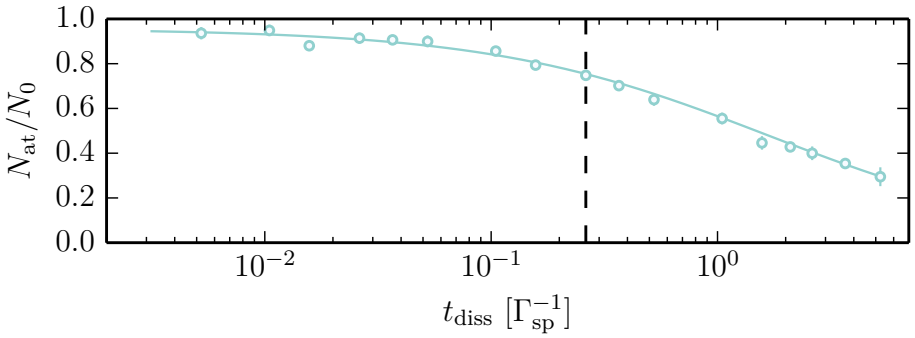

Figure 4.7: Time evolution of the normalised total atom number N_{at}/N_0. The solid line is an empirical fit using (4.16). The dashed line shows the crossover time between the exponential and the algebraic regimes. Parameters for this figure are identical to those in Figure 4.2.

4.8b) and with the spontaneous emission rate (Figure 4.8d), and is close to unity. This indicates that the losses are driven by the near-resonant laser and the spatial confinement of the atoms.

The observation that the lifetime of the atomic sample is close to $\Gamma_{\mathrm{sp}}^{-1}$ when dissipation or atomic confinement are strong enough confirms that light-induced interactions might be at the heart of the observed loss mechanism (DePue et al. 1999; Vuletić et al. 1999). For completeness, we consider a number of other possible loss mechanisms in the following.

- Photoassociation resonances have been reported for ^{174}Yb in Tojo et al. (2006) and Kim et al. (2016). They are all located at negative detunings from the inter-combination transition. The closest one is the prevailing resonance with respect to our experiment and is located at $-4.2\,$MHz from the inter-combination transition. With our chosen laser detuning $\delta_{\mathrm{L}} = +15\Gamma_{\mathrm{g}}$, the two-body loss rate K_2 induced by

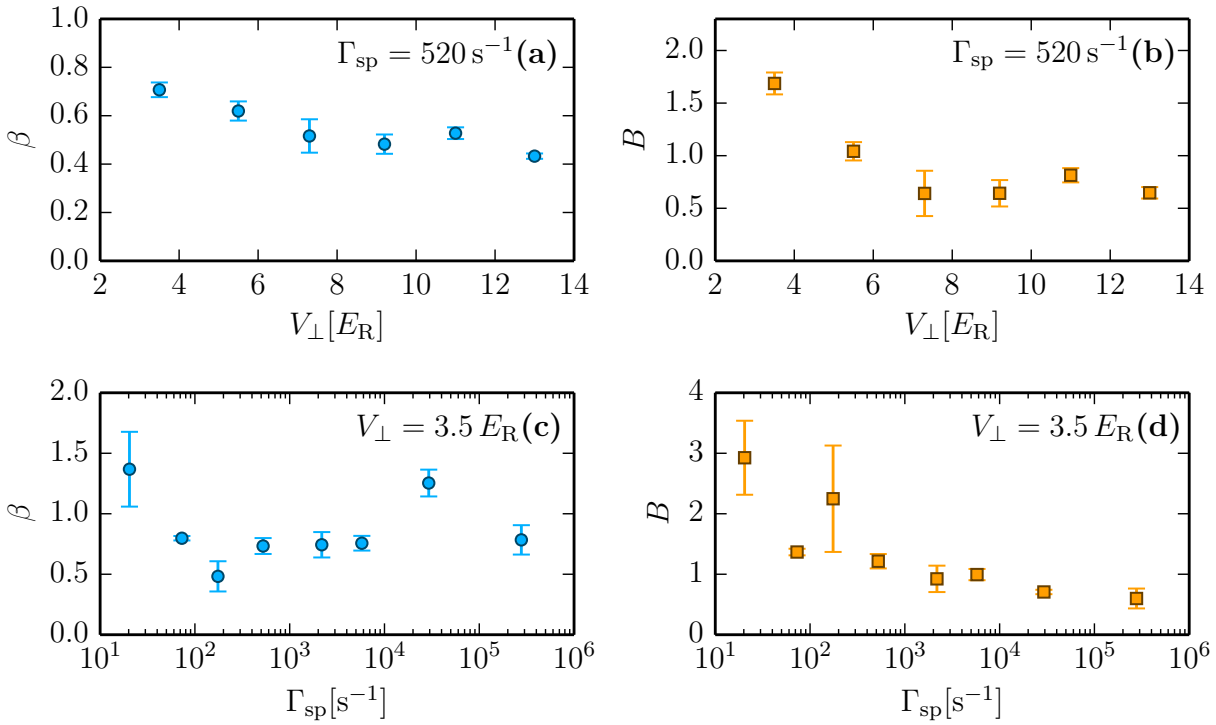

Figure 4.8: Fitted parameters on the time evolution of the total atom number for both set of experiments described previously. (a-b) Varying horizontal lattice depth as in Section 4.2.3. (c-d) Varying spontaneous emission rate as in Section 4.2.4. Losses seem to be enhanced by the lattice depth and the spontaneous emission rate.

this photoassociation resonance is (Kim et al. 2016)

$$K_2 \approx 0.18\,\mathrm{s}^{-1} \times \frac{P}{1\,\mu\mathrm{W}} \times \frac{n_0}{10^{14}\,\mathrm{cm}^{-3}}, \tag{4.17}$$

which is very small compared to Γ_{sp} for the densities $n_0 \approx 10^{14}\,\mathrm{cm}^{-3}$ explored in the experiment ($K_2 n_0/\Gamma_{sp} \approx 10^{-3}$). We thus neglect the possible role of photoassociation to a bound state in our experiment. The light-induced collisions are possibly due to purely repulsive potentials that do not support any bound state (Chin et al. 2010).

- The lifetime of the excited $^3P_1$ state is smaller than 1 µs. Thanks to the time-of-flight expansion of 20 ms, all atoms have decayed back to the ground state when the image is taken and as such the reduction in atom number cannot be attributed to a reduction in detection efficiency.
- The observed reduction in atom number is therefore purely due to processes that expel atoms from the trap. Due to the chosen positive laser detuning, the dissipation laser beam adds a repulsive force on the atoms, but the laser beam waist is much bigger than the atomic sample and the induced acceleration is then negligible.
- Another process for losses is three-body recombination. As shown in Section 3.1, for horizontal lattice depth around 25 E_R, deep in the Mott insulator regime, filling fractions in the lattice range from 1 to 3. We thus expect an average filling fraction between 1 and 2 in our system. The typical decay time for triplets at horizontal lattice depths around 10 E_R is about 500 ms, which is much bigger than the typical loss time Γ_{sp}^{-1}. As described in the next section, dissipation fosters the creation of

higher occupation numbers in the lattice, which are prone to three-body recombinations with an enhanced rate. The lifetime of a site with eight atoms reduces to 10 ms, and is still bigger than the observed loss time.

4.2.6 Overview

In this section we have observed the unconventional relaxation dynamics of a superfluid submitted to spontaneous emission. We have characterised the coherence properties of the atomic sample using a simple observable $\mathcal{P}_{k=0}$ in various experimental conditions. The relaxation dynamics always exhibit a drastic slowing down from an exponential decay to an algebraic decay with a power-law exponent smaller than one. This suggests a sub-diffusive behaviour that we attribute to the presence of interactions between atoms. These interactions are mostly controlled by the optical lattice parameters themselves, as observed in the dependence of the power-law exponent with respect to the lattice depth.

Incidentally, the spontaneous emission rate seems to affect mostly the initial decay, which might be an indication of super-radiant effects. In these conditions, we can also expect dipole-dipole interactions to play a significant role. Both effects are addressed in the next chapter. Interactions might also be responsible for the observed strong atom losses through light-assisted collisions for example (DePue et al. 1999).

4.3 Dissipative Bose-Hubbard model

In the last section, we observed that the dynamics of a superfluid under dissipation exhibit a relaxation dynamics with a power-law exponent smaller than one. We attributed this unconventional algebraic relaxation to interactions between atoms. Incidentally, the interplay between dissipation and interactions in the system seems non-trivial. In this section, I present a first theoretical approach to grasp the forces at play, and give key elements for the understanding of the previous observations. Inspired by a theoretical work on the decoherence of a bosonic many-body quantum system (Poletti et al. 2012; Poletti et al. 2013), this approach provides a simple description of the dissipation that permits to explore the long-term dynamics of the system in terms of Fock space diffusion. Some strong approximations, which do not necessarily hold in our system, are necessary to make progress and I discuss them at the end of the section.

4.3.1 Dissipation in optical lattices

In order to describe an absorption-spontaneous emission process for an atom in an optical lattice, we introduce the following quantum jump operators $\hat{C}(\boldsymbol{u})$ (similar to the one introduced in Section 4.1)

$$\hat{C}(\boldsymbol{u}) = \sum_{\substack{\text{sites } i,j \\ \text{bands } l,m}} \langle w_i^l | \, \mathrm{e}^{-\mathrm{i}(k_0 \boldsymbol{u} - \boldsymbol{k}_\mathrm{L})\cdot\hat{\boldsymbol{R}}} \, | w_j^m \rangle \, \hat{a}_i^{l\dagger} \hat{a}_j^m . \tag{4.18}$$

This operator describes the process of absorption of a laser photon with wavevector $\boldsymbol{k}_\mathrm{L}$ and subsequent spontaneous emission of a photon in the direction $\boldsymbol{u}$ with wavevector k_0. This very general description can be simplified by keeping only local terms ($i = j$). This is motivated by the fact that $k_0 d = \pi \lambda_\mathrm{m}/\lambda_0 \approx 2.3$ is bigger than one ($d = \lambda_\mathrm{m}/2$ is the

lattice period). In the single-band approximation, we also neglect the contributions of higher excited bands in the lattice ($l = m = 0$). This leads to a local dissipative operator

$$\hat{C}(\boldsymbol{u}) \simeq \langle w_i^0 |\, \mathrm{e}^{-\mathrm{i}(k_0 \boldsymbol{u} - \boldsymbol{k}_\mathrm{L})\cdot \hat{\boldsymbol{R}}}\, |w_i^0\rangle\, \hat{a}_i^{0\dagger} \hat{a}_i^0 \approx \hat{n}_i, \tag{4.19}$$

where $\hat{n}_i$ is the density operator on the site i. This holds in the limit of deep lattices.

This model which describes atoms undergoing local dissipation in an optical lattice has been studied in details by Poletti et al. (2012). The main assumptions are the tight-binding regime (only nearest-neighbour tunnelling), the single-band approximation and the strictly on-site dissipation. Such a description is well suited for far-off-resonant light scattering (from the optical lattice beams for example) but do not take into account either resonant or collective effects (see Section 4.3.5 for a discussion).

4.3.2 Lindblad master equation

As described in Section 2.3, I consider a 2D Bose-Hubbard system described by the following single-band Hamiltonian,

$$\hat{H} = -J_\perp \sum_{\langle i,j \rangle} (\hat{a}_i^\dagger \hat{a}_j + \hat{a}_j^\dagger \hat{a}_i) + \frac{U}{2} \sum_i \hat{n}_i \left(\hat{n}_i - 1\right), \tag{4.20}$$

where we discarded the external confinement for simplicity.

The dissipative evolution of an atomic sample in such a 2D Bose-Hubbard system can be captured in the dynamics of its density matrix $\hat{\rho}$ (Cohen-Tannoudji et al. 1992; Pichler et al. 2010),

$$\frac{\partial \hat{\rho}}{\partial t} = \frac{1}{\mathrm{i}\hbar} \left[\hat{H}, \hat{\rho}\right] + \kappa \hat{D}[\hat{\rho}], \tag{4.21}$$

$$\hat{D}[\hat{\rho}] = \sum_i \hat{n}_i \hat{\rho} \hat{n}_i - \frac{1}{2} \hat{n}_i^2 \hat{\rho} - \frac{1}{2} \hat{\rho} \hat{n}_i^2, \tag{4.22}$$

which describes both the unitary evolution of the system with $\hat{H}$ and the dissipation process with $\hat{D}$. The dissipative coupling to a Markovian environment is characterised by a site-resolved density measurement strength κ and the operator $\hat{D}$, defined using the on-site density operators $\hat{C}_i \approx \hat{n}_i$. The measurement strength κ can be identified to the spontaneous emission rate Γ_sp given in the sections above.

We consider a lattice of N_s sites with N atoms (filling fraction $\bar{n} = N/N_\mathrm{s}$), and give a Fock space representation of the density matrix

$$\hat{\rho} = \sum_{\boldsymbol{n},\boldsymbol{m}} \rho_{\boldsymbol{m}}^{\boldsymbol{n}} |\boldsymbol{n}\rangle\langle\boldsymbol{m}|, \tag{4.23}$$

where $|\boldsymbol{n}\rangle$ is a state of occupations numbers n_i on each site i, i.e. $\boldsymbol{n} = (n_1, ..., n_{N_\mathrm{s}})$. The asymptotic steady-state $\hat{\rho}_\mathrm{ss}$ of (4.21) is a fully mixed state where all Fock state configurations are equally likely (Poletti et al. 2012),

$$\hat{\rho}_\mathrm{ss} = \sum_{\boldsymbol{n}} \frac{1}{\mathcal{M}} |\boldsymbol{n}\rangle\langle\boldsymbol{n}|, \tag{4.24}$$

where $\mathcal{M} = (N + N_\mathrm{s} - 1)!/[N!(N_\mathrm{s} - 1)!]$ is the number of configurations in which N atoms can be distributed between N_s sites.

The dynamics described by the master equation (4.21) results from the competition between three different energy scales:

1. dissipation with strength κ that causes damping and spatial coherence destruction,
2. coherent tunnelling with time $\hbar/J_\perp$ that restores coherence over the lattice,
3. inter-atomic interactions that obstructs the dynamics due to the energy cost U.

The master equation (4.21) is valid only if spatial coherences are short-ranged, which is the case for an initial Fock state, but not for a superfluid state. However, spontaneous emission destroys long-range spatial coherences on a time $\sim \kappa^{-1}$. Poletti et al. (2013) identified two time scales that separate three different regimes for the dissipative dynamics:

- An initial stage where long-range coherences decay exponentially because of dissipation, on a time scale κ^{-1}. This regime is not described by (4.21).
- A second, intermediate stage where relaxation slows down due to the interplay between dissipation, tunnelling and interactions. In this regime, only local and nearest-neighbour coherences remain, and the master equation (4.21) becomes valid. Dissipation destroys spatial coherence and localises atoms in Fock space (due to the form of the dissipator $\hat{C} \approx \hat{n}_i$). This is balanced by coherent tunnelling that restores short-ranged spatial coherence, and on-site interactions that favours the creation of small filling fraction Fock states.
- After a time t^*, the dynamics gets finally dominated by the population of rare configurations in Fock space which correspond to the occupation of sites with a very large number of atoms. In this thermalisation stage, the density matrix reaches its uniform steady-state (4.24). The time scale t^* associated with this final stage can be much bigger than κ^{-1} if interactions or tunnelling time are big enough.

A crucial finding in Poletti et al. (2012) is to give an analytical expression for t^* in the limit where U dominates over $J_\perp$ and κ:

$$t^* = \left(\frac{U}{J_\perp}\right)^2 \frac{\bar{n}^2}{2\kappa z}, \tag{4.25}$$

with z the number of nearest neighbours. As mentioned before, this time scale is greatly enhanced by the strength of interactions and separates well from the time scale κ^{-1}. For example, in 2D with $z = 4$, $\bar{n} = 1$ and $U = 10\,J_\perp$ ($V_\perp \approx 7.5\,E_\mathrm{R}$), $t^* \approx 12\,\kappa^{-1}$. In practice, this thermalisation time scale might not be accessible.

Following the notation used in Poletti et al. (2013), I introduce the vector $\boldsymbol{e}_i^j$ which is 0 everywhere except at positions i and j where it takes respectively the values $+1$ and -1, i.e. $\boldsymbol{n} + \boldsymbol{e}_i^{i+1} = (n_1, ..., n_i + 1, n_{i+1} - 1, ..., n_{N_\mathrm{s}})$. Coherent tunnelling connects Fock configurations separated by $\boldsymbol{e}_i^j$, and enables coherences of the type $\rho_{\boldsymbol{n}}^{\boldsymbol{n}+\boldsymbol{e}_i^j}$, with i, j referring to nearest-neighbours.

Dissipation, represented by $\hat{D}$, only affects the coherences and not the populations. In the limit identified in Poletti et al. (2013), $U, \kappa \gg J_\perp$, the coherences $\rho_{\boldsymbol{n}}^{\boldsymbol{n}+\boldsymbol{e}_i^j}$ are *slave* variables with respect to the populations $\rho_{\boldsymbol{n}}^{\boldsymbol{n}}$: the faster evolution of $\rho_{\boldsymbol{n}}^{\boldsymbol{n}+\boldsymbol{e}_i^j}$ averages out to a time-dependent steady-state that follows the slower dynamics of the populations

$$\rho_{\boldsymbol{n}}^{\boldsymbol{n}+\boldsymbol{e}_i^j}\big|_\mathrm{ss} \approx \frac{J_\perp \sqrt{n_j(n_i+1)}}{U(n_i - n_j + 1) - \mathrm{i}\hbar\kappa} \left(\rho_{\boldsymbol{n}}^{\boldsymbol{n}} - \rho_{\boldsymbol{n}+\boldsymbol{e}_i^j}^{\boldsymbol{n}+\boldsymbol{e}_i^j}\right). \tag{4.26}$$

This allows to write a secular master equation for the populations

$$\frac{\mathrm{d}}{\mathrm{d}\tau}\rho_{\boldsymbol{n}}^{\boldsymbol{n}} = -\frac{\bar{n}^2}{z} \sum_{(i,j)} \frac{n_j(n_i+1)}{(n_i - n_j + 1)^2 + \epsilon^2} \left(\rho_{\boldsymbol{n}}^{\boldsymbol{n}} - \rho_{\boldsymbol{n}+\boldsymbol{e}_i^j}^{\boldsymbol{n}+\boldsymbol{e}_i^j}\right), \tag{4.27}$$

where $\tau = t/t^*$ and $\epsilon = \hbar\kappa/U$. The notation (i, j) refers to all nearest-neighbour pairs, counted both ways. Such a summation is equivalent to a double sum over all lattice sites i firstly, and their nearest-neighbours j secondly. A detailed derivation of (4.27) is provided in Appendix B.2.

Master equation with a factorisation ansatz

In order to obtain predictions that can be compared with our experimental results, we need to solve the master equation (4.27). A numerical solution of (4.27) seems out of reach for realistic lattice sizes. Following again Poletti et al. (2013) we choose to perform the approximation that the diagonal part of the density matrix factorises over all sites,

$$\hat{\rho} \simeq \prod_i \left(\sum_{n_i=0}^{+\infty} \rho(n_i) |n_i\rangle\langle n_i| \right), \text{ with } \sum_i \rho(n_i) n_i = \bar{n}. \tag{4.28}$$

Using the factorisation ansatz (4.28), the master equation (4.27) reduces to a differential equation for the on-site occupation probability distribution $\rho(n)$,

$$\frac{\mathrm{d}\rho(n)}{\mathrm{d}\tau} = \sum_{m,\nu=\pm 1} \bar{n}^2 \frac{(n+\delta_{1,\nu})(m+\delta_{-1,\nu})}{(n-m+\nu)^2+\epsilon^2} \left[\rho(n+\nu)\rho(m-\nu) - \rho(n)\rho(m)\right], \tag{4.29}$$

where $\delta_{\pm 1,\nu}$ is the Kronecker delta. We use this form in the remainder of the section. The master equation (4.29) preserves the norm and the mean occupation number,

$$\sum_n \rho(n) = 1, \text{ and } \sum_n n\rho(n) = \bar{n}. \tag{4.30}$$

However, fluctuations of the on-site occupation number Δn are not preserved [$\Delta n^2 = \sum_n (n-\bar{n})^2 \rho(n)$].

4.3.3 Anomalous diffusion in Fock space

Using (4.29), Poletti et al. (2013) described explicitly the relaxation dynamics to the steady-state through the three distinct regimes mentioned earlier.

- During the initial stage the occupation number distribution broadens and long-range correlations decay exponentially (if they already existed at all). The time scale associated with this regime is κ^{-1}.
- Then relaxation slows down drastically and an algebraic regime emerges. In this second stage, the many-body state is already mainly a mixture of Fock state configurations with small filling fractions which belong to a decoherence-free subspace and do not decay. However, the appearance of such configurations is slowed down by two effects. First, nearest-neighbour tunnelling events partially restore coherences and slow down relaxation. Second, on-site interactions add a cost to the creation of Fock states with more than one atom, which also slows down relaxation. Additionally, the broadening of the Fock space distribution $\rho(n)$ with time is characterised by an exponent equal to 1/2, indicating anomalous diffusion (compared to the Brownian diffusion case where the exponent is equal to one). The time scale associated with this regime is t^*, the time it takes for rare configurations of high occupation numbers on a single site to get populated.

- In the final regime, the density matrix reaches its steady-state expression (4.24) with a stretched exponential evolution. This thermalisation stage is driven by the population of rare configurations with high occupation numbers on a single site, because of their suppressed probability to occur.

In the following we focus on the second stage, where the density matrix is mostly diagonal with weak contributions of off-diagonal coherences between Fock configurations differing by one-atom tunnelling events. Before solving (4.29) numerically, we consider the limit of large filling fractions where analytical results can be obtained.

Continuum approximation for large fillings

A very insightful result is obtained in the limit of large filling fraction $\bar{n} \gg 1$. In this case, the discrete variable n can be replaced by a continuous variable $x \mapsto n/\bar{n} \in \mathbb{R}^+$ and the occupation number distribution becomes $\rho(n) \mapsto p(x)/\bar{n}$. The master equation (4.29) then maps to a Fokker-Planck equation, as shown in Poletti et al. (2013) (see also Appendix B.3 for more details), from which analytical results can be derived. In that respect, and for times $\kappa^{-1} \leq t \leq t^*$, the solution of the master equation obeys a scaling form f (Poletti et al. 2013), which takes a simple analytical expression in the limit of weak dissipation, $\kappa \to 0$,

$$p(x,\tau) = \frac{1}{\tau^\alpha} f\left(\frac{x-1}{\tau^\alpha}\right) \tag{4.31}$$

$$\underset{\kappa\to 0}{=} \frac{1}{4\Gamma(5/4)\tau^{1/4}} \mathrm{e}^{-(x-1)^4/(16\tau)}, \tag{4.32}$$

where Γ is the Gamma function. Note that this scaling form is only valid in the window $\kappa^{-1} \leq t \leq t^*$ and for a peaked occupation number distribution, i.e. $\Delta n \ll \bar{n}$ (Poletti et al. 2013).

In the limit of weak dissipation, the exponent α is $1/4$, giving the scaling for the broadening of the distribution $\Delta x^2 \propto \tau^{1/2}$. This demonstrates anomalous diffusion in Fock space (more precisely sub-diffusion), much slower than the standard Brownian motion case presented in Section 4.1 that is expected for non-interacting atoms, for which $\alpha = 1/2$ and $\Delta x^2 \propto \tau$.

Numerical solution of the master equation

A numerical solution of (4.29) is shown in Figure 4.9 with the parameters $U = 10\,J_\perp$, $\epsilon = 0.1$, $\bar{n} = 2$ and $t^* = 50\,\kappa^{-1}$. The initial state is a Fock state with $\bar{n} = 2$. Figure 4.9a shows the evolution of $\rho(n)$ with time, the initial narrow distribution broadens with time and reaches the asymptotic steady-state value $\rho_{\mathrm{ss}}(n) \underset{t\to\infty}{=} \bar{n}^n/(1+\bar{n})^{n+1}$.

The width of the distribution ρ increases with time. This width characterises occupation number fluctuations. Figure 4.9b shows the time evolution of the normalised width along with a power-law fit for $\tau \in [0.01; 0.1]$. The exponent is ~ 0.30, close to the continuum limit prediction of $1/4$, and also demonstrates anomalous diffusion.

4.3.4 Relaxation of spatial coherence

Long-range correlations decay during the first stage of the relaxation. In the second stage we expect only short-ranged coherences to survive. These coherences are captured by the

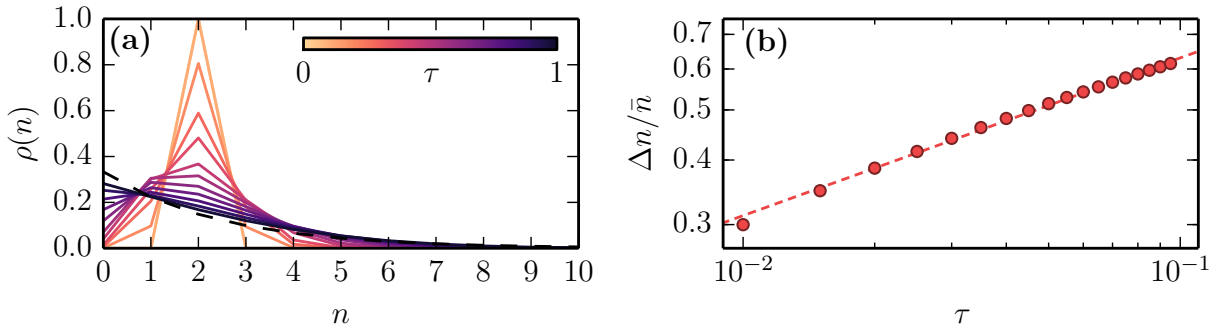

Figure 4.9: (a) Numerical integration of (4.29), the asymptotic distribution is plotted as a black dashed line. (b) Normalised atom number fluctuations $\Delta n/\bar{n}$. The dashed line is a power-law fit with exponent ~ 0.30. For all these curves the parameters are: $U = 10\,J_\perp$, $\hbar\kappa = 0.1\,J_\perp$, $\bar{n} = 2$ and $t^* = 50\,\kappa^{-1}$. The algebraic regime $\kappa^{-1} \leq t \leq t^*$ thus corresponds to $\tau \in [0.02, 1]$.

one-body nearest-neighbour correlator C_1 defined as

$$C_1 = \langle \hat{a}_i^\dagger \hat{a}_j \rangle_{|i-j|=1} = \sum_{\substack{\boldsymbol{n},\boldsymbol{m} \\ |i-j|=1}} \langle \boldsymbol{n}|\hat{a}_i^\dagger \hat{a}_j|\boldsymbol{m}\rangle\, \rho_{\boldsymbol{m}}^{\boldsymbol{n}} = \sum_{\substack{\boldsymbol{n} \\ |i-j|=1}} \sqrt{n_j(n_i+1)}\rho_{\boldsymbol{n}}^{\boldsymbol{n}+\boldsymbol{e}_i^j}. \tag{4.33}$$

Using the steady-state approximation for the density matrix coherences (4.26) and the factorisation ansatz we get

$$C_1 = \frac{J_\perp}{U} \sum_{n,m=0}^{+\infty} \frac{(m+1)(n+1)}{n-m-\mathrm{i}\epsilon} \left[\rho(n)\rho(m+1) - \rho(n+1)\rho(m)\right]. \tag{4.34}$$

Continuum approximation for large fillings

We can go further by considering the continuous distribution $p(x)$ presented earlier. For this we write $\rho(n+1) = p(x+1/\bar{n})/\bar{n} \approx p(x)/\bar{n} + p'(x)/\bar{n}^2$ and thus

$$\rho(n)\rho(m+1) - \rho(n+1)\rho(m) \approx \frac{1}{\bar{n}^3}\left[p(x)p'(y) - p'(x)p(y)\right], \tag{4.35}$$

where $x = n/\bar{n}$ and $y = m/\bar{m}$. The nearest-neighbour correlator then becomes

$$C_1^{\bar{n}\gg 1} = \frac{J_\perp}{U} \int_{\mathbb{R}^{+2}} \mathrm{d}x\mathrm{d}y\, \frac{xy}{x-y-\mathrm{i}\epsilon/\bar{n}} \left[p(x)p'(y) - p'(x)p(y)\right]. \tag{4.36}$$

In the limit of weak dissipation, we can use the scaling form (4.31) and show that (see Appendix B.3)

$$C_1^{\bar{n}\gg 1} \approx \frac{\xi J_\perp}{U}\frac{1}{\sqrt{\tau}} = \frac{\xi\bar{n}}{\sqrt{2z}}\frac{1}{\sqrt{\kappa t}} \text{ with } \xi = 2\frac{\Gamma(3/4)}{\Gamma(1/4)} \approx 0.6760, \tag{4.37}$$

where Γ is the Gamma function. Note that this analytical result is identical to the one obtained by Poletti et al. (2012) for a BEC in a double-well, and does not depend on the microscopic parameters U and $J_\perp$. In the algebraic regime, only nearest-neighbour coherences remain, and we expect the 2D lattice to behave in a way similar to a collection of double-wells. This is confirmed by the numerical calculation above.

In Figure 4.10b, a numerical computation of (4.36) is compared to the asymptotic evaluation (4.37) with the scaling form. The agreement is good for times $\tau \lesssim 0.1$.

Numerical computation

A numerical computation of C_1 from (4.34) is plotted in Figure 4.10a, along with a power-law fit giving an exponent ~ -0.54. This power-law exponent is remarkably close to the $-1/2$ exponent found in the limit of large fillings (4.37).

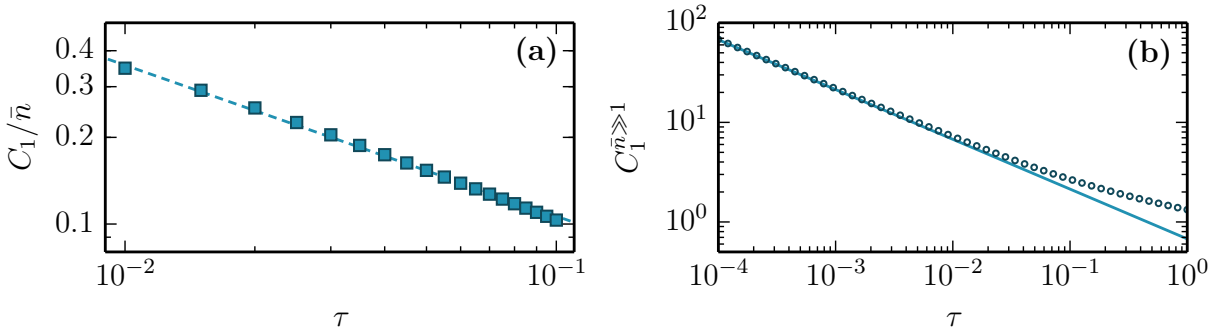

Figure 4.10: (a) Normalised nearest-neighbour correlator $C_1/\bar{n}$, the dashed line is a power-law fit with exponent ~ -0.54. The initial state is a Fock state with $\bar{n} = 2$ and the parameters are: $U = 10\,J_\perp$, $\hbar\kappa = 0.1\,J_\perp$ and $t^* = 50\,\kappa^{-1}$. (b) Nearest-neighbour correlator $C_1^{\bar{n}\gg 1}$ in the continuum approximation. Dots are computed from (4.36). The solid line is the asymptotic evaluation (4.37) with the scaling form (4.31).

Table 4.2 summarises our numerical investigation for various occupation numbers. The initial state is always a Fock state with occupation number $\bar{n}$. The case $\bar{n} = 1$ differs substantially from the scaling limit, but this is not a surprise since it is very far from the continuum approximation underlying the scaling prediction.

Occupation number $\bar{n}$	1	2	3
t^* $[\kappa^{-1}]$	12	50	110
$\Delta n/\bar{n}$ exponent	0.44	0.30	0.26
$C_1/\bar{n}$ exponent	-0.21	-0.54	-0.56

Table 4.2: Fitted power-law exponents for atom number fluctuations and nearest-neighbour correlator for different mean occupation numbers $\bar{n}$.

4.3.5 Limitations

The previous analytical description makes use of various assumptions that do not necessarily hold in our system. Here I summarise and discuss the limitations of the theory presented in this section. For this I need to take the dissipation strength κ as the rate of spontaneous emission Γ_{sp} used in our experiments.

1. As presented in Section 4.2, we expect inter-band transitions to occur over a time scale of a few Γ_{sp}^{-1}. The single-band approximation therefore does not hold.
2. The treatment with a local density measurement $\hat{C} \propto \hat{n}_i$ does not account for resonant nor collective effects in light scattering. Such a simplified description of atom-light interaction might not be sufficient to account for all the observations of Section 4.2.

3. The condition $U \gg J_\perp, \Gamma_{\mathrm{sp}}$ used for the adiabatic elimination of the coherences is not always verified in the experiments, where $U/J_\perp$ is on the order of one for the smallest horizontal lattice depths.
4. Atom losses (see Section 4.2.5) can also affect the dynamics, even though we disregarded this aspect by normalising the distributions. This is not at all included in the model.

Influence of three-body recombination processes

The observed broadening of the occupation number distribution leads to the formation of Fock states with relatively high n. In the experiment, these states are prone to three-body recombinations, leading to atom losses. For example, the typical lifetime for three atoms on the same site is a few hundred milliseconds, and decreases rapidly with increasing occupation number. The method developed in this section cannot be used directly in the presence of losses because they induce a coupling between different Fock subspaces, complicating the calculation substantially. In order to incorporate these losses in the model, we add *by hand* a loss term to the master equation (4.29),

$$\left.\frac{\mathrm{d}\rho(n)}{\mathrm{d}t}\right|_{\mathrm{losses}} = L_{3\mathrm{B}}\left[(n+3)(n+2)(n+1)\rho(n+3) - n(n-1)(n-2)\rho(n)\right], \tag{4.38}$$

where $L_{3\mathrm{B}}$ characterises the rate of these losses. This procedure is justified provided that the losses are slow enough to affect only the populations but not the coherences, which requires $L_{3\mathrm{B}}\bar{n} \ll \kappa$.

In the experiment, the actual three-body recombination rate is around $\hbar L_{3\mathrm{B}} \approx 10^{-3}\, J_\perp$, which corresponds to $L_{3\mathrm{B}}t^* = 0.5$. A numerical computation of (4.29) including the loss process (4.38) is shown in Figure 4.11. The initial state is a Fock state with $\bar{n} = 2$. High occupation numbers are suppressed as expected but the relaxation dynamics is qualitatively not much affected. The fitted exponents for the atom number fluctuations and nearest-neighbour correlator are renormalised to respectively ~ 0.33 and ~ -0.52, which does not differ much from the case where the losses are absent.

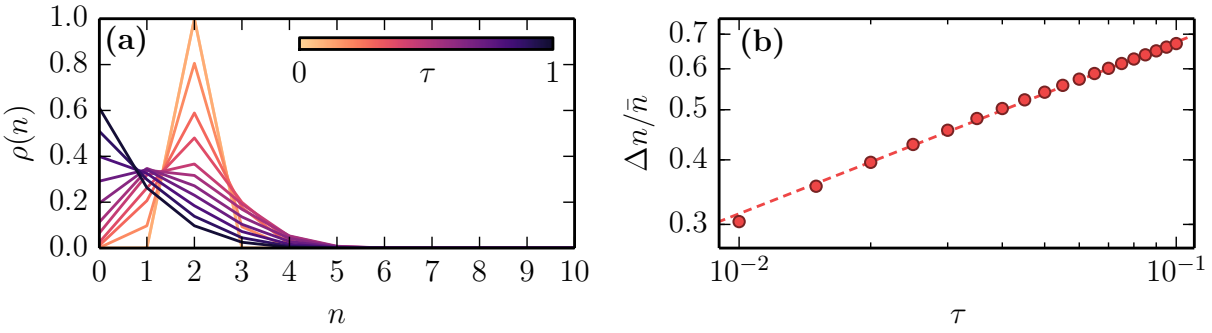

Figure 4.11: (a) Numerical integration of (4.29) with three-body losses (4.38). The initial state is a Fock state with $\bar{n} = 2$. (b) Normalised atom number fluctuations. The dashed line is a power-law fit with exponent ~ 0.33. For all these curves the parameters are: $U = 10\, J_\perp$, $\hbar\kappa = 0.1\, J_\perp$, $\bar{n} = 2$, $t^* = 50\, \kappa^{-1}$ and $L_{3\mathrm{B}}t^* = 0.5$.

4.4 Relaxation dynamics in the algebraic regime

The theoretical analysis provided in Section 4.3 supports some of our observations, and encourage a more detailed investigation. The early attempt to capture the relaxation dynamics from a simple observable presented in Section 4.2 can be improved for the algebraic regime where only a few parameters are required to describe faithfully the experimental momentum distributions. In this section, I present an analysis of the momentum distribution profiles in the algebraic regime of the decay. I directly extract valuable quantities from the profiles, such as band populations and correlators.

4.4.1 Momentum distribution description

We describe the momentum distribution for the system using the one-particle field operator $\hat{\psi}(\boldsymbol{r}, t)$ of an atom released from the optical lattice. The atomic density for long times-of-flight is $n_{\mathrm{tof}}(\boldsymbol{k}) = \langle \hat{\psi}^\dagger(\boldsymbol{k}, t_{\mathrm{tof}}) \hat{\psi}(\boldsymbol{k}, t_{\mathrm{tof}}) \rangle$ where $\boldsymbol{k} = M\boldsymbol{r}/(\hbar t_{\mathrm{tof}})$ is the rescaled position due to ballistic expansion. Assuming that interactions do not significantly modify the expansion and that time-of-flight is long enough (Gerbier et al. 2008), the momentum distribution is exactly determined by the following expression,

$$n_{\mathrm{tof}}(\boldsymbol{k}) = \sum_{\text{bands } n,m} \mathcal{S}_{n,m}(\boldsymbol{k}) \mathcal{W}_{n,m}(\boldsymbol{k}). \tag{4.39}$$

$\mathcal{W}_{n,m}$ is a smooth envelope function given by the Fourier transform W of the on-site Wannier function w: $\mathcal{W}_{n,m}(\boldsymbol{k}) \propto W_n(\boldsymbol{k}) W_m^*(\boldsymbol{k})$. $\mathcal{S}_{n,m}$ is a structure factor, given by the Fourier transform of the first-order correlation function $\langle \hat{a}_{\boldsymbol{i}}^{n\dagger} \hat{a}_{\boldsymbol{j}}^{m} \rangle$,

$$\mathcal{S}_{n,m}(\boldsymbol{k}) = \sum_{\text{sites } \boldsymbol{i},\boldsymbol{j}} \mathrm{e}^{\mathrm{i}\boldsymbol{k}\cdot(\boldsymbol{r}_{\boldsymbol{i}} - \boldsymbol{r}_{\boldsymbol{j}})} \langle \hat{a}_{\boldsymbol{i}}^{n\dagger} \hat{a}_{\boldsymbol{j}}^{m} \rangle. \tag{4.40}$$

In the algebraic regime we expect the coherences to be already short-ranged. We therefore only keep local $\boldsymbol{i} = \boldsymbol{j}$, as well as the first three nearest-neighbour terms[5]:

1. the first neighbours are located at $\boldsymbol{i} = \boldsymbol{j} \pm (0, 1)$ and $\boldsymbol{i} = \boldsymbol{j} \pm (1, 0)$,
2. the second neighbours are on the diagonals $\boldsymbol{i} = \boldsymbol{j} + (\pm 1, \pm 1)$,
3. the third neighbours are located at $\boldsymbol{i} = \boldsymbol{j} \pm (0, 2)$ and $\boldsymbol{i} = \boldsymbol{j} \pm (2, 0)$.

The initial state of our system is prepared in the fundamental band of the lattice and spontaneous emission does not create coherences between bands. We therefore have for the fundamental band:

$$\begin{aligned} \mathcal{S}_{0,0}(\boldsymbol{k}) \simeq \sum_{\boldsymbol{i}} \langle \hat{a}_{\boldsymbol{i}}^\dagger \hat{a}_{\boldsymbol{i}} \rangle &+ \sum_{\langle \boldsymbol{i},\boldsymbol{j} \rangle_1} 2 \langle \hat{a}_{\boldsymbol{i}}^\dagger \hat{a}_{\boldsymbol{j}} \rangle \left[\cos(k_x d) + \cos(k_y d) \right] \\ &+ \sum_{\langle \boldsymbol{i},\boldsymbol{j} \rangle_2} 2 \langle \hat{a}_{\boldsymbol{i}}^\dagger \hat{a}_{\boldsymbol{j}} \rangle \left[\cos(k_x d + k_y d) + \cos(k_x d - k_y d) \right] \\ &+ \sum_{\langle \boldsymbol{i},\boldsymbol{j} \rangle_3} 2 \langle \hat{a}_{\boldsymbol{i}}^\dagger \hat{a}_{\boldsymbol{j}} \rangle \left[\cos(2k_x d) + \cos(2k_y d) \right]. \end{aligned} \tag{4.41}$$

where we omitted the band index $n = 0$. $d = \lambda_{\mathrm{m}}/2$ is the lattice period and $\langle \boldsymbol{i}, \boldsymbol{j} \rangle_m$ denotes m^{th} neighbour pairs. Band populations may evolve due to the coupling with the

[5] Note that we assume a perfect square symmetry for simplicity. This is fulfilled up to 10 % in the experiment and we have not quantified the deviations.

resonant laser. We keep only the lowest $n = 4$ energy levels to describe the distributions, assuming that all degenerate excited bands are equally populated (the level n corresponds to all bands (n_x, n_y) which satisfy $n = n_x + n_y$). We treat the components in the excited energy levels (initially empty) as fully incoherent, i.e.

$$\mathcal{S}_{n,n}(\boldsymbol{k}) \simeq \sum_{\boldsymbol{i}} \langle \hat{a}_{\boldsymbol{i}}^{n\dagger} \hat{a}_{\boldsymbol{i}}^{n} \rangle \text{ for } n > 0. \tag{4.42}$$

In the case where some long-range coherences remain, i.e. a BEC is still present, the previous description must be amended. Inspired by the Bogoliubov theory of the weakly interacting Bose gas, we write the annihilation operator $\hat{a}_{\boldsymbol{i}}^{n} \approx \alpha_{\boldsymbol{i}} \delta_{n,0} + \hat{\delta a}_{\boldsymbol{i}}$, where $\alpha_{\boldsymbol{i}}$ is the condensate order parameter, $\delta_{n,0}$ is the Kronecker delta and $\hat{\delta a}_{\boldsymbol{i}}$ is a perturbation with zero expectation value in the fundamental band. The BEC structure factor reads

$$\mathcal{S}_{\mathrm{BEC}}(\boldsymbol{k}) \approx \sum_{\text{sites } \boldsymbol{i},\boldsymbol{j}} \alpha_{\boldsymbol{i}}^{*} \alpha_{\boldsymbol{j}}. \tag{4.43}$$

We empirically model the structure factor $\mathcal{S}_{\mathrm{BEC}}$ by a Gaussian distribution G with variable amplitude $\mathcal{G}$ but fixed width and centred on the distribution (the width is set to match the central peak width at early times). This is motivated by the quadratic dependence in space of the near-field phase correction terms (Gerbier et al. 2008).

We can finally write the approximate expression for the momentum distribution

$$n_{\mathrm{tof}}(\boldsymbol{k}) \simeq \underbrace{\mathcal{G} G(\boldsymbol{k})}_{\mathrm{BEC}} + \underbrace{\sum_{m=0}^{3} \mathcal{C}_m \left| W_0(\boldsymbol{k}) \right|^2 \sum_{m_1,m_2} \cos\left(m_1 k_x d + m_2 k_y d\right)}_{\text{fundamental band}} + \underbrace{\sum_{n=1}^{3} \mathcal{P}_n \left| W_n(\boldsymbol{k}) \right|^2}_{\text{excited energy levels}}, \tag{4.44}$$

with the normalisation condition $\int \mathrm{d}^3 k \, n_{\mathrm{tof}}(\boldsymbol{k}) = N_{\mathrm{at}}$ and m_1, m_2 chosen to match the description in (4.41). We use the following short-hand notations:

$$\mathcal{C}_0 = \sum_{\boldsymbol{i}} \langle \hat{a}_{\boldsymbol{i}}^{\dagger} \hat{a}_{\boldsymbol{i}} \rangle \,, \tag{4.45}$$

$$\mathcal{C}_m = \sum_{\langle \boldsymbol{i},\boldsymbol{j} \rangle_m} 2 \langle \hat{a}_{\boldsymbol{i}}^{\dagger} \hat{a}_{\boldsymbol{j}} \rangle \text{ for } m \in \{1,2,3\}, \tag{4.46}$$

$$\mathcal{P}_n = \sum_{\boldsymbol{i}} \langle \hat{a}_{\boldsymbol{i}}^{n\dagger} \hat{a}_{\boldsymbol{i}}^{n} \rangle \text{ for } n \in \{1,2,3\}. \tag{4.47}$$

4.4.2 Experimental profiles and fits

We use the momentum distribution description given in (4.44) to fit the 2D experimental profiles in the algebraic regime of the decay ($t_{\mathrm{diss}} \geq t_{\mathrm{cross}}$). Figure 4.12 shows typical one-dimensional profiles obtained from cuts through the 2D profiles along one lattice axis. The duration of the dissipation laser pulse t_{diss} increases from bottom to top. In Figure 4.12a, smooth solid lines correspond to the fits.

Figure 4.12b shows the residuals of the fit, they are comparable to the image noise almost everywhere, which indicates that the model is sufficient to capture the profiles adequately. A detailed discussion of the fitting procedure is given in Appendix B.4.

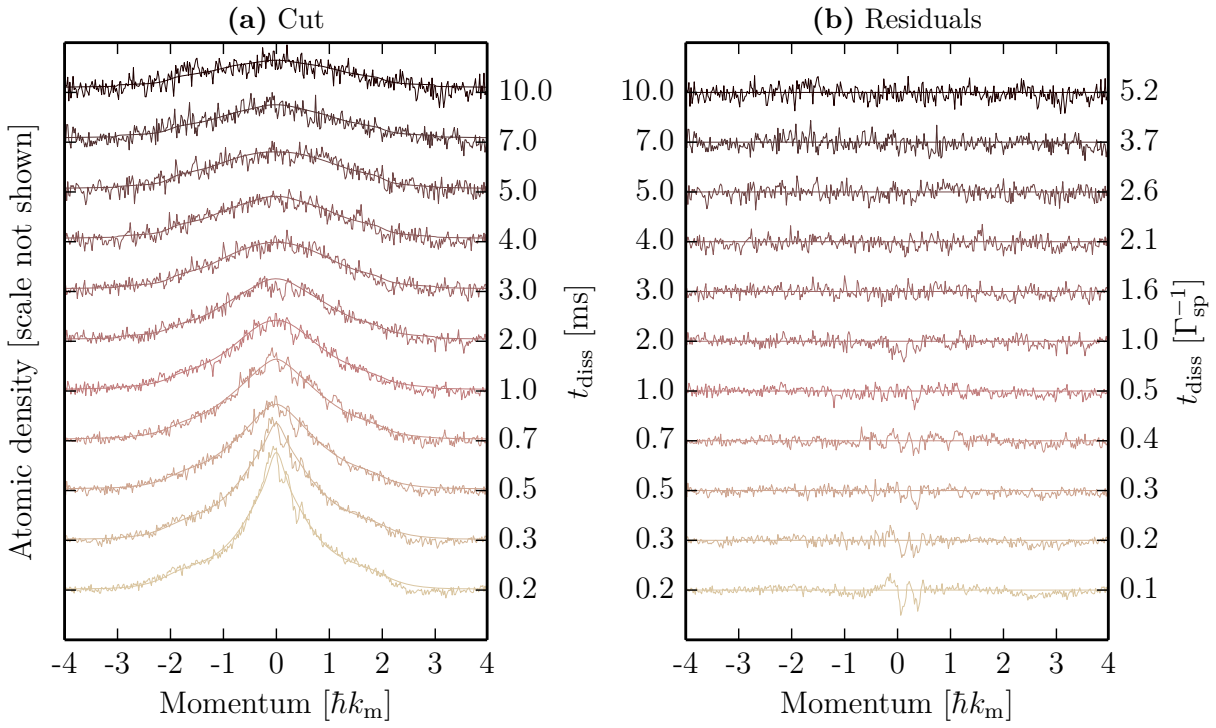

Figure 4.12: Momentum profile evolution with respect to dissipation pulse time in the algebraic regime of the decay with parameters $V_\perp = 7.3\,E_{\mathrm{R}}$ and $\Gamma_{\mathrm{sp}} = 520\,\mathrm{s}^{-1}$. As indicated by the vertical scale in the middle, dissipation pulse time grows upwards. (a) Cuts along one axis of the optical lattice, smooth solid lines are fits. The atomic density scale is not shown for clarity: the corresponding peak optical density is $\mathrm{OD}_{\mathrm{max}} \approx 0.1$ for the bottom curve. (b) Residuals of the fit.

4.4.3 Band population evolution

We obtain band populations from the best-fit parameters computed as described previously. The total population in the fundamental band $\mathcal{P}_0$ is obtained from the coefficients $\mathcal{C}_0$ and given by

$$\mathcal{P}_0 = \int \mathrm{d}^3k\, \mathcal{C}_0\, |W_0(\boldsymbol{k})|^2 = \mathcal{C}_0. \tag{4.48}$$

Excited energy level populations $\mathcal{P}_n$ are readily obtained from the best-fit parameters.

In Figure 4.13, the time evolution of the relative population of the different energy levels in the algebraic regime ($t_{\mathrm{diss}} \geq t_{\mathrm{cross}}$) is shown for fixed $\Gamma_{\mathrm{sp}} = 520\,\mathrm{s}^{-1}$ and various horizontal lattice depths. We observe substantial inter-band transitions during dissipation. The transfer to higher bands is suppressed as the horizontal lattice depth is increased. The regime when excited band populations get non-negligible happens for $\Gamma_{\mathrm{sp}} t_{\mathrm{diss}} \approx 1$.

Atoms in excited bands have a higher tunnelling energy and a slightly reduced interaction energy compared to fundamental band atoms. This can modify the dynamics and we therefore expect deviations from the single-band model presented in Section 4.3 when the populations in higher bands become substantial, this is discussed below. A theoretical study and interpretation of the energy level population evolution is given in the next chapter.

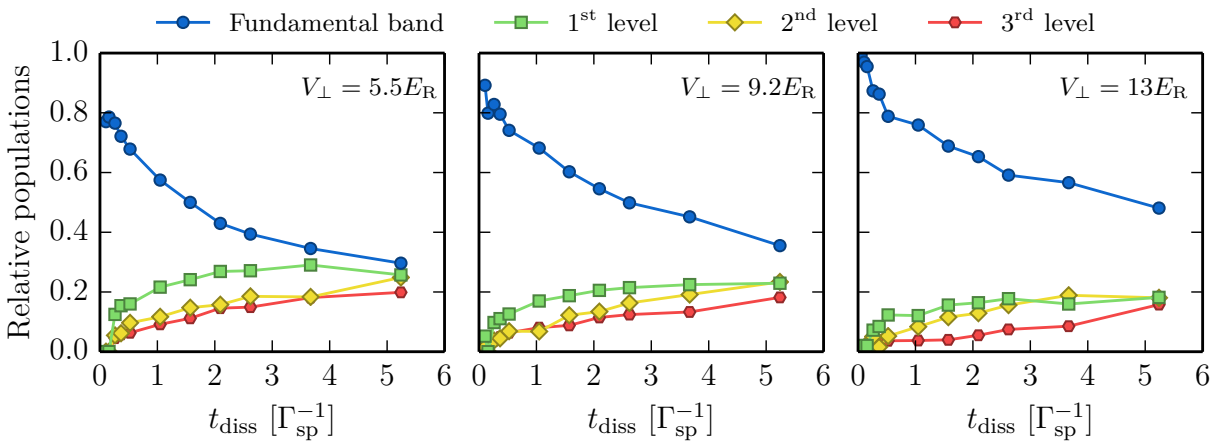

Figure 4.13: Fitted relative populations in the various bands with respect to dissipation pulse time. $\Gamma_{sp} = 520\,s^{-1}$ is the same for all curves.

4.4.4 Nearest-neighbour coherence evolution

We obtain spatial coherences in the fundamental band from the best-fit parameters computed as described previously. In Figure 4.14, the time evolution of the nearest-neighbour correlator $\mathcal{C}_1$ in the algebraic regime ($t_{diss} \geq t_{cross}$) is shown for $\Gamma_{sp} = 520\,s^{-1}$ and various horizontal lattice depths. The axes are in double logarithmic scale. We performed a power-law fit on the data points above the detection floor. The detection floor for the evaluation of $\mathcal{C}_1$ is situated at around 0.015, and stems from the noise on the absorption images. The results presented in Figure 4.14 are a compilation of the data presented in Section 4.2.3, where we varied the horizontal lattice depth $V_\perp$, and a more recent data set taken during the writing of the manuscript (they are shown as filled and hollow points respectively).

The decay of coherences seems algebraic for sufficiently large lattice depth (roughly $V_\perp \gtrsim 7\,E_R$). We observe a departure from the power-law scaling at long times $t_{diss} \geq \Gamma_{sp}^{-1}$ for smaller lattice depth. This departure is less pronounced as lattice depth is increased. While this could be consistent with the regime where excited energy level populations are non-negligible, it might as well be predicted by the model presented in Section 4.3. Indeed, the scaling form derived in the continuum approximation requires a peaked occupation number distribution, this does not necessarily hold for the lowest lattice depth where the initial distribution is expected to be broad.

Figure 4.15 presents the fitted exponents for the power-law decay of the nearest-neighbour correlator corresponding to the set of experiments presented in Figure 4.14. The exponents are close to one for low $V_\perp$ and seem to converge to a value close to ~ 0.5 as lattice depth is increased. This crossover from a standard diffusion to an anomalous sub-diffusion is remarkably consistent with the prediction of Section 4.3.

In Figure 4.16, I show the fitted exponents for the algebraic decay of $\mathcal{C}_1$ corresponding to the set of experiments presented in Section 4.2.4, where we varied the spontaneous emission rate Γ_{sp}. The exponents seem to scatter above a value close to ~ 1, compatible with a standard diffusion in Fock space. However, due to the small value of the lattice depth, the tight-binding and single-band approximations are dubious. In principle we could also extract the further-neighbour correlators $\mathcal{C}_2$ and $\mathcal{C}_3$, but the signal was too noisy to exhibit any feature.

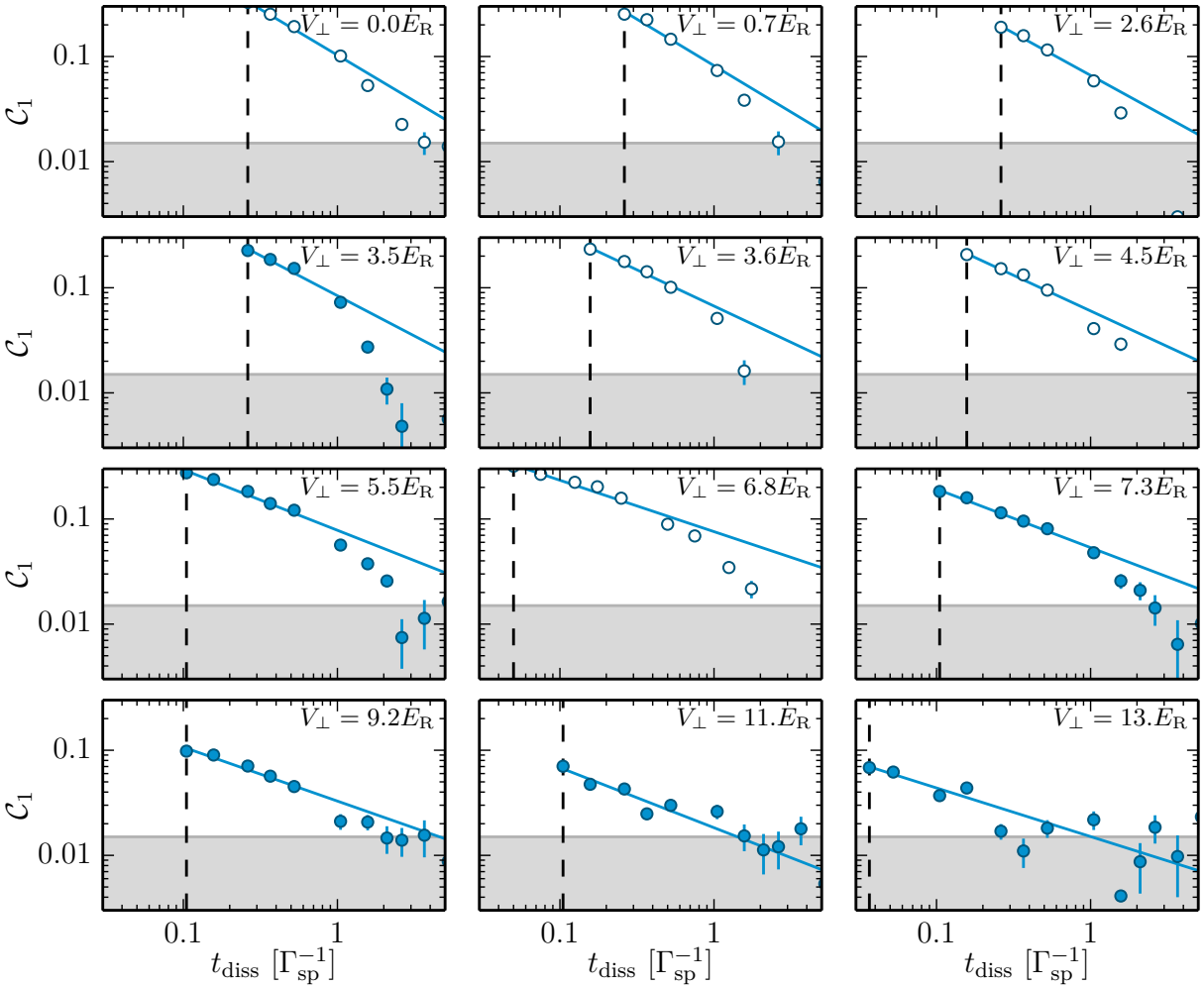

Figure 4.14: Fitted nearest-neighbour coherences with respect to dissipation pulse time. $\Gamma_{sp} = 520\,s^{-1}$ is the same for all curves and lines are power-law fits. The estimated detection floor is located at around 0.02 as indicated by the shaded area. The crossover time t_{cross} giving the start of the algebraic regime is displayed as a vertical dashed line. Filled data points correspond to the experiments of Section 4.2.3, hollow data points correspond to measurements taken several months later.

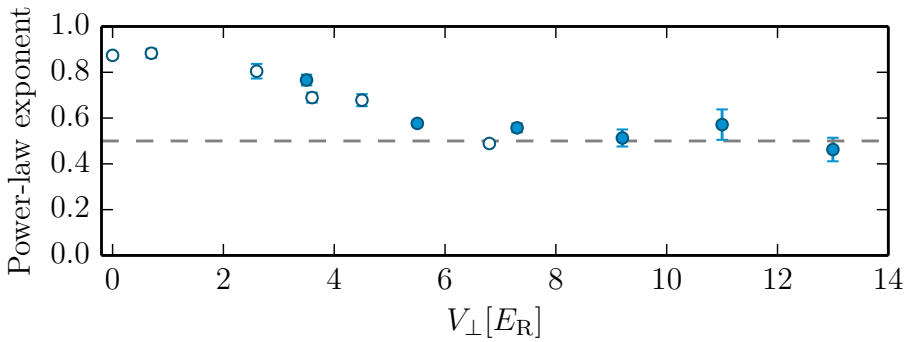

Figure 4.15: Fitted exponents for the algebraic decay of the coherence $\mathcal{C}_1$ with varying $V_\perp$ and fixed $\Gamma_{sp} = 520\,s^{-1}$. Filled data points correspond to the experiments of Section 4.2.3, hollow data points correspond to measurements to measurements taken several months later.

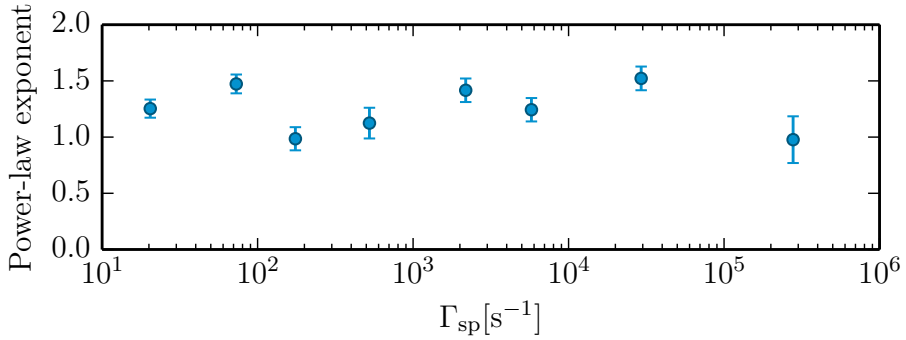

Figure 4.16: Fitted exponents for the algebraic decay of the coherence $\mathcal{C}_1$ with varying Γ_{sp} and fixed $V_\perp = 3.5\,E_R$. Data correspond to the experiments of Section 4.2.4.

In conclusion, interactions seem to slow down the coherence relaxation dynamics. As explained in Poletti et al. (2012), this *interaction-induced impeding of decoherence* stems from the suppression of localisation processes and diffusion in Fock space as normally induced by dissipation. Indeed, on-site interactions make high occupation numbers energetically onerous. As a final piece of evidence, we explore this interpretation of Fock space diffusion in what follows.

4.5 Detection of Fock space dynamics through inelastic losses

As demonstrated in the last section, interactions play a key role in the relaxation dynamics, leading to a sub-diffusive relaxation in momentum space. Thanks to the theoretical framework developed in Section 4.3, we also understand this behaviour in terms of anomalous diffusion in Fock space. Dissipation induced by spontaneous emission triggers localisation in Fock space, followed by a much slower diffusion resulting from the competition between on-site interactions, tunnelling and diffusion. In this section, I present an experimental investigation of the Fock space dynamics induced by dissipation. This is performed by measuring inelastic losses coming from three-body recombination events, a robust signature of Fock states with more than three atoms.

4.5.1 Freezing the spatial dynamics to observe the Fock space distribution

As before, we prepare superfluid phases at a given horizontal lattice depth $V_\perp$ and submit it to spontaneous emission with the dissipation laser. In order to probe the occupation number dynamics in Fock space, we switch off the dissipation and freeze the density distribution by a quench to deep lattice depth ($\sim 25\,E_R$). The quench is performed in 10 µs, fast enough to prevent any spatial redistribution during the quench but slow enough to avoid inter-band transitions. We subsequently observe the evolution of the atom number with respect to the hold time in the deep lattice.

In principle, we should observe (i) a first decrease (on the order of 100 ms) of the atom number corresponding to sites with triple or higher occupancies, caused by three-body

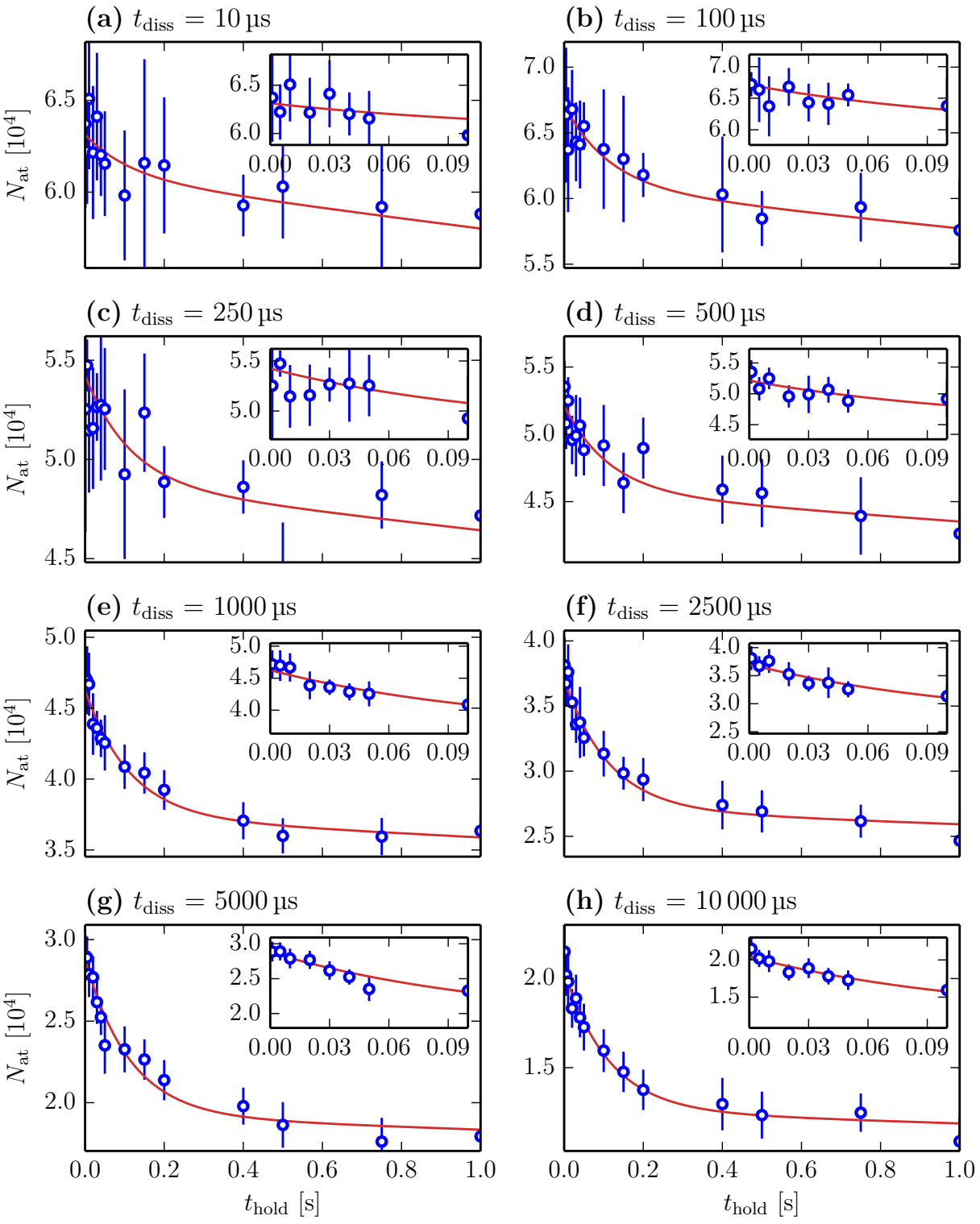

Figure 4.17: Atom number decay after freezing for various dissipation times, the spontaneous emission rate is $\Gamma_{\mathrm{sp}} = 250\,\mathrm{s}^{-1}$ and the horizontal lattice depth is $V_\perp = 8.6\,E_{\mathrm{R}}$. The insets show the evolution at short times. Solid lines are fits using the model presented in Appendix B.5.

recombination processes, (ii) a plateau when all highly-occupied sites have decayed to singly- or doubly- occupied sites.

Figure 4.17 shows typical experimental sequences. The atomic ensemble is prepared in a superfluid phase at a given $V_\perp$. The dissipation laser is applied for a time t_{diss} and then switched off while simultaneously quenching to deep lattice depth. We observe the total atom number varying the hold time t_{hold} in the lattice.

As expected, we observe an initial decay of the atom number over a time $t_{\mathrm{hold}} \leq 100\,\mathrm{ms}$, more pronounced as t_{diss} increases. However, we also observe a further decay with a much longer time scale. Before discussing the dynamics of triply-occupied sites, we shall analyse this long-time behaviour, which is the point of the next paragraph.

4.5.2 Calibration of the two-body loss rate

In order to understand the long-time decay of the atom number in the previously described experiments, we studied the time evolution of the atom number without spontaneous emission in deep lattices by preparing Mott insulator phases as in Chapter 3. Figure 4.18 shows the measurements. We observe a substantial reduction of atom loss when decreasing the atom number, which we interpret as a consequence of a two-body loss mechanism.

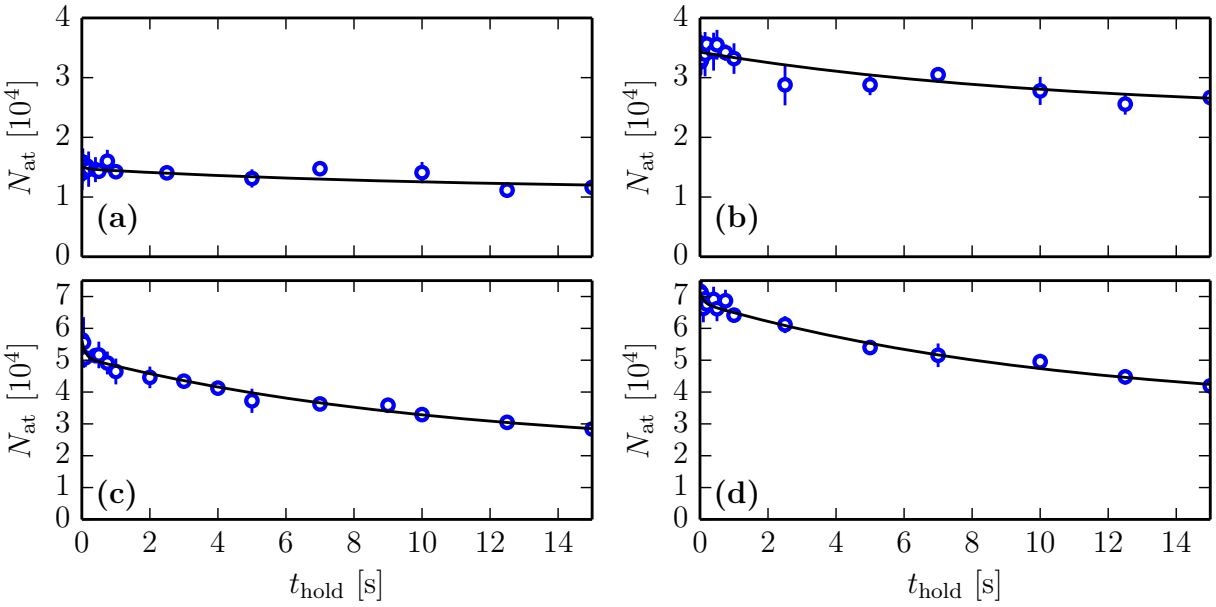

Figure 4.18: Atom number decay without spontaneous emission for Mott insulator phases with different total atom numbers. The long-time decay is more pronounced as initial atom number increases [from (a) to (d)].

In order to extract a loss rate from the measurements, we model the time evolution of the system by assuming that tunnelling is negligible over the course of the decay and that decay processes are purely local. We restrict the discussion to 2- and 3-body inelastic processes with characteristic rates $\gamma_{k=2,3}$. The system of equations governing the time dynamics in provided in Appendix B.5 and we recall it here (p_n is the spatially-averaged

probability of finding n atoms per site):

$$p_0(t) = (1 - \mathrm{e}^{-2\gamma_2 t})p_2(0) + (1 - \mathrm{e}^{-6\gamma_3 t})p_3(0), \tag{4.49}$$
$$p_1(t) = p_1(0), \tag{4.50}$$
$$p_2(t) = \mathrm{e}^{-2\gamma_2 t}p_2(0), \tag{4.51}$$
$$p_3(t) = \mathrm{e}^{-6\gamma_3 t}p_3(0). \tag{4.52}$$

We analysed the data in Figure 4.18 with this set of equations, where we have truncated the Fock space to $n = 3$ (no Mott shell with $n = 4$ or higher is expected, see Figure 3.2). We set γ_3 to its expected value [using the three-body recombination rate $L_3 \approx 7 \times 10^{-30}\,\mathrm{cm}^6\,\mathrm{s}^{-1}$ measured in Fukuhara et al. (2009), see Appendix B.5]. The initial probabilities and γ_2 are free parameters. The results of this fit are shown in Figure 4.19.

The populations $N_n = np_n$ are plotted in Figure 4.19a. They are in rough agreement with the theoretically expected value in the atomic limit at zero-temperature, computed from our loading model (see Section 3.1). For high atom number, we observe a deviation with a smaller occupation of triply-occupied sites, very similar to what we already observed previously (see Figure 3.7).

The fitted two-body loss rate γ_2 is shown in Figure 4.19b. It takes on a consistent value when the atom number is sufficient. An average of the last three points gives $\gamma_2 \approx 5 \times 10^{-2}\,\mathrm{s}^{-1}$. A further combined fit of the four data sets with a single γ_2 common to all sets returns $\gamma_2 \approx 4.7(15) \times 10^{-2}\,\mathrm{s}^{-1}$.

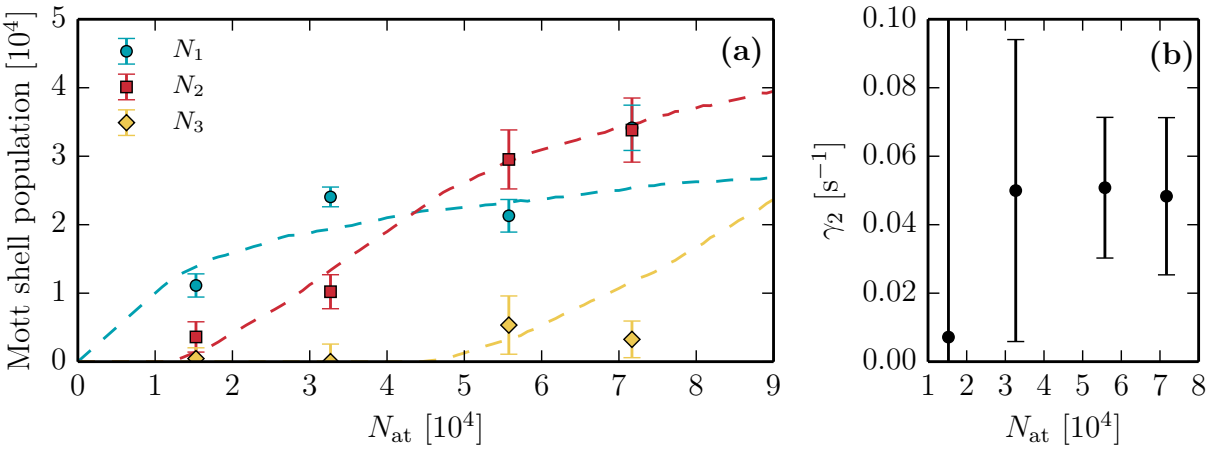

Figure 4.19: Best-fit parameters from the analysis of the data in Figure 4.18. (a) Mott shell populations N_1, N_2 and N_3 versus total atom number. Dashed lines are the expected Mott shell populations in the atomic limit at zero-temperature (see Section 3.1). (b) Fitted two-body loss rate γ_2. Only the last three points are relevant since atom number in doubly-occupied sites is too small for the first one.

4.5.3 Dynamics of triply-occupied sites

With the calibration of γ_2, we can perform a quantitative analysis of the dynamics of multi-occupied sites when spontaneous emission is present. We use the same model as in the previous paragraph, fixing γ_2 to its fitted value and γ_3 to its expected value[6] but

[6]Letting γ_2 or γ_3 as free parameters was not conclusive since 2- and 3-body processes can be mixed up by the fit procedure. We decided to fix both and only let the populations as free parameters.

leaving the populations as free parameters. Three different data sets were taken, the experimental parameters of which are summarised in Table 4.3 (data presented in Figure 4.17 correspond to the set 2).

Set	$N_{\mathrm{at}}(0)$	$V_\perp[E_\mathrm{R}]$	$V_{0,z}[E_\mathrm{R}]$	$\gamma_3[\mathrm{s}^{-1}]$
1	6.3×10^4	5.5	25.9	0.21
2	6.4×10^4	8.6	26.7	0.38
3	5.5×10^4	27.4	26.7	1.48

Table 4.3: Experimental parameters for the study of triply-occupied site dynamics, as shown in Figure 4.17.

The fit results are summarised in Figure 4.20, they are compatible with our previous conclusions[7]:

1. we observe a small (but finite in Sets 1 and 2) population for triply-occupied sites at short times, simply due to the occupation probability in the initial state,
2. then we measure a rise in the population occurring for times $t_\mathrm{diss} \gtrsim t_\mathrm{cross}$, compatible with a dissipation-induced diffusion in Fock space.

We note that the rise of triply-occupied sites in the deep Mott insulator regime is quite unexpected since density redistribution should be prohibited within the experimental time scale due to the small value of the tunnelling time $\hbar/J_\perp \approx 100\,\mathrm{ms}$. However, the occurrence of inter-band transitions could be responsible for this rise in triply-occupied sites, caused by enhanced tunnelling in the excited bands ($\hbar/J_\perp^1 \approx 3.5\,\mathrm{ms} \sim \Gamma_\mathrm{sp}^{-1}$).

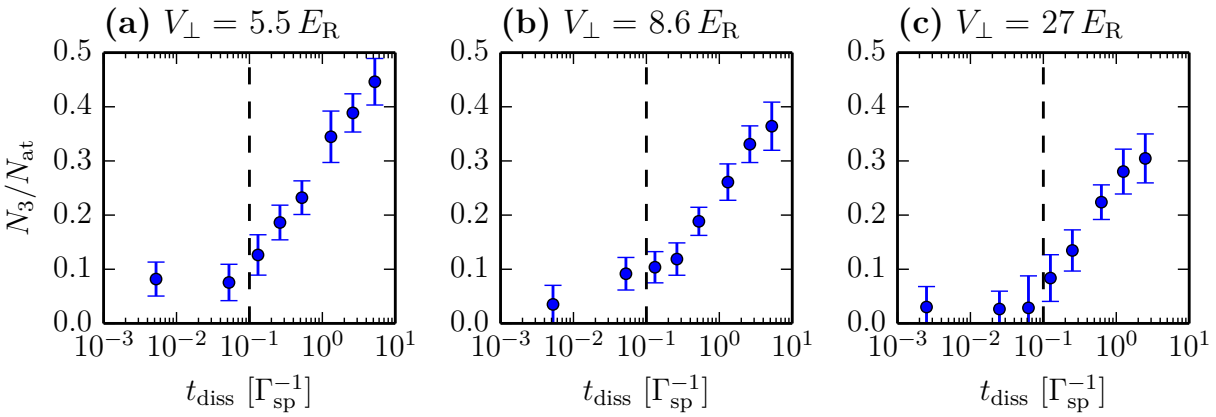

Figure 4.20: Best-fit parameters from the analysis of atom losses for the three data sets described in Table 4.3. The crossover times t_cross giving the beginning of the algebraic regime are displayed as vertical dashed lines. For all data sets $\Gamma_\mathrm{sp} = 250\,\mathrm{s}^{-1}$.

4.6 Conclusion

In this chapter, I have demonstrated anomalous momentum diffusion for an ultracold atomic gas in optical lattices. I first recalled how dissipation with spontaneous emission

[7] Note that we also included $n = 4$ for this fit, but the fitted population N_4 was zero almost everywhere with big fit uncertainties. We thus do not show it.

affects the dynamics of a single atom, focusing on momentum diffusion and the loss of spatial quantum coherences. I then showed our measurements displaying a dramatic change in the relaxation of a superfluid subjected to spontaneous emission, the long-time dynamics of which being governed by a 'slow' power-law decay. Thereupon, I described a 'simple' theoretical model which captures the main features of our observations. In this model, inter-atomic interactions are essential to understand the slow down of relaxation, as observed in the experiments. I then detailed two quantitative studies of the experimental data providing evidence for anomalous sub-diffusion in momentum space. I could relate these results to the theoretical model by comparing the predictions with our observation of power-law exponents and site occupation distributions. While quantitative agreement has been found, a number of experimental observations could not be explained by the model:

- The relatively high rate in the exponential regime of the decay (see Figure 4.4).
- The weak dependence of the crossover on the spontaneous emission rate (see Figure 4.6).
- The observation of atom losses (see Section 4.2.5).
- The departure from power-law in the decay of coherences for shallow lattice depths (see Figure 4.14).
- The rise of triply-occupied sites in the deep Mott insulator regime.

I shall address some of these discrepancies in the following chapter, but I can already discuss them using simple arguments based on the band structure of the lattice. Substantial inter-band transitions occur due to dissipation for times $t_{\mathrm{diss}} \gtrsim \Gamma_{\mathrm{sp}}^{-1}$. The dynamics of excited atoms is a priori different from the one in the fundamental band. In Figure 4.21, I show the ratio $U/J_\perp$ and the time scale t^* for atoms in the fundamental band $n = 0$ and for atoms in the first excited energy level $n = 1$. The interaction energy U for atoms in the first excited energy level is calculated with the assumption that excited atoms are not numerous and thus interact mostly with atoms in the fundamental band.

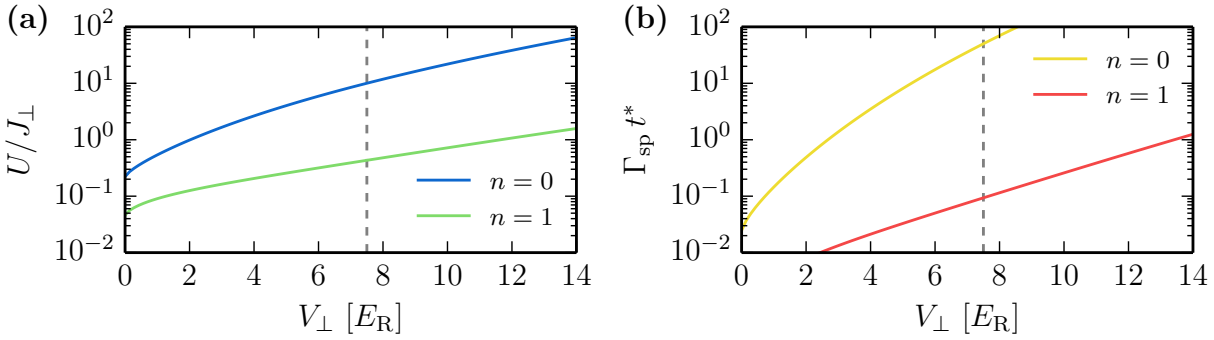

Figure 4.21: Figures of merit for the validity of the model presented in Section 4.3 for atoms in the fundamental band $n = 0$ and atoms in the first excited energy level $n = 1$. In both curves the vertical gray dashed line denote the depth above which the first excited band is bound. (a) Ratio $U/J_\perp$. (b) Time scale $\Gamma_{\mathrm{sp}} t^*$.

- For atoms in the fundamental band, the validity condition $U \gg J_\perp$ for the model developed in Section 4.3 occurs for $V_\perp \gtrsim 5\, E_\mathrm{R}$ (Figure 4.21a). This corresponds roughly to the depth where momentum diffusion becomes anomalous with the exponent 0.5 (see Figure 4.15). Below this depth, the treatment is not valid any longer and neither is the prediction of an algebraic decay with exponent 1/2.

- Atoms in the first excited band are much more mobile. The first excited band is bound only for $V_\perp \gtrsim 7.5\, E_\mathrm{R}$. Moreover, $U/J_\perp$ for that band is much smaller than one for $V_\perp \lesssim 8\, E_\mathrm{R}$. This might explain the departure from the power-law regime observed for depth $V_\perp \lesssim 7\, E_\mathrm{R}$.
- The observation of an algebraic regime in the decay of coherences is expected from the model in Section 4.3 if the time scales Γ_sp^{-1} and t^* are well separated. This is the case for atoms in the fundamental band for $V_\perp \gtrsim 5\, E_\mathrm{R}$ but not at all for atoms in the first excited energy level (see Figure 4.21b). This goes along the previous argument for the departure from the power-law regime at small lattice depth.
- The observed rise in triply-occupied sites in the Mott insulator regime $\sim 25\, E_\mathrm{R}$ is possibly caused by atoms in the first excited energy level which can move in the lattice, the tunnelling time $\hbar/J_\perp^1$ at that depth is roughly Γ_sp^{-1}. However, in this regime, the time scales Γ_sp^{-1} and t^* are well separated and the behaviour of excited band atoms should be close to the ones in the lowest band.
- The observed atom loss might also reflect the anomalous momentum diffusion if we consider that those losses are a direct observation of the dynamics in Fock space. In this way, note the similarity between the curves for the atom loss (Figure 4.7) and the fraction of atoms at zero momentum $\mathcal{P}_{k=0}$ (Figure 4.2a). Also, the exponent characterising the atom loss (Figure 4.8a) is close to the exponent for the decay of coherences (Figure 4.4).

Refining the theory to include short-time collective effects and excited bands is very challenging. Especially for two dimensional systems for which we are not aware of a theoretical framework encompassing this problem truly for realistic system sizes. We have started a collaboration with the theory groups of Antoine Georges in Paris and Corinna Kollath in Bonn to try to understand our observations better. With this in mind, the same kind of experiments in a one-dimensional regime could be helpful to check with theory, since exact numerical tools are available for that matter, for example with density-matrix renormalisation group techniques (Verstraete et al. 2004; White et al. 2004). Such experiments are readily achieved in the experiment by raising two lattice arms to their maximal depth, thus preparing an ensemble of 1D tubes. One should then pay attention to minimise the coupling between the tubes, by choosing cleverly the polarisation of the dissipation laser for example. If light-induced dipole-dipole interactions play a significant role in the dissipation dynamics, it might then be impossible to reach a true 1D regime without preparing a single tube. A solution to this problem would then be to create the tubes with a bigger spacing. While the use of far-infrared lasers for their long wavelengths (for example CO_2 lasers) are technically challenging, one can create bigger lattice spacings using co-propagating beams with a small angle (Gross et al. 2011).

5

Theoretical approach to the relaxation dynamics in optical lattices

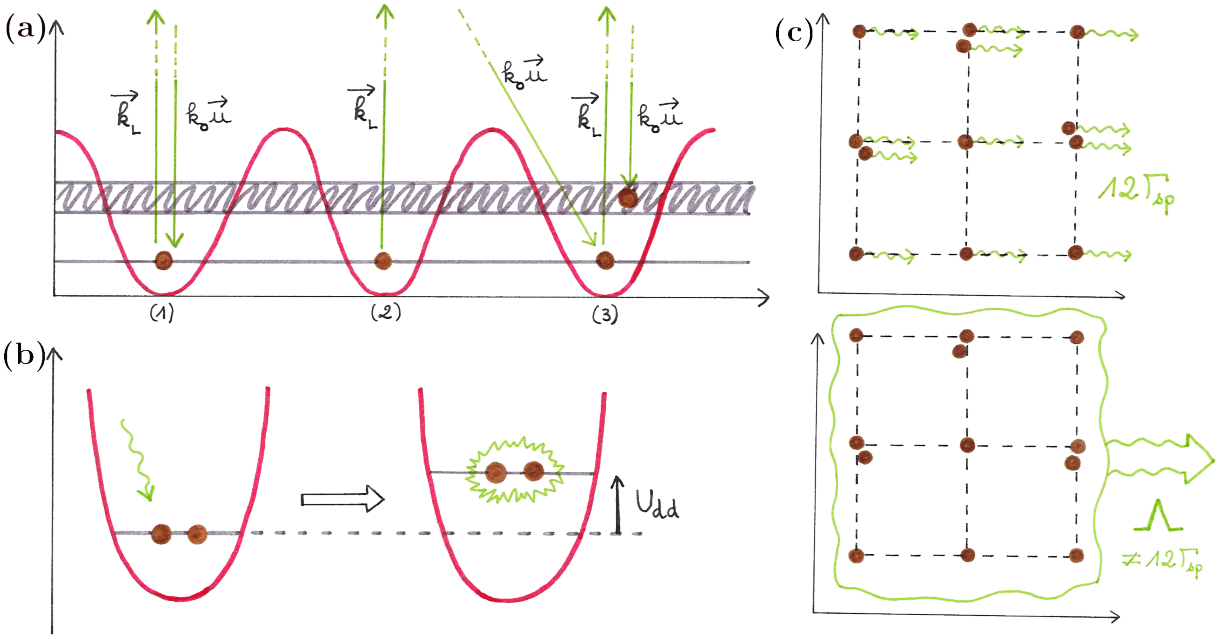

Figure 5.1: Pictorial description of various effects related to spontaneous emission in optical lattices. (a) The absorption of a laser photon (wavevector $\boldsymbol{k}_\mathrm{L}$) and its subsequent emission (wavevector $k_0\boldsymbol{u}$) can either leave an atom in place (see site 1), transfer an atom to the next site (see site 2) or promote it to another band (see site 3). (b) The absorption of a photon on a site with two atoms leads to an energy shift U_dd associated to the exchange of this photon between the two atoms, also called induced dipole-dipole interaction. (c) Spontaneous emission for independent emitters (here 12 atoms contribute to a rate $12\,\Gamma_\mathrm{sp}$) is sketched on the top. Collective emission with a rate Λ a priori different from $12\,\Gamma_\mathrm{sp}$ is sketched on the bottom. *Figure designed with Marion Bouganne.*

As presented in Chapter 4, the quantised motion of atoms subjected to spontaneous emission in optical lattices exhibits a very unusual anomalous diffusion dynamics. This diffusion dynamics was quantitatively explained and understood by a theoretical model developed in Poletti et al. (2013) where inter-particle interactions in the fundamental band play a crucial part. However, this model is only a minimal description of the very rich physics of interacting atoms excited coherently by a laser and coupled to the electromagnetic field. In this chapter, I provide a description of this problem starting from

a quantum master equation describing the coupling between the atoms and the electromagnetic field (Pichler et al. 2010). This framework allows me to characterise a number of phenomena left out in the *Poletti* model: inter-band transitions, dipole-dipole interactions or collective effects in light emission. I use this description to explain a number of our experimental observations from Chapter 4.

Firstly, I present a single-particle quantum master equation and study the inter-band transition dynamics, as well as light-induced tunnelling activated by absorption-spontaneous emission cycles. Secondly, I generalise the treatment to many atoms, providing a many-body quantum master equation. This equation allows me to calculate the magnitude of light-induced dipole-dipole interactions, leading to a shift of the on-site interaction energy and to weak nearest-neighbour interaction. It also allows me to calculate the importance of collective effects in the spontaneous emission rate. Finally, I compare the theoretical predictions to our experimental observations and conclude the study by highlighting the issues that remain open.

5.1 Theoretical description of spontaneous emission by a two-level atom: the quantum optical master equation

In this introductory section, I first consider a single atom (or a collection of non-interacting ones) subjected to spontaneous emission in an optical potential. The goal is to justify the expression of the master equation given in (5.14) and used in Section 5.2. The treatment is generalised to the case of interacting atoms in Section 5.3.

5.1.1 Quantum theory of relaxation: the quantum master equation

Here we first provide a concise account of the general theoretical framework. In order to derive a useful equation of motion for a quantum system undergoing dissipation, we distinguish a *system of interest* {the atom} from the other degrees of freedom grouped in an *environment* or *reservoir* {the electro-magnetic field}. The unitary evolution of both sub-systems, when isolated from each other is described by the Hamiltonian $\hat{H}_0$; we also consider a coupling operator $\hat{V}$ linking them. The exact equation of motion for the total density matrix $\tilde{\rho}_{\mathrm{tot}}$, written in the *interaction picture* with respect to $\hat{H}_0$ (operators in this picture are denoted with a tilde instead of a hat), is given by an integro-differential equation (Cohen-Tannoudji et al. 1992)

$$\frac{\mathrm{d}\tilde{\rho}_{\mathrm{tot}}}{\mathrm{d}t} = \frac{1}{\mathrm{i}\hbar}\left[\tilde{V}(t), \tilde{\rho}_{\mathrm{tot}}(0)\right] - \frac{1}{\hbar^2}\int_0^t \mathrm{d}t' \left[\tilde{V}(t), \left[\tilde{V}(t'), \tilde{\rho}_{\mathrm{tot}}(t')\right]\right]. \tag{5.1}$$

Two essential assumptions are required to derive a simpler equation for the evolution of the density matrix $\tilde{\rho}_{\mathrm{s}}$ of the system of interest only:

- the first assumption is the factorisation of the total density matrix at all times $\tilde{\rho}_{\mathrm{tot}} \approx \tilde{\rho}_{\mathrm{s}} \otimes |\varnothing\rangle\langle\varnothing|_{\mathrm{R}}$, where $|\varnothing\rangle_{\mathrm{R}}$ is the vacuum state of the reservoir. This amounts to neglecting the correlations between the atom and the reservoir, a detailed discussion of this approximation is given in Cohen-Tannoudji et al. (1992);

- the second assumption is the Born-Markov approximation, which allows to calculate a *coarse-grained* speed of variation for $\tilde{\rho}_\mathrm{s}$ which we use to approach $\mathrm{d}\tilde{\rho}_\mathrm{s}/\mathrm{d}t$ (Cohen-Tannoudji et al. 1992).

These two assumptions lead to the general form of the master equation written in the interaction picture,

$$\frac{\mathrm{d}\tilde{\rho}_\mathrm{s}}{\mathrm{d}t} = -\frac{1}{\hbar^2}\int_0^{+\infty}\mathrm{d}\tau\,\mathrm{Tr}_\mathrm{R}\left\{\tilde{V}(t)\tilde{V}(t-\tau)\left[\tilde{\rho}_\mathrm{s}(t)\otimes|\varnothing\rangle\langle\varnothing|_\mathrm{R}\right] + \left[\tilde{\rho}_\mathrm{s}(t)\otimes|\varnothing\rangle\langle\varnothing|_\mathrm{R}\right]\tilde{V}(t-\tau)\tilde{V}(t)\right\}$$
$$+\frac{1}{\hbar^2}\int_0^{+\infty}\mathrm{d}\tau\,\mathrm{Tr}_\mathrm{R}\left\{\tilde{V}(t)\left[\tilde{\rho}_\mathrm{s}(t)\otimes|\varnothing\rangle\langle\varnothing|_\mathrm{R}\right]\tilde{V}(t-\tau) + \tilde{V}(t-\tau)\left[\tilde{\rho}_\mathrm{s}(t)\otimes|\varnothing\rangle\langle\varnothing|_\mathrm{R}\right]\tilde{V}(t)\right\}, \tag{5.2}$$

with the partial traces taken over the degrees of freedom of the reservoir.

The first line of (5.2) describes the decay of the populations and coherences and represent *departure* terms labelled $\tilde{A}$. The second line describes the growth of the populations and coherences and represent *feeding* terms labelled $\tilde{B}$. We write (5.2) with the new notations

$$\frac{\mathrm{d}\tilde{\rho}_\mathrm{s}}{\mathrm{d}t} = -(\tilde{A}\tilde{\rho}_\mathrm{s} + \tilde{\rho}_\mathrm{s}\tilde{A}^\dagger) + \tilde{B}[\tilde{\rho}_\mathrm{s}]. \tag{5.3}$$

5.1.2 Hamiltonian and notations

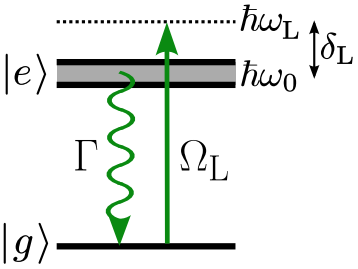

Figure 5.2: Sketch of the internal atomic structure.

The internal atomic structure is taken identical to the experimental situation in Chapter 4: a $J = 0$ ground state $|g\rangle$ with zero energy and a $J = 1$ excited state manifold $|e_m\rangle$ ($m = 0, \pm 1$) with energy $\hbar\omega_0$ and width $\hbar\Gamma$ (as depicted in Figure 5.2). The Hamiltonian $\hat{H}_0$ of the uncoupled {atom, electro-magnetic field} system is

$$\hat{H}_0 = \hat{H}_\mathrm{em} + \hat{H}_\mathrm{at}. \tag{5.4}$$

$\hat{H}_\mathrm{em}$ describes the electro-magnetic field vacuum, a bath of harmonic oscillators. Each mode μ of the electro-magnetic field is specified by a wavevector $\boldsymbol{k}_\mu$ and a polarisation vector $\boldsymbol{\varepsilon}_\mu \perp \boldsymbol{k}_\mu$. The annihilation operator for a photon in mode μ is $\hat{a}_\mu$ and $\hat{H}_\mathrm{em}$ is given by:

$$\hat{H}_\mathrm{em} = \sum_\mu \hbar\omega_\mu \hat{a}_\mu^\dagger \hat{a}_\mu. \tag{5.5}$$

$\hat{H}_\mathrm{at}$ refers to the atom and comprises a motional part describing the external degrees of freedom and an internal part describing the internal degrees of freedom:

$$\hat{H}_\mathrm{at} = \hat{H}_\mathrm{motion} + \hat{H}_\mathrm{intern}. \tag{5.6}$$

We work in a first quantised formalism where the external degrees of freedom of the atom are described by the position and momentum operators $\hat{\boldsymbol{R}}$, $\hat{\boldsymbol{P}}$. The motional Hamiltonian is given by

$$\hat{H}_\mathrm{motion} = \frac{\hat{\boldsymbol{P}}^2}{2M} + V_\mathrm{opt}(\hat{\boldsymbol{R}}), \tag{5.7}$$

where V_opt is a spatially dependent optical potential. The internal Hamiltonian is

$$\hat{H}_\mathrm{intern} = \hbar\omega_0 \hat{P}_e, \tag{5.8}$$

with $\hat{P}_e = \sum_m |e_m\rangle\langle e_m|$ the projector on the excited state manifold.

5.1.3 Atom-light interaction

Vacuum field

Here we follow the well-established treatment in quantum optics, making the dipolar-electric approximation[1] in the Coulomb gauge (Cohen-Tannoudji et al. 1992). The atoms and the electro-magnetic field are coupled by a dipolar-electric Hamiltonian

$$\hat{V}_{\text{vac}} = -\hat{\boldsymbol{D}} \cdot \hat{\boldsymbol{E}}_{\perp}. \tag{5.9}$$

$\hat{\boldsymbol{D}}$ is the electric dipole operator with components

$$\hat{D}_m = d|e_m\rangle\langle g| + d|g\rangle\langle e_m|, \tag{5.10}$$

with d the dipole matrix element of the transition. In the Coulomb gauge, the interaction involves the transverse component of the electric field,

$$\hat{\boldsymbol{E}}_{\perp} = \mathrm{i}\sum_{\mu} E_{\mu}\boldsymbol{\varepsilon}_{\mu}\mathrm{e}^{\mathrm{i}\boldsymbol{k}_{\mu}\cdot\hat{\boldsymbol{R}}}\hat{a}_{\mu} + \text{h.c.}, \tag{5.11}$$

with $E_{\mu} = \sqrt{\hbar\omega_{\mu}/(2\epsilon_0 L^3)}$. Here L is the size of the box with periodic boundary conditions containing the system of interest, chosen much larger than all other relevant length scales in the problem.

Laser field

We also consider the coupling with a near-resonant laser light field, taken as a plane wave for simplicity, with frequency ω_{L} and wavevector $\boldsymbol{k}_{\text{L}}$. The laser detuning from the atomic transition is $\delta_{\text{L}} = \omega_{\text{L}} - \omega_0$. The laser polarisation $\boldsymbol{\varepsilon}_{\text{L}}$ is linear along the quantisation axis so that only the π-transition from $|g\rangle$ to $|e_0\rangle$ is excited. The coupling operator is

$$\hat{V}_{\text{las}} = \frac{\hbar\Omega_{\text{L}}}{2}\mathrm{e}^{\mathrm{i}(\boldsymbol{k}_{\text{L}}\cdot\hat{\boldsymbol{R}}-\omega_{\text{L}}t)}|e_0\rangle\langle g| + \text{h.c.}, \tag{5.12}$$

where Ω_{L} is the Rabi frequency quantifying the coupling. The quantum field generated by the laser is described to a very good approximation by a coherent state. Here we only consider its mean value because the number of photons in this mode is very large compared to one, and corrections for that matter due to quantum fluctuations are negligible.

5.1.4 Single-particle master equation

We want to derive a master equation for the dynamics of an atom driven by a laser field, in addition to its coupling with the electro-magnetic field vacuum. We perform a Mollow transformation (Mollow 1975), which amounts to considering the external electro-magnetic field as a product of a coherent state with a large number of photons and vacuum in the other modes. The evolution due to the interaction of the atom with laser photons

[1] We focus on physical processes happening on a length-scale set by the photon wavelength and we disregard the dynamics happening on the scale of the atom, except for the matter of the dipole transition of interest.

is given by $[\hat{V}_{\text{las}}, \hat{\rho}_{\text{s}}]/(\text{i}\hbar)$, and the relaxation due to the interaction $\hat{V}_{\text{vac}}$ with the electromagnetic field vacuum is given by (5.2). In the *Schrödinger picture* the master equation takes the form[2]

$$\frac{\text{d}\hat{\rho}_{\text{s}}}{\text{d}t} = \frac{1}{\text{i}\hbar}\left[\hat{H}_{\text{at}} + \hat{V}_{\text{las}}, \hat{\rho}_{\text{s}}\right] - (\hat{A}\hat{\rho}_{\text{s}} + \hat{\rho}_{\text{s}}\hat{A}^{\dagger}) + \hat{B}[\hat{\rho}_{\text{s}}], \tag{5.13}$$

where the explicit forms of the departure and feeding terms are given in Appendix C.3.

5.1.5 Adiabatic elimination for small saturation

The density matrix $\hat{\rho}_{\text{s}}$ describes both motional and internal degrees of freedom of the atom. As such we can split the internal description into reduced matrices describing the external dynamics of the populations $\hat{\rho}_{\text{s}}|_{gg}$, $\hat{\rho}_{\text{s}}|_{ee}$ and coherences $\hat{\rho}_{\text{s}}|_{eg} = \hat{\rho}_{\text{s}}^{\dagger}\big|_{ge}$.

The laser detuning from the atomic transition $\delta_{\text{L}} = \omega_{\text{L}} - \omega_0$ is chosen such that the saturation parameter $s = \Omega_{\text{L}}^2/(2\delta_{\text{L}}^2 + \Gamma^2/2)$ is much smaller than one. In that case, the excited state population is negligible ($\hat{\rho}_{\text{s}}|_{ee} \ll \hat{\rho}_{\text{s}}|_{gg}$) and the coherences $\hat{\rho}_{\text{s}}|_{eg}$ between the excited and the ground states evolve much faster than the ground state population $\hat{\rho}_{\text{s}}|_{gg}$. This allows us to assume that the coherences and population of the excited state reach their *steady-state* value much faster than the ground state population. These steady-state values are calculated assuming constant ground state variables and then injected in the equations describing the time evolution of $\hat{\rho} = \hat{\rho}_{\text{s}}|_{gg}$. As a result the coherences and population of the excited state adiabatically follow the time evolution of the slower variables, this procedure is known as 'adiabatic elimination' of the excited state (Cohen-Tannoudji et al. 1992).

With this procedure the master equation (5.13) for $\hat{\rho}_{\text{s}}$ can be simplified in a master equation for $\hat{\rho}_{\text{s}}|_{gg}$, giving the time evolution of the external degrees of freedom of the atom in the ground state only (Pichler et al. 2010). The single-particle master equation takes on the form:

$$\frac{\text{d}\hat{\rho}}{\text{d}t} = \frac{1}{\text{i}\hbar}\left(\hat{H}_{\text{eff}}\hat{\rho} - \hat{\rho}\hat{H}_{\text{eff}}^{\dagger}\right) + \Gamma_{\text{sp}}\int \text{d}^2u\, N(\boldsymbol{u})\text{e}^{\text{i}(\boldsymbol{k}_{\text{L}} - k_0\boldsymbol{u})\cdot\hat{\boldsymbol{R}}}\hat{\rho}\text{e}^{-\text{i}(\boldsymbol{k}_{\text{L}} - k_0\boldsymbol{u})\cdot\hat{\boldsymbol{R}}}, \tag{5.14}$$

$$\Gamma_{\text{sp}} = \Gamma\frac{s}{2}, \tag{5.15}$$

$$\hat{H}_{\text{eff}} = \hat{H}_{\text{motion}} - \text{i}\hbar\frac{\Gamma_{\text{sp}}}{2}, \tag{5.16}$$

$$N(\boldsymbol{u}) = \frac{3}{8\pi}[1 - (\boldsymbol{u}\cdot\boldsymbol{\varepsilon}_{\text{L}})^2]. \tag{5.17}$$

N is the normalised directional factor for spontaneous emission ($\int \text{d}^2u\, N(\boldsymbol{u}) = 1$).

Lindblad form Such a master equation, describing the time evolution of a reduced system under its coupling to an environment can be generally written in the Lindblad form[3] (Haroche et al. 2006). This can be done here using the quantum jump operators $\hat{C}(\boldsymbol{u}) = \text{e}^{\text{i}(\boldsymbol{k}_{\text{L}} - k_0\boldsymbol{u})\cdot\hat{\boldsymbol{R}}}$. With this (5.14) can be rewritten as:

$$\frac{\text{d}\hat{\rho}}{\text{d}t} = \frac{1}{\text{i}\hbar}\left[\hat{H}_{\text{motion}}, \hat{\rho}\right] + \Gamma_{\text{sp}}\int \text{d}^2u\, N(\boldsymbol{u})\left\{\hat{C}(\boldsymbol{u})\hat{\rho}\hat{C}^{\dagger}(\boldsymbol{u}) - \frac{1}{2}\hat{C}^{\dagger}(\boldsymbol{u})\hat{C}(\boldsymbol{u})\hat{\rho} - \frac{1}{2}\hat{\rho}\hat{C}^{\dagger}(\boldsymbol{u})\hat{C}(\boldsymbol{u})\right\}. \tag{5.18}$$

[2] In the derivation of (5.13), we neglected the contribution of the photon recoil and of the Doppler effect, which amounts to considering that all photons are emitted at a frequency $\omega \approx \omega_0 = ck_0$.

[3] See Appendix B.1 for a reminder of the derivation of this equation.

The reduced system time evolution is given by the unitary evolution under the Hamiltonian $\hat{H}_{\text{motion}}$ and the occurrence of quantum jumps captured by the jump operators $\hat{C}$ describing the change in motional state after an absorption-spontaneous emission cycle. This master equation is used in the theoretical description of laser cooling (Dalibard et al. 1985) and we already introduced it to describe momentum diffusion in Chapter 4.

5.2 Dissipative dynamics of a single atom in an optical lattice

In this section, I apply the single-particle master equation (5.14) to derive predictions for the time evolution of an atom subjected to spontaneous emission in an optical lattice. I first introduce the Lamb-Dicke regime of tight trapping. I then explore the dynamics in a simple one-dimensional lattice, where I show the expected time dependence of position/momentum diffusion. I then show the importance of inter-band transitions and extend the calculation to the more realistic 3D case to provide quantitative predictions on the band population time evolution. I finally calculate tunnelling matrix elements induced by the interaction with the near-resonant light.

5.2.1 Suppression of momentum recoil for tight trapping

The effects of spontaneous emission on the momentum of an atom can be strongly altered by the presence of a trapping potential. I first introduce the Lamb-Dicke regime in the simpler case of the harmonic potential, then I discuss what changes when the atom is trapped in an optical lattice.

Harmonic trap and Lamb-Dicke regime

Here we consider the case of an atom trapped in a 1D harmonic potential with trapping frequency ω_{ho}. The atom is illuminated by a resonant laser field. In the regime where $\omega_{\text{ho}} \ll \Gamma$, the quantised mode structure of the atom in the trap can be neglected and the situation is not very different from the free space treatment characterised by a Brownian diffusion in momentum space (Wineland et al. 1979). The situation in the opposite limit of tight-trapping changes radically. When $\omega_{\text{ho}} \gg \Gamma$, the motional states of the trapped atom are well-resolved in the excitation spectrum. The square of the matrix element $\langle n| \, \mathrm{e}^{\mathrm{i}k_0\hat{x}} \, |0\rangle$ describing the laser-induced coupling between the ground state $|0\rangle$ and an excited motional state $|n\rangle$ is

$$\mathcal{L}_{\text{ho}}^{0\leftrightarrow n} = |\, \langle n| \, \mathrm{e}^{\mathrm{i}k_0\hat{x}} \, |0\rangle \, |^2 = \mathrm{e}^{-\eta^2} \frac{\eta^{2n}}{n!}. \tag{5.19}$$

The parameter describing the 'binding strength' is the so-called Lamb-Dicke parameter $\eta = k_0\sigma_{\text{ho}}/\sqrt{2}$, with the harmonic oscillator length $\sigma_{\text{ho}} = \sqrt{\hbar/(M\omega_{\text{ho}})}$ (Wineland et al. 1979). In the Lamb-Dicke regime, where $\eta \ll 1$, the transitions for which the motional state changes are strongly suppressed: $\mathcal{L}_{\text{ho}}^{0\leftrightarrow n}/\mathcal{L}_{\text{ho}}^{0\leftrightarrow 0} = \eta^{2n}/n! \ll 1$ for $n > 0$ (see Figure 5.3). Therefore, spontaneous emission does not modify the motional degrees of freedom of a tightly-trapped particle, leading to a *recoil-free* spontaneous emission.

This phenomenon is very similar to the Mössbauer effect in nuclear physics in which the nucleus of an atom in a crystal can be probed without recoil, the photon momentum

being absorbed by the crystal as a whole. The Lamb-Dicke regime is paramount for laser cooling and was successfully used to cool down ions to the motional ground state in linear Paul traps (Diedrich et al. 1989; Monroe et al. 1995), and later with neutral atoms in deep 1D optical lattices (Perrin et al. 1998; Vuletić et al. 1998).

Optical lattices

In the limit of infinitely deep optical lattices, one recovers the case of a tight harmonic trap [see (1.14)in Section 1.2]. For finite lattice depths however, and even in a regime described by a tight-binding Hubbard Hamiltonian, the harmonic trap approximation can be dubious. The recoil due to absorption-spontaneous emission processes can transfer atoms from the lowest band of the lattice to higher bands (provided Γ is much larger than the band gaps). In optical lattices, localised states are described by Wannier functions w which do not have direct analytical expressions (see Section 1.2). We compute numerically the factor $\mathcal{L}$ defined in one-dimension by the square of a matrix element

$$\mathcal{L}^{n\leftrightarrow m} = \left|\langle w_0^m(x)|\, \mathrm{e}^{\mathrm{i}k_0\hat{x}}\, |w_0^n(x)\rangle\right|^2, \tag{5.20}$$

where n, m are the band indices. In sufficiently deep lattices, above a few recoil energies, the Wannier functions are exponentially localised so that matrix elements between neighbouring sites of the type $\left|\langle w_1^m(x)|\, \mathrm{e}^{\mathrm{i}k_0\hat{x}}\, |w_0^n(x)\rangle\right|^2$ are suppressed and negligible. Figure 5.3a shows the comparison between the Lamb-Dicke factors $\mathcal{L}^{0\leftrightarrow n}$ and the harmonic oscillator case $\mathcal{L}_{\mathrm{ho}}^{0\leftrightarrow n}$. The agreement is excellent for deep lattices but substantial deviations arise for depths smaller than ten recoil energies, which correspond to the regime of the experiments presented in Chapter 4. In particular, the ratio $\mathcal{L}^{0\leftrightarrow 1}/\mathcal{L}^{0\leftrightarrow 0}$ is higher in an optical lattice than in the harmonic oscillator case.

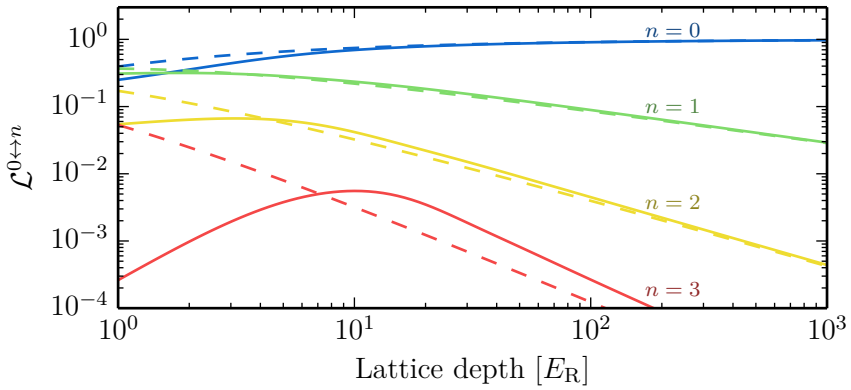

Figure 5.3: Lamb-Dicke factors $\mathcal{L}^{0\leftrightarrow n}$ for a 1D sinusoidal potential (solid lines) calculated from (5.20), and $\mathcal{L}_{\mathrm{ho}}^{0\leftrightarrow n}$ for a harmonic oscillator potential (dashed line) calculated from (5.19).

Lamb-Dicke factors

Due to the anisotropy of the optical lattice used in Chapter 4, we numerically computed the Lamb-Dicke factors $\mathcal{L}^{n\leftrightarrow m}$ as defined previously for both the vertical direction z and the horizontal directions $\perp$. The results are given in Table 5.1. None of the Lamb-Dicke parameters $\mathcal{L}^{0\leftrightarrow 1}$ are very small compared to one. We thus expect inter-band transitions

to occur over a time scale of a few $\Gamma_{\mathrm{sp}}^{-1}$, in line with the observations of the last chapter (see Section 4.4.3).

Direction	Depth $[E_{\mathrm{R}}]$	$\mathcal{L}^{0\leftrightarrow 0}$	$\mathcal{L}^{0\leftrightarrow 1}$	$\mathcal{L}^{0\leftrightarrow 1}/\mathcal{L}^{0\leftrightarrow 0}$
z	27	0.82	0.16	0.2
$\perp$	3.5	0.48	0.30	0.6
$\perp$	13	0.73	0.22	0.3

Table 5.1: Lamb-Dicke factors for the relevant lattice depths explored in the experiments presented in last chapter.

5.2.2 Inter-band transitions in a 1D optical lattice

The previous discussion suggests that inter-band transitions cannot be ignored. We thus look at the dynamics of a single atom using the Bloch basis to explore the time-evolution of the bands population. We apply the master equation (5.14) to the example of an atom moving in a 1D optical lattice with period d:

$$\hat{H}_{\mathrm{motion}} = \frac{\hat{P}_x^2}{2M} + V_0 \sin^2\left(\frac{\pi \hat{x}}{d}\right). \tag{5.21}$$

We note $|n,q\rangle$ the Bloch waves in the 1D lattice for band n and quasi-momentum q. We are interested in the evolution of the populations in this basis:

$$\Pi_q^n = \langle n,q|\,\hat{\rho}\,|n,q\rangle\,. \tag{5.22}$$

We project (5.14) on the Bloch waves basis to obtain the time evolution of the populations:

$$\frac{\mathrm{d}\Pi_q^n}{\mathrm{d}t} = -\Gamma_{\mathrm{sp}}\Pi_q^n + \Gamma_{\mathrm{sp}}\int \mathrm{d}^2u\, N(\boldsymbol{u})\,\langle n,q|\,\mathrm{e}^{-\mathrm{i}(k_0\boldsymbol{u}-\boldsymbol{k}_L)\cdot\hat{\boldsymbol{R}}}\hat{\rho}\mathrm{e}^{\mathrm{i}(k_0\boldsymbol{u}-\boldsymbol{k}_L)\cdot\hat{\boldsymbol{R}}}\,|n,q\rangle\,, \tag{5.23}$$

where we used the fact that the Bloch waves are eigenvectors of the motional Hamiltonian, i.e. $\langle n,q|\,[\hat{H}_{\mathrm{motion}},\hat{\rho}]\,|n,q\rangle = 0$. The atom is compelled to move in one space dimension x and we define a reduced directional factor integrated over the two perpendicular directions y, z:

$$N'(u_x) = \frac{3}{8}\left(u_x^2+1\right)\Theta\left[1-|u_x|\right], \tag{5.24}$$

with the normalisation $\int \mathrm{d}u_x\, N'(u_x) = 1$ and where Θ is the Heaviside step function. Equation (5.23) becomes

$$\frac{\mathrm{d}\Pi_q^n}{\mathrm{d}t} = -\Gamma_{\mathrm{sp}}\Pi_q^n + \Gamma_{\mathrm{sp}}\int \mathrm{d}u\, N'(u)\,\langle n,q|\,\mathrm{e}^{-\mathrm{i}k_0u\hat{x}}\hat{\rho}\mathrm{e}^{\mathrm{i}k_0u\hat{x}}\,|n,q\rangle\,. \tag{5.25}$$

The first term in (5.25) is a departure from the state $|n,q\rangle$ after absorption of a photon, it gives an exponential-like decay. The second term describes the feeding from other Bloch waves $|n',q'\rangle \neq |n,q\rangle$ due to spontaneous emission. We now introduce the matrix elements α given by:

$$\alpha_{q,q'}^{n,n'}(k) = \langle n',q'|\,\mathrm{e}^{\mathrm{i}k\hat{x}}\,|n,q\rangle\,, \tag{5.26}$$

for which an explicit expression is provided in Appendix C.1.1. Inserting two resolutions of identity in (5.25) leads to

$$\frac{\mathrm{d}\Pi_q^n}{\mathrm{d}t} = -\Gamma_{\mathrm{sp}}\Pi_q^n + \Gamma_{\mathrm{sp}} \int \mathrm{d}u\, N'(u) \sum_{n_1,n_2} \int \mathrm{d}q_1 \mathrm{d}q_2 \, \left[\alpha_{q,q_2}^{n,n_2}(k_0 u)\right]^* \alpha_{q,q_1}^{n,n_1}(k_0 u) \left\langle n_2, q_2\right| \hat{\rho} \left|n_1, q_1\right\rangle . \tag{5.27}$$

The product of the matrix elements α does not vanish if and only if $q_1 = q_2$ (see Appendix C.1.2 for a proof), which stems from momentum conservation. Additionally, we make the approximation that coherences between different bands of the lattice can be neglected

$$\left\langle n_2, q'\right| \hat{\rho} \left|n_1, q'\right\rangle \approx \Pi_{q'}^{n_1} \delta_{n_1,n_2}. \tag{5.28}$$

Such a secular approximation (Cohen-Tannoudji et al. 1992) is safe because: (i) the initial state is in the fundamental band with zero initial coherences, (ii) coherences created by spontaneous emission are small and decay much more rapidly than populations. We then have a simplified master equation:

$$\frac{\mathrm{d}\Pi_q^n}{\mathrm{d}t} \approx -\Gamma_{\mathrm{sp}}\Pi_q^n + \Gamma_{\mathrm{sp}} \sum_{n'} \int \mathrm{d}q'\, \Pi_{q'}^{n'} \int \mathrm{d}u\, N'(u) \left|\alpha_{q,q'}^{n,n'}(k_0 u)\right|^2 \tag{5.29}$$

$$= -\Gamma_{\mathrm{sp}}\Pi_q^n + \Gamma_{\mathrm{sp}} \sum_{n'} \int \mathrm{d}q'\, \Pi_{q'}^{n'} \beta_{q,q'}^{n,n'} . \tag{5.30}$$

The set of differential equations (5.30) forms a closed set for the populations, which can be numerically integrated. Extending the result from Appendix C.1.1 concerning $\alpha_{q,q'}^{n,n'}$, the normalised rates $\beta_{q,q'}^{n,n'}$ ensure momentum conservation and band transfer (in the tight-binding limit we have $\beta_{q,q'}^{n,n'} \propto \mathcal{L}^{n\leftrightarrow n'}$). In the following we restrict our discussion of the 1D case to a short times expansion where an analytical result can be obtained. Integration for longer times is performed in the 3D case in Section 5.2.3.

Short times expansion

The atom is initially prepared in the lowest Bloch band of the lattice $\Pi_q^n(0) = \Pi_0 \delta_{0,n} \delta^{(1)}(q)$. We can calculate the evolution of the populations perturbatively, at short times, replacing Π_q^n by its initial value on the right-hand-side of (5.30):

$$\Pi_q^n(t) \approx \Pi_0 \delta_{0,n} \delta^{(1)}(q)(1 - \Gamma_{\mathrm{sp}} t) + \Pi_0 \beta_{q,0}^{n,0} \Gamma_{\mathrm{sp}} t. \tag{5.31}$$

The normalised rate of transfer $\beta_q^n = \beta_{q,0}^{n,0}$ to the state $|n, q\rangle$ is given by the integral:

$$\beta_q^n = \int_{-1}^{1} \mathrm{d}u\, \frac{3}{8}(u^2+1) \left|\alpha_{q,0}^{n,0}(k_0 u)\right|^2 . \tag{5.32}$$

Figure 5.4a shows β_q^n for $V_0 = 10\, E_{\mathrm{R}}$. The transfer rate to higher bands follows the expectation from Lamb-Dicke factors (see Figure 5.3), in particular excitation to the first band is substantial. Strong redistribution in quasi-momentum space following from momentum conservation is observed.

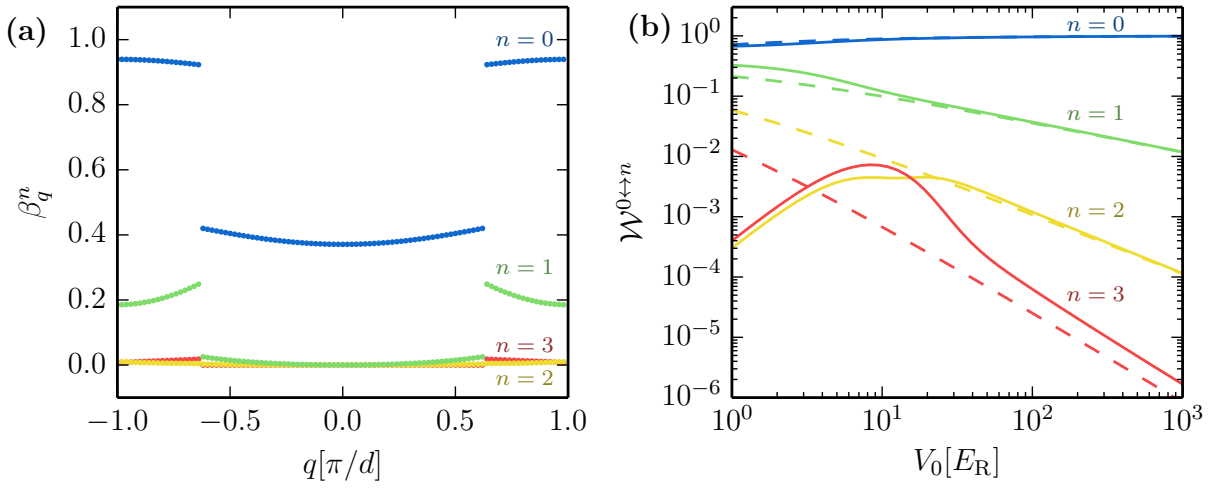

Figure 5.4: 1D lattice with orthogonal dissipation laser wavevector and polarisation. (a) Initial normalised rate of change β_q^n [defined in (5.32)] of the population Π_q^n for a lattice depth $V_0 = 10\,E_R$. The observed discontinuities are due to the folding in quasi-momentum space. Indeed, spontaneous emission redistributes momentum on an interval with extremal values $\pm k_0$, which are bigger than the first Brillouin zone. In quasi-momentum space, this results in a folding of the emission spectrum. Discontinuities exactly happen at the folding values $\pm k_0 \mp 2\pi/d$ (or $q \approx \pm 0.63\pi/d$). (b) Integrated matrix elements $\mathcal{W}^{0\leftrightarrow n}$ [defined in (5.33)] for the first four bands. The dashed lines are the predictions $\mathcal{W}_{\text{ho}}^{0\leftrightarrow n}$ [defined in (5.34)] for the harmonic oscillator case.

Transfer rates

We can compare our numerical estimation of the matrix elements α with the exact values known for a harmonic oscillator (see the discussion in Section 5.2.1). The integrated transfer rate from band 0 to band n in an optical lattice is given by:

$$\mathcal{W}^{0\leftrightarrow n} = \int \mathrm{d}q\, \beta_q^n = \int \mathrm{d}q \int_{-1}^{1} \mathrm{d}u\, \frac{3}{8}(1+u^2) \left|\alpha_{q,0}^{n,0}(k_0 u)\right|^2 . \tag{5.33}$$

We can compare this quantity with the expectation from the harmonic oscillator with frequency ω_{ho} and length $x_{\text{ho}} = \sqrt{\hbar/(M\omega_{\text{ho}})}$, the Lamb-Dicke parameter is $\eta = k_0 x_{\text{ho}}/\sqrt{2}$:

$$\mathcal{W}_{\text{ho}}^{0\leftrightarrow n} = \int_{-1}^{1} \mathrm{d}u\, \frac{3}{8}(1+u^2)\mathcal{L}_{\text{ho}}^{0\leftrightarrow n}(k_0 u) = \int_{-1}^{1} \mathrm{d}u\, \frac{3}{8}(1+u^2) e^{-(\eta u)^2} \frac{(\eta u)^{2n}}{n!}. \tag{5.34}$$

Figure 5.4b shows both transfer rates versus lattice depth. The agreement is excellent in the limit of high lattice depth, where the harmonic oscillator approximation is legitimate. However substantial deviations arise at low lattice depth, where the transfer rate to the first band is larger in the optical lattice case. We conclude that the Lamb-Dicke approximation is not sufficient and that band structure calculations are necessary for a precise estimation of the transfer rates.

5.2.3 Inter-band transitions in a cubic optical lattice

We now apply the master equation (5.14) to the case of an atom moving in a cubic lattice, which corresponds to our experimental situation:

$$\hat{H}_{\text{motion}} = \frac{\hat{\boldsymbol{P}}^2}{2M} + V_\perp \sin^2\left(\frac{\pi\hat{x}}{d}\right) + V_\perp \sin^2\left(\frac{\pi\hat{y}}{d}\right) + V_{0,z} \sin^2\left(\frac{\pi\hat{z}}{d}\right). \tag{5.35}$$

The near-resonant laser field illuminating the atom is a plane wave which propagates along the vertical direction and π-polarised along $\boldsymbol{e}_x + \boldsymbol{e}_y$. We note $|\boldsymbol{n}, \boldsymbol{q}\rangle$ the Bloch functions in the 3D lattice for band $\boldsymbol{n} = (n_x, n_y, n_z)$ and quasi-momentum $\boldsymbol{q} = (q_x, q_y, q_z)$. We are interested in the evolution of the populations in this basis:

$$\Pi_{\boldsymbol{q}}^{\boldsymbol{n}} = \langle \boldsymbol{n}, \boldsymbol{q}| \, \hat{\rho} \, |\boldsymbol{n}, \boldsymbol{q}\rangle \, . \tag{5.36}$$

As in the previous 1D case, we project the master equation (5.14) on the Bloch waves basis to obtain the time evolution of the populations. The same derivation applies and we also make the approximation that coherences between different bands of the lattice can be neglected. This leads to a system of differential equations for the populations:

$$\frac{\mathrm{d}\Pi_{\boldsymbol{q}}^{\boldsymbol{n}}}{\mathrm{d}t} = -\Gamma_{\text{sp}}\Pi_{\boldsymbol{q}}^{\boldsymbol{n}} + \Gamma_{\text{sp}} \sum_{\boldsymbol{n}'} \int \mathrm{d}^3q' \, \Pi_{\boldsymbol{q}'}^{\boldsymbol{n}'} \beta_{\boldsymbol{q},\boldsymbol{q}'}^{\boldsymbol{n},\boldsymbol{n}'} . \tag{5.37}$$

Integration along the vertical direction

Since we are only interested in the evolution in a plane perpendicular to the laser propagation, we can integrate over n_z and q_z. This considerably alleviates the numerical computation. Indeed, the 3D Bloch waves are given by a product of 1D Bloch waves, because of the separability of the optical potential. This extends to the β coefficients so that $\beta_{\boldsymbol{q},\boldsymbol{q}'}^{\boldsymbol{n},\boldsymbol{n}'} = \beta_{q_x,q_x'}^{n_x,n_x'} \beta_{q_y,q_y'}^{n_y,n_y'} \beta_{q_z,q_z'}^{n_z,n_z'}$. Moreover, after integration over n_z and q_z, the coefficients $\beta_{\boldsymbol{q},\boldsymbol{q}'}^{\boldsymbol{n},\boldsymbol{n}'}$ do not depend on n_z' nor q_z' any longer. This is clear with the following equality:

$$\sum_{n_z} \int \mathrm{d}q_z \, \beta_{q_z,q_z'}^{n_z,n_z'} = \sum_{n_z} \int \mathrm{d}q_z \, \langle n_z', q_z'|\mathrm{e}^{\mathrm{i}k_0(u_z-1)z}|n_z, q_z\rangle\langle n_z, q_z|\mathrm{e}^{-\mathrm{i}k_0(u_z-1)z}|n_z', q_z'\rangle = 1. \tag{5.38}$$

We now denote with an upper bar a quantity that has been integrated over n_z and q_z. The differential equation (5.37) becomes:

$$\frac{\mathrm{d}\overline{\Pi}_{\boldsymbol{q}}^{\boldsymbol{n}}}{\mathrm{d}t} = -\Gamma_{\text{sp}}\overline{\Pi}_{\boldsymbol{q}}^{\boldsymbol{n}} + \Gamma_{\text{sp}} \sum_{n_x', n_y'} \int \mathrm{d}q_x' \mathrm{d}q_y' \, \overline{\Pi}_{\boldsymbol{q}'}^{\boldsymbol{n}'} \overline{\beta}_{\boldsymbol{q},\boldsymbol{q}'}^{\boldsymbol{n},\boldsymbol{n}'} . \tag{5.39}$$

Short times expansion

The atom is initially prepared in the lowest Bloch band of the lattice $\Pi_{\boldsymbol{q}}^{\boldsymbol{n}}(0) = \Pi_0 \delta_{0,\boldsymbol{n}} \delta^{(3)}(\boldsymbol{q})$. We calculate the evolution of the populations perturbatively, replacing $\Pi_{\boldsymbol{q}}^{\boldsymbol{n}}$ by its initial value in the right-hand-side of (5.37). This gives

$$\Pi_{\boldsymbol{q}}^{\boldsymbol{n}}(t) \approx \Pi_0 \delta_{0,\boldsymbol{n}} \delta^{(3)}(\boldsymbol{q})(1 - \Gamma_{\text{sp}} t) + \Pi_0 \beta_{\boldsymbol{q},\boldsymbol{0}}^{\boldsymbol{n},\boldsymbol{0}} \Gamma_{\text{sp}} t. \tag{5.40}$$

The initial rate of change $\beta_{\boldsymbol{q}}^{\boldsymbol{n}} = \beta_{\boldsymbol{q},\boldsymbol{0}}^{\boldsymbol{n},\boldsymbol{0}}$ of the population $\Pi_{\boldsymbol{q}}^{\boldsymbol{n}}$ normalised by Γ_{sp} is given by the integral:

$$\beta_{\boldsymbol{q}}^{\boldsymbol{n}} = \int \mathrm{d}^2 u \, N(\boldsymbol{u}) \left| \alpha_{\boldsymbol{q},0}^{\boldsymbol{n},0}(k_0 \boldsymbol{u} - \boldsymbol{k}_L) \right|^2 . \tag{5.41}$$

Figure 5.5 shows the initial normalised rate of change $\overline{\beta}_{\boldsymbol{q}}^{\boldsymbol{n}}$ for $V_0 = 10\, E_{\mathrm{R}}$ and the first four horizontal energy levels. The level n corresponds to all bands (n_x, n_y) which satisfy $n = n_x + n_y$. Quasi-momentum redistribution is manifest. In contrast with the previous 1D case, quasi-momentum can now redistribute in all space directions. At short times it is given by a folded version of the spontaneous emission spherical distribution in free space. Inter-band transitions occur mostly towards the first energy level.

Longer times computation

A numerical integration of (5.39) is shown in Figure 5.6 for the first four energy levels (labelled $n = 0..3$). Some considerations on how to compute the coefficients β are given in Appendix C.1.3. Transitions to higher energy levels is manifest after a few $\Gamma_{\mathrm{sp}}^{-1}$. The short times expansion is valid up to $t \lesssim \Gamma_{\mathrm{sp}}^{-1}$.

Conclusion

The computation of inter-band transitions was best performed in the Bloch basis, which is the natural basis to describe the spectrum of the lattice problem (5.35). In this study we noted substantial transfer to the first excited energy levels, and significant quasi-momentum redistribution. Both effects strongly alter the spatial motion of the atom subjected to spontaneous emission. The study of the spatial dynamics in the tight-binding regime is best performed in the Wannier basis, which is the topic of the next paragraph.

5.2.4 Spatial diffusion in a 1D optical lattice

As a complementary analysis of the dissipative dynamics in an optical lattice, we now characterise the spatial diffusion of the atom. We thus consider a tight-binding, single band description of the optical lattice. The near-resonant laser field illuminating the atom is a plane wave which propagates perpendicularly to the lattice ($\boldsymbol{k}_{\mathrm{L}} = k_{\mathrm{L}} \boldsymbol{e}_y$) and π-polarised ($\boldsymbol{\varepsilon}_{\mathrm{L}} = \boldsymbol{e}_z$).

The Hamiltonian of the system in the Wannier basis is

$$\hat{H}_{\mathrm{motion}} = -J \sum_i |w_i^n\rangle \langle w_{i+1}^n| + \mathrm{h.c.}, \tag{5.42}$$

with J the tunnelling energy. We project the master equation (5.14) on the Wannier basis to obtain the populations and spatial coherences in the lattice, $\rho_{i,j} = \langle w_j^{n=0}| \hat{\rho} |w_i^{n=0}\rangle$. We start with an atom in the fundamental band and omit the band indices. We perform again a projection on the lattice axis $[N'(u) = 3/8(u^2+1)\Theta(1-|u|)]$:

$$\begin{aligned} \frac{\mathrm{d}\rho_{i,j}}{\mathrm{d}t} &= \frac{1}{\mathrm{i}\hbar} \langle w_j| \left[\hat{H}_{\mathrm{motion}}, \hat{\rho}\right] |w_i\rangle - \Gamma_{\mathrm{sp}} \rho_{i,j} + \Gamma_{\mathrm{sp}} \int \mathrm{d}u \, N'(u) \langle w_j| \, \mathrm{e}^{-\mathrm{i}k_0 u \hat{x}} \hat{\rho} \mathrm{e}^{\mathrm{i}k_0 u \hat{x}} |w_i\rangle \\ &\approx \frac{J}{\mathrm{i}\hbar} (\rho_{i,j\pm1} - \rho_{i\pm1,j}) - \Gamma_{\mathrm{sp}} \rho_{i,j} + \Gamma_{\mathrm{sp}} \sum_{k,l} \rho_{k,l} \int \mathrm{d}u \, N'(u) \langle w_j| \, \mathrm{e}^{-\mathrm{i}k_0 u \hat{x}} |w_l\rangle \langle w_k| \, \mathrm{e}^{\mathrm{i}k_0 u \hat{x}} |w_i\rangle . \end{aligned} \tag{5.43}$$

In the last line we have neglected feeding of the fundamental band from excited ones for simplicity. However, the decay from the fundamental band is taken into account.

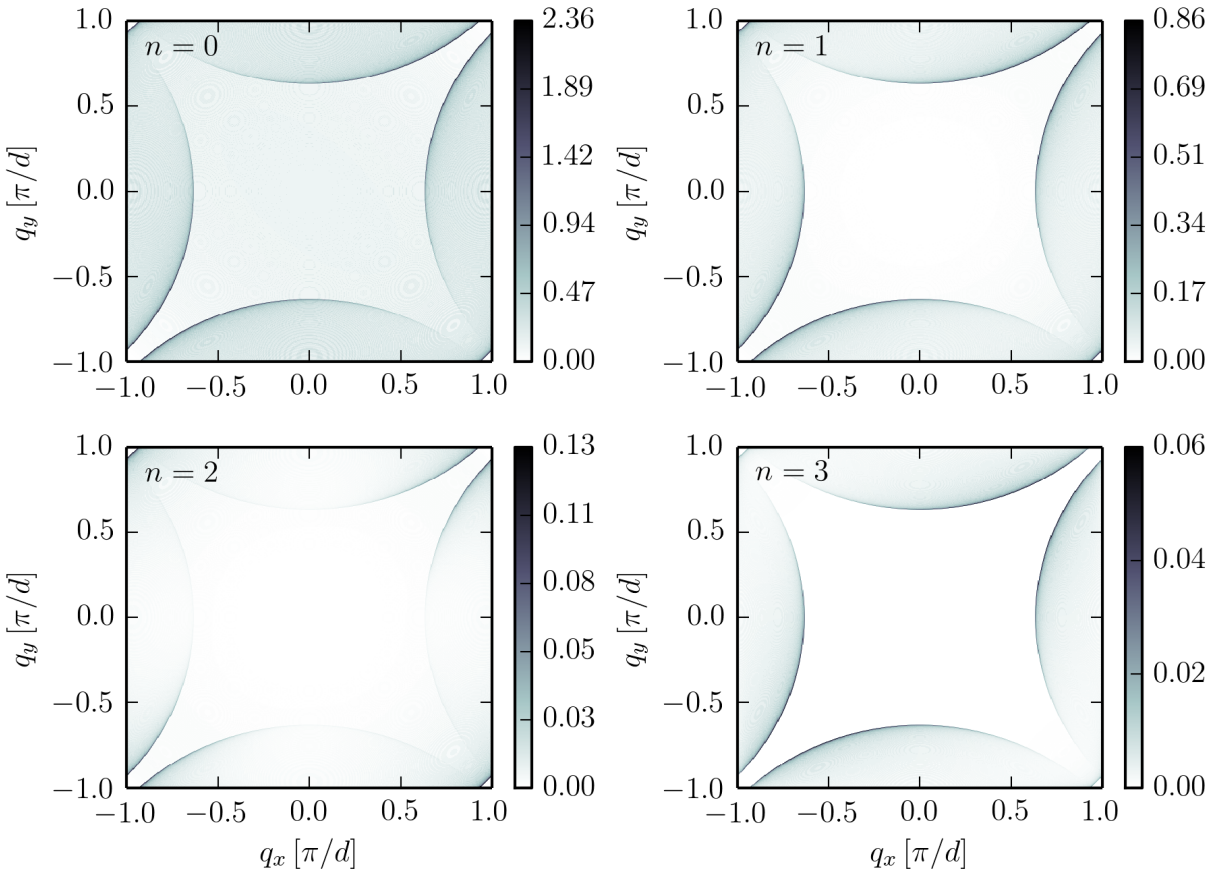

Figure 5.5: Initial rate of transfer $\overline{\beta}_{\boldsymbol{q}}^{\boldsymbol{n}}$ integrated along the vertical direction, for $V_\perp = 10\,E_\mathrm{R}$ and the first four energy levels n. The diagrams can be understood as a folded version of the spherical dipole pattern due to spontaneous emission in free space. As already mentioned in the 1D case, since $k_0 > \pi/d$, the sphere of spontaneous emission exceeds the first Brillouin zone and gets folded back on the opposite sides.

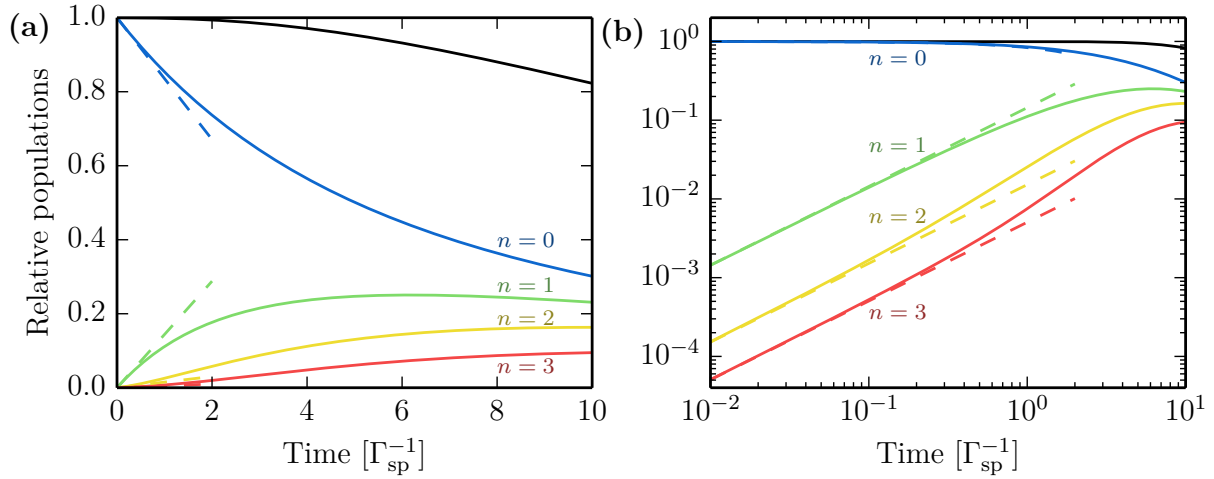

Figure 5.6: Numerical integration of (5.39), shown as solid lines, for the first four bands and $V_\perp = 10\,E_\mathrm{R}$. The black solid line indicates the total population in the first four energy levels, which decreases slightly when $t \gtrsim 5\Gamma_\mathrm{sp}^{-1}$ as higher bands get populated. The dashed lines show the computation using the short times expansion of (5.40). (a) Linear scale on both axes. (b) Logarithmic scale on both axes to zoom on the short times behaviour.

Initially localised state: spatial diffusion

We numerically solve the set of differential equations defined by (5.43) with an atom initially prepared in the center of the lattice. Numerical calculations are performed on a lattice with 64 sites with periodic boundary conditions and the Wannier basis is calculated for a lattice depth of $V_0 = 10\,E_\mathrm{R}$. The spontaneous emission rate Γ_sp is chosen equal to the tunnelling rate $J/\hbar$. In Figure 5.7, we show the result of the numerical integration[4]. In Figure 5.7a we show the time evolution of the position distribution, which broadens with time. In Figure 5.7b we show the time evolution of the variance of the position distribution Δx^2. At short times, the diffusion is dominated by a ballistic expansion due to coherent tunnelling, characterised by a quadratic dependence of Δx^2 with time. At longer times, spontaneous emission takes over and the spreading of the wave packet becomes diffusive. We retrieve the Brownian diffusion characterised by a linear dependence of Δx^2 with time.

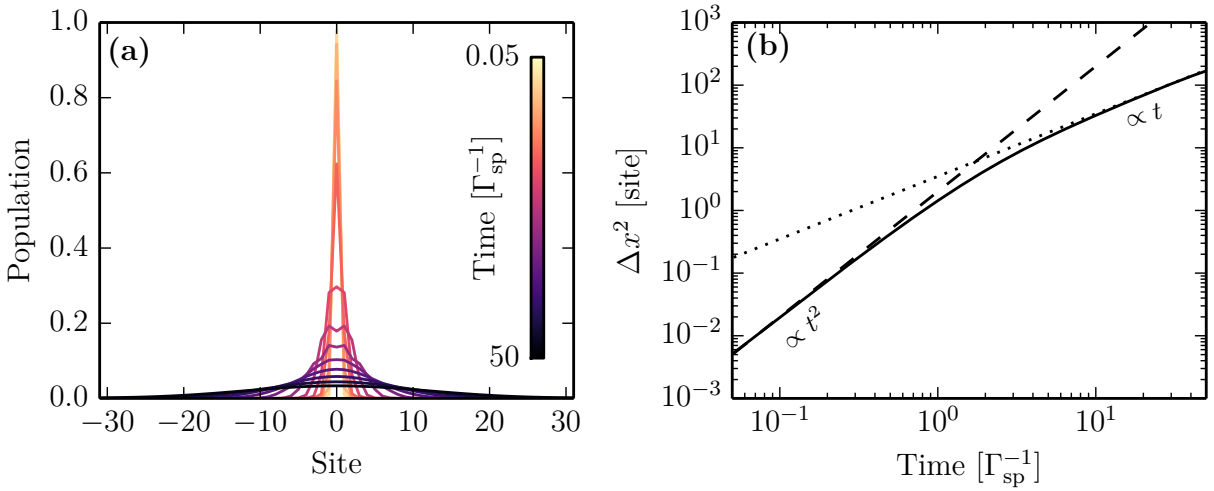

Figure 5.7: Numerical integration of (5.43) for a depth $V_0 = 10\,E_\mathrm{R}$. The atom is initially in the Wannier function of the lowest band in the centre of the lattice and $\Gamma_\mathrm{sp} = J/\hbar$. (a) Position distribution in the lattice as a function of time. (b) Time evolution of the variance of the position distribution Δx^2. At short times, the diffusion is dominated by a ballistic expansion due to coherent tunnelling, characterised by a quadratic dependence of Δx^2 with time (slope two in logarithmic scales, dashed line). At longer times, spontaneous emission comes into play and we retrieve the Brownian diffusion, characterised by a linear dependence of Δx^2 with time (slope one in logarithmic scales, dotted line).

Initially delocalised state: loss of spatial coherence

We now numerically solve (5.43) with an initial Bloch state with zero quasi-momentum and in the fundamental band, delocalised over the entire lattice. Otherwise the calculation is performed with the same parameters as before. In order to measure the coherence properties of the atom in the lattice we calculate the global spatial coherence function

$$\mathcal{F}(i) = \sum_j \rho_{j,j+i}, \tag{5.44}$$

[4]Note that after integration the position distributions are normalised to eliminate the changes due to inter-band transitions removing atoms from the fundamental band.

which is the sum of all the spatial coherences between sites separated by i sites (see Section 4.1.1). Figure 5.8 presents the results of this numerical integration. Figure 5.8a shows the time evolution of $\mathcal{F}$, the width of which shrinks with time. Figure 5.8b shows the time evolution of the coherence length ℓ_c defined as the root-mean-square width of $\mathcal{F}$. The coherence length decreases exponentially with dissipation time. In Figure 5.8c, we also show the peak amplitude $\mathcal{P}_{k=0}$ of the momentum distribution defined as the Fourier transform of $\mathcal{F}$ (see Section 4.1.1). It also exhibits an exponential decay towards zero.

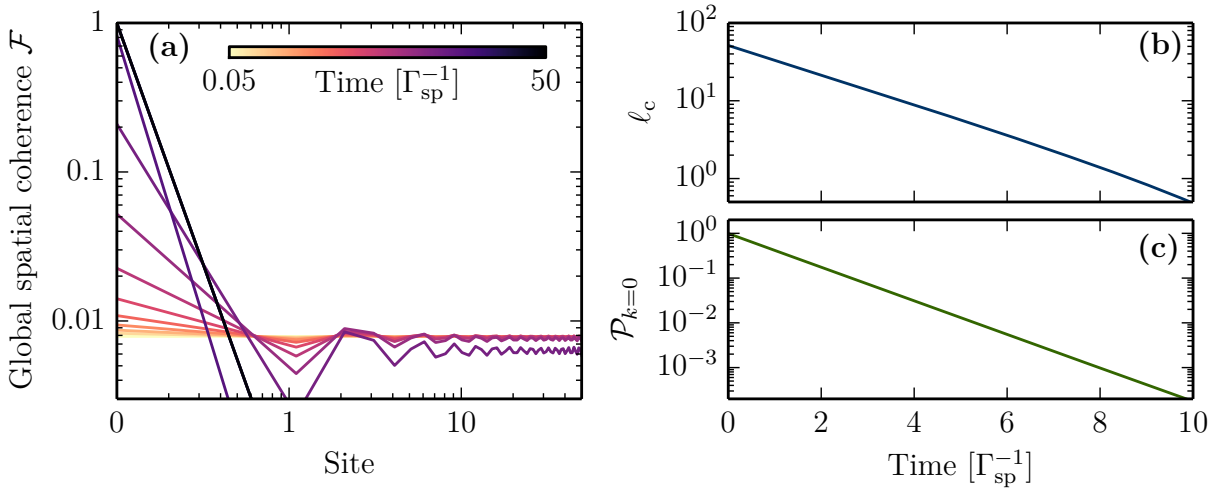

Figure 5.8: Numerical integration of (5.43) for a depth $V_0 = 10\,E_R$. The atom is initially in the $q = 0$ Bloch wavefunction of the lowest band and we choose $\Gamma_{sp} = J/\hbar$. (a) Global spatial coherence function as a function of time. (b) Time evolution of the coherence length ℓ_c of the atom in the lattice. The decay is exponential with a rate $\sim \Gamma_{sp}/2$, as can be seen by the straight line in semi-logarithmic scale. (c) Time evolution of the momentum distribution amplitude $\mathcal{P}_{k=0}$. The decay is also exponential with a rate $\sim \Gamma_{sp}$.

Conclusion

A single atom subjected to spontaneous emission in a 1D optical lattice exhibits a diffusion dynamics that is very different from the observations of the last chapter. In the study of this section we noted what follows.

- Diffusion in position is characterised by a ballistic-to-diffusive expansion crossover (see Figure 5.7).
- The loss of quantum coherences is exponential with a rate Γ_{sp}, both for the coherence length ℓ_c and the probability density at zero-momentum $\mathcal{P}_{k=0}$ (see Figure 5.8).

We believe that the extension to a 3D optical lattice would not qualitatively change these statements and the only missing ingredient in the description of our experiments is the presence of many atoms, and hence the presence of interactions.

This supports our conclusion that the experimental observation of an algebraic decay can be viewed as a piece of evidence for unconventional relaxation dynamics coming from atomic interactions.

5.2.5 Tunnelling induced by the resonant light

In this section we address the following question: can a process of absorption-spontaneous emission bring an atom from one site to another?

As was described in Chapter 1, atoms in an optical lattice move through coherent tunnelling. The Hamiltonian part describing nearest-neighbour tunnelling is:

$$\hat{T} = -\sum_{\boldsymbol{n},\langle \boldsymbol{i},\boldsymbol{j}\rangle} J_1^{\boldsymbol{n}} \left|w_{\boldsymbol{j}}^{\boldsymbol{n}}\right\rangle \left\langle w_{\boldsymbol{i}}^{\boldsymbol{n}}\right| . \tag{5.45}$$

We project the Hamiltonian part of the master equation (5.14) to obtain the evolution due to tunnelling of the population on a given site, for example the site $\mathbf{0}$, $\langle w_{\mathbf{0}}^{\boldsymbol{n}}| \hat{\rho} |w_{\mathbf{0}}^{\boldsymbol{n}}\rangle$:

$$\mathrm{i}\hbar \frac{\mathrm{d}\left\langle w_{\mathbf{0}}^{\boldsymbol{n}}\right| \hat{\rho} \left|w_{\mathbf{0}}^{\boldsymbol{n}}\right\rangle}{\mathrm{d}t}\bigg|_{\text{tunnel.}} = \left\langle w_{\mathbf{0}}^{\boldsymbol{n}}\right| \left[\hat{T}, \hat{\rho}\right] \left|w_{\mathbf{0}}^{\boldsymbol{n}}\right\rangle = \sum_{\text{n.n. } \boldsymbol{i}} -J_1^{\boldsymbol{n}} \left\langle w_{\boldsymbol{i}}^{\boldsymbol{n}}\right| \hat{\rho} \left|w_{\mathbf{0}}^{\boldsymbol{n}}\right\rangle + J_1^{\boldsymbol{n}} \left\langle w_{\mathbf{0}}^{\boldsymbol{n}}\right| \hat{\rho} \left|w_{\boldsymbol{i}}^{\boldsymbol{n}}\right\rangle . \tag{5.46}$$

Within a band, tunnelling couples the population to the neighbours coherences through the tunnelling matrix elements $J_1^{\boldsymbol{n}}$. Coherent tunnelling increases with band index and decreases with lattice depth.

Does a process of absorption-spontaneous emission induce such a tunnelling event? We proceed to the same kind of calculation on the dissipative part of the master equation (5.14). We are interested in the coefficients $T_1^{\boldsymbol{n}}$ coupling the population $\langle w_{\mathbf{0}}^{\boldsymbol{n}}| \hat{\rho} |w_{\mathbf{0}}^{\boldsymbol{n}}\rangle$ to the coherences $\langle w_{\boldsymbol{i}}^{\boldsymbol{n}}| \hat{\rho} |w_{\mathbf{0}}^{\boldsymbol{n}}\rangle$, where $\boldsymbol{i}$ is a nearest-neighbour of the central site (a more complete analysis of the tunnelling dynamics in the Wannier basis is provided in Appendix C.2):

$$T_1^{\boldsymbol{n}} = \hbar\Gamma_{\text{sp}} \int \mathrm{d}^2 u \, N(\boldsymbol{u}) \left\langle w_{\mathbf{0}}^{\boldsymbol{n}}\right| \mathrm{e}^{\mathrm{i}\Delta\boldsymbol{k}\cdot\hat{\boldsymbol{R}}} \left|w_{\mathbf{0}}^{\boldsymbol{n}}\right\rangle \left\langle w_{\mathbf{0}}^{\boldsymbol{n}}\right| \mathrm{e}^{-\mathrm{i}\Delta\boldsymbol{k}\cdot\hat{\boldsymbol{R}}} \left|w_{\boldsymbol{i}}^{\boldsymbol{n}}\right\rangle . \tag{5.47}$$

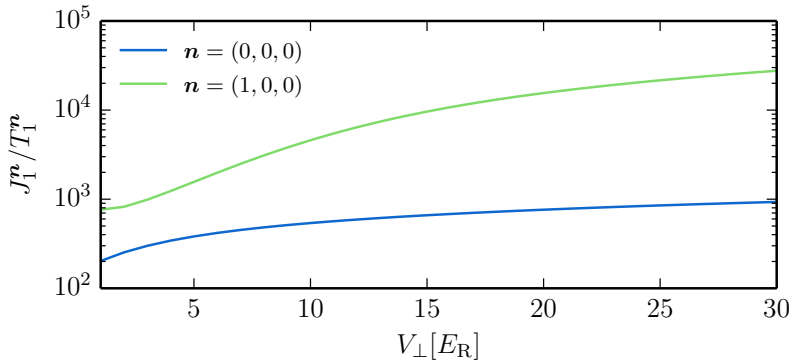

Figure 5.9: Comparison between coherent and light-induced tunnellings for various lattice depth $V_\perp$. The rate of spontaneous emission is $\hbar\Gamma_{\text{sp}} = 0.1\, E_{\text{R}}$.

As shown in Figure 5.9, the modification of tunnelling by spontaneous emission is negligible. This stems from the coherent angular integration over the spontaneous emission directions which averages out the contributions of the finite Lamb-Dicke factors $\langle w_{\boldsymbol{i}}^{\boldsymbol{n}}| \mathrm{e}^{\mathrm{i}\Delta\boldsymbol{k}\cdot\hat{\boldsymbol{R}}} |w_{\mathbf{0}}^{\boldsymbol{n}}\rangle$.

5.3 Dipole-dipole interactions and collective effects in spontaneous emission

In this section, I go beyond the single-particle approach and derive a many-body master equation equivalent to (5.13) which incorporate interactions in the model. I then concentrate on the specific features arising from the presence of the resonant laser field: induced dipole-dipole interactions and collective effects in spontaneous emission. The excitation created by the absorption of a photon can be shared between two atoms thanks to elementary emission and absorption processes. This exchange of photon modifies the energy of the atom pair, leading to an effective interaction[5] between the two atoms (Cohen-Tannoudji 1974). In the master equation formalism presented in Section 5.3.1, this interaction appears in a Hamiltonian part $\hat{V}_{\rm dd}$ related to the interaction energy of a many-body state, and a dissipative part $\hat{\gamma}_{\rm coll}$ related to the collective spontaneous emission rate of the many-body state. In Section 5.3.3 I present a calculation of the energy shift induced by the electric dipole-dipole interactions for two atoms on a same site. In Section 5.3.4 I describe how collective effects can modify the spontaneous emission rate.

5.3.1 Master equation for many atoms subjected to spontaneous emission

I use the formalism of second quantisation to deal with the many-body description of the atomic ensemble. We consider an ensemble of bosons described by a field operator $\hat{\Psi}(\boldsymbol{r})$. The internal atomic structure is identical to the one given in Section 5.1.2 with a ground state $|g\rangle$ and an excited state manifold $|e_m\rangle$. The corresponding atomic field operators are written $\hat{\Psi}_g(\boldsymbol{r})$ and $\hat{\Psi}_{e_m}(\boldsymbol{r})$. The Hamiltonian describing the atoms is made of both motional and internal parts as before [see (5.6)] but also includes an interaction term which captures the short-range atomic collision processes:

$$\hat{H}_{\rm at} = \hat{H}_{\rm motion} + \hat{H}_{\rm intern} + \hat{H}_{\rm contact}, \tag{5.48}$$

$$\hat{H}_{\rm motion} = \sum_{\alpha=g,e_m} \int \mathrm{d}^3 r\, \hat{\Psi}^\dagger_\alpha(\boldsymbol{r}) \left\{ -\frac{\hbar^2}{2M}\nabla^2 + V_{\rm trap}(\boldsymbol{r}) \right\} \hat{\Psi}_\alpha(\boldsymbol{r}), \tag{5.49}$$

$$\hat{H}_{\rm intern} = \sum_m \int \mathrm{d}^3 r\, \hat{\Psi}^\dagger_{e_m}(\boldsymbol{r}) \hat{\Psi}_{e_m}(\boldsymbol{r}). \tag{5.50}$$

The interaction term $\hat{H}_{\rm contact}$ encapsulates low-energy short-range collisions captured by the scattering length (Ketterle et al. 1999).

The interaction between the atoms and the light field is still given by the dipolar-electric coupling Hamiltonians in (5.9) and (5.12), which read in second quantised form:

$$\hat{V}_{\rm vac} = -\hat{\boldsymbol{D}} \cdot \hat{\boldsymbol{E}}_\perp, \tag{5.51}$$

$$\hat{D}_m = d \int \mathrm{d}^3 r\, \hat{\Psi}^\dagger_{e_m}(\boldsymbol{r}) \hat{\Psi}_g(\boldsymbol{r}) + d \int \mathrm{d}^3 r\, \hat{\Psi}^\dagger_g(\boldsymbol{r}) \hat{\Psi}_{e_m}(\boldsymbol{r}), \tag{5.52}$$

$$\hat{V}_{\rm las} = \frac{\hbar\Omega_{\rm L}}{2} \mathrm{e}^{\mathrm{i}(\boldsymbol{k}_{\rm L}\cdot\boldsymbol{r}-\omega_{\rm L}t)} \hat{\Psi}^\dagger_{e,0}(\boldsymbol{r}) \hat{\Psi}_g(\boldsymbol{r}) + \text{h.c.}. \tag{5.53}$$

[5] Note that such an induced electric dipole-dipole interaction is different from the static dipole-dipole interaction between two permanent dipoles.

In principle, the atom-light interaction Hamiltonian also includes contact terms (Cohen-Tannoudji 1974; Morice 1995). These terms can absorbed in $\hat{H}_{\text{contact}}$ and we do not discuss them further.

As before, we add independently the coherent evolution due to the interaction of the atoms with laser photons $[\hat{V}_{\text{las}}, \hat{\rho}_{\text{s}}]/(\mathrm{i}\hbar)$, and the relaxation due to the interaction $\hat{V}_{\text{vac}}$ with the electro-magnetic field vacuum given by (5.2). The resulting master equation is then formally the same as (5.13).

Final master equation for the ground state variables

After adiabatic elimination of the excited state, we obtain a master equation for the external degrees of freedom in the ground state (Pichler et al. 2010):

$$\frac{\mathrm{d}\hat{\rho}}{\mathrm{d}t} = \frac{1}{\mathrm{i}\hbar}\left(\hat{H}_{\text{eff}}\hat{\rho} - \hat{\rho}\hat{H}_{\text{eff}}^{\dagger}\right) + \mathcal{J}[\hat{\rho}]. \tag{5.54}$$

Here $\hat{H}_{\text{eff}}$ is a non-hermitian Hamiltonian given by

$$\hat{H}_{\text{eff}} = \hat{H}_{\text{motion}} + \hat{H}_{\text{contact}} + \hat{V}_{\text{dd}} - \frac{\mathrm{i}\hbar}{2}\left(\hat{\gamma}_{\text{sp}} + \hat{\gamma}_{\text{many}}\right). \tag{5.55}$$

The departure terms $A[\hat{\rho}]$ in (5.13) are included in the radiative terms of $\hat{H}_{\text{eff}}$ ($\hat{V}_{\text{dd}}$, $\hat{\gamma}_{\text{sp}}$ and $\hat{\gamma}_{\text{many}}$) whereas the feeding terms $B[\hat{\rho}]$ are included in the recycling term $\mathcal{J}$ (see also Appendix C.3). From now on, we omit the g subscript in the field operators for simplicity, i.e. $\hat{\Psi} = \hat{\Psi}_g$.

$\hat{H}_{\text{motion}}$ is given by (5.49), considered only for the ground state. $\hat{H}_{\text{contact}}$ contains the description of short-range collisions between atoms. In the presence of laser light, but away from photoassociation resonances, the description given in Chapter 1 is expected to hold with a renormalisation of the scattering length due to the presence of the excited state. However, the exact contribution of all molecular and/or diffusive states in the interaction potential is not known, and light-assisted collisions may play an important role (Chin et al. 2010). At this point, we do not include this in our model for simplicity and take $\hat{H}_{\text{contact}}$ to be the same as without resonant light.

$\hat{V}_{\text{dd}}$ is the dipole-dipole interaction due to the exchange of photons between the atoms:

$$\hat{V}_{\text{dd}} = \hbar\Gamma_{\text{sp}} \int \mathrm{d}^3r\mathrm{d}^3r'\, \mathrm{e}^{\mathrm{i}\boldsymbol{k}_{\text{L}}\cdot(\boldsymbol{r}'-\boldsymbol{r})} G(\boldsymbol{r}-\boldsymbol{r}')\hat{\Psi}^{\dagger}(\boldsymbol{r})\hat{\Psi}^{\dagger}(\boldsymbol{r}')\hat{\Psi}(\boldsymbol{r}')\hat{\Psi}(\boldsymbol{r}), \tag{5.56}$$

with the phase factor $\mathrm{e}^{\mathrm{i}\boldsymbol{k}_{\text{L}}\cdot(\boldsymbol{r}'-\boldsymbol{r})}$ coming from the Rabi driving of the laser field. The function G, shown in Figure 5.10b, is calculated in Appendix C.4 and recalled below. At very short distances, $rk_0 \ll 1$ (with k_0 the emitted photon wavenumber), G is close to the static dipole-dipole interaction, diverging as $1/r^3$. It falls off at distances longer than the emitted photon wavelength $\lambda_0 = 2\pi/k_0$. The spatial dependence at long distances is either $1/r$ if $\boldsymbol{r} \perp \boldsymbol{\varepsilon}_{\text{L}}$, or $1/r^2$ if $\boldsymbol{r} \parallel \boldsymbol{\varepsilon}_{\text{L}}$.

$\hat{\gamma}_{\text{sp}}$ is a one-body decay term describing an absorption-spontaneous emission cycle

$$\hat{\gamma}_{\text{sp}} = \Gamma_{\text{sp}} \int \mathrm{d}^3r\, \hat{\Psi}^{\dagger}(\boldsymbol{r})\hat{\Psi}(\boldsymbol{r}). \tag{5.57}$$

$\hat{\gamma}_{\text{many}}$ is a two-body collective decay term corresponding to super- or sub-radiance

$$\hat{\gamma}_{\text{many}} = \Gamma_{\text{sp}} \int \mathrm{d}^3r\mathrm{d}^3r'\, \mathrm{e}^{\mathrm{i}\boldsymbol{k}_{\text{L}}\cdot(\boldsymbol{r}'-\boldsymbol{r})} F(\boldsymbol{r}-\boldsymbol{r}')\hat{\Psi}^{\dagger}(\boldsymbol{r})\hat{\Psi}^{\dagger}(\boldsymbol{r}')\hat{\Psi}(\boldsymbol{r}')\hat{\Psi}(\boldsymbol{r}), \tag{5.58}$$

with the function F, shown in Figure 5.10a, calculated in Appendix C.4 and recalled below. The function F is equal to one at the origin and falls off in the same way as G.

Finally, the recycling term $\mathcal{J}[\hat{\rho}]$ describes the 'feeding' part of the master equation (5.54), it involves one-body operators and the function F

$$\mathcal{J}[\hat{\rho}] = \Gamma_{\mathrm{sp}} \int \mathrm{d}^3 r \mathrm{d}^3 r' \, \mathrm{e}^{\mathrm{i}\boldsymbol{k}_{\mathrm{L}}\cdot(\boldsymbol{r}'-\boldsymbol{r})} F(\boldsymbol{r}-\boldsymbol{r}') \hat{\Psi}^\dagger(\boldsymbol{r}') \hat{\Psi}(\boldsymbol{r}') \hat{\rho} \hat{\Psi}^\dagger(\boldsymbol{r}) \hat{\Psi}(\boldsymbol{r}). \tag{5.59}$$

Lindblad form

The previous way of writing the master equation (5.54) was convenient to describe the many-body terms arising from the interaction with the laser field. We can also rewrite it in a form close to the Lindblad form if we group the terms comprising the function F. Using the bosonic commutation relation for the field operators $[\hat{\Psi}(\boldsymbol{r}), \hat{\Psi}^\dagger(\boldsymbol{r}')] = \delta^{(3)}(\boldsymbol{r}-\boldsymbol{r}')$ and the fact that $F(\boldsymbol{0}) = 1$, the master equation (5.54) can be rewritten in the form:

$$\frac{\mathrm{d}\hat{\rho}}{\mathrm{d}t} = \frac{1}{\mathrm{i}\hbar}\left(\hat{H}\hat{\rho} - \hat{\rho}\hat{H}^\dagger\right) + \Gamma_{\mathrm{sp}} \int \mathrm{d}^3 r \mathrm{d}^3 r' \, K(\boldsymbol{r}-\boldsymbol{r}') \left[\hat{n}(\boldsymbol{r}')\hat{\rho}\hat{n}(\boldsymbol{r}) - \frac{1}{2}\hat{n}(\boldsymbol{r})\hat{n}(\boldsymbol{r}')\hat{\rho} - \frac{1}{2}\hat{\rho}\hat{n}(\boldsymbol{r})\hat{n}(\boldsymbol{r}')\right], \tag{5.60}$$

where $\hat{n}(\boldsymbol{r}) = \hat{\Psi}^\dagger(\boldsymbol{r})\hat{\Psi}(\boldsymbol{r})$, $\hat{H} = \hat{H}_{\mathrm{motion}} + \hat{H}_{\mathrm{contact}} + \hat{V}_{\mathrm{dd}}$ and $K(\boldsymbol{s}) = \mathrm{e}^{-\mathrm{i}\boldsymbol{k}_{\mathrm{L}}\cdot\boldsymbol{s}} F(\boldsymbol{s})$. This form shows that resonant atom-light interaction acts as a position-resolved density measurement. The emitted photons could thus be used to measure the position of the atoms.

Shape of dipole-dipole functions F and G

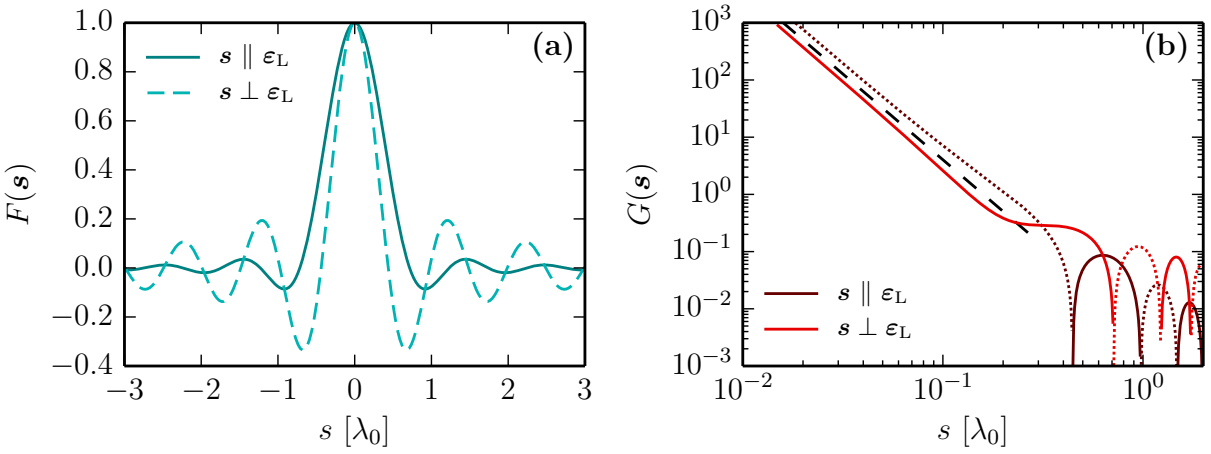

Figure 5.10: Spontaneous emission and dipole-dipole functions $F(\boldsymbol{s})$ and $G(\boldsymbol{s})$ defined in (5.62) and (5.64). The relative distance $\boldsymbol{s}$ is chosen either along the polarisation of the laser or perpendicular to it ($s = |\boldsymbol{s}|$). (a) Plot of F. The function is localised on a length scale set by the wavelength of the emitted photon λ_0. (b) Plot of G. Solid lines denote positive values while dotted lines denote negative values. The function diverges at the origin as $1/s^3$ (black dashed line).

Here $s = |\boldsymbol{s}|$ and $\bar{\boldsymbol{s}} = \boldsymbol{s}/s$:

$$F(\boldsymbol{s}) = \frac{3}{8\pi} \int \mathrm{d}^2 u \, \mathrm{e}^{\mathrm{i}k_0 \boldsymbol{u}\cdot\boldsymbol{s}} \sum_{\boldsymbol{\varepsilon}\perp\boldsymbol{u}} \boldsymbol{\varepsilon}_0 \cdot \boldsymbol{\varepsilon}_0^* \tag{5.61}$$

$$= \frac{3}{2} \left\{ \left[1 - (\bar{\boldsymbol{s}} \cdot \boldsymbol{\varepsilon}_\mathrm{L})^2\right] \frac{\sin(k_0 s)}{k_0 s} + \left[1 - 3(\bar{\boldsymbol{s}} \cdot \boldsymbol{\varepsilon}_\mathrm{L})^2\right] \left(\frac{\cos(k_0 s)}{(k_0 s)^2} - \frac{\sin(k_0 s)}{(k_0 s)^3} \right) \right\}, \tag{5.62}$$

$$G(\boldsymbol{s}) = \frac{1}{2\pi} \mathrm{PV} \left[\int \mathrm{d}x \, \frac{x^3}{1-x} F(x\boldsymbol{s}) \right] \tag{5.63}$$

$$= \frac{3}{4} \left\{ - \left[1 - (\bar{\boldsymbol{s}} \cdot \boldsymbol{\varepsilon}_\mathrm{L})^2\right] \frac{\cos(k_0 s)}{k_0 s} + \left[1 - 3(\bar{\boldsymbol{s}} \cdot \boldsymbol{\varepsilon}_\mathrm{L})^2\right] \left(\frac{\sin(k_0 s)}{(k_0 s)^2} + \frac{\cos(k_0 s)}{(k_0 s)^3} \right) \right\}. \tag{5.64}$$

5.3.2 Many-body effects for atoms in the fundamental band

We now specialise the previous general formalism to the description of atoms in an optical lattice. Having already discussed the role of inter-band transitions for a single particle in Section 5.2, we simplify the discussion here by considering only atoms in the fundamental band. In the remainder of this section, we evaluate the role of many-body effects in light-matter interactions for atoms in optical lattices. For this we expand the field operators in the Wannier basis (we omit the band index):

$$\hat{\Psi}(\boldsymbol{r}) = \sum_{\boldsymbol{i}} w_{\boldsymbol{i}}(\boldsymbol{r}) \hat{a}_{\boldsymbol{i}}. \tag{5.65}$$

For simplicity, we consider here the dynamics of the reduced density matrix $\hat{\rho}_0$ of the fundamental band. We neglect the role of all other bands and omit the band index from now on.

The master equation (5.60) written in the Wannier basis, keeping only the fundamental band, reads

$$\frac{\mathrm{d}\hat{\rho}_0}{\mathrm{d}t} = \frac{1}{\mathrm{i}\hbar} \left[\hat{H}, \hat{\rho}_0\right] + \Gamma_\mathrm{sp} \sum_{\boldsymbol{i},\boldsymbol{j},\boldsymbol{k},\boldsymbol{l}} \Lambda_{\boldsymbol{i},\boldsymbol{j},\boldsymbol{k},\boldsymbol{l}} \left[\hat{a}_{\boldsymbol{k}}^\dagger \hat{a}_{\boldsymbol{l}} \hat{\rho} \hat{a}_{\boldsymbol{i}}^\dagger \hat{a}_{\boldsymbol{j}} - \frac{1}{2} \hat{a}_{\boldsymbol{i}}^\dagger \hat{a}_{\boldsymbol{j}} \hat{a}_{\boldsymbol{k}}^\dagger \hat{a}_{\boldsymbol{l}} \hat{\rho} - \frac{1}{2} \hat{\rho} \hat{a}_{\boldsymbol{i}}^\dagger \hat{a}_{\boldsymbol{j}} \hat{a}_{\boldsymbol{k}}^\dagger \hat{a}_{\boldsymbol{l}} \right], \tag{5.66}$$

with the matrix elements given by

$$\Lambda_{\boldsymbol{i},\boldsymbol{j},\boldsymbol{k},\boldsymbol{l}} = \int \mathrm{d}^3 r \mathrm{d}^3 r' \, K(\boldsymbol{r} - \boldsymbol{r}') w_{\boldsymbol{i}}^*(\boldsymbol{r}) w_{\boldsymbol{j}}(\boldsymbol{r}) w_{\boldsymbol{k}}^*(\boldsymbol{r}') w_{\boldsymbol{l}}(\boldsymbol{r}'). \tag{5.67}$$

Due to the exponentially localised form of the Wannier functions, the dominant matrix elements have $\boldsymbol{i} = \boldsymbol{j}$ and $\boldsymbol{k} = \boldsymbol{l}$. We thus consider only these elements $\Lambda_{\boldsymbol{i},\boldsymbol{j}} = \Lambda_{\boldsymbol{i},\boldsymbol{i},\boldsymbol{j},\boldsymbol{j}}$ and:

$$\frac{\mathrm{d}\hat{\rho}_0}{\mathrm{d}t} = \frac{1}{\mathrm{i}\hbar} \left[\hat{H}, \hat{\rho}_0\right] + \Gamma_\mathrm{sp} \sum_{\boldsymbol{i},\boldsymbol{j}} \Lambda_{\boldsymbol{i},\boldsymbol{j}} \left[\hat{n}_{\boldsymbol{j}} \hat{\rho} \hat{n}_{\boldsymbol{i}} - \frac{1}{2} \hat{n}_{\boldsymbol{i}} \hat{n}_{\boldsymbol{j}} \hat{\rho} - \frac{1}{2} \hat{\rho} \hat{n}_{\boldsymbol{i}} \hat{n}_{\boldsymbol{j}} \right]. \tag{5.68}$$

First-order correlation function

We are interested in the time evolution of the spatial coherence in the system. For this we can look at the first-order correlation function $\rho^{(1)}(\boldsymbol{r}, \boldsymbol{r}') = \langle \hat{\Psi}^\dagger(\boldsymbol{r}) \hat{\Psi}(\boldsymbol{r}') \rangle$ which

characterises the coherence between two atoms separated by the distance $|\boldsymbol{r}-\boldsymbol{r}'|$. Because we deal with atoms in an optical lattice we consider the following correlator:

$$\mathcal{C}_{\boldsymbol{i},\boldsymbol{j}} = \langle \hat{a}_{\boldsymbol{i}}^\dagger \hat{a}_{\boldsymbol{j}} \rangle = \int \mathrm{d}^3 r \mathrm{d}^3 r' \, w_{\boldsymbol{i}}^*(\boldsymbol{r}) w_{\boldsymbol{j}}(\boldsymbol{r}') \mathcal{C}_1(\boldsymbol{r},\boldsymbol{r}'). \tag{5.69}$$

The time evolution of the first-order correlator $\mathcal{C}_{\boldsymbol{i},\boldsymbol{j}}$ can be calculated from (5.68) using bosonic commutation relations (5.72):

$$\frac{\mathrm{d}\mathcal{C}_{\boldsymbol{i},\boldsymbol{j}}}{\mathrm{d}t} = \mathrm{Tr}\left[\hat{a}_{\boldsymbol{i}}^\dagger \hat{a}_{\boldsymbol{j}} \frac{\mathrm{d}\hat{\rho}_0}{\mathrm{d}t}\right] \tag{5.70}$$

$$= \frac{1}{\mathrm{i}\hbar}\left\langle \left[\hat{a}_{\boldsymbol{i}}^\dagger \hat{a}_{\boldsymbol{j}}, \hat{H}\right]\right\rangle + \Gamma_{\mathrm{sp}} \sum_{\boldsymbol{l}} \frac{\Lambda_{\boldsymbol{i},\boldsymbol{l}} - \Lambda_{\boldsymbol{j},\boldsymbol{l}}}{2} \left\langle \hat{a}_{\boldsymbol{i}}^\dagger \hat{a}_{\boldsymbol{j}} \hat{n}_{\boldsymbol{l}} \right\rangle + \Gamma_{\mathrm{sp}} \sum_{\boldsymbol{k}} \frac{\Lambda_{\boldsymbol{k},\boldsymbol{j}} - \Lambda_{\boldsymbol{k},\boldsymbol{i}}}{2} \left\langle \hat{n}_{\boldsymbol{k}} \hat{a}_{\boldsymbol{i}}^\dagger \hat{a}_{\boldsymbol{j}} \right\rangle, \tag{5.71}$$

$$\left[\hat{n}_{\boldsymbol{k}}, \hat{a}_{\boldsymbol{i}}^\dagger \hat{a}_{\boldsymbol{j}}\right] = \delta_{\boldsymbol{i},\boldsymbol{k}} \hat{a}_{\boldsymbol{i}}^\dagger \hat{a}_{\boldsymbol{j}} - \delta_{\boldsymbol{j},\boldsymbol{k}} \hat{a}_{\boldsymbol{i}}^\dagger \hat{a}_{\boldsymbol{j}}. \tag{5.72}$$

We also have:

$$\Lambda_{\boldsymbol{i},\boldsymbol{j}} = \int \mathrm{d}^3 r \mathrm{d}^3 r' \, K(\boldsymbol{r}-\boldsymbol{r}') |w_{\boldsymbol{i}}(\boldsymbol{r})|^2 |w_{\boldsymbol{j}}(\boldsymbol{r}')|^2 \tag{5.73}$$

$$= \int \mathrm{d}^3 r \mathrm{d}^3 r' \, \mathrm{e}^{\mathrm{i}\boldsymbol{k}_{\mathrm{L}}\cdot(\boldsymbol{r}'-\boldsymbol{r}+\boldsymbol{r}_{\boldsymbol{j}}-\boldsymbol{r}_{\boldsymbol{i}})} F(\boldsymbol{r}-\boldsymbol{r}'+\boldsymbol{r}_{\boldsymbol{i}}-\boldsymbol{r}_{\boldsymbol{j}}) |w_{\boldsymbol{0}}(\boldsymbol{r})|^2 |w_{\boldsymbol{0}}(\boldsymbol{r}')|^2. \tag{5.74}$$

Coherences between different planes are zero and we are interested in the coherence within each planes $z_{\boldsymbol{i}} = z_{\boldsymbol{j}}$. We make the approximation of infinitely deep vertical lattice depth (Lamb-Dicke parameter $\eta_z \to 0$) for simplicity. In that case the expression of the matrix element simplifies into

$$\Lambda_{\boldsymbol{i},\boldsymbol{j}} \approx \int \mathrm{d}^2 r \mathrm{d}^2 r' \, F(\boldsymbol{r}-\boldsymbol{r}'+\boldsymbol{r}_{\boldsymbol{i}}-\boldsymbol{r}_{\boldsymbol{j}}) |w_{\boldsymbol{0}}(\boldsymbol{r})|^2 |w_{\boldsymbol{0}}(\boldsymbol{r}')|^2, \tag{5.75}$$

where the integration is now performed in a two-dimensional plane. Due to the even parity of F we have $\Lambda_{\boldsymbol{i},\boldsymbol{j}} = \Lambda_{\boldsymbol{j},\boldsymbol{i}}$. We thus have:

$$\frac{\mathrm{d}\mathcal{C}_{\boldsymbol{i},\boldsymbol{j}}}{\mathrm{d}t} = \frac{1}{\mathrm{i}\hbar}\left\langle \left[\hat{a}_{\boldsymbol{i}}^\dagger \hat{a}_{\boldsymbol{j}}, \hat{H}\right]\right\rangle + \Gamma_{\mathrm{sp}} \sum_{\boldsymbol{l}} \frac{\Lambda_{\boldsymbol{i},\boldsymbol{l}} - \Lambda_{\boldsymbol{j},\boldsymbol{l}}}{2} \left\langle \left[\hat{a}_{\boldsymbol{i}}^\dagger \hat{a}_{\boldsymbol{j}}, \hat{n}_{\boldsymbol{l}}\right]\right\rangle \tag{5.76}$$

$$= \underbrace{\frac{1}{\mathrm{i}\hbar}\left\langle \left[\hat{a}_{\boldsymbol{i}}^\dagger \hat{a}_{\boldsymbol{j}}, \hat{H}\right]\right\rangle}_{\text{coherent evolution}} \underbrace{-\Gamma_{\mathrm{sp}} \left(\Lambda_{\boldsymbol{i},\boldsymbol{i}} - \Lambda_{\boldsymbol{i},\boldsymbol{j}}\right) \mathcal{C}_{\boldsymbol{i},\boldsymbol{j}}}_{\text{dissipation}}. \tag{5.77}$$

The differential equation (5.77) shows two parts. The first one describes the coherent evolution due to the Hamiltonian part of the master equation as well as the dipole-dipole interaction term. The second term gives the evolution related to spontaneous emission. This dissipative evolution is zero for the on-site correlation (the density) and increases with distance. However the rate $\Gamma_{\mathrm{sp}}\left(\Lambda_{\boldsymbol{i},\boldsymbol{i}} - \Lambda_{\boldsymbol{i},\boldsymbol{j}}\right)$ is bound by Γ_{sp} (simply because $|F| \leq 1$).

We thus conclude that spontaneous emission can not result in a decay of the coherence faster than the rate of spontaneous emission Γ_{sp} expected for a single atom. The fast initial decay of the coherence observed in the experiments of the last chapter (normalised rate γ bigger than unity in Section 4.2.3 and Section 4.2.4) is thus either due to dephasing from dipole-dipole interactions or to atom losses.

5.3.3 Energy shift due to dipole-dipole interactions

The radiative interaction associated to the exchange of a resonant photon between two atoms is captured by the dipole-dipole operator $\hat{V}_{\mathrm{dd}}$ given in (5.56), which we write:

$$\hat{V}_{\mathrm{dd}} = \sum_{\boldsymbol{i},\boldsymbol{j},\boldsymbol{k},\boldsymbol{l}} U_{\boldsymbol{i},\boldsymbol{j},\boldsymbol{k},\boldsymbol{l}} \hat{a}_{\boldsymbol{i}}^\dagger \hat{a}_{\boldsymbol{j}}^\dagger \hat{a}_{\boldsymbol{k}} \hat{a}_{\boldsymbol{l}}, \tag{5.78}$$

with the matrix elements given by

$$U_{\boldsymbol{i},\boldsymbol{j},\boldsymbol{k},\boldsymbol{l}} = \hbar\Gamma_{\mathrm{sp}} \int \mathrm{d}^3r \mathrm{d}^3r' \, \mathrm{e}^{\mathrm{i}\boldsymbol{k}_{\mathrm{L}}\cdot(\boldsymbol{r}'-\boldsymbol{r})} G(\boldsymbol{r}-\boldsymbol{r}') w_{\boldsymbol{i}}^*(\boldsymbol{r}) w_{\boldsymbol{j}}^*(\boldsymbol{r}') w_{\boldsymbol{k}}(\boldsymbol{r}') w_{\boldsymbol{l}}(\boldsymbol{r}). \tag{5.79}$$

Again, due to the exponentially localised form of the Wannier functions, the dominant matrix elements have $\boldsymbol{i} = \boldsymbol{l}$ and $\boldsymbol{j} = \boldsymbol{k}$. We can thus write

$$\hat{V}_{\mathrm{dd}} = \frac{1}{2} \sum_{\boldsymbol{i},\boldsymbol{j}} U_{\mathrm{dd}}^{|\boldsymbol{i}-\boldsymbol{j}|} \hat{a}_{\boldsymbol{i}}^\dagger \hat{a}_{\boldsymbol{j}}^\dagger \hat{a}_{\boldsymbol{i}} \hat{a}_{\boldsymbol{j}}, \tag{5.80}$$

with the energy shift due to dipole-dipole interactions of an atom pair separated by a lattice vector $\boldsymbol{r}_{\boldsymbol{i}}$ is given by:

$$U_{\mathrm{dd}}^{\boldsymbol{i}} = 2\hbar\Gamma_{\mathrm{sp}} \int \mathrm{d}^3r \mathrm{d}^3r' \, \cos\left[\boldsymbol{k}_{\mathrm{L}} \cdot (\boldsymbol{r}'-\boldsymbol{r})\right] G(\boldsymbol{r}'-\boldsymbol{r}) |w_{\boldsymbol{i}}(\boldsymbol{r})|^2 |w_{\boldsymbol{0}}(\boldsymbol{r}')|^2. \tag{5.81}$$

Wannier functions do not have analytical expressions and the numerical computation of U_{dd} is more easily performed in momentum space. Using twice the convolution theorem (see Appendix C.5), one can rewrite (5.81) in momentum space,

$$U_{\mathrm{dd}}^{\boldsymbol{i}} = \frac{2\hbar\Gamma_{\mathrm{sp}}}{(2\pi)^3} \int \mathrm{d}^3k \, \cos\left[(\boldsymbol{k}-\boldsymbol{k}_{\mathrm{L}}) \cdot \boldsymbol{r}_{\boldsymbol{i}}\right] \tilde{G}(\boldsymbol{k}) |\tilde{n}(\boldsymbol{k}-\boldsymbol{k}_{\mathrm{L}})|^2, \tag{5.82}$$

where $\tilde{G}$ is the Fourier transform of G and $\tilde{n}$ is the Fourier transform of the density function $|w_{\boldsymbol{0}}|^2$. A direct computation of the Fourier transform of G gives (with $\bar{\boldsymbol{k}} = \boldsymbol{k}/k$)

$$\tilde{G}(\boldsymbol{k}) = \frac{3\pi}{k_0^3} \left\{ (\bar{\boldsymbol{k}} \cdot \boldsymbol{\varepsilon}_{\mathrm{L}})^2 - \frac{1}{3} + \left[1 - (\bar{\boldsymbol{k}} \cdot \boldsymbol{\varepsilon}_{\mathrm{L}})^2\right] \frac{k_0}{2k} \mathrm{PV}\left[\frac{1}{1-k/k_0}\right] \right\}. \tag{5.83}$$

In the long-wavelength limit $k/k_0 \to +\infty$, the last term in (5.83) vanishes and we are left with an interaction form analogous to the interaction between two permanent dipoles (Lahaye et al. 2009). Note that in a realistic experiment we have $k \sim k_0$.

Dominant terms

The function G is localised over the length λ_0, we thus expect $U_{\mathrm{dd}}^{\boldsymbol{i}}$ to decay fast with site distance. At short distances G scales as $1/r^3$, therefore the on-site matrix element is roughly captured by $U_{\mathrm{dd}}^{\boldsymbol{0}} \approx \hbar\Gamma_{\mathrm{sp}}/(k_0^3\sigma_\perp^2\sigma_z)$. At larger distances G scales in the worst case as $1/r$, therefore the nearest-neighbour matrix element is roughly given by $U_{\mathrm{dd}}^{\boldsymbol{1}} \approx 2\hbar\Gamma_{\mathrm{sp}}/(k_0 d)$. In a lattice with $V_\perp = 10\,E_{\mathrm{R}}$ and $V_{0,z} = 27\,E_{\mathrm{R}}$ we get $U_{\mathrm{dd}}^{\boldsymbol{1}}/U_{\mathrm{dd}}^{\boldsymbol{0}} \approx 8\,\%$, the ratio gets smaller for farther neighbours, decaying as $1/r$. A $1/r$ decay is not very fast, and the number of neighbours increases with distance such that the off-site terms, even if individually small, can sum up to produce an non-negligible contribution. For the sake of simplicity, in the following we only discuss the on-site term.

Numerical computation

The numerical computation of principal value integrals as in (5.83) for $\tilde{G}$ can be problematic. In order to check our numerical calculations, we have thus also analytically calculated (5.81) with the harmonic oscillator wavefunction, valid in the limit of deep lattice depths. This approximation allows us to derive an analytical approximation of $U_{\mathrm{dd}}^{\mathbf{0}}$.

Figure 5.11a shows the dipole-dipole interaction energy $U_{\mathrm{dd}}^{\mathbf{0}}$ (the inset also shows $U_{\mathrm{dd}}^{\mathbf{1}}$ for comparison). The harmonic oscillator wavefunction gives a prediction close to the Wannier wavefunction computation even for low lattice depths. We have checked that the two predictions become equal for very deep lattices (for lattice depths above $100\,E_{\mathrm{R}}$ the relative error is smaller than five percent). In the configuration of the experiments of Chapter 4 [$\boldsymbol{\varepsilon}_{\mathrm{L}} = (\boldsymbol{e}_x + \boldsymbol{e}_y)/\sqrt{2}$] dipole-dipole interactions are attractive.

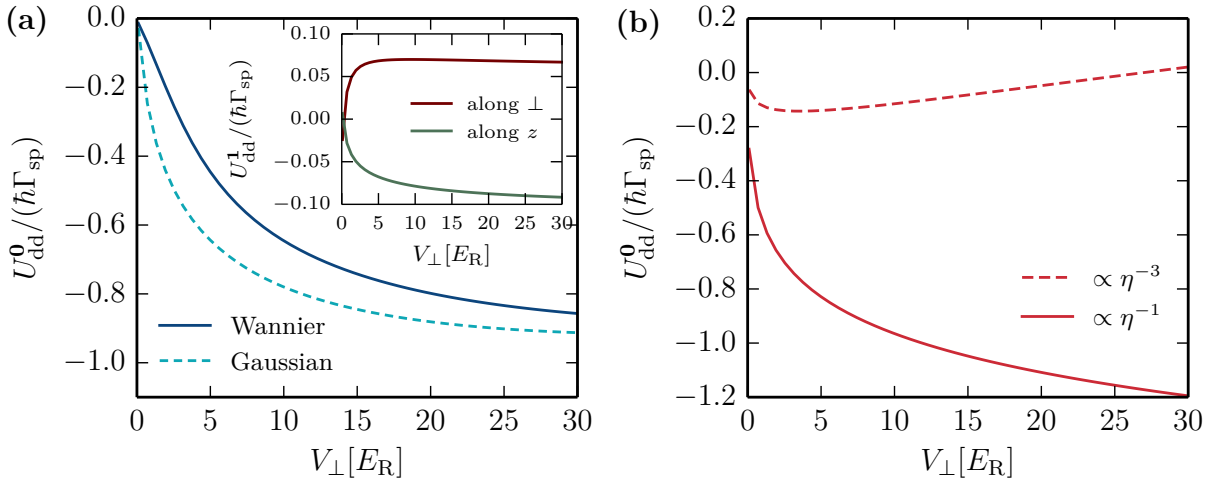

Figure 5.11: Dipole-dipole interaction energies in units of the dissipation strength $\hbar\Gamma_{\mathrm{sp}}$, for various horizontal lattice depth $V_\perp$. The vertical lattice depth is $V_{0,z} = 27\,E_{\mathrm{R}}$. (a) On-site interaction energy $U_{\mathrm{dd}}^{\mathbf{0}}$. The solid line shows the numerical computation using Wannier wavefunctions. The dashed line shows the analytical expression for the harmonic oscillator wavefunction (Gaussian). The inset shows the nearest-neighbour terms $U_{\mathrm{dd}}^{\mathbf{1}}$. (b) Expansion of $U_{\mathrm{dd}}^{\mathbf{0}}$ in powers of the Lamb-Dicke parameter $\eta = k_0\sigma_\perp/\sqrt{2}$.

Power expansion in the Lamb-Dicke parameter

The function G is dominated by a radial dependence in $1/r^3$ at short distances (see Figure 5.10b). We thus expect $U_{\mathrm{dd}}^{\mathbf{0}} \propto 1/\eta^3$ as a first estimate, with $\eta = k_0\sigma_\perp/\sqrt{2}$ the Lamb-Dicke parameter in the horizontal direction. In order to check this we make a power expansion of $U_{\mathrm{dd}}^{\mathbf{0}}$ in the small parameter η. The parity of G gives only odd powers starting from -3. Since η is smaller than one, we expect the negative powers to dominate. In Figure 5.11b, we show the expansion of $U_{\mathrm{dd}}^{\mathbf{0}}$ up to first two powers. For lattice depths in the range $V_\perp \in [3, 13]$ we have roughly

$$\frac{U_{\mathrm{dd}}^{\mathbf{0}}}{\hbar\Gamma_{\mathrm{sp}}} \approx -\frac{1}{50}\eta^{-3} - \frac{1}{2}\eta^{-1} + O(\eta). \tag{5.84}$$

As shown in Figure 5.11b, the dominant contribution comes from the $1/\eta$ term. This stems from the $1/\eta^3$ pre-factor, which is small because of angular integration in $U_{\mathrm{dd}}^{\mathbf{0}}$. This

is consistent with the Wannier wave function being almost isotropic (the $1/\eta^3$ pre-factor vanishes exactly at $V_\perp = V_{0,z} = 27\,E_\mathrm{R}$). For the same reason, the energy due to static dipole-dipole interactions in a dipolar BEC vanish for an isotropic wave function (Lahaye et al. 2009).

5.3.4 Collective effects in spontaneous emission

Single-particle spontaneous emission is described with the operator $\hat{\gamma}_\mathrm{sp}$ and the recycling term $\mathcal{J}[\hat{\rho}]$, which contain one-body operators. Dipole-dipole interactions modify this behaviour by adding collective effects via the exchange of a resonant photon between two atoms. This is captured by the decay operator $\hat{\gamma}_\mathrm{many}$ given in (5.58), which we write:

$$\hat{\gamma}_\mathrm{many} = \sum_{\boldsymbol{i},\boldsymbol{j},\boldsymbol{k},\boldsymbol{l}} \Gamma_{\boldsymbol{i},\boldsymbol{j},\boldsymbol{k},\boldsymbol{l}} \hat{a}^\dagger_{\boldsymbol{i}} \hat{a}^\dagger_{\boldsymbol{j}} \hat{a}_{\boldsymbol{k}} \hat{a}_{\boldsymbol{l}}, \tag{5.85}$$

with the matrix elements given by

$$\Gamma_{\boldsymbol{i},\boldsymbol{j},\boldsymbol{k},\boldsymbol{l}} = \Gamma_\mathrm{sp} \int \mathrm{d}^3 r \mathrm{d}^3 r'\, \mathrm{e}^{\mathrm{i}\boldsymbol{k}_\mathrm{L}\cdot(\boldsymbol{r}'-\boldsymbol{r})} F(\boldsymbol{r}-\boldsymbol{r}') w^*_{\boldsymbol{i}}(\boldsymbol{r}) w^*_{\boldsymbol{j}}(\boldsymbol{r}') w_{\boldsymbol{k}}(\boldsymbol{r}') w_{\boldsymbol{l}}(\boldsymbol{r}). \tag{5.86}$$

Again, due to the exponentially localised form of the Wannier functions, the dominant matrix elements have $\boldsymbol{i} = \boldsymbol{l}$ and $\boldsymbol{j} = \boldsymbol{k}$. The collective emission rate for an atom pair separated by a lattice vector $\boldsymbol{r_i}$ is therefore given by:

$$\Gamma^{\boldsymbol{i}}_\mathrm{many} = \Gamma_\mathrm{sp} \int \mathrm{d}^3 r \mathrm{d}^3 r'\, \cos\left[\boldsymbol{k}_\mathrm{L}\cdot(\boldsymbol{r}'-\boldsymbol{r})\right] F(\boldsymbol{r}-\boldsymbol{r}') |w_{\boldsymbol{i}}(\boldsymbol{r})|^2 |w_{\boldsymbol{0}}(\boldsymbol{r}')|^2. \tag{5.87}$$

As before, we compute the matrix elements in momentum space,

$$\Gamma^{\boldsymbol{i}}_\mathrm{many} = \frac{\Gamma_\mathrm{sp}}{(2\pi)^3} \int \mathrm{d}^3 k\, \cos\left[(\boldsymbol{k}-\boldsymbol{k}_\mathrm{L})\cdot\boldsymbol{r_i}\right] \tilde{F}(\boldsymbol{k}) |\tilde{n}(\boldsymbol{k}-\boldsymbol{k}_\mathrm{L})|^2, \tag{5.88}$$

where $\tilde{F}$ is the Fourier transform of F given by

$$\tilde{F}(\boldsymbol{k}) = \frac{3\pi^2}{k_0^3}\left[1-(\bar{\boldsymbol{k}}\cdot\boldsymbol{\varepsilon}_\mathrm{L})^2\right] \delta^{(1)}\left(1-\frac{k}{k_0}\right). \tag{5.89}$$

Dominant terms

As F goes to one at the origin and decreases slowly (as $1/r^2$ at most), the contribution of nearest-neighbours can not be neglected. Due to the localised form of the Wannier functions, the magnitude of the collective emission rate $\Gamma^{\boldsymbol{i}}_\mathrm{coll}$ is roughly given by $|\mathrm{Re}[F(\boldsymbol{r_i})\mathrm{e}^{\mathrm{i}\boldsymbol{k}_\mathrm{L}\cdot\boldsymbol{r_i}}]|$. We find $\Gamma^{\boldsymbol{0}}_\mathrm{many} \approx 1$, $\Gamma^{\boldsymbol{1}}_\mathrm{many} \approx 0.15$, and farther neighbours evaluate to less than 7 %.

Numerical computation

Figure 5.12a shows the on-site collective emission rate $\Gamma^{\boldsymbol{0}}_\mathrm{coll}$. The on-site term is positive, with a value approaching one for deep lattice depths. We also computed (5.87) using the harmonic oscillator wavefunction, as described in the previous paragraph, and it gives a prediction close to the Wannier wavefunction computation. We have checked that both

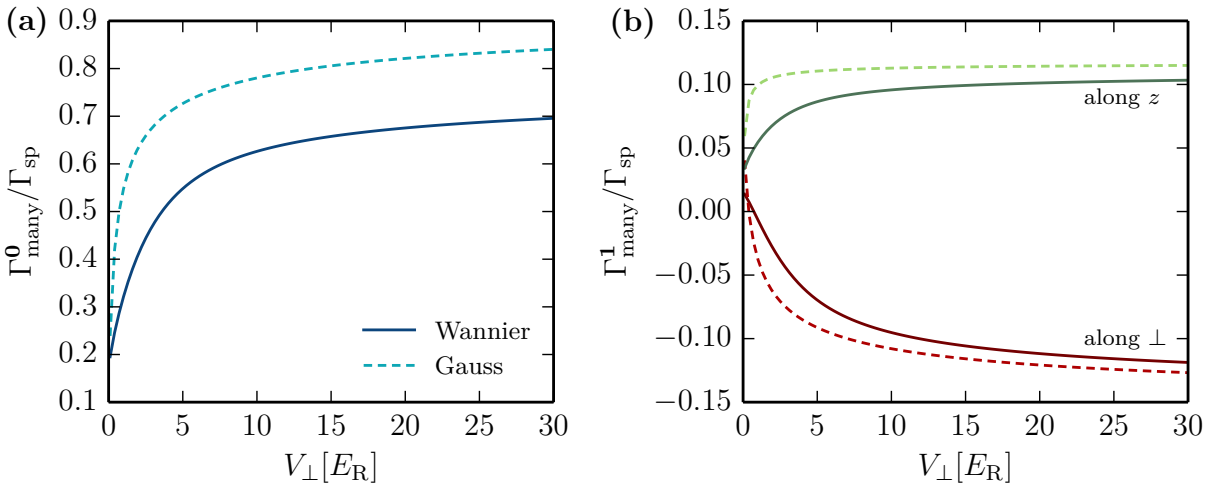

Figure 5.12: Two-body collective contribution $\Gamma^{\boldsymbol{i}}_{\text{many}}$ to the spontaneous emission rate in units of the single-particle spontaneous emission rate Γ_{sp}, for various horizontal lattice depth $V_\perp$. The vertical lattice depth is $V_{0,z} = 27\,E_{\text{R}}$. Solid lines show the numerical computation using Wannier wavefunctions. Dashed lines shows the analytical expression for a Gaussian ansatz. (a) On-site rate $\Gamma^{\mathbf{0}}_{\text{many}}$. (b) Nearest-neighbour rate $\Gamma^{\mathbf{1}}_{\text{many}}$ for nearest-neighbour along the vertical z direction and along the horizontal $\perp$ direction.

become equal in the deep lattice limit (for depths above $100\,E_{\text{R}}$ the relative error is smaller than five percent). Figure 5.12b shows the nearest-neighbour collective emission rate $\Gamma^{\mathbf{1}}_{\text{many}}$ for both the vertical and horizontal directions.

For two atoms on a same site, the spontaneous emission rate is enhanced ($\Gamma^{\mathbf{0}}_{\text{many}} > 0$) due to constructive interference in the emitted fields. This enhancement corresponds to super-radiance for which the total rate of spontaneous emission is greater than for independent emitters. This is expected in the Dicke model for super-radiance (Dicke 1954) because the two atoms are located in a volume of dimension smaller than the emitted photon wavelength λ_0. For nearest-neighbour atoms in the horizontal direction (but not the vertical direction) the spontaneous emission rate is reduced ($\Gamma^{\mathbf{1}}_{\text{many}} < 0$) due to destructive interference in the emitted fields. This reduction corresponds to sub-radiance for which the total rate of spontaneous emission is smaller than for independent emitters. We cannot already conclude about the rate of spontaneous emission for a general many-body state since it depends on the particular density distribution and spatial correlations between the particles. We come back to this point in Section 5.4.3.

5.4 Comparison with the experimental results of Chapter 4

In this section, I use the results derived in Sections 5.2 and 5.3 to give a better understanding of the experimental observations of Chapter 4. I first show a comparison of the band population time evolution between the data presented in Section 4.4.3 and the numerical evaluation of Section 5.2.3. Secondly, I discuss the importance of dipole-dipole interactions, comparing the energy shift calculated in Section 5.3.3 to the on-site contact interaction. Thirdly, I calculate the collective modification of the spontaneous emission

rate expected in our system.

5.4.1 Band population time evolution

In Figure 5.13, the numerical solution of the master equation projected on the Bloch basis in a 3D optical lattice (5.39) is compared to the data of the experiments described in Section 4.2.3. In these experiments we varied the lattice depth of the horizontal lattices, and the spontaneous emission rate was set to $\Gamma_{\mathrm{sp}} = 520\,\mathrm{s}^{-1}$.

For all lattice depths, the behaviour of the band populations is qualitatively reproduced, but not quantitatively. There is a substantial disagreement at short times ($t_{\mathrm{diss}} \lesssim \Gamma_{\mathrm{sp}}^{-1}$), compatible with the observation of an enhanced decay rate for the coherence in the exponential regime (coefficient γ bigger than one in Sections 4.2.3 and 4.2.4). The population in the first excited band typically exceeds 10 % after a time $t_{\mathrm{diss}} \gtrsim 0.1\Gamma_{\mathrm{sp}}^{-1}$.

Inter-band transitions happen at a higher rate than predicted by the single-particle master equation (5.39), which points toward an effect of dipole-dipole interactions or collective light scattering. However, at the level of discussion of Section 5.3 we can not demonstrate this assertion. A more complete treatment is required to understand this feature.

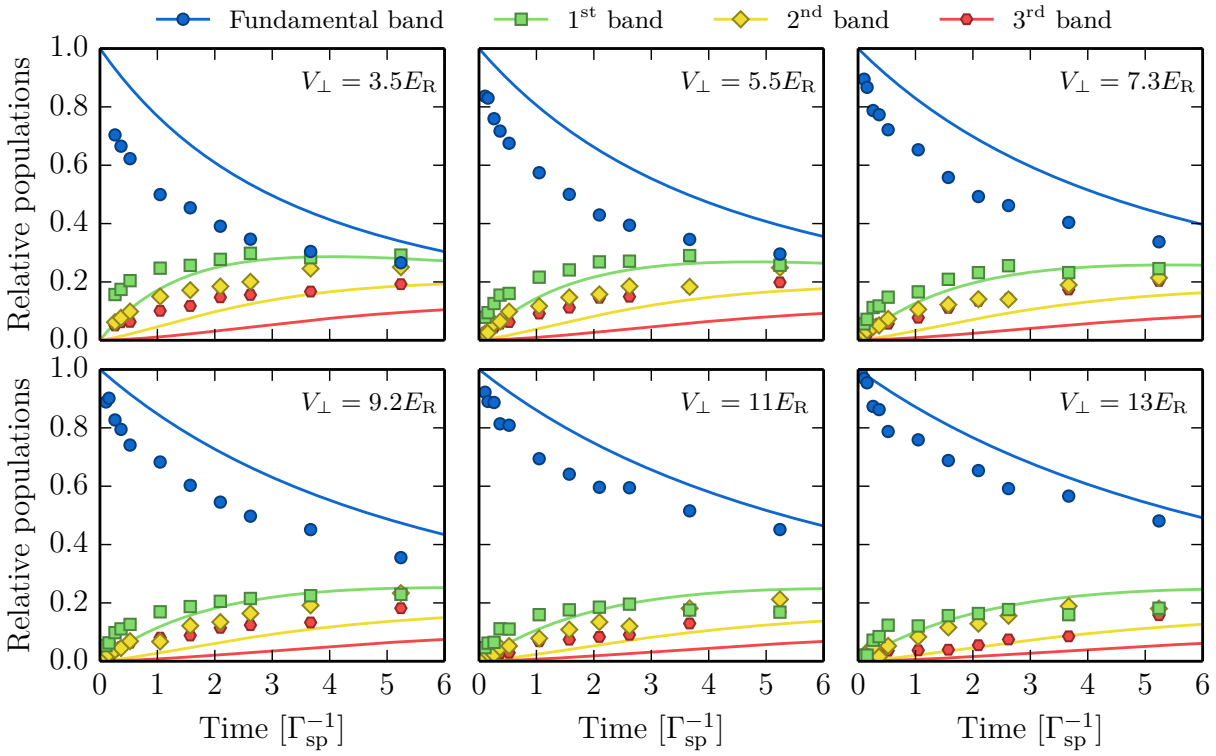

Figure 5.13: Comparison between the numerically computed time evolution of the relative populations and the data of the experiments described in Section 4.2.3 ($\Gamma_{\mathrm{sp}} = 520\,\mathrm{s}^{-1}$). The qualitative behaviour is correct but the exact time evolution is not well reproduced. There seems to be a substantial enhancement of inter-band transitions at short times.

5.4.2 On-site interaction energy

We now look at the influence of induced dipole-dipole interactions on the energy of an atom in the lattice. The total on-site interaction energy U_{tot} is modified by dipole-dipole interactions:

$$U_{\mathrm{tot}} = U_{gg} + U_{\mathrm{dd}}^{\mathbf{0}}, \tag{5.90}$$

where U_{gg} is the contact interaction in the ground state.

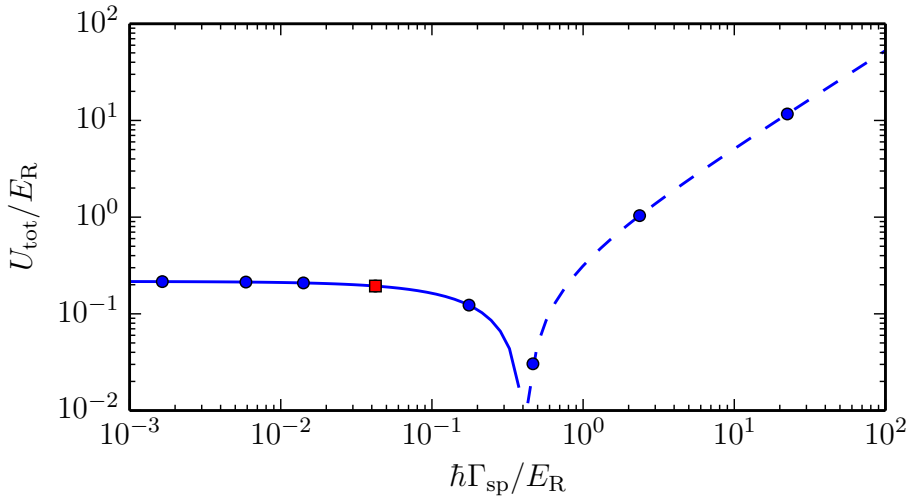

Figure 5.14: On-site interaction energy U_{tot} in units of the dissipation strength. The solid line shows $+U_{\mathrm{tot}}$ and the dashed line shows $-U_{\mathrm{tot}}$. Dots correspond to the values explored in the experiments described in Section 4.2.4, where we varied the spontaneous emission rate. The red square correspond to the experiments described in Section 4.2.3, where we varied the lattice depth. The horizontal lattice depth is $V_\perp = 3.5\,E_{\mathrm{R}}$, and the Bose-Hubbard parameters are $U_{gg} \approx 0.2\,E_{\mathrm{R}}$ and $J_\perp = 0.1\,E_{\mathrm{R}}$.

Figure 5.14 shows $U_{\mathrm{tot}}/E_{\mathrm{R}}$ for varying dissipation strength. For small dissipation strength, the contact interaction U_{gg} dominates. As dissipation increases, because dipole-dipole interactions are attractive in our configuration, the on-site interaction energy crosses zero and becomes negative. The experimental conditions of the last chapter are highlighted with markers on the figure. There is only a small window where one can have $|U_{\mathrm{tot}}| \ll \hbar\Gamma_{\mathrm{sp}}$, which has two consequences:

- For most of our experimental conditions, dipole-dipole interactions in our system make $|U_{\mathrm{tot}}|$ bigger or on the order of $\hbar\Gamma_{\mathrm{sp}}$. This might explain why we did not observe any strong dependence of the relaxation dynamics on the spontaneous emission rate in Section 4.2.4.
- An important approximation used to derive the master equation of Section 4.3 is the secular approximation which requires $U_{\mathrm{tot}}, \hbar\Gamma_{\mathrm{sp}} \gg J_\perp$. Moreover, analytical results are found in the strongly interacting limit $U_{\mathrm{tot}} \gg \hbar\Gamma_{\mathrm{sp}}$. Our findings here show that the limits identified in Poletti et al. (2013) are roughly verified for all the parameters chosen in the experiments presented in the last chapter.

5.4.3 Collective emission rate

Single-particle spontaneous emission is captured in the term $\hat{\gamma}_{\mathrm{sp}}$ of the master equation (5.54). Collective effects arise through the term $\hat{\gamma}_{\mathrm{many}}$, which is associated to super- or sub-radiance. The total rate of spontaneous emission Λ from atoms in the lattice is given by (Pichler et al. 2010):

$$\frac{\Lambda}{\Gamma_{\mathrm{sp}}} = \int \mathrm{d}^3 r \,\mathrm{Tr}\left[\hat{\Psi}^\dagger(\boldsymbol{r})\hat{\Psi}(\boldsymbol{r})\hat{\rho}\right] + \int \mathrm{d}^3 r \mathrm{d}^3 r' \,\mathrm{e}^{\mathrm{i}\boldsymbol{k}_{\mathrm{L}}\cdot(\boldsymbol{r}'-\boldsymbol{r})} F(\boldsymbol{r}-\boldsymbol{r}')\mathrm{Tr}\left[\hat{\Psi}^\dagger(\boldsymbol{r})\hat{\Psi}^\dagger(\boldsymbol{r}')\hat{\Psi}(\boldsymbol{r}')\hat{\Psi}(\boldsymbol{r})\hat{\rho}\right]. \tag{5.91}$$

The first term is equal to the number of atoms N_{at}, and means that each atom emits a spontaneous photon with a rate Γ_{sp} independently from the others. The second term is however not readily evaluated and depends on the many-body state of the system. In order to give an estimate we consider two limiting cases: a coherent state modelling the superfluid phase and a Fock state modelling the Mott insulator phase. In the following we restrict our discussion to the dominant matrix elements $\Gamma_{\boldsymbol{i},\boldsymbol{j}} = \Gamma_{\boldsymbol{i},\boldsymbol{j},\boldsymbol{j},\boldsymbol{i}}$.

Fock state We first consider a Fock state with a filling fraction $\bar{n}$ constant over all N_{s} lattice sites, described as a product of Fock states over each site:

$$|\Psi\rangle = \bigotimes_{\text{sites } i} |\bar{n}\rangle_i \,. \tag{5.92}$$

We expand the field operators in the Wannier basis and restrict the discussion to the lowest band of the lattice. The second term in (5.91) reads

$$\sum_{\boldsymbol{i},\boldsymbol{j},\boldsymbol{k},\boldsymbol{l}} \Gamma_{\boldsymbol{i},\boldsymbol{j},\boldsymbol{k},\boldsymbol{l}} \langle\Psi|\hat{a}_{\boldsymbol{i}}^\dagger\hat{a}_{\boldsymbol{j}}^\dagger\hat{a}_{\boldsymbol{k}}\hat{a}_{\boldsymbol{l}}|\Psi\rangle \approx \sum_{\boldsymbol{i},\boldsymbol{j},\boldsymbol{k},\boldsymbol{l}} \delta_{\boldsymbol{i},\boldsymbol{l}}\delta_{\boldsymbol{j},\boldsymbol{k}}(1-\delta_{\boldsymbol{i},\boldsymbol{j}})\Gamma_{\boldsymbol{i},\boldsymbol{j}}\bar{n}^2 + \delta_{\boldsymbol{i},\boldsymbol{j}}\delta_{\boldsymbol{k},\boldsymbol{l}}\delta_{\boldsymbol{i},\boldsymbol{k}}\Gamma_{\boldsymbol{i},\boldsymbol{i}}\bar{n}(\bar{n}-1) \tag{5.93}$$

$$= \sum_{\boldsymbol{i}} \Gamma_{\boldsymbol{i},\boldsymbol{i}}\bar{n}(\bar{n}-1) + \sum_{\boldsymbol{i}\neq\boldsymbol{j}} \Gamma_{\boldsymbol{i},\boldsymbol{j}}\bar{n}^2 \tag{5.94}$$

$$= N_{\mathrm{s}}\Gamma_{\boldsymbol{0},\boldsymbol{0}}\bar{n}(\bar{n}-1) + N_{\mathrm{s}}\sum_{\boldsymbol{i}\neq\boldsymbol{0}} \Gamma_{\boldsymbol{i},\boldsymbol{0}}\bar{n}^2, \tag{5.95}$$

The normalised spontaneous emission rate is finally given by:

$$\Lambda = N_{\mathrm{at}}\left[\Gamma_{\mathrm{sp}} + \bar{n}\left(\Gamma^{\boldsymbol{0}}_{\mathrm{many}} + \sum_{\boldsymbol{i}\neq\boldsymbol{0}}\Gamma_{\boldsymbol{i},\boldsymbol{0}}\right) - \Gamma^{\boldsymbol{0}}_{\mathrm{many}}\right]. \tag{5.96}$$

Coherent state We then consider a coherent state, described as a product of coherent states over each site:

$$|\Psi\rangle = \bigotimes_{\text{sites } i} |\alpha\rangle_i \,, \tag{5.97}$$

with $|\alpha|^2 = \bar{n}$. We expand the field operators in the Wannier basis and restrict the discussion to the lowest band of the lattice. The second term in (5.91) reads

$$\sum_{\boldsymbol{i},\boldsymbol{j},\boldsymbol{k},\boldsymbol{l}} \Gamma_{\boldsymbol{i},\boldsymbol{j},\boldsymbol{k},\boldsymbol{l}} \langle\Psi|\hat{a}_{\boldsymbol{i}}^\dagger\hat{a}_{\boldsymbol{j}}^\dagger\hat{a}_{\boldsymbol{k}}\hat{a}_{\boldsymbol{l}}|\Psi\rangle = \sum_{\boldsymbol{i},\boldsymbol{j},\boldsymbol{k},\boldsymbol{l}} \Gamma_{\boldsymbol{i},\boldsymbol{j},\boldsymbol{k},\boldsymbol{l}}\bar{n}^2 \tag{5.98}$$

$$\approx \sum_{\boldsymbol{i}} \Gamma_{\boldsymbol{i},\boldsymbol{i}}\bar{n}^2 + \sum_{\boldsymbol{i}\neq\boldsymbol{j}} \Gamma_{\boldsymbol{i},\boldsymbol{j}}\bar{n}^2 \tag{5.99}$$

$$= N_{\mathrm{s}}\Gamma_{\boldsymbol{0},\boldsymbol{0}}\bar{n}^2 + N_{\mathrm{s}}\sum_{\boldsymbol{i}\neq\boldsymbol{0}} \Gamma_{\boldsymbol{i},\boldsymbol{0}}\bar{n}^2, \tag{5.100}$$

The normalised spontaneous emission rate is then given by:

$$\Lambda = N_{\mathrm{at}} \left[\Gamma_{\mathrm{sp}} + \bar{n} \left(\Gamma^{\mathbf{0}}_{\mathrm{many}} + \sum_{\boldsymbol{i} \neq \mathbf{0}} \Gamma_{\boldsymbol{i},\mathbf{0}} \right) \right]. \tag{5.101}$$

Conclusion The total scattering rate in both limits only differ by the coefficient $\Gamma^{\mathbf{0}}_{\mathrm{many}}$ which we evaluated to be ~ 0 for vanishing lattice depth, and ~ 0.8 in the Mott insulator regime. This points towards a reduction of the spontaneous emission rate with lattice depth.

The slow decay of the function F with distance does not really makes it possible to define a cut-off in the summation over the neighbours in (5.96) and (5.101). We can try to evaluate the 'dominant' contribution by completely neglecting the sum over neighbours and only keep the local terms. Figure 5.15 shows the expected total spontaneous emission rate for uniform systems with different filling fractions $\bar{n}$, where only local terms are considered.

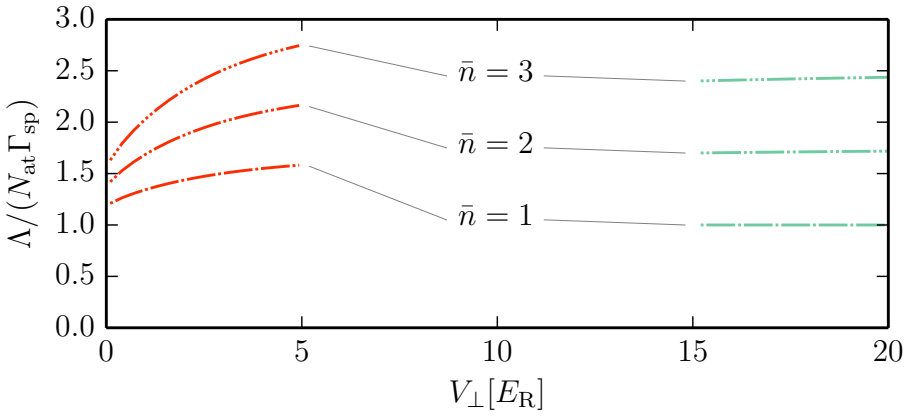

Figure 5.15: Normalised spontaneous emission rate Λ as a function of horizontal lattice depth $V_\perp$. For shallow lattice depth, Λ is calculated using a coherent state in (5.101). For deep lattice depth, Λ is calculated using a Fock state in (5.96). Standard spontaneous emission without collective effects would give $\Lambda = 1$.

The calculated values indicate super-radiance for all average filling fractions. This could be an explanation for the higher rate of interband transitions observed in Figure 5.13. While this could also be consistent with the observed values for the initial decay rate of the fraction of atoms at zero momentum (coefficient γ in Sections 4.2.3 and 4.2.4), we noted in Section 5.3.2 that the decoherence rate was bounded by Γ_{sp}. We therefore conclude that we expect super-radiant effects in our system but that they can not be seen in the decay of the coherence.

A proper account of the total spontaneous emission rate would include the summation over the neighbours. We tried to perform this summation in the limit of infinite lattice depth where $\Gamma_{\boldsymbol{i},\mathbf{0}} \approx |F(\boldsymbol{r_i}) \cos(\boldsymbol{k}_{\mathrm{L}} \cdot \boldsymbol{r_i})|$. However the slow decay of F makes the summation not to converge and to depend on the exact size of the system.

5.5 Conclusion

In this chapter, I have initiated a theoretical study of dissipation in optical lattices, including many-body effects in light-matter interactions. I first recalled the theoretical description of spontaneous emission by a two-level atom, presenting the derivation of the quantum master equation. I then studied various aspects related to diffusion of a single-particle in an optical lattice, showing how the predictions differ from the observations made in the previous chapter. Thereupon, I included a many-body description in the quantum master equation to account for a certain number of phenomena which might explain our observations. I have then shown that these collective effects are small but in principle not negligible, especially when considering the full dynamics in space and time. This should be accounted for in a proper modelling.

The complexity of the theoretical framework have limited me to the calculation of mere matrix elements, only allowing for a perturbative approach in the study of the relaxation dynamics. Numerical simulations of this system could be helpful to check whether dipole-dipole interactions do play a role in the initial decay of the coherences or in the higher transfer rates to excited bands. The predicted super-radiance of the superfluid phase could also be investigated in an experiment measuring the time-resolved fluorescence of the atomic sample. Finally, the observed and not quantitatively explained atom loss could be explored further in an experiment changing the detuning of the dissipation laser.

6

Summary and perspectives

In this thesis, I have presented an experimental investigation into the dynamics of ultracold ytterbium atoms loaded into optical lattices and driven by a laser light field. I have highlighted the crucial part played by inter-particle interactions on the atomic internal and external degrees of freedom dynamics, in limits both of coherent driving and dissipative dynamics. On the one hand, the coherent driving on the clock transition made possible the observation of interaction energy shifts and inelastic loss rates dependent on the internal state of the atoms. For that reason we have measured all relevant low-energy scattering properties of ^{174}Yb involving the clock states. On the other hand, the relaxation of a of a Bose-Hubbard gas subjected to spontaneous emission turned out to be slowed down by inter-atomic interactions. In that respect we have observed a remarkable change in the relaxation of a superfluid towards an anomalous momentum diffusion regime, brought about by the competition between interactions, motion and dissipation.

In Chapters 1 and 2, I presented all the ingredients required to witness the aforementioned observations. I first outlined the specific features of alkaline-earth-like atoms that are of great interest in recent works, both theoretical and experimental. I focused on the low-lying narrow transitions (the intercombination and the clock transitions) which correspond to the driving transitions used in the experiments mentioned above. After a concise reminder of the physics of ultracold atoms in optical lattices, I then described the contemplated implementation of artificial gauge fields in our laboratory. I explained why this is of major significance in the study of strongly correlated phases of matter in a magnetic field. I finally gave an account of the apparatus used to make the experiments described above. I explained how we create Bose-Einstein condensates of ^{174}Yb and load them into two-dimensional optical lattices. I also described our detection tool based on absorption imaging and the laser used to drive the clock transition.

In Chapter 3, I reported on the high-resolution optical spectroscopy of interacting ^{174}Yb atoms in deep optical lattices and demonstrated coherent control of isolated atoms and atom pairs. I first showed Rabi oscillations on the clock transition for singly-occupied isolated sites and then for both singly- and doubly-occupied isolated sites. The observed change in the time dynamics of these two experiments revealed strong inelastic losses in the excited clock state which allowed to characterise the loading sequence of the optical lattices. I quantitatively compared these measurements to a prediction from a simplified loading model based on the expected phase diagram of a Mott insulator. Using spectroscopy on the clock transition I finally presented the measurements of the intra- and inter-state scattering lengths involving both clock states. These results have been published in Bouganne et al. (2017). A simultaneous though independent work in Florence obtained results in agreement with our observations (Franchi et al. 2017).

In Chapter 4, I reported on the anomalous momentum diffusion of a Bose-Hubbard gas under dissipation. I first displayed the dramatic change in the relaxation dynamics of a superfluid subjected to spontaneous emission, which was activated by driving the

intercombination transition of ^{174}Yb. The analysis of momentum distributions revealed a sub-diffusive behaviour, the power-law exponent of which quantitatively agree with a model developed in Poletti et al. (2013). In this model, the slowing down of relaxation is interpreted with an anomalous diffusion in Fock space, where interactions compete with dissipation and coherent tunnelling. As a complementary evidence we also probed this diffusion in Fock space. However the model describes light-matter interaction simplified to its bare bones, and is insufficient to fully account for all our observations. I theoretically investigated the role of many-body effects for light-matter interactions in Chapter 5, based on a formalism presented in Pichler et al. (2010) and references therein. I first reviewed the diffusive dynamics of a single-particle in optical lattices and highlighted how this was very different from our observations. Using the quantum master equation formalism I then investigated the importance of many-body effects in the system: dipole-dipole interactions and collective spontaneous emission. I showed that these effects are not negligible and should be accounted for in a proper modelling of time dynamics. This experimental and theoretical work is under preparation for publication.

Perspectives

In the specific context of this experiment, we have already demonstrated the coherent driving of a degenerate cloud in magic optical lattices. This work was important to harness our experimental apparatus both concerning the loading of a degenerate quantum gas in optical lattices and the construction of a narrow laser to address the clock transition. The characterisation of the scattering properties of the clock states of ^{174}Yb was also important to foresee the implementation of strongly-correlated phases in a magnetic field. In order to realise the contemplated design proposed in Gerbier et al. (2010), various improvements have to be carried out.

- First, we need to implement the anti-magic and super-lattice potentials, the laser systems of which have been prepared by my colleague Manel Bosch Aguilera. This will allow us to realise a two-leg ladder for example, where the atomic motion is affected by the gauge field generated by the clock laser driving (Stuhl et al. 2015; Mancini et al. 2015).
- Secondly, we need to prepare a purely 2D atomic sample. At the beginning of my thesis work, I developed a transfer optical lattice with a period of 4 µm, intermediate between the Thomas-Fermi size of the condensate ($\sim$ 10 µm) and the vertical lattice period ($\sim$ 400 nm), that should allow the reproducible adiabatic transfer of the condensate into a single node of the vertical lattice. The stability of the central fringe of this transfer lattice was characterised to be 4 µm K^{-1} with a short-term position stability of the fringe maximum around 10 nm.
- Thirdly, we plan to set up an enhanced imaging system based on a high-resolution microscope objective combined with an EMCCD camera [see the diploma thesis of Elisa Soave (2016)]. The resolution of the objective was characterised to be $\sim$ 1 µm. This imaging system will be of importance to detect many-body features such as incompressible states.
- Finally, in order to reduce the inhomogeneities of the lattice potential due to the residual harmonic confinement, a tailored laser beam derived from a digital micro-mirror device will be added to the experiment in order to flatten the potential and create an area of uniform density in the center of the cloud. This is currently developed by my colleague Alexis Ghermaoui (2017).

In order to explore further the dissipation dynamics induced by spontaneous emission, the loading of a single plane in the vertical lattice combined with high-resolution imaging and compensated harmonic potential will be useful. With such a scheme we should be able to address experimentally the many-body effects in light-matter interactions with a better level of control. For example we could prepare a Mott insulator phase with only doubly-occupied sites and measure the dipole-dipole interaction shift using the clock transition. We could also try to study the influence of the spatial decay of dipole-dipole interactions by tuning the laser polarisation orientation. Furthermore, spatially-resolved fluorescence imaging could also provide insight into the collective effects in spontaneous emission, as well as studying in-situ spatial correlations in the cloud. Finally, we could use an infrared transition $\sim 2\,\mu$m from the metastable clock state to reach a regime where the wavelength of the emitted photon is larger than the lattice spacing. In this regime, many interesting collective effects arise (Olmos et al. 2013; Zhu et al. 2015; Shahmoon et al. 2017).

With our system we plan to realise effective magnetic fields in tight-binding systems, first using ladders and then going to genuine 2D systems. There is also an interesting opportunity to explore this physics in a bulk system. With the preparation of a two-dimensional BEC in a magic trap, one can realise an artificial magnetic field using the adiabatic following of a dressed state (Goldman et al. 2014). A suitably chosen propagating laser beam near-resonant with the clock transition creates a gradient of coupling strength orthogonal to the laser propagation. The eigenstate with the smallest energy connects adiabatically to the bare ground state of the atom on one side of the gradient and to the bare excited state on the other side. An atom moving in this laser beam can adiabatically follow this dressed state and acquire momentum perpendicular to its motional direction, thereby mimicking the effect of the Lorentz force on a charged particle. In this way an artificial magnetic field perpendicular to the 2D atomic sample is generated. This can possibly nucleate vortices in the sample if the artificial magnetic field is strong enough. However, losses in the excited clock state might prevent such an observation, or at least the stabilisation of a vortex lattice.

In a broader perspective, our system provides a natural playground to study the role of interactions and correlations in an open many-body system. We already discussed the work performed by inducing dissipation with spontaneous emission. Yet another way to engineer dissipation is to use the losses in the excited clock state. The effective Hamiltonian describing the physics of two atoms driven by the clock transition is non-Hermitian [see (3.18) in Chapter 3], which makes the 'eigenvectors' to separate into different subspaces with radically different lifetimes (these are referred to as gain and loss eigenvectors). When the energy levels associated to these eigenvectors become equal (they are said to 'coalesce') it creates a singularity called exceptional point (Heiss 2012). The tunability of the Hamiltonian parameters (the Rabi frequency and the laser detuning) could be used to perform loops around the exceptional points, which is expected to provide non-trivial chiral mode switching behaviours as well as topological properties (Mailybaev et al. 2005; Milburn et al. 2015; Doppler et al. 2016). This can be readily implemented in the experiment in deep optical lattices by performing ramps with the clock laser intensity and detuning. After preparing the system in a lossless subspace and studying the lifetime of the atomic sample while changing the Hamiltonian parameters, one can explore the physics around such exceptional points. Moreover, we have the additional ability to go from isolated atom pairs in deep lattices to a many-body phase for smaller lattice depths where atoms become mobile. In this regime the physics might change significantly.

A

Supplemental material for Chapter 2

A.1 Best-reference picture algorithm performance

In order to demonstrate the efficiency of the best-reference picture algorithm, we assess it on a set of 237 image pairs taken without atoms. We consider a 400-pixel wide square region of interest (ROI) with a 25-pixel wide background frame around it. We compare three different ways to analyse the image pairs (I_f being the image supposedly with atoms and I_i the reference image without atoms):

1. The *low-intensity* treatment where we compute the optical density on the assumption of small intensity of the light probe $\mathrm{OD}|_{I \ll I_{\mathrm{sat},0}} = -\ln(I_\mathrm{f}/I_\mathrm{i})$.

2. The *scaling* treatment where we compute the optical depth from (2.6) using a rescaled reference image κI_i, where κ is chosen to minimise the distance between the backgrounds of I_f and κI_i.

3. The *best-reference* treatment where we compute the optical depth from (2.6) with the best-reference picture Q as the reference image (see Section 2.2.3).

The results presented here are analysed on the region of interest only, whereas rescaling and optimisation for the second and third treatments are performed on the background frames only.

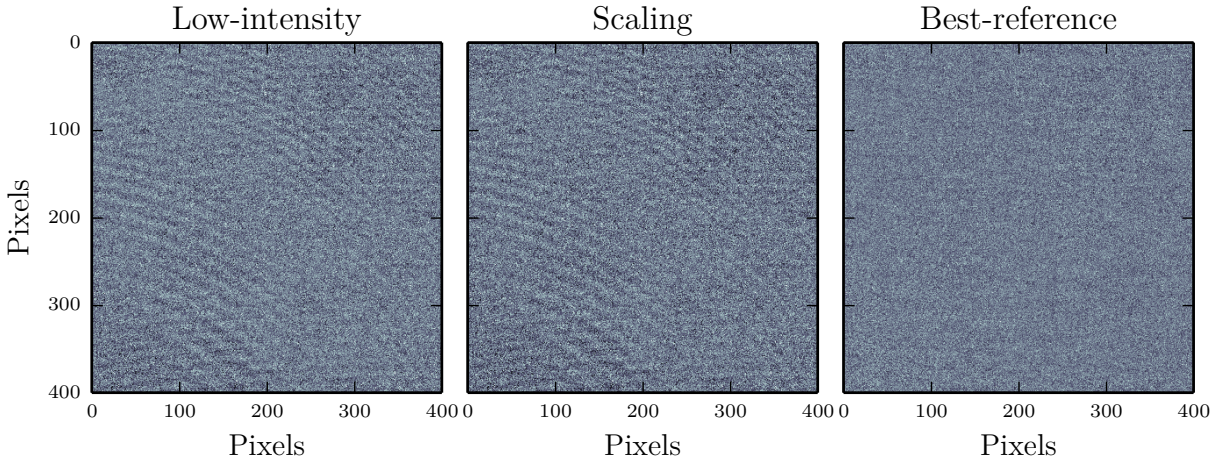

Figure A.1: Optical depths in the region of interest obtained from the different methods. It is clear that the fringes appearing in the low-intensity treatment cannot be removed using only a rescaling of the reference image. The best-reference picture provides a way to do so.

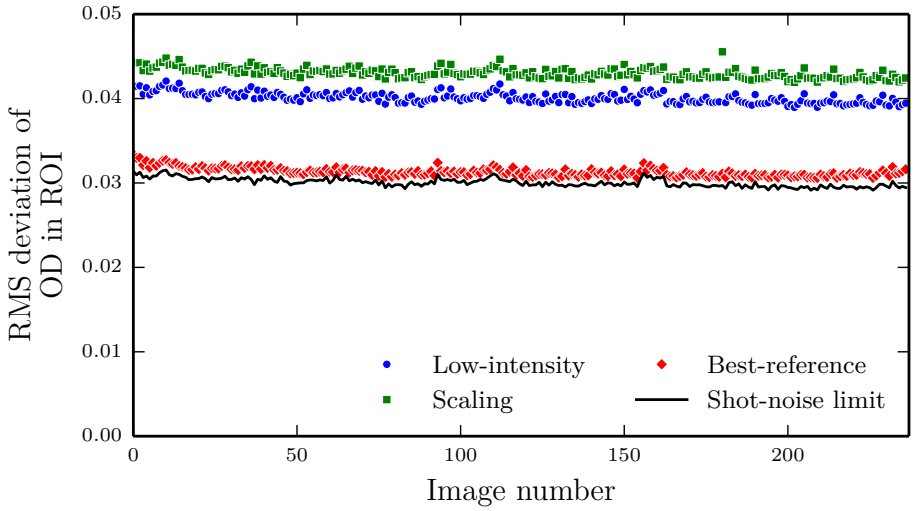

Figure A.2: Standard deviation (RMS) of the optical depth (OD) over the region of interest (ROI) for all the images of the set. While the scaling treatment degrades the quality of the pixel-to-pixel noise, the best-reference picture method gives a substantial improvement. The solid line is the predicted photon shot-noise limit, calculated from the average intensity over the region of interest.

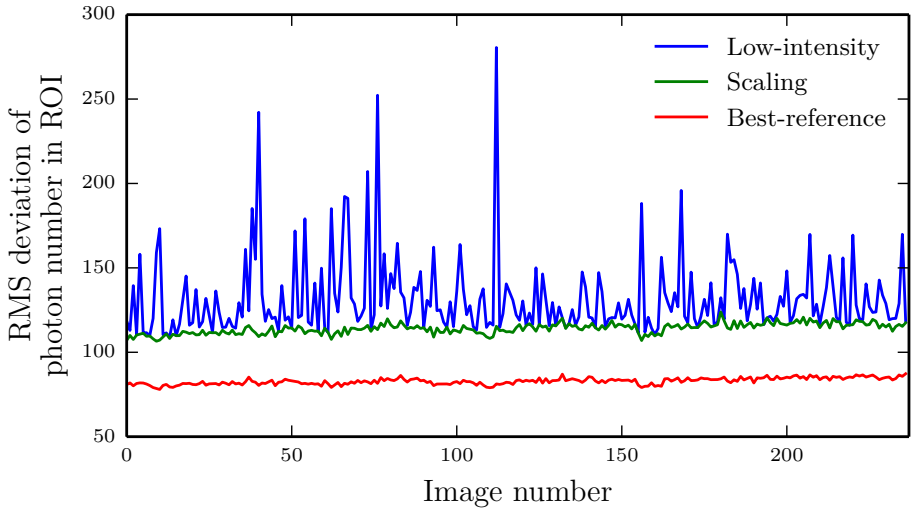

Figure A.3: Standard deviation of the difference between the image and its reference, in photon number. Here we clearly see that on many image pairs, there is a substantial change in the global intensity, which can be corrected using a simple rescaling of the reference picture. The best-reference picture treatment again improves the situation.

B

Supplemental material for Chapter 4

B.1 Dissipation in optical lattices: density matrix formalism

In this appendix I recall fundamental concepts used in this thesis to look at the relaxation of a quantum system. One of the most important tools to understand the physics in this context is the *density matrix* $\hat{\rho}$ which fully describes a quantum system in a statistical sense (Fano 1957). It is invaluable whenever there is some lack of knowledge about part of the system. I start by recalling some basic principles regarding the density matrix formalism, and then discuss the master equation in the Lindblad form.

B.1.1 Density matrix

The density matrix associated to a system represented by the state $|\Psi\rangle$ is the projection operator on that state:

$$\hat{\rho} = |\Psi\rangle\langle\Psi|. \tag{B.1}$$

The normalisation of the state $|\Psi\rangle$ makes the trace of $\hat{\rho}$ equal to one: $\mathrm{Tr}[\hat{\rho}] = 1$. The matrix elements $\rho_{nm} = \langle m|\,\hat{\rho}\,|n\rangle$ represent the coherence between the states $|n\rangle$ and $|m\rangle$ (those can originate from an infinite dimension basis such as the position basis with states $|\boldsymbol{r}\rangle$). The density matrix can equally represent pure states, for which $\mathrm{Tr}[\hat{\rho}^2] = 1$ or statistical mixtures for which $\mathrm{Tr}[\hat{\rho}^2] < 1$. The expectation value of an observable $\hat{\mathcal{O}}$ can be computed with the trace operator

$$\langle\hat{\mathcal{O}}\rangle = \mathrm{Tr}[\hat{\rho}\hat{\mathcal{O}}]. \tag{B.2}$$

From the Schrödinger equation governing the time evolution of $|\Psi\rangle$, one can derive an equation of motion for $\hat{\rho}$, called the Von-Neumann equation:

$$\mathrm{i}\hbar\frac{\mathrm{d}\hat{\rho}}{\mathrm{d}t} = [\hat{H}, \hat{\rho}], \tag{B.3}$$

which allows to track the dynamical evolution of the system under a Hamiltonian evolution. The eigenvalues of $\hat{\rho}$, its trace and the trace of $\hat{\rho}^2$ are conserved in this dynamics.

The density matrix approach is interesting when considering subsystems of the full system S. This is of particular importance when the state of the complete system cannot be known or measured. One can construct a partial density operator for a subsystem A by tracing over the degrees of freedom that do not belong to A:

$$\hat{\rho}_A = \mathrm{Tr}_{S\setminus A}\left[\hat{\rho}\right]. \tag{B.4}$$

In general, and even if $\hat{\rho}$ describes a pure state, $\hat{\rho}_A$ is not a projector on a quantum state any more: A and S are then said to be *entangled*. While constructing a partial

density operator is useful to derive properties of a subsystem, this opens up the way to decoherence. In the time evolution of the system S, correlations can build up between A and any other sub-part of S and as a result our knowledge of A gets reduced over time as information 'leaks out'.

B.1.2 Master equation

We now describe the theory of relaxation in quantum mechanics, that is to say the evolution of a system A coupled to an environment E the complexity of which makes it impossible to follow the detailed evolution of the complete system $A + E$. Under certain assumptions on the environment, an equation of motion for $\hat{\rho}_A$ can be derived: the *master equation*. The essential property that the environment must satisfy is the short memory time or Markov approximation, i.e. the correlation time τ_c of the environment is much smaller than the evolution time T_A of the system:

$$\tau_c \ll T_A. \tag{B.5}$$

Into what does this condition translates for the coupling strength between the system and the environment? Let us consider an environment or *reservoir* the energy levels of which span a wide energy range $\hbar\Delta\omega$. The correlation time τ_c of the observables of E is thus very short:

$$\tau_c = \frac{1}{\Delta\omega}. \tag{B.6}$$

The system A, coupled to such an amnesic environment through a weak coupling of magnitude V, undergoes a random walk with time steps $\sim \tau_c$. The phase dispersion $\Delta\varphi$ accumulated over a time t is thus given by :

$$\Delta\varphi^2 \approx \frac{V^2\tau_c^2}{\hbar^2}\frac{t}{\tau_c}. \tag{B.7}$$

This defines an evolution time scale for the system:

$$T_A = \frac{t}{\Delta\varphi^2} = \frac{\hbar^2}{V^2\tau_c^2}\tau_c. \tag{B.8}$$

The short memory time for the environment is thus equivalent to:

$$\tau_c \ll T_A \Leftrightarrow \frac{V\tau_c}{\hbar} \ll 1. \tag{B.9}$$

This condition is usually well-satisfied in quantum optics or atomic systems for which the correlation time of the reservoir is on the order of the inverse of an atom or photon frequency (Cohen-Tannoudji et al. 1992), while the coupling $V/\hbar$ (the Rabi frequency) is many orders of magnitude smaller.

This short memory time condition implies that the time differential equation for $\hat{\rho}_A$ cannot be too precise, and can only describe the 'coarse-grained' evolution of A, with a typical time step Δt much larger than τ_c. Such a description captures the time evolution of A if Δt is much smaller than the typical evolution time of A. This is summarised in the following condition:

$$\tau_c \ll \Delta t \ll T_A. \tag{B.10}$$

The Markov condition (B.9) allows to achieve (B.10). We can now define the coarse-grained time derivative of $\hat{\rho}_A$ as

$$\frac{\Delta\hat{\rho}_A}{\Delta t} = \frac{\hat{\rho}_A(t+\Delta t) - \hat{\rho}_A(t)}{\Delta t}. \tag{B.11}$$

$\hat{\rho}_A(t+\Delta t)$ is defined by a *quantum map* on $\hat{\rho}_A(t)$, $\mathcal{L}[\hat{\rho}_A(t)] = \hat{\rho}_A(t+\Delta t)$, i.e. a linear super-operator acting on the Hilbert space of the operators acting in the Hilbert space of A. It can be shown that such a quantum map $\mathcal{L}$ can always be represented in a simple form called the *Kraus sum representation* (Haroche et al. 2006):

$$\mathcal{L}[\hat{\rho}_A] = \Delta t \sum_{\mu=0}^{N_\mathrm{L}} \hat{C}_\mu \hat{\rho}_A \hat{C}_\mu^\dagger, \tag{B.12}$$

where N_L is smaller than the square of the Hilbert space dimension of A. Note that this number is independent from the size of the environment. The Lindblad operators $\hat{C}_\mu$ are not uniquely defined.

With some algebra (Haroche et al. 2006), one gets to the final expression of the master equation in the *Lindblad form*:

$$\frac{\mathrm{d}\hat{\rho}_A}{\mathrm{d}t} \equiv \frac{\Delta\hat{\rho}_A}{\Delta t} = \frac{1}{\mathrm{i}\hbar}\left[\hat{H}_A, \hat{\rho}_A\right] + \sum_{\mu>0}\left(\hat{C}_\mu\hat{\rho}_A\hat{C}_\mu^\dagger - \frac{1}{2}\hat{C}_\mu^\dagger\hat{C}_\mu\hat{\rho}_A - \frac{1}{2}\hat{\rho}_A\hat{C}_\mu^\dagger\hat{C}_\mu\right). \tag{B.13}$$

The specific form and ordering of the second term in (B.13) ensures the positivity and norm conservations of the master equation. The Lindblad operators can be seen as *quantum jump operators*, that make the system jump from a state $|\Psi\rangle$ to the completely different state $\hat{C}_\mu|\Psi\rangle$. The physical interpretation of the master equation is that the system evolves under a slow non-unitary evolution with rare quantum jump events. While the Lindblad master equation (B.13) is fairly general (provided the Markov condition holds), the difficulty lies in finding the proper Lindblad operators for a given physical situation.

While the master equation (B.13) can be solved analytically in simple cases, such as a two-level system coupled to the vacuum of photons [this leads to the well-known optical Bloch equations (Cohen-Tannoudji et al. 1992)], no general solution is known. Quantum Monte Carlo trajectories are one solution to numerically deal with (B.13) in that case, see the seminal proposition in Dalibard et al. (1992).

B.2 Master equation derivation for the dissipative Hubbard model

In this appendix, I derive the classical master equation (4.27) governing the evolution of the occupation number distribution at a given site $\rho(n)$, following closely Poletti et al. (2013). The starting point is the master equation for the density matrix $\hat{\rho}$ (Pichler et al. 2010; Cohen-Tannoudji et al. 1992),

$$\frac{\partial\hat{\rho}}{\partial t} = \frac{1}{\mathrm{i}\hbar}\left[\hat{H}, \hat{\rho}\right] + \kappa\hat{D}[\hat{\rho}], \tag{B.14}$$

$$\hat{D}[\hat{\rho}] = \sum_i \hat{n}_i\hat{\rho}\hat{n}_i - \frac{1}{2}\hat{n}_i^2\hat{\rho} - \frac{1}{2}\hat{\rho}\hat{n}_i^2. \tag{B.15}$$

We recall the Bose-Hubbard Hamiltonian governing the unitary dynamics of the system

$$\hat{H} = -J_\perp \sum_{\langle i,j \rangle} (\hat{a}_i^\dagger \hat{a}_j + \hat{a}_j^\dagger \hat{a}_i) + \frac{U}{2} \sum_i \hat{n}_i \left(\hat{n}_i - 1\right) = -J_\perp \hat{T} + \frac{U}{2} \hat{G}. \tag{B.16}$$

Coherences

We use (B.14) to calculate the time evolution of the coherences $\rho_{\boldsymbol{n}}^{\boldsymbol{n}+\boldsymbol{e}_i^j}$. We evaluate the local terms with $\hat{G}$ and $\hat{D}$

$$\langle \boldsymbol{n} + \boldsymbol{e}_i^j | \hat{G}\hat{\rho} - \hat{\rho}\hat{G} | \boldsymbol{n} \rangle = 2(n_i - n_j + 1) \rho_{\boldsymbol{n}}^{\boldsymbol{n}+\boldsymbol{e}_i^j},$$
$$\langle \boldsymbol{n} + \boldsymbol{e}_i^j | \hat{D}[\hat{\rho}] | \boldsymbol{n} \rangle = -\rho_{\boldsymbol{n}}^{\boldsymbol{n}+\boldsymbol{e}_i^j}.$$

Non-local tunnelling terms from $\hat{T}$ give

$$\hat{T}|\boldsymbol{n}\rangle = \sum_{\langle i,j \rangle} \sqrt{n_j(n_i+1)} |\boldsymbol{n} + \boldsymbol{e}_i^j\rangle + \sqrt{n_i(n_j+1)} |\boldsymbol{n} + \boldsymbol{e}_j^i\rangle.$$

The density matrix is dominated by its diagonal with weak contribution from off-diagonal coherences between Fock configurations differing by one-atom tunnelling events. Weaker higher-order tunnelling events create also off-diagonal elements, but we neglect them. Therefore we only keep the dominant terms that couple to the populations

$$\langle \boldsymbol{n} + \boldsymbol{e}_i^j | \hat{T}\hat{\rho} - \hat{\rho}\hat{T} | \boldsymbol{n} \rangle \approx \sqrt{n_j(n_i+1)} \left(\rho_{\boldsymbol{n}}^{\boldsymbol{n}} - \rho_{\boldsymbol{n}+\boldsymbol{e}_i^j}^{\boldsymbol{n}+\boldsymbol{e}_i^j} \right),$$

from which we get

$$\mathrm{i}\hbar \frac{\mathrm{d}}{\mathrm{d}t} \rho_{\boldsymbol{n}}^{\boldsymbol{n}+\boldsymbol{e}_i^j} = \left[U(n_i - n_j + 1) - \mathrm{i}\hbar\kappa \right] \rho_{\boldsymbol{n}}^{\boldsymbol{n}+\boldsymbol{e}_i^j} - J_\perp \sqrt{n_j(n_i+1)} \left(\rho_{\boldsymbol{n}}^{\boldsymbol{n}} - \rho_{\boldsymbol{n}+\boldsymbol{e}_i^j}^{\boldsymbol{n}+\boldsymbol{e}_i^j} \right). \tag{B.17}$$

In the limit where U dominates over $J_\perp$ and κ, the coherences evolve much more rapidly than the populations. The coherences are thus slave variables with respect to the populations, their faster evolution average out to a time-dependent steady-state that follows the slower dynamics of the populations. In this case we can perform an adiabatic elimination of the coherences (Cohen-Tannoudji et al. 1992) and approximate the coherences by their steady-state value

$$\rho_{\boldsymbol{n}}^{\boldsymbol{n}+\boldsymbol{e}_i^j}\big|_{\mathrm{ss}} \approx \frac{J_\perp \sqrt{n_j(n_i+1)}}{U(n_i - n_j + 1) - \mathrm{i}\hbar\kappa} \left(\rho_{\boldsymbol{n}}^{\boldsymbol{n}} - \rho_{\boldsymbol{n}+\boldsymbol{e}_i^j}^{\boldsymbol{n}+\boldsymbol{e}_i^j} \right). \tag{B.18}$$

Populations

Similarly, we calculate the evolution of the populations $\rho_{\boldsymbol{n}}^{\boldsymbol{n}}$

$$\mathrm{i}\hbar \frac{\mathrm{d}}{\mathrm{d}t} \rho_{\boldsymbol{n}}^{\boldsymbol{n}} = -J_\perp \sum_{\langle i,j \rangle} \sqrt{n_j(n_i+1)} \left(\rho_{\boldsymbol{n}}^{\boldsymbol{n}+\boldsymbol{e}_i^j} - \rho_{\boldsymbol{n}+\boldsymbol{e}_i^j}^{\boldsymbol{n}} \right) + \sqrt{n_i(n_j+1)} \left(\rho_{\boldsymbol{n}}^{\boldsymbol{n}+\boldsymbol{e}_j^i} - \rho_{\boldsymbol{n}+\boldsymbol{e}_j^i}^{\boldsymbol{n}} \right). \tag{B.19}$$

Replacing the nearest-neighbour coherences by their steady-state value (B.18), and neglecting coherences at longer range, we can write

$$\frac{\mathrm{d}}{\mathrm{d}t} \rho_{\boldsymbol{n}}^{\boldsymbol{n}} = -\frac{2J_\perp^2 \kappa}{U^2} \sum_{(i,j)} \frac{n_j(n_i+1)}{(n_i - n_j + 1)^2 + \epsilon^2} \left(\rho_{\boldsymbol{n}}^{\boldsymbol{n}} - \rho_{\boldsymbol{n}+\boldsymbol{e}_i^j}^{\boldsymbol{n}+\boldsymbol{e}_i^j} \right), \tag{B.20}$$

with $\epsilon = \hbar\kappa/U$ and the notation (i,j) referring to all nearest-neighbour pairs, counted both ways. This summation is equivalent to a double sum over all lattice sites i firstly, and their nearest-neighbours j secondly. Following Poletti et al. (2013), we introduce the time t^*

$$t^* = \left(\frac{U}{J_\perp}\right)^2 \frac{\bar{n}^2}{2\kappa z}, \tag{B.21}$$

with z the number of nearest neighbours, and a reduced time $\tau = t/t^*$. We then have

$$\frac{\mathrm{d}}{\mathrm{d}\tau}\rho_{\boldsymbol{n}}^{\boldsymbol{n}} = -\frac{\bar{n}^2}{z}\sum_{(i,j)} \frac{n_j(n_i+1)}{(n_i-n_j+1)^2+\epsilon^2}\left(\rho_{\boldsymbol{n}}^{\boldsymbol{n}} - \rho_{\boldsymbol{n}+\boldsymbol{e}_i^j}^{\boldsymbol{n}+\boldsymbol{e}_i^j}\right). \tag{B.22}$$

The timescales that govern the three regimes mentioned in Section 4.3 are (Poletti et al. 2013):

- $t \leq \kappa^{-1}$, initial exponential relaxation of coherences,
- $\kappa^{-1} \leq t \leq t^*$, algebraic regime with slow decay of populations,
- $t \geq t^*$, stretched exponential regime, final relaxation towards the steady-state.

B.3 Continuum approximation for large fillings

In this appendix, I give more details about the continuum approximation for large fillings as used in Poletti et al. (2013) to obtain analytical expressions. I also derive the scaling form of the nearest-neighbour correlator (4.37). In the limit of large filling fractions $\bar{n} \gg 1$, the discrete occupation number n can be replaced by a continuous variable $x \mapsto n/\bar{n} \in \mathbb{R}^+$ and the occupation number distribution becomes $\rho(n,\tau) \mapsto p(x,\tau)/\bar{n}$. We can use $1/\bar{n}$ as an infinitesimal quantity and thus

$$\rho(n+1,\tau) = \frac{1}{\bar{n}}p(x+1/\bar{n},\tau) \approx \frac{1}{\bar{n}}p(x,\tau) + \frac{1}{\bar{n}^2}\frac{\partial p(x,\tau)}{\partial x} + \frac{1}{2\bar{n}^3}\frac{\partial^2 p(x,\tau)}{\partial x^2}. \tag{B.23}$$

Fokker-Planck form

The master equation (4.29) written for the continuous distribution is

$$\frac{\partial p}{\partial \tau} = \bar{n}^2 \sum_{\nu=\pm 1}\int_{\mathbb{R}^+} \frac{(x\bar{n}+\delta_{1,\nu})(y\bar{n}+\delta_{-1,\nu})}{(x\bar{n}-y\bar{n}+\nu)^2+\epsilon^2}\left[p(x+\nu\mathrm{d}x,\tau)p(y-\nu\mathrm{d}y,\tau) - p(x,\tau)p(y,\tau)\right]\mathrm{d}y. \tag{B.24}$$

We define $\mathcal{D}(x,y) = xy/[(x-y)^2+\bar{\epsilon}^2]$ with $\bar{\epsilon} = \epsilon/\bar{n}$. Noting that $\nu = \delta_{1,\nu} - \delta_{-1,\nu}$,

$$\frac{\partial p}{\partial \tau} = \bar{n}^2 \sum_{\nu=\pm 1}\int_{\mathbb{R}^+} \mathcal{D}(x+\delta_{1,\nu}\mathrm{d}x, y+\delta_{-1,\nu}\mathrm{d}y)\left[p(x+\nu\mathrm{d}x,\tau)p(y-\nu\mathrm{d}y,\tau) - p(x,\tau)p(y,\tau)\right]\mathrm{d}y. \tag{B.25}$$

We expand the integrand up to second order in $1/\bar{n}$, leading to

$$\frac{\partial p(x,\tau)}{\partial \tau} = \int_{\mathbb{R}^+}\left(\frac{\partial \mathcal{D}(x,y)}{\partial x} - \frac{\partial \mathcal{D}(x,y)}{\partial y}\right)\left[\frac{\partial p(x,\tau)}{\partial x}p(y,\tau) - p(x,\tau)\frac{\partial p(y,\tau)}{\partial y}\right] \tag{B.26}$$

$$+ \mathcal{D}(x,y)\left[\frac{\partial^2 p(x,\tau)}{\partial x^2}p(y,\tau) + \frac{\partial^2 p(y,\tau)}{\partial y^2}p(x,\tau) - 2\frac{\partial p(x,\tau)}{\partial x}\frac{\partial p(y,\tau)}{\partial y}\right]\mathrm{d}y. \tag{B.27}$$

We can rewrite this in a more compact form

$$\frac{\partial p(x,\tau)}{\partial \tau} = \int_{\mathbb{R}^+} \left(\frac{\partial}{\partial x} - \frac{\partial}{\partial y}\right) \left[\mathcal{D}(x,y) \left(\frac{\partial}{\partial x} - \frac{\partial}{\partial y}\right) p(x,\tau)p(y,\tau)\right] \mathrm{d}y. \tag{B.28}$$

This integrand is the sum of two integrands if we expand the first partial derivatives. In the first term, we can swap the integral and the partial derivative with respect to x. In the second term we have the integral of a derivative on the same variable, which evaluates to zero because $\mathcal{D}(x,y)$ vanishes in 0 and $+\infty$ and p is a bounded function. Therefore we can write the master equation in the integro-differential form

$$\frac{\partial p(x,\tau)}{\partial \tau} = \frac{\partial}{\partial x}\left[D(x,\tau)\frac{\partial p(x,\tau)}{\partial x} - F(x,\tau)p(x,\tau)\right], \tag{B.29}$$

with

$$D(x,\tau) = \int_{\mathbb{R}^+} \frac{xy\ p(y,\tau)}{(x-y)^2+\bar{\epsilon}^2}\mathrm{d}y \text{ and } F(x,\tau) = \int_{\mathbb{R}^+} \frac{xy\ \partial p(y,\tau)/\partial y}{(x-y)^2+\bar{\epsilon}^2}\mathrm{d}y. \tag{B.30}$$

The master equation in the form (B.29) is a Fokker-Planck equation. With this expression one can prove the conservation of the norm and of the mean value of p. It is the starting point of the analytical derivation performed in Poletti et al. (2013) where they demonstrate a scaling form in the algebraic regime of the decay and a stretched exponential form in the final stage.

Spatial coherence

We perform the same type of calculation for the one-body nearest-neighbour correlator C_1. Its expression (4.34) written for the continuous distribution is

$$C_1(\tau) = \frac{J_\perp}{U}\int_{\mathbb{R}+2} \frac{xy}{x-y-\mathrm{i}\bar{\epsilon}}\left[p(x,\tau)\frac{\partial p(y,\tau)}{\partial y} - \frac{\partial p(x,\tau)}{\partial x}p(y,\tau)\right]\mathrm{d}x\mathrm{d}y. \tag{B.31}$$

In the limit of weak dissipation ($\bar{\epsilon}\to 0$), we can use the scaling form (4.31) so that

$$C_1(\tau) = \frac{J_\perp}{U}\int_{\mathbb{R}+2} \frac{xy}{x-y}p(x,\tau)p(y,\tau)\frac{1}{4\tau}\left[(x-1)^3-(y-1)^3\right]\mathrm{d}x\mathrm{d}y. \tag{B.32}$$

We then perform a change of variables $(x,y)\mapsto(u=(x-1)/\tau^{1/4}, v=(y-1)/\tau^{1/4})$

$$C_1(\tau) = \frac{J_\perp}{4U}\int_\Upsilon \left(1+u\tau^{1/4}\right)\left(1+v\tau^{1/4}\right)p(u,\tau)p(v,\tau)\left[u^2+uv+v^2\right]\mathrm{d}u\mathrm{d}v, \tag{B.33}$$

where the integral is now performed on the domain $\Upsilon = [-\tau^{-1/4},+\infty]^2$.

For short enough times, the distribution p is peaked around $u=0$ so that we can (i) extend the domain of integration to $\mathbb{R}^2$, (ii) neglect $u\tau^{1/4}$ and $v\tau^{1/4}$ compared to 1:

$$\begin{aligned} C_1(\tau) &\approx \frac{J_\perp}{4U}\int_{\mathbb{R}^2} p(u,\tau)p(v,\tau)\left[u^2+uv+v^2\right]\mathrm{d}u\mathrm{d}v && \text{(B.34)}\\ &= \frac{J_\perp}{U\sqrt{\tau}}\times\frac{1}{64\Gamma(5/4)^2}\int_{\mathbb{R}^2}\left(u^2+uv+v^2\right)\mathrm{e}^{-(u^4+v^4)/16}\mathrm{d}u\mathrm{d}v && \text{(B.35)}\\ &= \frac{J_\perp}{U\sqrt{\tau}}\frac{2\Gamma(3/4)}{\Gamma(1/4)}, && \text{(B.36)} \end{aligned}$$

where Γ is the Gamma function. This is the result given in (4.37).

B.4 Fitting procedure for the momentum distribution

In order to fit the measured momentum distributions with the model of (4.44), we perform a χ^2 minimisation

$$\chi^2 = \sum_{\text{pixels}} \left(\frac{\tilde{n} - n_{\text{tof}}}{\sigma} \right)^2, \tag{B.37}$$

where $\tilde{n}$ is the measured momentum distribution (image of the atoms using resonant absorption, with $N_{\text{pix}} \times N_{\text{pix}}$ pixels squared) and n_{tof} defined in (4.44). We assume normally distributed intensities on the pixels with variance σ (typical noise of roughly 10 % of the maximal optical density, assumed uniform across the image). I normalise all distributions to 1, i.e. $\sum_{\text{pixels}} \tilde{n} = 1$ and $\sum_{\text{pixels}} n_{\text{tof}} = 1$.

The minimisation of (B.37) is performed using $M = 7$ free parameters that we group into a vector $\mathbf{x} = (\mathcal{P}_1, \mathcal{P}_2, \mathcal{P}_3, \mathcal{C}_0, \mathcal{C}_1, \mathcal{C}_2, \mathcal{G})$. We also write $n_{\text{tof}} = \mathbf{p} \cdot \mathbf{x}$ with

$$\mathbf{p} = \left(|W_1|^2, |W_2|^2, |W_3|^2, 2|W_0|^2, |W_0|^2 \sum_{\alpha=x,y} \cos\left(k_\alpha d\right), |W_0|^2 \sum_{\alpha=x,y} \cos\left(2k_\alpha d\right), G \right). \tag{B.38}$$

χ^2 is a therefore a quadratic form with respect to $\mathbf{x}$ which we write

$$\chi^2 = a + \mathbf{b} \cdot \mathbf{x} + \mathbf{x}^T \cdot Q \cdot \mathbf{x}, \text{ with the normalisation } \mathbf{d} \cdot \mathbf{x} = 1, \tag{B.39}$$

where we identify

$$a = \sum_{\text{pixels}} \frac{\tilde{n}^2}{\sigma^2}, \ \mathrm{b}_i = \sum_{\text{pixels}} \frac{-2\tilde{n}\mathrm{p}_i}{\sigma^2}, \ Q_{ij} = \sum_{\text{pixels}} \frac{\mathrm{p}_i \mathrm{p}_j}{\sigma^2}, \ \mathrm{d}_i = \sum_{\text{pixels}} \mathrm{p}_i. \tag{B.40}$$

The matrix Q is symmetric and positive definite. I hence need to minimise the Lagrangian $\mathcal{L} = \chi^2 + \mu(\mathbf{d} \cdot \mathbf{x} - 1)$, which is still a quadratic form and where μ is a Lagrange multiplier that includes the normalisation constraint. Taking the first-order derivatives to zero leads to an invertible linear system of equations

$$\begin{cases} \partial\mathcal{L}/\partial x_i = 0, \forall i \\ \partial\mathcal{L}/\partial\mu = 0 \end{cases} \iff \begin{cases} 2Q \cdot \mathbf{x} + \mathbf{b} + \mu\mathbf{d} = 0 \\ \mathbf{d} \cdot \mathbf{x} - 1 = 0 \end{cases} \tag{B.41}$$

The solution of this system gives the optimal set of parameters $\mathbf{x}^0$ and the optimal χ^2 value should be close to the number of degrees of freedom $N_{\text{pix}}^2 - M$. Confidence intervals on these parameters are calculated by computing surfaces of iso-χ^2 with the normalisation condition $\mathbf{d} \cdot \mathbf{x} = 1$. A convenient way to do this is to write the quadratic form of the χ^2 as (true if we assume the normalisation condition to always hold):

$$\Delta\chi^2 = \chi^2 - \chi^2_{\text{min}} = (\mathbf{x} - \mathbf{x}^0)^T \cdot Q \cdot (\mathbf{x} - \mathbf{x}^0) = \delta\mathbf{x}^T \cdot Q \cdot \delta\mathbf{x}. \tag{B.42}$$

The covariance matrix of this optimisation problem is given by $R = Q^{-1}$. The quantity $\Delta\chi^2$ is distributed as a χ^2 distribution with M degrees of freedom (Press 2007). The ellipsoid defined by $\Delta\chi^2 = p_M$ encloses a volume which includes the true parameters with a probability that depends on the value of p_M. A χ^2 distribution with M degrees of freedom is identical to a Γ-distribution with shape $M/2$ and scale $1/2$ (Bohm et al.

2010). One can calculate p_M in such a way that the cumulative density function of the latter Γ-distribution equals 68.3%. In our case $p_7 \approx 8.18$.

Confidence intervals are given by the projection of the ellipsoid on the parameters axes, this is done by intersecting the axes with the tangential planes of the ellipsoid which are normal to the axes. The gradient of the ellipsoid surface gives a normal vector $\boldsymbol{J}$ to the surface $\boldsymbol{J} = 2Q \cdot \delta\mathbf{x}$. This normal vector defines a relevant tangential plane when it is collinear to one of the parameter axes $\boldsymbol{e}_i$. I therefore need to solve the linear system

$$2Q \cdot \delta\mathbf{x}^i = \eta \boldsymbol{e}_i. \tag{B.43}$$

Since Q is positive definite, it is invertible and $\delta x^i_j = R_{ij}\eta/2$. $\delta\mathbf{x}^i$ is simply the ith column of R multiplied by $\eta/2$. The ellipsoid surface equation becomes

$$\frac{\eta^2}{4}\sum_{kl} R_{ik}R_{il}Q_{kl} = p_M \Longleftrightarrow \frac{\eta^2}{4}R_{ii} = p_M, \tag{B.44}$$

which gives two solutions for η (the two opposite sides of the ellipsoid). The confidence interval on the ith parameter is therefore given by:

$$x_i = x_i^0 \pm \delta x_i^i = x_i^0 \pm \sqrt{p_M R_{ii}}. \tag{B.45}$$

B.5 Analysis of atom losses in a quenched optical lattice

The loss dynamics of atoms in a deep lattice is described generally by a master equation for the density matrix $\hat{\rho}$ with Lindblad operators $\hat{L}_k = \hat{a}^k_{\boldsymbol{i}}$ describing the destruction of k atoms in site $\boldsymbol{i}$ (we dropped the band index for clarity):

$$\frac{\mathrm{d}\hat{\rho}}{\mathrm{d}t} = \frac{1}{\mathrm{i}\hbar}\left[\hat{H}, \hat{\rho}\right] + \sum_{k=2,3}\gamma_k \sum_{\boldsymbol{i}}\left[\hat{a}^k_{\boldsymbol{i}}\hat{\rho}\hat{a}^{\dagger k}_{\boldsymbol{i}} - \frac{1}{2}\hat{a}^{\dagger k}_{\boldsymbol{i}}\hat{a}^k_{\boldsymbol{i}}\hat{\rho} - \frac{1}{2}\hat{\rho}\hat{a}^{\dagger k}_{\boldsymbol{i}}\hat{a}^k_{\boldsymbol{i}}\right], \tag{B.46}$$

$$\gamma_k = L_k \int \mathrm{d}^3 r\, |w_{\mathbf{0}}|^{2k}. \tag{B.47}$$

The loss constants L_k only depend on the atom and we assume that γ_k does not depend on the site position (the inhomogeneity of the potential does not appreciably change the Wannier function). The time evolution of the probability $p^{\boldsymbol{i}}_n$ of finding n atoms at a particular site $\boldsymbol{i}$ is computed by projecting the master equation (B.46) on the state $|n\rangle_{\boldsymbol{i}}$:

$$\frac{\mathrm{d}p^{\boldsymbol{i}}_n}{\mathrm{d}t} = \sum_{k=2,3}\gamma_k\left[(n+1)\dots(n+k)p^{\boldsymbol{i}}_{n+k} - n(n-1)\dots(n-k+1)p^{\boldsymbol{i}}_n\varepsilon_k\right], \tag{B.48}$$

with $\varepsilon_k = 0$ if $n < k$ and 1 otherwise. The space with n atoms decays to the $n-k$ space and is fed by the $n+k$ space. The mean atom number per site $\langle n\rangle_{\boldsymbol{i}} = \sum_n n p^{\boldsymbol{i}}_n$ evolves as

$$\frac{\mathrm{d}\langle n\rangle_{\boldsymbol{i}}}{\mathrm{d}t} = -\sum_{k=2,3} k\gamma_k \sum_{n\geq k} n(n-1)\dots(n-k+1)p^{\boldsymbol{i}}_n, \tag{B.49}$$

$$N_{\mathrm{at}}(t) = \sum_{\boldsymbol{i}}\langle n\rangle_{\boldsymbol{i}}(t). \tag{B.50}$$

We define a cumulative probability $p_n = \sum_{\boldsymbol{i}} p_n^{\boldsymbol{i}}$, we have:

$$\frac{\mathrm{d}p_n}{\mathrm{d}t} = \sum_{k=2,3} \gamma_k \left[(n+1)\dots(n+k)p_{n+k} - n(n-1)\dots(n-k+1)p_n\varepsilon_k\right], \tag{B.51}$$

$$N_{\mathrm{at}}(t) = \sum_n n p_n(t) = \sum_n N_n(t), \tag{B.52}$$

where N_n corresponds to the number of atoms in the Mott shell with n atoms per site. The solution of this system can be readily computed in the experimentally relevant limit $\gamma_2 \ll \gamma_3$, and we truncate the Fock space to $n \leq 4$ since higher occupancies are not expected (see Section 4.3.5):

$$p_0(t) = (1 - \mathrm{e}^{-2\gamma_2 t})p_2(0) + (1 - \mathrm{e}^{-6\gamma_3 t})p_3(0), \tag{B.53}$$

$$p_1(t) = p_1(0) + (1 - \mathrm{e}^{-24\gamma_3 t})p_4(0), \tag{B.54}$$

$$p_2(t) = \mathrm{e}^{-2\gamma_2 t}p_2(0), \tag{B.55}$$

$$p_3(t) = \mathrm{e}^{-6\gamma_3 t}p_3(0), \tag{B.56}$$

$$p_4(t) = \mathrm{e}^{-24\gamma_3 t}p_4(0). \tag{B.57}$$

C

Supplemental material for Chapter 5

C.1 Bloch waves matrix elements α

In this section, I give the derivation of various results used in the main text. The calculations are performed in the 3D case with the dissipation laser wavevector $\boldsymbol{k}_\mathrm{L}$ oriented along $\boldsymbol{e}_z$.

C.1.1 Explicit form of the matrix elements α

We write the Bloch waves[1]

$$|\boldsymbol{n},\boldsymbol{q}\rangle = \mathrm{e}^{\mathrm{i}\boldsymbol{q}\cdot\boldsymbol{R}} \sum_{\boldsymbol{K}} C^{\boldsymbol{n}}_{\boldsymbol{q}+\boldsymbol{K}} \,|\boldsymbol{K}\rangle\,, \tag{C.1}$$

where $\boldsymbol{K}$ designates a reciprocal lattice vector and $|\boldsymbol{k}\rangle$ a plane wave with wavevector $\boldsymbol{k}$. We are interested in the effect of the translation operator on a Bloch wave $|\boldsymbol{n},\boldsymbol{q}\rangle$. Let then consider a shift of momentum $\hbar\boldsymbol{p}$,

$$\begin{aligned}
\alpha^{\boldsymbol{n},\boldsymbol{n}'}_{\boldsymbol{q},\boldsymbol{q}'}(\boldsymbol{p}) &= \langle \boldsymbol{n}',\boldsymbol{q}'|\, \mathrm{e}^{\mathrm{i}\boldsymbol{p}\cdot\hat{\boldsymbol{R}}}\, |\boldsymbol{n},\boldsymbol{q}\rangle && \text{(C.2)}\\
&= \langle \boldsymbol{n}',\boldsymbol{q}'| \sum_{\boldsymbol{K}} C^{\boldsymbol{n}}_{\boldsymbol{q}+\boldsymbol{K}} \,|\boldsymbol{K}+\boldsymbol{q}+\boldsymbol{p}\rangle && \text{(C.3)}\\
&= \sum_{\boldsymbol{K},\boldsymbol{K}'} \left(C^{\boldsymbol{n}'}_{\boldsymbol{q}'+\boldsymbol{K}'}\right)^* C^{\boldsymbol{n}}_{\boldsymbol{q}+\boldsymbol{K}} \,\langle \boldsymbol{K}'+\boldsymbol{q}'|\boldsymbol{K}+\boldsymbol{q}+\boldsymbol{p}\rangle && \text{(C.4)}\\
&= \left(\frac{2\pi}{L}\right)^3 \sum_{\boldsymbol{K},\boldsymbol{L}} \left(C^{\boldsymbol{n}'}_{\boldsymbol{q}'+\boldsymbol{K}-\boldsymbol{L}}\right)^* C^{\boldsymbol{n}}_{\boldsymbol{q}+\boldsymbol{K}} \delta^{(3)}\left(\boldsymbol{q}+\boldsymbol{p}-\boldsymbol{q}'+\boldsymbol{L}\right). && \text{(C.5)}
\end{aligned}$$

We can obtain a further understanding of α by going to the Wannier basis:

$$|\boldsymbol{n},\boldsymbol{q}\rangle = \left(\frac{d}{L}\right)^{3/2} \sum_{\boldsymbol{i}} \mathrm{e}^{\mathrm{i}\boldsymbol{q}\cdot\boldsymbol{r}_{\boldsymbol{i}}} \,|w^{\boldsymbol{n}}_{\boldsymbol{i}}\rangle\,. \tag{C.6}$$

[1] Here we adopt the notation from Ashcroft et al. (1976) for compactness.

We can thus write

$$\alpha_{\boldsymbol{q},\boldsymbol{q}'}^{\boldsymbol{n},\boldsymbol{n}'}(\boldsymbol{p}) = \left(\frac{d}{L}\right)^3 \sum_{\boldsymbol{i},\boldsymbol{j}} \mathrm{e}^{\mathrm{i}(\boldsymbol{q}'\cdot\boldsymbol{r_j}-\boldsymbol{q}\cdot\boldsymbol{r_i})} \langle w_{\boldsymbol{i}}^{\boldsymbol{n}}| \, \mathrm{e}^{\mathrm{i}\boldsymbol{p}\cdot\hat{\boldsymbol{R}}} \, |w_{\boldsymbol{j}}^{\boldsymbol{n}'}\rangle \tag{C.7}$$

$$\approx \left(\frac{d}{L}\right)^3 \sum_{\boldsymbol{i}} \mathrm{e}^{\mathrm{i}(\boldsymbol{q}'-\boldsymbol{q})\cdot\boldsymbol{r_i}} \langle w_{\boldsymbol{i}}^{\boldsymbol{n}}| \, \mathrm{e}^{\mathrm{i}\boldsymbol{p}\cdot\hat{\boldsymbol{R}}} \, |w_{\boldsymbol{i}}^{\boldsymbol{n}'}\rangle \tag{C.8}$$

$$= \left(\frac{d}{L}\right)^3 \sum_{\boldsymbol{i}} \mathrm{e}^{\mathrm{i}(\boldsymbol{q}'-\boldsymbol{q}+\boldsymbol{p})\cdot\boldsymbol{r_i}} \langle w_{\boldsymbol{0}}^{\boldsymbol{n}}| \, \mathrm{e}^{\mathrm{i}\boldsymbol{p}\cdot\hat{\boldsymbol{R}}} \, |w_{\boldsymbol{0}}^{\boldsymbol{n}'}\rangle \tag{C.9}$$

$$= \left(\frac{2\pi}{L}\right)^3 \delta^{(3)}(\boldsymbol{q}'-\boldsymbol{q}+\boldsymbol{p}) \langle w_{\boldsymbol{0}}^{\boldsymbol{n}}| \, \mathrm{e}^{\mathrm{i}\boldsymbol{p}\cdot\hat{\boldsymbol{R}}} \, |w_{\boldsymbol{0}}^{\boldsymbol{n}'}\rangle \, . \tag{C.10}$$

The second equality is obtained in the tight-binding limit where only local terms are kept. We show here that the matrix element α characterises the coupling with a photon of momentum $\hbar\boldsymbol{p}$: the Dirac distribution reflects momentum conservation and the square modulus of the second term is the Lamb-Dicke factor (5.20) which characterises band transfer.

C.1.2 Product of two matrix elements α

We now consider the product of two α terms as encountered in the derivation of (5.30) and (5.37). The expansion of $(\alpha_{\boldsymbol{q},\boldsymbol{q}_2}^{\boldsymbol{n},\boldsymbol{n}_2})^* \alpha_{\boldsymbol{q},\boldsymbol{q}_1}^{\boldsymbol{n},\boldsymbol{n}_1}$ in plane waves gives

$$\sum_{\boldsymbol{K}_1,\boldsymbol{L}_1,\boldsymbol{K}_2,\boldsymbol{L}_2} C_{\boldsymbol{q}_2+\boldsymbol{K}_2-\boldsymbol{L}_2}^{\boldsymbol{n}_2} \left(C_{\boldsymbol{q}+\boldsymbol{K}_2}^{\boldsymbol{n}}\right)^* \left(C_{\boldsymbol{q}_1+\boldsymbol{K}_1-\boldsymbol{L}_1}^{\boldsymbol{n}_1}\right)^* C_{\boldsymbol{q}+\boldsymbol{K}_1}^{\boldsymbol{n}} \delta^{(3)}\left(\boldsymbol{q}+\boldsymbol{p}-\boldsymbol{q}_2+\boldsymbol{L}_2\right) \delta^{(3)}\left(\boldsymbol{q}+\boldsymbol{p}-\boldsymbol{q}_1+\boldsymbol{L}_1\right). \tag{C.11}$$

The delta distributions are simultaneously non-zero if the wavevectors $\boldsymbol{q}+\boldsymbol{p}-\boldsymbol{q}_1+\boldsymbol{L}_1$ and $\boldsymbol{q}+\boldsymbol{p}-\boldsymbol{q}_2+\boldsymbol{L}_2$ are equal, or evenly $-\boldsymbol{q}_1+\boldsymbol{L}_1$ and $-\boldsymbol{q}_2+\boldsymbol{L}_2$ are equal. By definition of the quasi-momenta $\boldsymbol{q}$ and the reciprocal lattice vectors $\boldsymbol{L}$, this is equivalent to $\boldsymbol{q}_1=\boldsymbol{q}_2$ and $\boldsymbol{L}_1=\boldsymbol{L}_2$.

C.1.3 Integration over emission directions

In (5.30) and (5.37), the matrix elements are integrated over the directions of spontaneous emission. The delta distribution in the matrix elements prescribes a finite number of direction values for which the matrix element is finite. The condition to be fulfilled is:

$$\boldsymbol{q}-\boldsymbol{q}'+k_0\boldsymbol{u}-\boldsymbol{k}_L+\boldsymbol{L}=0. \tag{C.12}$$

The laser detuning δ_L is small enough to neglect the difference between k_L and k_0 and we take $k_\mathrm{L}\approx k_0$. We note $\nu=k_0 d/\pi\approx 1.37$, $q=\kappa\pi/d$ with $\kappa\in]-1,1]$ and $\boldsymbol{L}=2\pi/d(a\boldsymbol{e}_x+b\boldsymbol{e}_y+c\boldsymbol{e}_z)$ with $(a,b,c)\in\mathbb{Z}^3$. We project (C.12) on the lattice axes:

$$\kappa_x-\kappa_x'+\nu u_x+2a=0, \tag{C.13}$$

$$\kappa_y-\kappa_y'+\nu u_y+2b=0, \tag{C.14}$$

$$\kappa_z-\kappa_z'+\nu(u_z-1)+2c=0. \tag{C.15}$$

The bounds on the quasi-momenta ($\kappa \in]-1,1]$) and the norm of $\boldsymbol{u}$ ($|\boldsymbol{u}| = 1$) restrict the possible integer values taken by a, b and c. Since $\kappa' - \kappa \in]-2,2[$ and $\nu < 2$, we have

$$u_x \in [-1,1] \Rightarrow a \in \{-1,0,1\}, \tag{C.16}$$
$$u_y \in [-1,1] \Rightarrow b \in \{-1,0,1\}, \tag{C.17}$$
$$u_z - 1 \in [-2,0] \Rightarrow c \in \{0,1,2\}. \tag{C.18}$$

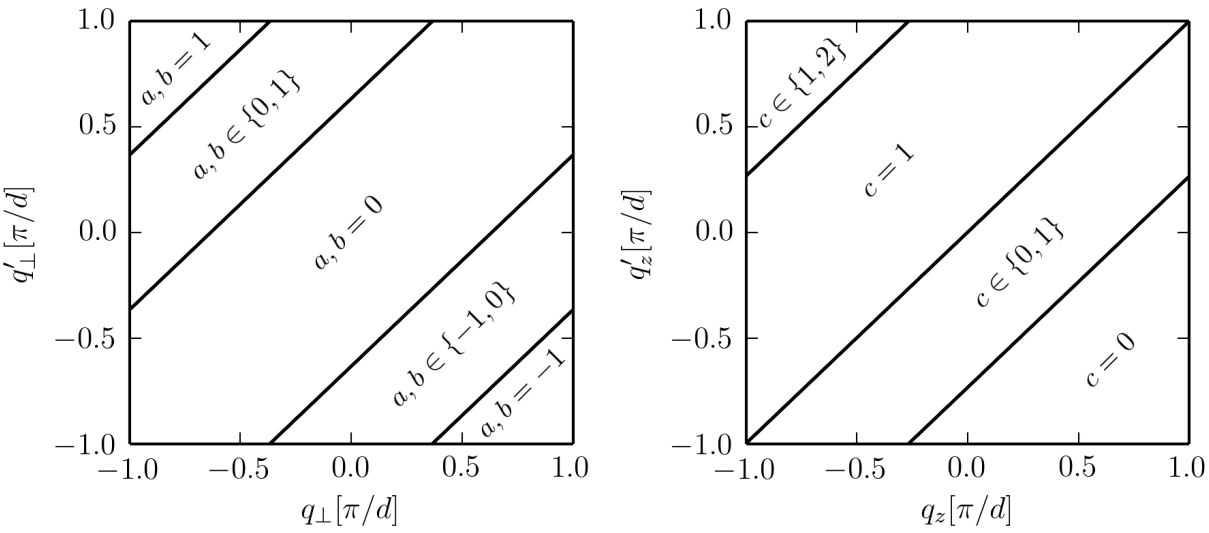

Figure C.1: Map of the possible values taken by the integers a, b and c with respect to the quasi-momenta q and q' in the horizontal directions $\perp = x$ or y (left), and in the vertical direction z (right).

A map for the possible values of a, b and c with respect to the quasi-momenta q and q' is provided in Figure C.1.

C.2 Light-induced tunnelling

We are interested in the dissipative part of the master equation (5.14), which we project on the Wannier state $|w_{\boldsymbol{0}}^{\boldsymbol{n}}\rangle$. We insert two resolutions of identity in order to expand the couplings due to the dissipation (with $\Delta\boldsymbol{k} = k_0\boldsymbol{u} - \boldsymbol{k}_\mathrm{L}$):

$$\langle w_{\boldsymbol{0}}^{\boldsymbol{n}}| \, \mathrm{e}^{-\mathrm{i}\Delta\boldsymbol{k}\cdot\hat{\boldsymbol{R}}} \hat{\rho} \mathrm{e}^{\mathrm{i}\Delta\boldsymbol{k}\cdot\hat{\boldsymbol{R}}} \, |w_{\boldsymbol{0}}^{\boldsymbol{n}}\rangle = \sum_{\boldsymbol{i},\boldsymbol{j},\boldsymbol{l},\boldsymbol{m}} \langle w_{\boldsymbol{0}}^{\boldsymbol{n}}| \, \mathrm{e}^{-\mathrm{i}\Delta\boldsymbol{k}\cdot\hat{\boldsymbol{R}}} \, |w_{\boldsymbol{j}}^{\boldsymbol{m}}\rangle \, \langle w_{\boldsymbol{j}}^{\boldsymbol{m}}| \, \hat{\rho} \, |w_{\boldsymbol{i}}^{\boldsymbol{l}}\rangle \, \langle w_{\boldsymbol{i}}^{\boldsymbol{l}}| \, \mathrm{e}^{\mathrm{i}\Delta\boldsymbol{k}\cdot\hat{\boldsymbol{R}}} \, |w_{\boldsymbol{0}}^{\boldsymbol{n}}\rangle \, . \tag{C.19}$$

We now introduce the coefficients $\tau_{\boldsymbol{i}}^{\boldsymbol{l}}(\Delta\boldsymbol{k}) = \langle w_{\boldsymbol{i}}^{\boldsymbol{l}}| \, \mathrm{e}^{\mathrm{i}\Delta\boldsymbol{k}\cdot\hat{\boldsymbol{R}}} \, |w_{\boldsymbol{0}}^{\boldsymbol{n}}\rangle$ and integrate over the spontaneous emission directions:

$$\Gamma_\mathrm{sp} \int \mathrm{d}^2u \, N(\boldsymbol{u}) \, \langle w_{\boldsymbol{0}}^{\boldsymbol{n}}| \, \mathrm{e}^{-\mathrm{i}\Delta\boldsymbol{k}\cdot\hat{\boldsymbol{R}}} \hat{\rho} \mathrm{e}^{\mathrm{i}\Delta\boldsymbol{k}\cdot\hat{\boldsymbol{R}}} \, |w_{\boldsymbol{0}}^{\boldsymbol{n}}\rangle = \Gamma_\mathrm{sp} \sum_{\boldsymbol{i},\boldsymbol{j},\boldsymbol{l},\boldsymbol{m}} \langle w_{\boldsymbol{j}}^{\boldsymbol{m}}| \, \hat{\rho} \, |w_{\boldsymbol{i}}^{\boldsymbol{l}}\rangle \int \mathrm{d}^2u \, N(\boldsymbol{u}) \tau_{\boldsymbol{i}}^{\boldsymbol{l}}(\Delta\boldsymbol{k}) \tau_{\boldsymbol{j}}^{\boldsymbol{m}*}(\Delta\boldsymbol{k}) \tag{C.20}$$

$$= \sum_{\boldsymbol{i},\boldsymbol{j},\boldsymbol{l},\boldsymbol{m}} \mathcal{T}_{\boldsymbol{i},\boldsymbol{j}}^{\boldsymbol{l},\boldsymbol{m}} \, \langle w_{\boldsymbol{j}}^{\boldsymbol{m}}| \, \hat{\rho} \, |w_{\boldsymbol{i}}^{\boldsymbol{l}}\rangle \, . \tag{C.21}$$

Here again we neglect coherences between different bands of the lattice, hence we restrict the discussion to $\boldsymbol{l} = \boldsymbol{m}$. Moreover, due to the localised nature of the Wannier functions, dominant terms will have either $\boldsymbol{i}$ or $\boldsymbol{j}$ equal to zero. With the reduced notation $\mathcal{T}_{\boldsymbol{i}}^{\boldsymbol{l}} = \mathcal{T}_{\boldsymbol{i},\boldsymbol{0}}^{\boldsymbol{l},\boldsymbol{l}}$

$$\Gamma_{\mathrm{sp}} \int \mathrm{d}^2 u \, N(\boldsymbol{u}) \, \langle w_{\boldsymbol{0}}^{\boldsymbol{n}}| \, \mathrm{e}^{-\mathrm{i}\Delta\boldsymbol{k}\cdot\hat{\boldsymbol{R}}} \hat{\rho} \mathrm{e}^{\mathrm{i}\Delta\boldsymbol{k}\cdot\hat{\boldsymbol{R}}} \, |w_{\boldsymbol{0}}^{\boldsymbol{n}}\rangle \approx \sum_{\boldsymbol{i}\neq\boldsymbol{0},\boldsymbol{l}} \mathcal{T}_{\boldsymbol{i}}^{\boldsymbol{l}^*} \, \langle w_{\boldsymbol{i}}^{\boldsymbol{l}}| \, \hat{\rho} \, |w_{\boldsymbol{0}}^{\boldsymbol{l}}\rangle + \mathcal{T}_{\boldsymbol{i}}^{\boldsymbol{l}} \, \langle w_{\boldsymbol{0}}^{\boldsymbol{l}}| \, \hat{\rho} \, |w_{\boldsymbol{i}}^{\boldsymbol{l}}\rangle \, . \quad \text{(C.22)}$$

Two main effects arise from the dissipative part of the master equation given in (C.22).

Band transfer

The main effect, as we already saw in the Bloch basis, is to induce band transfers. This is mostly found in the local terms $\mathcal{T}_{\boldsymbol{0}}^{\boldsymbol{l}}$ which couples the population at site $\boldsymbol{0}$ and band $\boldsymbol{n}$ to populations on the same site but in other bands. In Figure C.2a we show the evolution of the inter-band transition rates $P_0^n = \mathcal{T}_{(0,0,0)}^{(n,0,0)}$ between the fundamental band and higher excited bands in the horizontal direction with respect to the horizontal lattice depth $V_\perp$. These transition rates describes the growth or decay of the fundamental band population

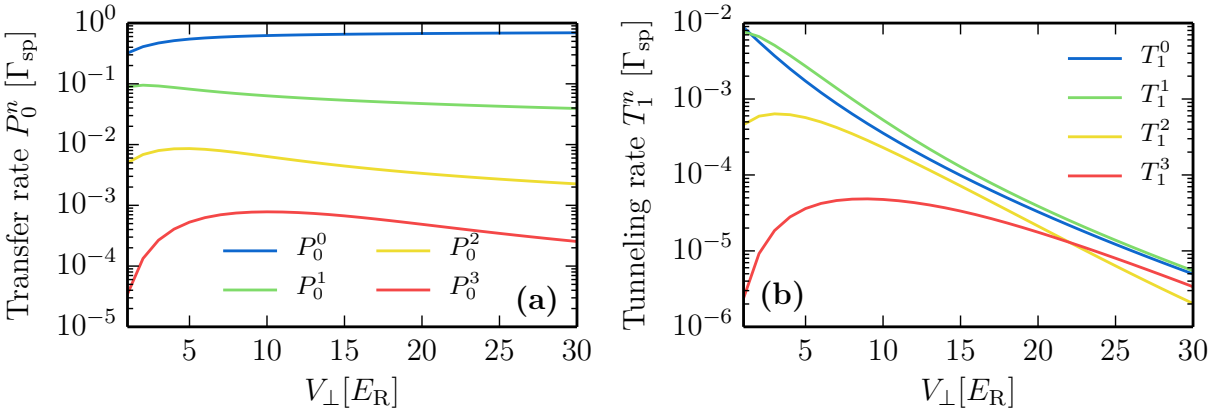

Figure C.2: Rates of transfer for the first four bands in the horizontal direction with varying depth $V_\perp$. (a) On-site transfer rates to excited bands. Note that the rate of transfer to the fundamental band P_0^0 is not the actual rate in the master equation (5.43). One must add -1 to obtain the correct rate. (b) Nearest-neighbour tunnelling rates within bands.

due to transfer from higher excited bands. Given the symmetry of the matrix elements they also describe the rate of transfer from the fundamental band to excited bands. We observe that transfer to the first excited band occurs at a rate of ten percent of Γ_{sp}, and decreases only slightly when increasing the lattice depth.

Coherent hopping

The secondary effect is to create coherences between sites, this can be found in the terms $T_1^n = \mathcal{T}_{(1,0,0)}^{(n,0,0)}$ which describes the coherent tunnelling induced by an absorption-spontaneous emission cycle. In Figure C.2b we show the evolution of these tunnelling rates T_1^n with respect to the horizontal lattice depth $V_\perp$. The localised nature of the Wannier functions and the angular integration over the spontaneous emission directions

make the matrix elements T_1^n very small compared to Γ_{sp}, even in the small horizontal lattice depth regime.

We conclude that the main effect of spontaneous emission is to excite atoms to higher bands, direct tunnelling events induced by dissipation can be neglected.

C.3 Departure and feeding terms

In this section, I derive the analytical expressions for the departure and feeding terms of the master equation (5.2). I use the formalism of second quantisation and derive the expressions described in Section 5.3. Calculations are performed in the interaction picture with respect to $\hat{H}_0$, indicated by a tilde instead of a hat on the operators. I define the electric polarisation operators $\hat{\mathbf{\Pi}}^+$ and $\hat{\mathbf{\Pi}}^-$ with components:

$$\hat{\Pi}_m^+ = \hat{\Psi}_{e_m}^\dagger \hat{\Psi}_g \text{ and } \hat{\Pi}_m^- = \left[\hat{\Pi}_m^+\right]^\dagger. \tag{C.23}$$

C.3.1 Atom-light interaction

The atom-light interaction $\hat{V}_{\mathrm{vac}}$ given by (5.9) can be rewritten as a sum of raising and lowering terms $\tilde{V}_{\mathrm{vac}} = \tilde{V}^+ + \tilde{V}^-$, with $\tilde{V}^- = (\tilde{V}^+)^\dagger$ and

$$\tilde{V}^+ = -\mathrm{i}\int \mathrm{d}^3 r \sum_\mu dE_\mu \hat{a}_\mu \left(\hat{\mathbf{\Pi}}^+(\boldsymbol{r})\cdot\boldsymbol{\varepsilon}_\mu \mathrm{e}^{\mathrm{i}(\omega_0-\omega_\mu)t} + \hat{\mathbf{\Pi}}^-(\boldsymbol{r})\cdot\boldsymbol{\varepsilon}_\mu \mathrm{e}^{-\mathrm{i}(\omega_0+\omega_\mu)t}\right)\mathrm{e}^{\mathrm{i}\boldsymbol{k}_\mu\cdot\boldsymbol{r}}. \tag{C.24}$$

Here we keep the anti-resonant terms so that we will later be able to define distributions properly, but we still make the two-level atom approximation.

We define purely atomic operators

$$\hat{W}_\mu(t) = dE_\mu \int \mathrm{d}^3 r\, \hat{\mathbf{\Pi}}^+(\boldsymbol{r})\cdot\boldsymbol{\varepsilon}_\mu \mathrm{e}^{\mathrm{i}\boldsymbol{k}_\mu\cdot\boldsymbol{r}}, \tag{C.25}$$

$$\hat{W}'_\mu(t) = dE_\mu \int \mathrm{d}^3 r\, \hat{\mathbf{\Pi}}^-(\boldsymbol{r})\cdot\boldsymbol{\varepsilon}_\mu \mathrm{e}^{\mathrm{i}\boldsymbol{k}_\mu\cdot\boldsymbol{r}}. \tag{C.26}$$

Note that $\hat{W}'_\mu \neq \hat{W}_\mu^\dagger$. The raising term (C.24) is thus

$$\tilde{V}^+ = -\mathrm{i}\sum_\mu \hat{W}_\mu \hat{a}_\mu \mathrm{e}^{\mathrm{i}(\omega_0-\omega_\mu)t} + \hat{W}'_\mu \hat{a}_\mu \mathrm{e}^{-\mathrm{i}(\omega_0+\omega_\mu)t}. \tag{C.27}$$

C.3.2 Departure terms

Here we want to evaluate the departure terms in the first line of the master equation (5.2). We recall that the expectation value in the vacuum state does not vanish only for products $\hat{a}_\mu \hat{a}_\mu^\dagger$ and as a result

$$\tilde{A} = \frac{1}{\hbar^2}\int_0^\infty \mathrm{d}\tau \left\langle \tilde{V}_{\mathrm{vac}}(t)\tilde{V}_{\mathrm{vac}}(t-\tau)\right\rangle_{\mathrm{R}} = \frac{1}{\hbar^2}\int_0^\infty \mathrm{d}\tau \left\langle \tilde{V}^+(t)\tilde{V}^-(t-\tau)\right\rangle_{\mathrm{R}}. \tag{C.28}$$

The relaxation time of the electro-magnetic vacuum field τ_{R} is on the order of an optical period or shorter so that we can safely neglect (i) the free flight of the atom during τ_{R}, (ii) the shift in frequency of the spontaneously emitted photons (on the order of the recoil

frequency) (Cohen-Tannoudji et al. 1992). We can therefore perform a Born-Markov approximation for the atomic operators and set $\hat{W}_\mu(t-\tau) \approx \hat{W}_\mu(t)$. We also introduce a convergence factor $\epsilon \to 0^+$, this leads to

$$\tilde{A} \underset{\epsilon\to 0^+}{\approx} \frac{1}{\hbar^2}\int_0^\infty \mathrm{d}\tau \sum_\mu \hat{W}_\mu(t)\hat{W}_\mu^\dagger(t)\mathrm{e}^{\mathrm{i}(\omega_0-\omega_\mu)\tau-\epsilon\tau} + \hat{W}'_\mu(t)\hat{W}'^\dagger_\mu(t)\mathrm{e}^{-\mathrm{i}(\omega_0+\omega_\mu-\epsilon\tau)\tau}. \tag{C.29}$$

We define $\boldsymbol{s} = \boldsymbol{r} - \boldsymbol{r}'$ and perform the integration over the time variable τ,

$$\tilde{A} \underset{\epsilon\to 0^+}{=} \frac{\mathrm{i}}{\hbar^2}\sum_\mu \frac{\hat{W}_\mu(t)\hat{W}_\mu^\dagger(t)}{\omega_0-\omega_\mu+\mathrm{i}\epsilon} + \frac{\hat{W}'_\mu(t)\hat{W}'^\dagger_\mu(t)}{-\omega_0-\omega_\mu+\mathrm{i}\epsilon}. \tag{C.30}$$

Next we expand the atomic operator products

$$\tilde{A} \underset{\epsilon\to 0^+}{=} \mathrm{i}\Gamma\sum_{m,n}\int \mathrm{d}^3r\mathrm{d}^3r' \left(H_{mn}(\boldsymbol{s}) - \mathrm{i}\frac{J_{mn}(\boldsymbol{s})}{2}\right)\hat{\Pi}_m^+(\boldsymbol{r})\hat{\Pi}_n^-(\boldsymbol{r}') \tag{C.31}$$

$$+\left(K_{mn}(\boldsymbol{s}) - \mathrm{i}\frac{L_{mn}(\boldsymbol{s})}{2}\right)\hat{\Pi}_m^-(\boldsymbol{r}')\hat{\Pi}_n^+(\boldsymbol{r}), \tag{C.32}$$

where we introduced the quantities H, J, K and L to minimise the length of the equation. They are given explicitly at the end of the calculation. In order to proceed we expand the field operators, and combine the equal terms:

$$\hat{\Pi}_m^+(\boldsymbol{r})\hat{\Pi}_n^-(\boldsymbol{r}') = \hat{\Psi}^\dagger_{e_m}(\boldsymbol{r})\hat{\Psi}_g(\boldsymbol{r})\hat{\Psi}^\dagger_g(\boldsymbol{r}')\hat{\Psi}_{e_n}(\boldsymbol{r}') \tag{C.33}$$

$$= \hat{\Psi}^\dagger_{e_m}(\boldsymbol{r})\hat{\Psi}^\dagger_g(\boldsymbol{r}')\hat{\Psi}_{e_n}(\boldsymbol{r}')\hat{\Psi}_g(\boldsymbol{r}) + \delta^{(3)}(\boldsymbol{s})\hat{\Psi}^\dagger_{e_m}(\boldsymbol{r})\hat{\Psi}_{e_n}(\boldsymbol{r}), \tag{C.34}$$

$$\hat{\Pi}_m^-(\boldsymbol{r}')\hat{\Pi}_n^+(\boldsymbol{r}) = \hat{\Psi}^\dagger_g(\boldsymbol{r}')\hat{\Psi}_{e_m}(\boldsymbol{r}')\hat{\Psi}^\dagger_{e_n}(\boldsymbol{r})\hat{\Psi}_g(\boldsymbol{r}) \tag{C.35}$$

$$= \hat{\Psi}^\dagger_{e_n}(\boldsymbol{r})\hat{\Psi}^\dagger_g(\boldsymbol{r}')\hat{\Psi}_{e_m}(\boldsymbol{r}')\hat{\Psi}_g(\boldsymbol{r}) + \delta_{m,n}\delta^{(3)}(\boldsymbol{s})\hat{\Psi}^\dagger_g(\boldsymbol{r})\hat{\Psi}_g(\boldsymbol{r}). \tag{C.36}$$

We first discuss the one-body terms involving two field operators. The excited state product corresponds to a single-particle interaction with the electro-magnetic field. The real part is the Lamb shift of the excited state, and the imaginary part is a decay term due to an absorption-spontaneous emission process. The ground state product appears only in the anti-resonant part. The real part is the Lamb shift of the ground state, and the imaginary part is zero (proportional to $\delta^{(1)}(\omega_\mu+\omega_0)$ with $\omega_\mu > 0$). The Lamb shifts can be incorporated into the definition of ω_0 and we no longer consider them in the following. The spontaneous decay term is:

$$\tilde{A}^{1\mathrm{B}} \underset{\epsilon\to 0^+}{=} \frac{\Gamma}{2}\sum_{m,n}\int \mathrm{d}^3r\, J_{mn}(\boldsymbol{0})\hat{\Psi}^\dagger_{e_m}(\boldsymbol{r})\hat{\Psi}_{e_n}(\boldsymbol{r}). \tag{C.37}$$

Regarding the two-body terms involving four field operators, we can regroup them by swapping the indices m and n, as a result we get the term

$$\tilde{A}^{2\mathrm{B}} \underset{\epsilon\to 0^+}{=} \mathrm{i}\Gamma\sum_{m,n}\int \mathrm{d}^3r\mathrm{d}^3r' \left(G_{mn}(\boldsymbol{s}) - \mathrm{i}\frac{F_{mn}(\boldsymbol{s})}{2}\right)\hat{\Xi}_{mn}(\boldsymbol{r},\boldsymbol{r}'), \tag{C.38}$$

$$\hat{\Xi}_{mn}(\boldsymbol{r},\boldsymbol{r}') = \hat{\Psi}^\dagger_{e_m}(\boldsymbol{r})\hat{\Psi}^\dagger_g(\boldsymbol{r}')\hat{\Psi}_{e_n}(\boldsymbol{r}')\hat{\Psi}_g(\boldsymbol{r}). \tag{C.39}$$

with $G_{mn}(\boldsymbol{s}) = H_{mn}(\boldsymbol{s}) + K_{nm}(\boldsymbol{s})$ and $F_{mn}(\boldsymbol{s}) = J_{mn}(\boldsymbol{s}) + L_{nm}(\boldsymbol{s})$. Moreover,

$$G_{mn}(\boldsymbol{s}) - \mathrm{i}\frac{F_{mn}(\boldsymbol{s})}{2} \underset{\epsilon\to 0^+}{=} \frac{d^2}{(2\pi)^3\hbar\Gamma\epsilon_0}\int \mathrm{d}^3k\,\frac{k}{2}\sum_{\boldsymbol{\varepsilon}\perp\boldsymbol{k}}\varepsilon_{\boldsymbol{k},m}\varepsilon^*_{\boldsymbol{k},n}\left(\frac{\mathrm{e}^{\mathrm{i}\boldsymbol{k}\cdot\boldsymbol{s}}}{k_0-k+\mathrm{i}\epsilon}+\frac{\mathrm{e}^{-\mathrm{i}\boldsymbol{k}\cdot\boldsymbol{s}}}{-k_0-k+\mathrm{i}\epsilon}\right) \tag{C.40}$$

$$\underset{\epsilon\to 0^+}{=} \frac{3\pi}{k_0^3}\frac{1}{(2\pi)^3}\int \mathrm{d}^3k\,\frac{k}{2}\sum_{\boldsymbol{\varepsilon}\perp\boldsymbol{k}}\varepsilon_{\boldsymbol{k},m}\varepsilon^*_{\boldsymbol{k},n}\left(\frac{1}{k_0-k+\mathrm{i}\epsilon}+\frac{1}{-k_0-k+\mathrm{i}\epsilon}\right)\mathrm{e}^{\mathrm{i}\boldsymbol{k}\cdot\boldsymbol{s}}, \tag{C.41}$$

where we have changed the sign of $\boldsymbol{k}$ in the second integral. We recognise here an inverse Fourier transform (see Appendix C.4). Now we separate the integrals over the angles and over the modulus and recognise special distributions (this is where the anti-resonant terms allow us to define mathematical distributions properly):

$$\int_0^\infty \mathrm{d}x\,f(x)\left(\frac{1}{1-x+\mathrm{i}\epsilon}+\frac{1}{-1-x+\mathrm{i}\epsilon}\right)\underset{\epsilon\to 0^+}{=}\mathrm{PV}\left[\frac{f(x)}{1-x}\right]-\mathrm{i}\pi\delta^{(1)}(1-x)f(1), \tag{C.42}$$

which holds true for any odd function f. Here PV stands for the Cauchy principal value integral. We deduce from this

$$G_{mn}(\boldsymbol{s}) = \frac{3}{16\pi^2}\mathrm{PV}\left[\int \mathrm{d}x\,\frac{x^3}{1-x}\int \mathrm{d}^2u\,\mathrm{e}^{\mathrm{i}xk_0\boldsymbol{u}\cdot\boldsymbol{s}}\sum_{\boldsymbol{\varepsilon}\perp\boldsymbol{u}}\varepsilon_{\boldsymbol{u},m}\varepsilon^*_{\boldsymbol{u},n}\right], \tag{C.43}$$

$$F_{mn}(\boldsymbol{s}) = \frac{3}{8\pi}\int \mathrm{d}^2u\,\mathrm{e}^{\mathrm{i}k_0\boldsymbol{u}\cdot\boldsymbol{s}}\sum_{\boldsymbol{\varepsilon}\perp\boldsymbol{u}}\varepsilon_{\boldsymbol{u},m}\varepsilon^*_{\boldsymbol{u},n}. \tag{C.44}$$

The departure terms of the master equation can finally be expressed as

$$\tilde{A} = \tilde{A}^{1\mathrm{B}} + \tilde{A}^{2\mathrm{B}}, \tag{C.45}$$

$$\tilde{A}^{1\mathrm{B}} = \frac{\Gamma}{2}\sum_{m,n}\int \mathrm{d}^3r\,\hat{\Psi}^\dagger_{e_m}(\boldsymbol{r})\hat{\Psi}_{e_n}(\boldsymbol{r}), \tag{C.46}$$

$$\tilde{A}^{2\mathrm{B}} = \sum_{m,n}\int \mathrm{d}^3r\mathrm{d}^3r'\left(\mathrm{i}\Gamma G_{mn}(\boldsymbol{s})+\frac{\Gamma}{2}F_{mn}(\boldsymbol{s})\right)\hat{\Xi}_{mn}(\boldsymbol{r},\boldsymbol{r}'). \tag{C.47}$$

Going back to the Schrödinger picture leaves the departure operators unchanged: $\hat{A} = \tilde{A}$.

C.3.3 Feeding terms

Here we want to evaluate the feeding terms in the second line of the master equation (5.2). As for the departure terms, we expand the operators $\tilde{V}$, and use a Born-Markov approximation on the atomic operators,

$$\tilde{B}_1[\tilde{\rho}_\mathrm{s}] = \frac{1}{\hbar^2}\int_0^{+\infty}\mathrm{d}\tau\,\mathrm{Tr}\left\{\tilde{V}_\mathrm{vac}(t)\left[\tilde{\rho}_\mathrm{s}\otimes|\varnothing\rangle\langle\varnothing|_\mathrm{R}\right]\tilde{V}_\mathrm{vac}(t-\tau)\right\} \tag{C.48}$$

$$= \frac{1}{\hbar^2}\int_0^{+\infty}\mathrm{d}\tau\,\mathrm{Tr}\left\{\tilde{V}^-(t)\left[\tilde{\rho}_\mathrm{s}\otimes|\varnothing\rangle\langle\varnothing|_\mathrm{R}\right]\tilde{V}^+(t-\tau)\right\} \tag{C.49}$$

$$\underset{\epsilon\to 0^+}{\approx}\frac{1}{\hbar^2}\int_0^{+\infty}\mathrm{d}\tau\sum_\mu \hat{W}^\dagger_\mu\tilde{\rho}_\mathrm{s}\hat{W}_\mu\mathrm{e}^{-\mathrm{i}(\omega_0-\omega_\mu)\tau-\epsilon\tau}+\hat{W}'^\dagger_\mu\tilde{\rho}_\mathrm{s}\hat{W}'_\mu\mathrm{e}^{\mathrm{i}(\omega_0+\omega_\mu)\tau-\epsilon\tau}. \tag{C.50}$$

where we have introduced a convergence factor $\epsilon \to 0^+$, this leads to

$$\tilde{B}_1[\tilde{\rho}_\mathrm{s}] \underset{\epsilon\to 0^+}{=} \frac{-\mathrm{i}}{\hbar^2}\sum_\mu \frac{\hat{W}_\mu^\dagger \tilde{\rho}_\mathrm{s}\hat{W}_\mu}{\omega_0-\omega_\mu-\mathrm{i}\epsilon} + \frac{\hat{W}_\mu'^\dagger \tilde{\rho}_\mathrm{s}\hat{W}'_\mu}{-\omega_0-\omega_\mu-\mathrm{i}\epsilon}. \tag{C.51}$$

And finally,

$$\begin{aligned}
\tilde{B}[\tilde{\rho}_\mathrm{s}] &= \tilde{B}_1[\tilde{\rho}_\mathrm{s}] + \tilde{B}_1[\tilde{\rho}_\mathrm{s}]^\dagger && \text{(C.52)}\\
&= \frac{1}{\hbar^2}\sum_\mu \frac{2\epsilon}{(\omega_0-\omega_\mu)^2+\epsilon^2}\hat{W}_\mu^\dagger\tilde{\rho}_\mathrm{s}\hat{W}_\mu + \frac{2\epsilon}{(\omega_0+\omega_\mu)^2+\epsilon^2}\hat{W}_\mu'^\dagger\tilde{\rho}_\mathrm{s}\hat{W}'_\mu && \text{(C.53)}\\
&= \frac{2\pi}{\hbar^2 c}\frac{L^3}{(2\pi)^3}\int \mathrm{d}^2u\mathrm{d}k\, k^2 \sum_{\boldsymbol{\varepsilon}\perp\boldsymbol{u}}\left[\delta^{(1)}(k_0-k)\hat{W}_\mu^\dagger\tilde{\rho}_\mathrm{s}\hat{W}_\mu + \delta^{(1)}(k_0+k)\hat{W}_\mu'^\dagger\tilde{\rho}_\mathrm{s}\hat{W}'_\mu\right] && \text{(C.54)}\\
&= \frac{3\Gamma}{8\pi}\sum_{m,n}\int \mathrm{d}^2u\mathrm{d}^3r\mathrm{d}^3r'\,\hat{\Pi}_m^-(\boldsymbol{r}')\mathrm{e}^{-\mathrm{i}k_0\boldsymbol{u}\cdot\boldsymbol{r}'}\tilde{\rho}_\mathrm{s}\mathrm{e}^{\mathrm{i}k_0\boldsymbol{u}\cdot\boldsymbol{r}}\hat{\Pi}_n^+(\boldsymbol{r})\sum_{\boldsymbol{\varepsilon}\perp\boldsymbol{u}}\varepsilon_{\boldsymbol{u},m}\varepsilon^*_{\boldsymbol{u},n} && \text{(C.55)}\\
&= \Gamma\sum_{m,n}\int \mathrm{d}^3r\mathrm{d}^3r'\,F_{mn}(\boldsymbol{s})\hat{\Pi}_m^-(\boldsymbol{r}')\tilde{\rho}_\mathrm{s}\hat{\Pi}_n^+(\boldsymbol{r}). && \text{(C.56)}
\end{aligned}$$

Going back to the Schrödinger picture gives

$$\hat{B}[\hat{\rho}_\mathrm{s}] = \Gamma\sum_{m,n}\int \mathrm{d}^3r\mathrm{d}^3r'\,F_{mn}(\boldsymbol{s})\hat{\Pi}_m^-(\boldsymbol{r}')\hat{\rho}_\mathrm{s}\hat{\Pi}_n^+(\boldsymbol{r}). \tag{C.57}$$

C.4 Dipole-dipole interaction and collective spontaneous emission functions

In this section, I derive the analytical expression of the dipole-dipole interaction and collective spontaneous emission functions F and G in (5.62) and (5.64). The directional factors $N_{mn}(\boldsymbol{u}) = 3/(8\pi)\sum_{\boldsymbol{\varepsilon}\perp\boldsymbol{u}}\varepsilon_{\boldsymbol{u},m}\varepsilon^*_{\boldsymbol{u},n}$ can be expressed in terms of the spherical harmonics:

$$\frac{8\pi}{3}N_{mn}(\boldsymbol{u}) = \sum_{\boldsymbol{\varepsilon}\perp\boldsymbol{u}}\varepsilon_{\boldsymbol{u},m}\varepsilon^*_{\boldsymbol{u},n} = \delta_{m,n} - u_m u_n^* = \delta_{m,n}\sqrt{4\pi}Y_0^0(\boldsymbol{u}) - \frac{4\pi}{3}Y_1^m(\boldsymbol{u})\left[Y_1^n(\boldsymbol{u})\right]^*. \tag{C.58}$$

We recall the definition of the spherical harmonics Y_ℓ^m in terms of the Legendre polynomials P_ℓ^m,

$$Y_\ell^m(\theta,\varphi) = (-1)^m\sqrt{\frac{2\ell+1}{4\pi}\frac{(\ell-m)!}{(\ell+m)!}}P_\ell^m(\cos\theta)\mathrm{e}^{\mathrm{i}m\varphi}. \tag{C.59}$$

And we note that:

$$Y_1^m\left[Y_1^n\right]^* = (-1)^n\frac{\sqrt{\delta_{m,n}(4\delta_{m,0}+|m|)+3|m-n|}}{\sqrt{20\pi}}Y_2^{m-n} + (-1)^n\delta_{m,n}\frac{1}{\sqrt{4\pi}}Y_0^0. \tag{C.60}$$

We assume that the laser excitation only populates the excited state $|e_0\rangle$ linked to $|g\rangle$ by the π-transition. As a result, we are only interested in the terms G_{00} and F_{00}. We have:

$$Y_1^0\left[Y_1^0\right]^* = \frac{1}{\sqrt{5\pi}}Y_2^0 + \frac{1}{\sqrt{4\pi}}Y_0^0. \tag{C.61}$$

We first perform the integration over the angles, using the decomposition of $\mathrm{e}^{\mathrm{i}k_0\boldsymbol{u}\cdot\boldsymbol{s}}$ in spherical harmonics and spherical Bessel functions j_ℓ (Ellinger et al. 1994). This gives, with $\bar{\boldsymbol{s}} = \boldsymbol{s}/s$,

$$F_{00}(\boldsymbol{s}) = \int \mathrm{d}^2u\, \mathrm{e}^{\mathrm{i}k_0\boldsymbol{u}\cdot\boldsymbol{s}} \frac{3}{8\pi} \sum_{\boldsymbol{\varepsilon}\perp\boldsymbol{u}} \varepsilon_{\boldsymbol{u},0}\varepsilon^*_{\boldsymbol{u},0} \tag{C.62}$$

$$= \int \mathrm{d}^2u \sum_{\ell,m} \mathrm{i}^\ell j_\ell(k_0 s) Y_\ell^m(\boldsymbol{u}) Y_\ell^m(\bar{\boldsymbol{s}})^* \left(\sqrt{4\pi} Y_0^0(\boldsymbol{u}) - \sqrt{\frac{4\pi}{5}} Y_2^0(\boldsymbol{u}) \right) \tag{C.63}$$

$$= j_0(k_0 s) + \sqrt{\frac{4\pi}{5}} j_2(k_0 s) Y_2^0(\bar{\boldsymbol{s}}) \tag{C.64}$$

$$= \frac{\sin(k_0 s)}{k_0 s} + \left[\left(\frac{3}{(k_0 s)^3} - \frac{1}{k_0 s} \right) \sin(k_0 s) - \frac{3}{(k_0 s)^2} \cos(k_0 s) \right] \frac{3(\bar{\boldsymbol{s}}\cdot\boldsymbol{\varepsilon}_\mathrm{L})^2 - 1}{2} \tag{C.65}$$

$$= \frac{3}{2} \left\{ \left[1 - (\bar{\boldsymbol{s}}\cdot\boldsymbol{\varepsilon}_\mathrm{L})^2 \right] \frac{\sin(k_0 s)}{k_0 s} + \left[1 - 3(\bar{\boldsymbol{s}}\cdot\boldsymbol{\varepsilon}_\mathrm{L})^2 \right] \left(\frac{\cos(k_0 s)}{(k_0 s)^2} - \frac{\sin(k_0 s)}{(k_0 s)^3} \right) \right\}. \tag{C.66}$$

This expression is equal to the function F in (5.62). It corresponds to the *dissipative* part of the atom-light interactions (Pichler et al. 2010): it is related to collective spontaneous emission.

The calculation of G_{00} is similar. We consider (C.43) and either use the residue theorem, or a direct integration using principal value integrals, both leading to the same result, provided $s > 0$:

$$G_{00}(\boldsymbol{s}) = \frac{3}{4} \left\{ - \left[1 - (\bar{\boldsymbol{s}}\cdot\boldsymbol{\varepsilon}_\mathrm{L})^2 \right] \frac{\cos(k_0 s)}{k_0 s} + \left[1 - 3(\bar{\boldsymbol{s}}\cdot\boldsymbol{\varepsilon}_\mathrm{L})^2 \right] \left(\frac{\sin(k_0 s)}{(k_0 s)^2} + \frac{\cos(k_0 s)}{(k_0 s)^3} \right) \right\}. \tag{C.67}$$

This expression is equal to the function G in (5.64). It corresponds to the *radiative* part of the atom-light interactions (Pichler et al. 2010): it is related to induced dipole-dipole interactions.

C.5 Convolution theorem for the computation of matrix elements

Here I give the proof for the Fourier space expression of the dipole-dipole interaction energies (5.82) and modified emission rates (5.88). In this section, I denote the Fourier transform operator by $\mathfrak{F}$, Fourier transforms with a tilde and the convolution product with $\star$. I start with the following integral for the Wannier functions in the fundamental band (band index omitted)

$$I_{\boldsymbol{i}} = \int \mathrm{d}^3r \mathrm{d}^3r'\, \mathrm{e}^{\mathrm{i}\boldsymbol{k}_\mathrm{L}\cdot(\boldsymbol{r}'-\boldsymbol{r})} f(\boldsymbol{r}'-\boldsymbol{r}) |w_{\boldsymbol{i}}(\boldsymbol{r})|^2 |w_{\boldsymbol{0}}(\boldsymbol{r}')|^2 \tag{C.68}$$

$$= \int \mathrm{d}^3r\, |w_{\boldsymbol{i}}(\boldsymbol{r})|^2 \mathrm{e}^{-\mathrm{i}\boldsymbol{k}_\mathrm{L}\cdot\boldsymbol{r}} \int \mathrm{d}^3r'\, f(\boldsymbol{r}'-\boldsymbol{r}) |w_{\boldsymbol{0}}(\boldsymbol{r}')|^2 \mathrm{e}^{\mathrm{i}\boldsymbol{k}_\mathrm{L}\cdot\boldsymbol{r}'}, \tag{C.69}$$

with $W_{\mathbf{0}}(\boldsymbol{r}) = |w_{\mathbf{0}}(\boldsymbol{r})|^2 \mathrm{e}^{\mathrm{i}\boldsymbol{k}_\mathrm{L}\cdot\boldsymbol{r}}$ and where we recognise a convolution product in the second integral. Then

$$I_{\boldsymbol{i}} = \int \mathrm{d}^3 r \, |w_{\boldsymbol{i}}(\boldsymbol{r})|^2 \mathrm{e}^{-\mathrm{i}\boldsymbol{k}_\mathrm{L}\cdot\boldsymbol{r}} f \star W_{\mathbf{0}}(\boldsymbol{r}) \tag{C.70}$$

$$= W_{\boldsymbol{i}} \star [f \star W_{\mathbf{0}}]|_{\boldsymbol{r}=\mathbf{0}} \,, \tag{C.71}$$

with $W_{\boldsymbol{i}}(\boldsymbol{r}) = |w_{\boldsymbol{i}}(-\boldsymbol{r})|^2 \mathrm{e}^{\mathrm{i}\boldsymbol{k}_\mathrm{L}\cdot\boldsymbol{r}}$. Using the convolution theorem (Arfken et al. 2013):

$$I_{\boldsymbol{i}} = \mathfrak{F}^{-1}\left[\widetilde{W_{\boldsymbol{i}}} \times \mathfrak{F}[f \star W_{\mathbf{0}}]\right]\Big|_{\boldsymbol{r}=\mathbf{0}} \tag{C.72}$$

$$= \frac{1}{(2\pi)^3} \int \mathrm{d}^3 k \, \widetilde{W_{\boldsymbol{i}}} \widetilde{W_{\mathbf{0}}} \widetilde{f}, \tag{C.73}$$

where we used the convolution theorem a second time to decompose $\mathfrak{F}[f \star W_{\mathbf{0}}]$. We now use the fact that $w_{\boldsymbol{i}}(-\boldsymbol{r}) = w_{\mathbf{0}}(\boldsymbol{r} + \boldsymbol{r}_{\boldsymbol{i}})$, which is true in the fundamental band of a cubic lattice where all Wannier functions can be chosen real and with even parity (Kohn 1959). We can now express $\widetilde{W_{\boldsymbol{i}}}$ as a function of $\widetilde{W_{\mathbf{0}}}$:

$$\widetilde{W_i} = \mathfrak{F}[|w_{\mathbf{0}}(\boldsymbol{r} + \boldsymbol{r}_{\boldsymbol{i}})|^2 \mathrm{e}^{\mathrm{i}\boldsymbol{k}_\mathrm{L}\cdot\boldsymbol{r}}] \tag{C.74}$$

$$= \mathrm{e}^{-\mathrm{i}\boldsymbol{k}_\mathrm{L}\cdot\boldsymbol{r}_{\boldsymbol{i}}} \mathfrak{F}[|w_{\mathbf{0}}(\boldsymbol{r} + \boldsymbol{r}_{\boldsymbol{i}})|^2 \mathrm{e}^{\mathrm{i}\boldsymbol{k}_\mathrm{L}\cdot(\boldsymbol{r}+\boldsymbol{r}_{\boldsymbol{i}})}] \tag{C.75}$$

$$= \mathrm{e}^{-\mathrm{i}\boldsymbol{k}_\mathrm{L}\cdot\boldsymbol{r}_{\boldsymbol{i}}} \mathrm{e}^{\mathrm{i}\boldsymbol{k}\cdot\boldsymbol{r}_{\boldsymbol{i}}} \mathfrak{F}[|w_{\mathbf{0}}(\boldsymbol{r})|^2 \mathrm{e}^{\mathrm{i}\boldsymbol{k}_\mathrm{L}\cdot\boldsymbol{r}}] \tag{C.76}$$

$$= \mathrm{e}^{\mathrm{i}(\boldsymbol{k}-\boldsymbol{k}_\mathrm{L})\cdot\boldsymbol{r}_{\boldsymbol{i}}} \widetilde{W_{\mathbf{0}}} \tag{C.77}$$

$$= \mathrm{e}^{\mathrm{i}(\boldsymbol{k}-\boldsymbol{k}_\mathrm{L})\cdot\boldsymbol{r}_{\boldsymbol{i}}} \, \widetilde{|w_{\mathbf{0}}|^2}\Big|_{\boldsymbol{k}-\boldsymbol{k}_\mathrm{L}} . \tag{C.78}$$

And finally,

$$I_{\boldsymbol{i}} = \frac{1}{(2\pi)^3} \int \mathrm{d}^3 k \, \mathrm{e}^{\mathrm{i}(\boldsymbol{k}-\boldsymbol{k}_\mathrm{L})\cdot\boldsymbol{r}_{\boldsymbol{i}}} \widetilde{f}(\boldsymbol{k}) [\widetilde{|w_{\mathbf{0}}|^2}(\boldsymbol{k} - \boldsymbol{k}_\mathrm{L})]^2. \tag{C.79}$$

Bibliography

Aharonov, Y. and D. Bohm (1959). *Significance of electromagnetic potentials in the quantum theory*. Physical Review **115.3**, 485–491 (cited in page 31).

Aidelsburger, M., M. Lohse, C. Schweizer, M. Atala, J. T. Barreiro, S. Nascimbène, N. R. Cooper, I. Bloch and N. Goldman (2015). *Measuring the Chern number of Hofstadter bands with ultracold bosonic atoms*. Nature Physics **11.2**, 162–166 (cited in pages 29, 36, 40).

Aidelsburger, M. (2018). *Artificial gauge fields and topology with ultracold atoms in optical lattices*. Journal of Physics B: Atomic, Molecular and Optical Physics (cited in page 29).

Aikawa, K., A. Frisch, M. Mark, S. Baier, A. Rietzler, R. Grimm and F. Ferlaino (2012). *Bose-Einstein condensation of erbium*. Physical Review Letters **108.21** (cited in page 13).

Anderson, M. H., J. R. Ensher, M. R. Matthews, C. E. Wieman and E. A. Cornell (1995). *Observation of Bose-Einstein condensation in a dilute atomic vapor*. Science **269.5221**, 198–201 (cited in page 12).

Andrews, M. R., C. G. Townsend, H.-J. Miesner, D. S. Durfee, D. M. Kurn and W. Ketterle (1997). *Observation of interference between two Bose condensates*. Science **275.5300**, 637–641 (cited in pages 13, 29).

Araújo, M. O., I. Krešić, R. Kaiser and W. Guerin (2016). *Superradiance in a large and dilute cloud of cold atoms in the linear-optics regime*. Physical Review Letters **117.7**, 073002 (cited in page 51).

Arfken, G. B., H.-J. Weber and F. E. Harris (2013). *Mathematical Methods for Physicists: A Comprehensive Guide*. Statistical and Nonlinear Physics. Academic Press (cited in page 181).

Ashcroft, N. W. and N. D. Mermin (1976). *Solid State Physics*. Harcourt College Publishers (cited in pages 22, 172).

Aspuru-Guzik, A. and P. Walther (2012). *Photonic quantum simulators*. Nature Physics **8.4**, 285–291 (cited in page 12).

Atala, M., M. Aidelsburger, J. T. Barreiro, D. Abanin, T. Kitagawa, E. Demler and I. Bloch (2013). *Direct measurement of the Zak phase in topological Bloch bands*. Nature Physics **9.12**, 795–800 (cited in page 29).

Awschalom, D. D., L. C. Bassett, A. S. Dzurak, E. L. Hu and J. R. Petta (2013). *Quantum spintronics: Engineering and manipulating atom-like spins in semiconductors*. Science **339.6124**, 1174–1179 (cited in page 11).

Bakr, W. S., A. Peng, M. E. Tai, R. Ma, J. Simon, J. I. Gillen, S. Fölling, L. Pollet and M. Greiner (2010). *Probing the superfluid-to-Mott insulator transition at the single-atom level*. Science **329.5991**, 547–550 (cited in page 21).

Barber, Z. W., C. W. Hoyt, C. W. Oates, L. Hollberg, A. V. Taichenachev and V. I. Yudin (2006). *Direct excitation of the forbidden clock transition in neutral ^{174}Yb atoms confined to an optical lattice*. Physical Review Letters **96.8**, 083002 (cited in pages 19, 74).

Barber, Z. W., J. E. Stalnaker, N. D. Lemke, N. Poli, C. W. Oates et al. (2008). *Optical lattice induced light shifts in an Yb atomic clock*. Physical Review Letters **100.10**, 103002 (cited in pages 20, 80–82).

Barontini, G., R. Labouvie, F. Stubenrauch, A. Vogler, V. Guarrera and H. Ott (2013). *Controlling the dynamics of an open many-body quantum system with localized dissipation*. Physical Review Letters **110.3**, 035302 (cited in pages 91, 93).

Barredo, D., S. de Léséleuc, V. Lienhard, T. Lahaye and A. Browaeys (2016). *An atom-by-atom assembler of defect-free arbitrary two-dimensional atomic arrays*. Science **354.6315**, 1021–1023 (cited in page 20).

Ben Dahan, M., E. Peik, J. Reichel, Y. Castin and C. Salomon (1996). *Bloch oscillations of atoms in an optical potential*. Physical Review Letters **76.24**, 4508–4511 (cited in page 58).

Bernevig, B. A. and T. L. Hughes (2013). *Topological Insulators and Topological Superconductors*. Condensed Matter Physics. Princeton University Press (cited in pages 33, 34).

Bidel, Y., B. Klappauf, J. C. Bernard, D. Delande, G. Labeyrie, C. Miniatura, D. Wilkowski and R. Kaiser (2002). *Coherent light transport in a cold strontium cloud*. Physical Review Letters **88.20** (cited in page 17).

Bilitewski, T. and N. R. Cooper (2015). *Scattering theory for Floquet-Bloch states*. Physical Review A **91.3**, 033601 (cited in page 36).

Billy, J., V. Josse, Z. Zuo, A. Bernard, B. Hambrecht, P. Lugan, D. Clément, L. Sanchez-Palencia, P. Bouyer and A. Aspect (2008). *Direct observation of Anderson localization of matter waves in a controlled disorder*. Nature **453.7197**, 891–894 (cited in page 11).

Black, E. D. (2000). *An introduction to Pound-Drever-Hall laser frequency stabilization*. American Journal of Physics **69.1**, 79–87 (cited in page 67).

Blatt, R. and C. F. Roos (2012). *Quantum simulations with trapped ions*. Nature Physics **8.4**, 277–284 (cited in page 11).

Bloch, I., T. W. Hänsch and T. Esslinger (2000). *Measurement of the spatial coherence of a trapped Bose gas at the phase transition*. Nature **403.6766**, 166–170 (cited in page 13).

Bloch, I. (2005). *Ultracold quantum gases in optical lattices*. Nature Physics **1.1**, 23–30 (cited in pages 11, 15, 21).

Bloch, I., J. Dalibard and W. Zwerger (2008). *Many-body physics with ultracold gases*. Reviews of Modern Physics **80.3**, 885–964 (cited in pages 13, 21, 22, 29, 35, 36, 62–64).

Bloch, I., J. Dalibard and S. Nascimbène (2012). *Quantum simulations with ultracold quantum gases*. Nature Physics **8.4**, 267–276 (cited in page 11).

Bloom, B. J., T. L. Nicholson, J. R. Williams, S. L. Campbell, M. Bishof, X. Zhang, W. Zhang, S. L. Bromley and J. Ye (2014). *An optical lattice clock with accuracy and stability at the 10^{-18} level*. Nature **506.7486**, 71–75 (cited in page 15).

Bohm, G. and G. Zech (2010). *Introduction to Statistics and Data Analysis for Physicists*. Electronic Book Library. Deutsches Elektronen-Synchrotron (cited in pages 89, 90, 169).

Bohnet, J. G., Z. Chen, J. M. Weiner, D. Meiser, M. J. Holland and J. K. Thompson (2012). *A steady-state superradiant laser with less than one intracavity photon*. Nature **484.7392**, 78–81 (cited in page 15).

Boll, M., T. A. Hilker, G. Salomon, A. Omran, J. Nespolo, L. Pollet, I. Bloch and C. Gross (2016). *Spin- and density-resolved microscopy of antiferromagnetic correlations in Fermi-Hubbard chains*. Science **353.6305**, 1257–1260 (cited in pages 21, 29).

Borkowski, M., A. A. Buchachenko, R. Ciuryło, P. S. Julienne, H. Yamada, Y. Kikuchi, K. Takahashi, Y. Takasu and Y. Takahashi (2017). *Beyond-Born-Oppenheimer effects in sub-kHz-precision photoassociation spectroscopy of ytterbium atoms*. Physical Review A **96.6**, 063405 (cited in pages 50, 90).

Bosch Aguilera, M., R. Bouganne, A. Dareau, M. Scholl, Q. Beaufils, J. Beugnon and F. Gerbier (2018). *Non-linear relaxation of interacting bosons coherently driven on a narrow optical transition*. EPL (Europhysics Letters) **123.4**, 40004 (cited in pages 4, 71, 93).

Bosch Aguilera, M. (2019). *To be defended*. PhD Thesis. Sorbonne Université (cited in pages 54, 71, 83).

Bouganne, R., M. Bosch Aguilera, A. Dareau, E. Soave, J. Beugnon and F. Gerbier (2017). *Clock spectroscopy of interacting bosons in deep optical lattices*. New Journal of Physics **19.11**, 113006 (cited in pages 4, 65, 78–80, 83, 86–91, 93, 157).

Bowers, C. J., D. Budker, E. D. Commins, D. DeMille, S. J. Freedman, A.-T. Nguyen, S.-Q. Shang and M. Zolotorev (1996). *Experimental investigation of excited-state lifetimes in atomic ytterbium*. Physical Review A **53.5**, 3103–3109 (cited in page 53).

Boyd, M. M., T. Zelevinsky, A. D. Ludlow, S. M. Foreman, S. Blatt, T. Ido and J. Ye (2006). *Optical atomic coherence at the 1-second time scale*. Science **314.5804**, 1430–1433 (cited in page 21).

Bradley, C. C., C. A. Sackett, J. J. Tollett and R. G. Hulet (1995). *Evidence of Bose-Einstein condensation in an atomic gas with attractive interactions*. Physical Review Letters **75.9**, 1687–1690 (cited in page 12).

Bromley, S. L., B. Zhu, M. Bishof, X. Zhang, T. Bothwell et al. (2016). *Collective atomic scattering and motional effects in a dense coherent medium*. Nature Communications **7**, 11039 (cited in page 17).

Brown, P. T., D. Mitra, E. Guardado-Sanchez, P. Schauß, S. S. Kondov, E. Khatami, T. Paiva, N. Trivedi, D. A. Huse and W. S. Bakr (2017). *Spin-imbalance in a 2D Fermi-Hubbard system*. Science **357.6358**, 1385–1388 (cited in pages 21, 29).

Burt, E. A., R. W. Ghrist, C. J. Myatt, M. J. Holland, E. A. Cornell and C. E. Wieman (1997). *Coherence, correlations, and collisions: what one learns about Bose-Einstein condensates from their decay*. Physical Review Letters **79.3**, 337–340 (cited in page 29).

Campbell, S. L., R. B. Hutson, G. E. Marti, A. Goban, N. D. Oppong et al. (2017). *A Fermi-degenerate three-dimensional optical lattice clock*. Science **358.6359**, 90–94 (cited in page 91).

Camy, G., C. Bordé and M. Ducloy (1982). *Heterodyne saturation spectroscopy through frequency modulation of the saturating beam*. Optics Communications **41.5**, 325–330 (cited in page 45).

Capogrosso-Sansone, B., N. V. Prokof'ev and B. V. Svistunov (2007). *Phase diagram and thermodynamics of the three-dimensional Bose-Hubbard model*. Physical Review B **75.13**, 134302 (cited in page 26).

Capogrosso-Sansone, B., Ş. G. Söyler, N. Prokof'ev and B. Svistunov (2008). *Monte Carlo study of the two-dimensional Bose-Hubbard model*. Physical Review A **77.1** (cited in pages 26, 62, 63).

Cappellini, G., M. Mancini, G. Pagano, P. Lombardi, L. Livi et al. (2014). *Direct observation of coherent interorbital spin-exchange dynamics*. Physical Review Letters **113.12**, 120402 (cited in page 91).

Cappellini, G., P. Lombardi, M. Mancini, G. Pagano, M. Pizzocaro, L. Fallani and J. Catani (2015). *A compact ultranarrow high-power laser system for experiments with 578nm ytterbium clock transition*. Review of Scientific Instruments **86.7**, 073111 (cited in pages 70, 90).

Cazalilla, M. A., A. F. Ho and M. Ueda (2009). *Ultracold gases of ytterbium: ferromagnetism and Mott states in an SU(6) Fermi system*. New Journal of Physics **11.10**, 103033 (cited in page 21).

Cazalilla, M. A. and A. M. Rey (2014). *Ultracold Fermi gases with emergent SU(N) symmetry*. Reports on Progress in Physics **77.12**, 124401 (cited in pages 15, 21).

Cheuk, L. W., M. A. Nichols, K. R. Lawrence, M. Okan, H. Zhang and M. W. Zwierlein (2016a). *Observation of 2D fermionic Mott insulators of ^{40}K with single-site resolution*. Physical Review Letters **116.23**, 235301 (cited in page 21).

Cheuk, L. W., M. A. Nichols, K. R. Lawrence, M. Okan, H. Zhang, E. Khatami, N. Trivedi, T. Paiva, M. Rigol and M. W. Zwierlein (2016b). *Observation of spatial charge and spin correlations in the 2D Fermi-Hubbard model*. Science **353.6305**, 1260–1264 (cited in pages 21, 29).

Childress, L. and R. Hanson (2013). *Diamond NV centers for quantum computing and quantum networks*. MRS Bulletin **38.2**, 134–138 (cited in page 12).

Chin, C., R. Grimm, P. Julienne and E. Tiesinga (2010). *Feshbach resonances in ultracold gases*. Reviews of Modern Physics **82.2**, 1225–1286 (cited in pages 105, 144).

Choi, J.-y., S. Hild, J. Zeiher, P. Schauß, A. Rubio-Abadal, T. Yefsah, V. Khemani, D. A. Huse, I. Bloch and C. Gross (2016). *Exploring the many-body localization transition in two dimensions*. Science **352.6293**, 1547–1552 (cited in pages 12, 22).

Chomaz, L., R. M. W. van Bijnen, D. Petter, G. Faraoni, S. Baier, J. H. Becher, M. J. Mark, F. Wächtler, L. Santos and F. Ferlaino (2018). *Observation of roton mode population in a dipolar quantum gas*. Nature Physics **14.5**, 442–446 (cited in page 13).

Chomaz, L., L. Corman, T. Bienaimé, R. Desbuquois, C. Weitenberg, S. Nascimbène, J. Beugnon and J. Dalibard (2015). *Emergence of coherence via transverse condensation in a uniform quasi-two-dimensional Bose gas*. Nature Communications **6**, 6162 (cited in page 20).

Chou, C. W., D. B. Hume, T. Rosenband and D. J. Wineland (2010). *Optical clocks and relativity*. Science **329**.**5999**, 1630–1633 (cited in page 13).

Chu, S. (1998). *Nobel Lecture: The manipulation of neutral particles*. Reviews of Modern Physics **70**.**3**, 685–706 (cited in page 12).

Cohen-Tannoudji, C., G. Grynberg and J. Dupont-Roc (1992). *Atom-Photon Interactions*. Atomic and Molecular Physics. John Wiley & Sons (cited in pages 97, 107, 128–131, 135, 164–166, 177).

Cohen-Tannoudji, C. (1974). *Interactions du champ électromagnétique avec des atomes*. Lectures at Collège de France 1974-1975. Unpublished (cited in pages 143, 144).

— (1989). *Cohérences quantiques et dissipation*. Lectures at Collège de France 1988-1989. Unpublished (cited in pages 93, 96, 97).

Cohen-Tannoudji, C. N. (1998). *Nobel Lecture: Manipulating atoms with photons*. Reviews of Modern Physics **70**.**3**, 707–719 (cited in page 12).

Cooper, N. R. (2008). *Rapidly rotating atomic gases*. Advances in Physics **57**.**6**, 539–616 (cited in page 36).

— (2011). *Optical flux lattices for ultracold atomic gases*. Physical Review Letters **106**.**17** (cited in page 20).

Cooper, N. R., J. Dalibard and I. B. Spielman (2018). *Topological bands for ultracold atoms*. arXiv:1803.00249 [cond-mat.quant-gas] (cited in pages 14, 15, 33, 35, 36).

Daley, A. J., M. M. Boyd, J. Ye and P. Zoller (2008). *Quantum computing with alkaline-earth-metal atoms*. Physical Review Letters **101**.**17** (cited in page 15).

Dalfovo, F., S. Giorgini, L. P. Pitaevskii and S. Stringari (1999). *Theory of Bose-Einstein condensation in trapped gases*. Reviews of Modern Physics **71**.**3**, 463–512 (cited in page 72).

Dalibard, J. and C. Cohen-Tannoudji (1985). *Atomic motion in laser light: connection between semiclassical and quantum descriptions*. Journal of Physics B: Atomic and Molecular Physics **18**.**8**, 1661 (cited in pages 95, 132).

Dalibard, J., Y. Castin and K. Mølmer (1992). *Wave-function approach to dissipative processes in quantum optics*. Physical Review Letters **68**.**5**, 580–583 (cited in page 165).

Dalibard, J., F. Gerbier, G. Juzeliūnas and P. Öhberg (2011). Colloquium*: Artificial gauge potentials for neutral atoms*. Reviews of Modern Physics **83**.**4**, 1523–1543 (cited in page 29).

Dareau, A., M. Scholl, Q. Beaufils, D. Döring, J. Beugnon and F. Gerbier (2015). *Doppler spectroscopy of an ytterbium Bose-Einstein condensate on the clock transition*. Physical Review A **91**.**2**, 023626 (cited in pages 66, 69, 70).

Dareau, A., E. Levy, M. B. Aguilera, R. Bouganne, E. Akkermans, F. Gerbier and J. Beugnon (2017). *Revealing the topology of quasicrystals with a diffraction experiment*. Physical Review Letters **119**.**21**, 215304 (cited in page 4).

Dareau, A. (2015). *Manipulation cohérente d'un condensat de Bose-Einstein d'ytterbium sur la transition d'horloge : de la spectroscopie au magnétisme artificiel*. PhD Thesis. École normale supérieure - Paris (cited in pages 36, 41, 44, 46, 65–67).

Davis, K. B., M. O. Mewes, M. R. Andrews, N. J. van Druten, D. S. Durfee, D. M. Kurn and W. Ketterle (1995). *Bose-Einstein condensation in a gas of sodium atoms*. Physical Review Letters **75**.**22**, 3969–3973 (cited in page 12).

DeMarco, B. and D. S. Jin (1999). *Onset of Fermi degeneracy in a trapped atomic gas*. Science **285**.**5434**, 1703–1706 (cited in page 12).

DePue, M. T., C. McCormick, S. L. Winoto, S. Oliver and D. S. Weiss (1999). *Unity occupation of sites in a 3D optical lattice*. Physical Review Letters **82**.**11**, 2262–2265 (cited in pages 21, 104, 106).

Descartes, R. (1637). *Discours de la méthode* (cited in page 11).

Devoret, M. H. and R. J. Schoelkopf (2013). *Superconducting circuits for quantum information: An outlook*. Science **339**.**6124**, 1169–1174 (cited in page 11).

Dicke, R. H. (1954). *Coherence in spontaneous radiation processes*. Physical Review **93**.**1**, 99–110 (cited in page 151).

Diedrich, F., J. C. Bergquist, W. M. Itano and D. J. Wineland (1989). *Laser cooling to the zero-point energy of motion*. Physical Review Letters **62**.**4**, 403–406 (cited in page 133).

Doppler, J., A. A. Mailybaev, J. Böhm, U. Kuhl, A. Girschik, F. Libisch, T. J. Milburn, P. Rabl, N. Moiseyev and S. Rotter (2016). *Dynamically encircling an exceptional point for asymmetric mode switching*. Nature **537**.**7618**, 76–79 (cited in page 159).

Dreon, D. (2017). *Designing and building an ultracold dysprosium experiment: A new framework for light-spin interaction*. PhD Thesis. PSL Research University (cited in page 36).

Drever, R. W. P., J. L. Hall, F. V. Kowalski, J. Hough, G. M. Ford, A. J. Munley and H. Ward (1983). *Laser phase and frequency stabilization using an optical resonator*. Applied Physics B **31**.**2**, 97–105 (cited in page 67).

Dubé, P., A. A. Madej, J. E. Bernard, L. Marmet and A. D. Shiner (2009). *A narrow linewidth and frequency-stable probe laser source for the $^{88}Sr^{+}$ single ion optical frequency standard*. Applied Physics B **95**.**1**, 43–54 (cited in page 66).

Dzuba, V. A. and A. Derevianko (2010). *Dynamic polarizabilities and related properties of clock states of the ytterbium atom*. Journal of Physics B: Atomic, Molecular and Optical Physics **43**.**7**, 074011 (cited in page 20).

Dzuba, V. A., V. V. Flambaum and S. Schiller (2018). *Testing physics beyond the standard model through additional clock transitions in neutral ytterbium*. Physical Review A **98**.**2**, 022501 (cited in page 17).

Einstein, A. (1905). *Über die von der molekularkinetischen Theorie der Wärme geforderte Bewegung von in ruhenden Flüssigkeiten suspendierten Teilchen*. Annalen der Physik **322**.**8**, 549–560 (cited in page 97).

Einstein, A. (1917). *Zur Quantentheorie der Strahlung*. Physikalische Zeitschrift **18** (cited in page 97).

Ejima, S., H. Fehske and F. Gebhard (2011). *Dynamic properties of the one-dimensional Bose-Hubbard model*. EPL (Europhysics Letters) **93**.**3**, 30002 (cited in page 26).

Ellinger, K., J. Cooper and P. Zoller (1994). *Light-pressure force in N-atom systems*. Physical Review A **49**.**5**, 3909–3933 (cited in pages 12, 180).

Endres, M., H. Bernien, A. Keesling, H. Levine, E. R. Anschuetz, A. Krajenbrink, C. Senko, V. Vuletic, M. Greiner and M. D. Lukin (2016). *Atom-by-atom assembly of defect-free one-dimensional cold atom arrays*. Science **354.6315**, 1024–1027 (cited in page 20).

Fano, U. (1957). *Description of states in quantum mechanics by density matrix and operator techniques*. Reviews of Modern Physics **29.1**, 74–93 (cited in page 163).

Ferrier-Barbut, I., H. Kadau, M. Schmitt, M. Wenzel and T. Pfau (2016). *Observation of quantum droplets in a strongly dipolar Bose gas*. Physical Review Letters **116.21**, 215301 (cited in page 13).

Feynman, R. P. (1982). *Simulating physics with computers*. International Journal of Theoretical Physics **21.6-7**, 467–488 (cited in page 11).

Fisher, M. P. A., P. B. Weichman, G. Grinstein and D. S. Fisher (1989). *Boson localization and the superfluid-insulator transition*. Physical Review B **40.1**, 546–570 (cited in page 25).

Fläschner, N., B. S. Rem, M. Tarnowski, D. Vogel, D.-S. Lühmann, K. Sengstock and C. Weitenberg (2016). *Experimental reconstruction of the Berry curvature in a Floquet Bloch band*. Science **352.6289**, 1091–1094 (cited in page 30).

Fölling, S., F. Gerbier, A. Widera, O. Mandel, T. Gericke and I. Bloch (2005). *Spatial quantum noise interferometry in expanding ultracold atom clouds*. Nature **434.7032**, 481–484 (cited in page 29).

Foot, C. J. (2004). *Atomic Physics*. Oxford Master Series in Physics. Oxford University Press (cited in pages 16, 75, 78).

Foss-Feig, M., M. Hermele, V. Gurarie and A. M. Rey (2010a). *Heavy fermions in an optical lattice*. Physical Review A **82.5** (cited in page 20).

Foss-Feig, M., M. Hermele and A. M. Rey (2010b). *Probing the Kondo lattice model with alkaline-earth-metal atoms*. Physical Review A **81.5** (cited in page 20).

Franchi, L., L. F. Livi, G. Cappellini, G. Binella, M. Inguscio, J. Catani and L. Fallani (2017). *State-dependent interactions in ultracold ^{174}Yb probed by optical clock spectroscopy*. New Journal of Physics **19.10**, 103037 (cited in pages 72, 90, 91, 157).

Frapolli, C. (2017). *Thermodynamics and magnetism of antiferromagnetic spinor Bose-Einstein condensates*. PhD Thesis. PSL Research University (cited in page 56).

Freimund, D. L., K. Aflatooni and H. Batelaan (2001). *Observation of the Kapitza-Dirac effect*. Nature **413.6852**, 142–143 (cited in page 60).

Friebel, S., C. D'Andrea, J. Walz, M. Weitz and T. W. Hänsch (1998). *CO_2-laser optical lattice with cold rubidium atoms*. Physical Review A **57.1**, R20–R23 (cited in page 47).

Fried, D. G., T. C. Killian, L. Willmann, D. Landhuis, S. C. Moss, D. Kleppner and T. J. Greytak (1998). *Bose-Einstein condensation of atomic hydrogen*. Physical Review Letters **81.18**, 3811–3814 (cited in page 71).

Fröhlich, B., T. Lahaye, B. Kaltenhäuser, H. Kübler, S. Müller, T. Koch, M. Fattori and T. Pfau (2007). *Two-frequency acousto-optic modulator driver to improve the beam pointing stability during intensity ramps*. Review of Scientific Instruments **78.4**, 043101 (cited in page 49).

Fukuhara, T., S. Sugawa, Y. Takasu and Y. Takahashi (2009). *All-optical formation of quantum degenerate mixtures*. Physical Review A **79.2**, 021601 (cited in pages 50, 79, 122).

Gadway, B., D. Pertot, R. Reimann, M. G. Cohen and D. Schneble (2009). *Analysis of Kapitza-Dirac diffraction patterns beyond the Raman-Nath regime*. Optics Express **17.21**, 19173–19180 (cited in page 60).

García-Ripoll, J. J., S. Dürr, N. Syassen, D. M. Bauer, M. Lettner, G. Rempe and J. I. Cirac (2009). *Dissipation-induced hard-core boson gas in an optical lattice*. New Journal of Physics **11.1**, 013053 (cited in page 84).

Gaunt, A. L., T. F. Schmidutz, I. Gotlibovych, R. P. Smith and Z. Hadzibabic (2013). *Bose-Einstein condensation of atoms in a uniform potential*. Physical Review Letters **110.20**, 200406 (cited in page 20).

Georgescu, I. M., S. Ashhab and F. Nori (2014). *Quantum simulation*. Reviews of Modern Physics **86.1**, 153–185 (cited in page 11).

Gerbier, F., S. Trotzky, S. Fölling, U. Schnorrberger, J. D. Thompson et al. (2008). *Expansion of a quantum gas released from an optical lattice*. Physical Review Letters **101.15**, 155303 (cited in pages 63, 101, 114, 115).

Gerbier, F., A. Widera, S. Fölling, O. Mandel, T. Gericke and I. Bloch (2005). *Phase coherence of an atomic Mott insulator*. Physical Review Letters **95.5**, 050404 (cited in page 63).

Gerbier, F., S. Fölling, A. Widera and I. Bloch (2007). *Visibility of a Bose-condensed gas released from an optical lattice at finite temperatures*. arXiv:cond-mat/0701420 [cond-mat.stat-mech] (cited in page 29).

Gerbier, F. and J. Dalibard (2010). *Gauge fields for ultracold atoms in optical superlattices*. New Journal of Physics **12.3**, 033007 (cited in pages 14, 15, 20, 30, 36, 37, 40, 158).

Gericke, T., F. Gerbier, A. Widera, S. Fölling, O. Mandel and I. Bloch (2007). *Adiabatic loading of a Bose-Einstein condensate in a 3D optical lattice*. Journal of Modern Optics **54.5**, 735–743 (cited in page 58).

Ghermaoui, A. (2017). *Modulation spatiale de lumière pour le façonnage du potentiel dans un réseau optique*. Master thesis. École polytechnique (cited in page 158).

Goldman, N., G. Juzeliūnas, P. Öhberg and I. B. Spielman (2014). *Light-induced gauge fields for ultracold atoms*. Reports on Progress in Physics **77.12**, 126401 (cited in pages 14, 29, 35, 159).

Goldman, N., J. C. Budich and P. Zoller (2016). *Topological quantum matter with ultracold gases in optical lattices*. Nature Physics **12.7**, 639–645 (cited in page 29).

Gordon, J. P. and A. Ashkin (1980). *Motion of atoms in a radiation trap*. Physical Review A **21.5**, 1606–1617 (cited in page 12).

Gorshkov, A. V., A. M. Rey, A. J. Daley, M. M. Boyd, J. Ye, P. Zoller and M. D. Lukin (2009). *Alkaline-earth-metal atoms as few-qubit quantum registers*. Physical Review Letters **102.11**, 110503 (cited in pages 15, 20, 21).

Gorshkov, A. V., M. Hermele, V. Gurarie, C. Xu, P. S. Julienne, J. Ye, P. Zoller, E. Demler, M. D. Lukin and A. M. Rey (2010). *Two-orbital SU(N) magnetism with*

ultracold alkaline-earth atoms. Nature Physics **6.4**, 289–295 (cited in pages 15, 20, 21).

Gould, P. L., G. A. Ruff and D. E. Pritchard (1986). *Diffraction of atoms by light: The near-resonant Kapitza-Dirac effect*. Physical Review Letters **56.8**, 827–830 (cited in page 60).

Greif, D., M. F. Parsons, A. Mazurenko, C. S. Chiu, S. Blatt, F. Huber, G. Ji and M. Greiner (2016). *Site-resolved imaging of a fermionic Mott insulator*. Science **351.6276**, 953–957 (cited in page 21).

Greiner, M. (2003). *Ultracold quantum gases in three-dimensional optical lattice potentials*. PhD Thesis. Ludwig-Maximilians-Universität München (cited in pages 22, 64).

Greiner, M., O. Mandel, T. W. Hänsch and I. Bloch (2002a). *Collapse and revival of the matter wave field of a Bose-Einstein condensate*. Nature **419.6902**, 51–54 (cited in pages 63, 64).

Greiner, M., O. Mandel, T. Esslinger, T. W. Hänsch and I. Bloch (2002b). *Quantum phase transition from a superfluid to a Mott insulator in a gas of ultracold atoms*. Nature **415.6867**, 39–44 (cited in pages 11, 13, 21, 25, 61).

Griesmaier, A., J. Werner, S. Hensler, J. Stuhler and T. Pfau (2005). *Bose-Einstein condensation of chromium*. Physical Review Letters **94.16**, 160401 (cited in page 13).

Grimm, R., M. Weidemüller and Y. B. Ovchinnikov (2000). *Optical dipole traps for neutral atoms*. Advances in Atomic, Molecular, and Optical Physics. **42**, 95–170 (cited in pages 19, 47).

Gross, C., H. Strobel, E. Nicklas, T. Zibold, N. Bar-Gill, G. Kurizki and M. K. Oberthaler (2011). *Atomic homodyne detection of continuous-variable entangled twin-atom states*. Nature **480.7376**, 219–223 (cited in page 125).

Gross, C. and I. Bloch (2017). *Quantum simulations with ultracold atoms in optical lattices*. Science **357.6355**, 995–1001 (cited in page 21).

Grynberg, G. and C. Robilliard (2001). *Cold atoms in dissipative optical lattices*. Physics Reports **355.5**, 335–451 (cited in pages 21, 22).

Hänsch, T. W. and A. L. Schawlow (1975). *Cooling of gases by laser radiation*. Optics Communications **13.1**, 68–69 (cited in page 12).

Hanson, R. and D. D. Awschalom (2008). *Coherent manipulation of single spins in semiconductors*. Nature **453.7198**, 1043–1049 (cited in page 11).

Haroche, S. (2013). *Nobel Lecture: Controlling photons in a box and exploring the quantum to classical boundary*. Reviews of Modern Physics **85.3**, 1083–1102 (cited in page 12).

Haroche, S. and J.-M. Raimond (2006). *Exploring the Quantum: Atoms, Cavities, and Photons*. Oxford Graduate Texts. Oxford University Press (cited in pages 12, 93, 95, 131, 165).

Hasan, M. Z. and C. L. Kane (2010). Colloquium*: Topological insulators*. Reviews of Modern Physics **82.4**, 3045–3067 (cited in page 33).

Heiss, W. D. (2012). *The physics of exceptional points*. Journal of Physics A: Mathematical and Theoretical **45.44**, 444016 (cited in page 159).

Hess, H. F. (1986). *Evaporative cooling of magnetically trapped and compressed spin-polarized hydrogen*. Physical Review B **34.5**, 3476–3479 (cited in page 12).

Hodgman, S. S., R. G. Dall, A. G. Manning, K. G. H. Baldwin and A. G. Truscott (2011). *Direct measurement of long-range third-order coherence in Bose-Einstein condensates*. Science **331**.**6020**, 1046–1049 (cited in page 29).

Hofstadter, D. R. (1976). *Energy levels and wave functions of Bloch electrons in rational and irrational magnetic fields*. Physical Review B **14**.**6**, 2239–2249 (cited in page 33).

Honda, K., Y. Takahashi, T. Kuwamoto, M. Fujimoto, K. Toyoda, K. Ishikawa and T. Yabuzaki (1999). *Magneto-optical trapping of Yb atoms and a limit on the branching ratio of the $^1P_1$ state*. Physical Review A **59**.**2**, R934–R937 (cited in page 16).

Hu, J., A. Urvoy, Z. Vendeiro, V. Crépel, W. Chen and V. Vuletić (2017). *Creation of a Bose-condensed gas of ^{87}Rb by laser cooling*. Science **358**.**6366**, 1078–1080 (cited in page 13).

Jaksch, D., C. Bruder, J. I. Cirac, C. W. Gardiner and P. Zoller (1998). *Cold bosonic atoms in optical lattices*. Physical Review Letters **81**.**15**, 3108–3111 (cited in pages 25, 61).

Jaksch, D. and P. Zoller (2003). *Creation of effective magnetic fields in optical lattices: the Hofstadter butterfly for cold neutral atoms*. New Journal of Physics **5**.**1**, 56 (cited in pages 15, 30, 37).

Jiménez-García, K., R. L. Compton, Y.-J. Lin, W. D. Phillips, J. V. Porto and I. B. Spielman (2010). *Phases of a two-dimensional Bose gas in an optical lattice*. Physical Review Letters **105**.**11**, 110401 (cited in page 62).

Jördens, R., N. Strohmaier, K. Günter, H. Moritz and T. Esslinger (2008). *A Mott insulator of fermionic atoms in an optical lattice*. Nature **455**.**7210**, 204–207 (cited in pages 21, 91).

Jotzu, G., M. Messer, R. Desbuquois, M. Lebrat, T. Uehlinger, D. Greif and T. Esslinger (2014). *Experimental realization of the topological Haldane model with ultracold fermions*. Nature **515**.**7526**, 237–240 (cited in page 30).

Kapitza, P. L. and P. a. M. Dirac (1933). *The reflection of electrons from standing light waves*. Mathematical Proceedings of the Cambridge Philosophical Society **29**.**2**, 297–300 (cited in page 60).

Kasevich, M., D. S. Weiss, E. Riis, K. Moler, S. Kasapi and S. Chu (1991). *Atomic velocity selection using stimulated Raman transitions*. Physical Review Letters **66**.**18**, 2297–2300 (cited in page 71).

Kaufman, A. M., M. E. Tai, A. Lukin, M. Rispoli, R. Schittko, P. M. Preiss and M. Greiner (2016). *Quantum thermalization through entanglement in an isolated many-body system*. Science **353**.**6301**, 794–800 (cited in page 12).

Ketterle, W., D. S. Durfee and D. M. Stamper-kurn (1999). *Making, probing and understanding Bose-Einstein condensates*. Proceedings of the International School of Physics Enrico Fermi. **140**, 67–176 (cited in pages 25, 50, 51, 143).

Killian, T. C., D. G. Fried, L. Willmann, D. Landhuis, S. C. Moss, T. J. Greytak and D. Kleppner (1998). *Cold collision frequency shift of the 1S-2S transition in hydrogen*. Physical Review Letters **81**.**18**, 3807–3810 (cited in page 71).

Kim, M.-S., J. Lee, J. H. Lee, Y. Shin and J. Mun (2016). *Measurements of optical Feshbach resonances of ^{174}Yb atoms*. Physical Review A **94.4**, 042703 (cited in pages 104, 105).

Kinoshita, T., T. Wenger and D. S. Weiss (2005). *Local pair correlations in one-dimensional Bose gases*. Physical Review Letters **95.19**, 190406 (cited in page 29).

Kitagawa, M., K. Enomoto, K. Kasa, Y. Takahashi, R. Ciuryło, P. Naidon and P. S. Julienne (2008). *Two-color photoassociation spectroscopy of ytterbium atoms and the precise determinations of s-wave scattering lengths*. Physical Review A **77.1**, 012719 (cited in pages 50, 90).

Kohn, W. (1959). *Analytic properties of Bloch waves and Wannier functions*. Physical Review **115.4**, 809–821 (cited in pages 23, 181).

Kuppens, S. J. M., K. L. Corwin, K. W. Miller, T. E. Chupp and C. E. Wieman (2000). *Loading an optical dipole trap*. Physical Review A **62.1**, 013406 (cited in page 48).

Labeyrie, G., F. de Tomasi, J.-C. Bernard, C. A. Müller, C. Miniatura and R. Kaiser (1999). *Coherent backscattering of light by cold atoms*. Physical Review Letters **83.25**, 5266–5269 (cited in page 17).

Labeyrie, G., E. Vaujour, C. A. Müller, D. Delande, C. Miniatura, D. Wilkowski and R. Kaiser (2003). *Slow diffusion of light in a cold atomic cloud*. Physical Review Letters **91.22** (cited in page 51).

Lahaye, T., C. Menotti, L. Santos, M. Lewenstein and T. Pfau (2009). *The physics of dipolar bosonic quantum gases*. Reports on Progress in Physics **72.12**, 126401 (cited in pages 148, 150).

Laloë, F. (2001). *Do we really understand quantum mechanics? Strange correlations, paradoxes, and theorems*. American Journal of Physics **69.6**, 655–701 (cited in page 12).

Landau, L. (1930). *Diamagnetismus der Metalle*. Zeitschrift für Physik **64.9-10**, 629–637 (cited in page 30).

Laughlin, R. B. (1983). *Anomalous quantum Hall effect: An incompressible quantum fluid with fractionally charged excitations*. Physical Review Letters **50.18**, 1395–1398 (cited in page 14).

Legero, T., T. Kessler and U. Sterr (2010). *Tuning the thermal expansion properties of optical reference cavities with fused silica mirrors*. Journal of the Optical Society of America B **27.5**, 914 (cited in page 69).

Lewenstein, M., A. Sanpera, V. Ahufinger, B. Damski, A. Sen(De) and U. Sen (2007). *Ultracold atomic gases in optical lattices: mimicking condensed matter physics and beyond*. Advances in Physics **56.2**, 243–379 (cited in page 21).

Lin, Y.-J., R. L. Compton, K. Jiménez-García, J. V. Porto and I. B. Spielman (2009). *Synthetic magnetic fields for ultracold neutral atoms*. Nature **462.7273**, 628–632 (cited in pages 29, 36).

Livi, L. F., G. Cappellini, M. Diem, L. Franchi, C. Clivati et al. (2016). *Synthetic dimensions and spin-orbit coupling with an optical clock transition*. Physical Review Letters **117.22** (cited in page 15).

Livi, L. F. (2018). *New quantum simulations with ultracold ytterbium gases*. PhD Thesis. Università degli Studi di Firenze (cited in page 33).

Lu, M., N. Q. Burdick, S. H. Youn and B. L. Lev (2011). *Strongly dipolar Bose-Einstein condensate of dysprosium*. Physical Review Letters **107.19** (cited in page 13).

Ludlow, A. D., N. D. Lemke, J. A. Sherman, C. W. Oates, G. Quéméner, J. von Stecher and A. M. Rey (2011). *Cold-collision-shift cancellation and inelastic scattering in a Yb optical lattice clock*. Physical Review A **84.5**, 052724 (cited in pages 72, 74, 91).

Ludlow, A. D., M. M. Boyd, J. Ye, E. Peik and P. O. Schmidt (2015). *Optical atomic clocks*. Reviews of Modern Physics **87.2**, 637–701 (cited in pages 13, 15, 17, 20, 74, 77).

Lüschen, H. P., P. Bordia, S. S. Hodgman, M. Schreiber, S. Sarkar, A. J. Daley, M. H. Fischer, E. Altman, I. Bloch and U. Schneider (2017). *Signatures of many-body localization in a controlled open quantum system*. Physical Review X **7.1** (cited in page 93).

Madison, K. W., F. Chevy, W. Wohlleben and J. Dalibard (2000). *Vortex formation in a stirred Bose-Einstein condensate*. Physical Review Letters **84.5**, 806–809 (cited in pages 13, 35).

Mailybaev, A. A., O. N. Kirillov and A. P. Seyranian (2005). *Geometric phase around exceptional points*. Physical Review A **72.1** (cited in page 159).

Mancini, M., G. Pagano, G. Cappellini, L. Livi, M. Rider et al. (2015). *Observation of chiral edge states with neutral fermions in synthetic Hall ribbons*. Science **349.6255**, 1510–1513 (cited in pages 15, 30, 158).

Marte, P., R. Dum, R. Taïeb and P. Zoller (1993). *Resonance fluorescence from quantized one-dimensional molasses*. Physical Review A **47.2**, 1378–1390 (cited in page 95).

Marti, G. E., R. B. Hutson, A. Goban, S. L. Campbell, N. Poli and J. Ye (2018). *Imaging optical frequencies with 100 μHz precision and 1.1 μm resolution*. Physical Review Letters **120.10** (cited in pages 13, 15).

Martin, M. J., M. Bishof, M. D. Swallows, X. Zhang, C. Benko, J. von-Stecher, A. V. Gorshkov, A. M. Rey and J. Ye (2013). *A quantum many-body spin system in an optical lattice clock*. Science **341.6146**, 632–636 (cited in page 15).

Maruyama, R., R. H. Wynar, M. V. Romalis, A. Andalkar, M. D. Swallows, C. E. Pearson and E. N. Fortson (2003). *Investigation of sub-Doppler cooling in an ytterbium magneto-optical trap*. Physical Review A **68.1** (cited in page 46).

Masuhara, N., J. M. Doyle, J. C. Sandberg, D. Kleppner, T. J. Greytak, H. F. Hess and G. P. Kochanski (1988). *Evaporative cooling of spin-polarized atomic hydrogen*. Physical Review Letters **61.8**, 935–938 (cited in page 13).

Matthews, M. R., B. P. Anderson, P. C. Haljan, D. S. Hall, C. E. Wieman and E. A. Cornell (1999). *Vortices in a Bose-Einstein condensate*. Physical Review Letters **83.13**, 2498–2501 (cited in page 13).

Mazurenko, A., C. S. Chiu, G. Ji, M. F. Parsons, M. Kanász-Nagy, R. Schmidt, F. Grusdt, E. Demler, D. Greif and M. Greiner (2017). *A cold-atom Fermi-Hubbard antiferromagnet*. Nature **545.7655**, 462–466 (cited in page 22).

Metcalf, H. J. and P. van der Straten (1999). *Laser Cooling and Trapping*. Graduate Texts in Contemporary Physics. Springer-Verlag New York (cited in pages 16, 44, 46, 55, 97).

Milburn, T. J., J. Doppler, C. A. Holmes, S. Portolan, S. Rotter and P. Rabl (2015). *General description of quasiadiabatic dynamical phenomena near exceptional points.* Physical Review A **92.5** (cited in page 159).

Mills, M., P. Puri, Y. Yu, A. Derevianko, C. Schneider and E. R. Hudson (2017). *Efficient repumping of a Ca magneto-optical trap.* Physical Review A **96.3**, 033402 (cited in page 16).

Milonni, P. W. and P. L. Knight (1974). *Retardation in the resonant interaction of two identical atoms.* Physical Review A **10.4**, 1096–1108 (cited in page 12).

Mollow, B. R. (1975). *Pure-state analysis of resonant light scattering: Radiative damping, saturation, and multiphoton effects.* Physical Review A **12.5**, 1919–1943 (cited in page 130).

Monroe, C., D. M. Meekhof, B. E. King, S. R. Jefferts, W. M. Itano, D. J. Wineland and P. Gould (1995). *Resolved-sideband Raman cooling of a bound atom to the 3D zero-point energy.* Physical Review Letters **75.22**, 4011–4014 (cited in page 133).

Morice, O. (1995). *Atomes refroidis par laser : du refroidissement sub-recul a la recherche d'effets quantiques collectifs.* PhD Thesis. Paris VI (cited in page 144).

Morsch, O. and M. Oberthaler (2006). *Dynamics of Bose-Einstein condensates in optical lattices.* Reviews of Modern Physics **78.1**, 179–215 (cited in page 59).

Moulder, S., S. Beattie, R. P. Smith, N. Tammuz and Z. Hadzibabic (2012). *Quantized supercurrent decay in an annular Bose-Einstein condensate.* Physical Review A **86.1**, 013629 (cited in page 13).

Myatt, C. J., B. E. King, Q. A. Turchette, C. A. Sackett, D. Kielpinski, W. M. Itano, C. Monroe and D. J. Wineland (2000). *Decoherence of quantum superpositions through coupling to engineered reservoirs.* Nature **403.6767**, 269–273 (cited in page 12).

Nogrette, F., H. Labuhn, S. Ravets, D. Barredo, L. Béguin, A. Vernier, T. Lahaye and A. Browaeys (2014). *Single-atom trapping in holographic 2D arrays of microtraps with arbitrary geometries.* Physical Review X **4.2**, 021034 (cited in pages 11, 20).

Norcia, M. A., J. R. K. Cline, J. A. Muniz, J. M. Robinson, R. B. Hutson, A. Goban, G. E. Marti, J. Ye and J. K. Thompson (2018a). *Frequency measurements of superradiance from the strontium clock transition.* Physical Review X **8.2**, 021036 (cited in page 15).

Norcia, M. A., J. R. K. Cline, J. P. Bartolotta, M. J. Holland and J. K. Thompson (2018b). *Narrow-line laser cooling by adiabatic transfer.* New Journal of Physics **20.2**, 023021 (cited in page 17).

Ockeloen-Korppi, C., A. Tauschinsky, R. Spreeuw and S. Whitlock (2010). *Detection of small atom numbers through image processing.* Physical Review A **82**, 061606 (cited in page 56).

Olmos, B., D. Yu, Y. Singh, F. Schreck, K. Bongs and I. Lesanovsky (2013). *Long-range interacting many-body systems with alkaline-earth-metal atoms.* Physical Review Letters **110.14** (cited in pages 18, 159).

Parsons, M. F., A. Mazurenko, C. S. Chiu, G. Ji, D. Greif and M. Greiner (2016). *Site-resolved measurement of the spin-correlation function in the Fermi-Hubbard model.* Science **353.6305**, 1253–1256 (cited in pages 21, 29).

Patil, Y. S., S. Chakram and M. Vengalattore (2015). *Measurement-induced localization of an ultracold lattice gas*. Physical Review Letters **115**.**14**, 140402 (cited in page 93).

Pedri, P., L. Pitaevskii, S. Stringari, C. Fort, S. Burger, F. S. Cataliotti, P. Maddaloni, F. Minardi and M. Inguscio (2001). *Expansion of a coherent array of Bose-Einstein condensates*. Physical Review Letters **87**.**22** (cited in page 29).

Peierls, R. (1933). *Zur Theorie des Diamagnetismus von Leitungselektronen*. Zeitschrift für Physik **80**.**11-12**, 763–791 (cited in page 31).

Perczel, J., J. Borregaard, D. E. Chang, H. Pichler, S. F. Yelin, P. Zoller and M. D. Lukin (2017). *Topological quantum optics in two-dimensional atomic arrays*. Physical Review Letters **119**.**2** (cited in page 18).

Perrin, H., A. Kuhn, I. Bouchoule and C. Salomon (1998). *Sideband cooling of neutral atoms in a far-detuned optical lattice*. EPL (Europhysics Letters) **42**.**4**, 395 (cited in page 133).

Phillips, W. D. (1998). *Nobel Lecture: Laser cooling and trapping of neutral atoms*. Reviews of Modern Physics **70**.**3**, 721–741 (cited in page 12).

Pichler, H., A. J. Daley and P. Zoller (2010). *Nonequilibrium dynamics of bosonic atoms in optical lattices: Decoherence of many-body states due to spontaneous emission*. Physical Review A **82**.**6**, 063605 (cited in pages 12, 107, 128, 131, 144, 154, 158, 165, 180).

Poletti, D., J.-S. Bernier, A. Georges and C. Kollath (2012). *Interaction-induced impeding of decoherence and anomalous diffusion*. Physical Review Letters **109**.**4**, 045302 (cited in pages 106–108, 111, 119).

Poletti, D., P. Barmettler, A. Georges and C. Kollath (2013). *Emergence of glasslike dynamics for dissipative and strongly interacting bosons*. Physical Review Letters **111**.**19**, 195301 (cited in pages 106, 108–110, 127, 153, 158, 165, 167, 168).

Pollet, L. (2012). *Recent developments in quantum Monte Carlo simulations with applications for cold gases*. Reports on Progress in Physics **75**.**9**, 094501 (cited in page 26).

Porsev, S. G., Y. G. Rakhlina and M. G. Kozlov (1999). *Electric-dipole amplitudes, lifetimes, and polarizabilities of the low-lying levels of atomic ytterbium*. Physical Review A **60**.**4**, 2781–2785 (cited in page 54).

Porsev, S. G., A. Derevianko and E. N. Fortson (2004). *Possibility of an optical clock using the $6^1S_0 \rightarrow 6^3P_0$ transition in ^{171,173}Yb atoms held in an optical lattice*. Physical Review A **69**.**2** (cited in page 17).

Preiss, P. M., R. Ma, M. E. Tai, J. Simon and M. Greiner (2015). *Quantum gas microscopy with spin, atom-number, and multilayer readout*. Physical Review A **91**.**4**, 041602 (cited in page 21).

Press, W. H. (2007). *Numerical Recipes 3rd Edition: The Art of Scientific Computing*. Numerical Recipes. Cambridge University Press (cited in page 169).

Prudnikov, O. N., D. V. Brazhnikov, A. V. Taichenachev, V. I. Yudin, A. E. Bonert, M. A. Tropnikov and A. N. Goncharov (2016). *New approaches in deep laser cooling of magnesium atoms for quantum metrology*. Laser Physics **26**.**9**, 095503 (cited in page 16).

Qi, X.-L. and S.-C. Zhang (2011). *Topological insulators and superconductors*. Reviews of Modern Physics **83**.**4**, 1057–1110 (cited in page 33).

Ramanathan, A., K. C. Wright, S. R. Muniz, M. Zelan, W. T. Hill, C. J. Lobb, K. Helmerson, W. D. Phillips and G. K. Campbell (2011). *Superflow in a toroidal Bose-Einstein condensate: An atom circuit with a tunable weak link*. Physical Review Letters **106**.**13**, 130401 (cited in page 13).

Regal, C. A., M. Greiner and D. S. Jin (2004). *Observation of resonance condensation of fermionic atom pairs*. Physical Review Letters **92**.**4**, 040403 (cited in page 13).

Riegger, L., N. Darkwah Oppong, M. Höfer, D. R. Fernandes, I. Bloch and S. Fölling (2018). *Localized magnetic moments with tunable spin exchange in a gas of ultracold fermions*. Physical Review Letters **120**.**14** (cited in pages 15, 20).

Roati, G., C. D'Errico, L. Fallani, M. Fattori, C. Fort, M. Zaccanti, G. Modugno, M. Modugno and M. Inguscio (2008). *Anderson localization of a non-interacting Bose-Einstein condensate*. Nature **453**.**7197**, 895–898 (cited in page 11).

Rokhsar, D. S. and B. G. Kotliar (1991). *Gutzwiller projection for bosons*. Physical Review B **44**.**18**, 10328–10332 (cited in page 26).

Rom, T., T. Best, D. van Oosten, U. Schneider, S. Fölling, B. Paredes and I. Bloch (2006). *Free fermion antibunching in a degenerate atomic Fermi gas released from an optical lattice*. Nature **444**.**7120**, 733–736 (cited in page 29).

Safronova, M. S., S. G. Porsev, C. Sanner and J. Ye (2018). *Two clock transitions in neutral Yb for the highest sensitivity to variations of the fine-structure constant*. Physical Review Letters **120**.**17** (cited in page 18).

Scazza, F., C. Hofrichter, M. Höfer, P. C. D. Groot, I. Bloch and S. Fölling (2014). *Observation of two-orbital spin-exchange interactions with ultracold SU(N)-symmetric fermions*. Nature Physics **10**.**10**, 779–784 (cited in pages 21, 91).

Scazza, F. (2015). *Probing SU(N)-symmetric orbital interactions with ytterbium Fermi gases in optical lattices*. PhD Thesis. Ludwig-Maximilians-Universität München (cited in page 54).

Schneider, U., L. Hackermüller, S. Will, T. Best, I. Bloch, T. A. Costi, R. W. Helmes, D. Rasch and A. Rosch (2008). *Metallic and insulating phases of repulsively interacting fermions in a 3D optical lattice*. Science **322**.**5907**, 1520–1525 (cited in page 21).

Scholl, M. (2014). *Probing an ytterbium Bose-Einstein condensate using an ultranarrow optical line: Towards artificial gauge fields in optical lattices*. PhD Thesis. Université Pierre et Marie Curie - Paris VI (cited in pages 41, 44, 46–49, 64).

Schreck, F., L. Khaykovich, K. L. Corwin, G. Ferrari, T. Bourdel, J. Cubizolles and C. Salomon (2001). *Quasipure Bose-Einstein condensate immersed in a Fermi sea*. Physical Review Letters **87**.**8**, 080403 (cited in page 12).

Schweigler, T., V. Kasper, S. Erne, I. Mazets, B. Rauer, F. Cataldini, T. Langen, T. Gasenzer, J. Berges and J. Schmiedmayer (2017). *Experimental characterization of a quantum many-body system via higher-order correlations*. Nature **545**.**7654**, 323–326 (cited in page 29).

Schweikhard, V., I. Coddington, P. Engels, V. P. Mogendorff and E. A. Cornell (2004). *Rapidly rotating Bose-Einstein condensates in and near the lowest Landau level*. Physical Review Letters **92**.**4** (cited in pages 14, 36).

Shahmoon, E., D. S. Wild, M. D. Lukin and S. F. Yelin (2017). *Cooperative resonances in light scattering from two-dimensional atomic arrays*. Physical Review Letters **118**.**11** (cited in page 159).

Sherson, J. F., C. Weitenberg, M. Endres, M. Cheneau, I. Bloch and S. Kuhr (2010). *Single-atom-resolved fluorescence imaging of an atomic Mott insulator*. Nature **467**.**7311**, 68–72 (cited in page 21).

Shirley, J. H. (1982). *Modulation transfer processes in optical heterodyne saturation spectroscopy*. Optics Letters **7**.**11**, 537 (cited in page 45).

Soave, E. (2016). *Production and high-resolution imaging of a quantum degenerate ytterbium atomic gas*. Tesi di Laurea. Università degli studi di Pisa (cited in page 158).

Spielman, I. B., W. D. Phillips and J. V. Porto (2007). *Mott-insulator transition in a two-dimensional atomic Bose gas*. Physical Review Letters **98**.**8**, 080404 (cited in pages 62, 63).

Sponselee, K., L. Freystatzky, B. Abeln, M. Diem, B. Hundt et al. (2018). *Dynamics of ultracold quantum gases in the dissipative Fermi-Hubbard model*. Quantum Science and Technology **4**.**1**, 014002 (cited in pages 91, 93).

Stellmer, S., B. Pasquiou, R. Grimm and F. Schreck (2013). *Laser cooling to quantum degeneracy*. Physical Review Letters **110**.**26** (cited in pages 13, 17).

Stenger, J., S. Inouye, A. P. Chikkatur, D. M. Stamper-Kurn, D. E. Pritchard and W. Ketterle (1999). *Bragg spectroscopy of a Bose-Einstein condensate*. Physical Review Letters **82**.**23**, 4569–4573 (cited in pages 29, 71).

Struck, J., C. Ölschläger, R. L. Targat, P. Soltan-Panahi, A. Eckardt, M. Lewenstein, P. Windpassinger and K. Sengstock (2011). *Quantum simulation of frustrated classical magnetism in triangular optical lattices*. Science **333**.**6045**, 996–999 (cited in page 11).

Stuhl, B. K., H.-I. Lu, L. M. Aycock, D. Genkina and I. B. Spielman (2015). *Visualizing edge states with an atomic Bose gas in the quantum Hall regime*. Science **349**.**6255**, 1514–1518 (cited in pages 30, 158).

Syassen, N., D. M. Bauer, M. Lettner, T. Volz, D. Dietze, J. J. García-Ripoll, J. I. Cirac, G. Rempe and S. Dürr (2008). *Strong dissipation inhibits losses and induces correlations in cold molecular gases*. Science **320**.**5881**, 1329–1331 (cited in pages 84, 91, 93).

Tai, M. E., A. Lukin, M. Rispoli, R. Schittko, T. Menke, D. Borgnia, P. M. Preiss, F. Grusdt, A. M. Kaufman and M. Greiner (2017). *Microscopy of the interacting Harper-Hofstadter model in the two-body limit*. Nature **546**.**7659**, 519–523 (cited in page 36).

Taichenachev, A. V., V. I. Yudin, C. W. Oates, C. W. Hoyt, Z. W. Barber and L. Hollberg (2006). *Magnetic field-induced spectroscopy of forbidden optical transitions with application to lattice-based optical atomic clocks*. Physical Review Letters **96**.**8**, 083001 (cited in pages 18, 74).

Takasu, Y., K. Maki, K. Komori, T. Takano, K. Honda, M. Kumakura, T. Yabuzaki and Y. Takahashi (2003). *Spin-singlet Bose-Einstein condensation of two-electron atoms*. Physical Review Letters **91**.**4**, 040404 (cited in page 13).

Teichmann, N., D. Hinrichs, M. Holthaus and A. Eckardt (2009). *Bose-Hubbard phase diagram with arbitrary integer filling*. Physical Review B **79**.**10**, 100503 (cited in pages 62, 63).

Thouless, D. J., M. Kohmoto, M. P. Nightingale and M. den Nijs (1982). *Quantized Hall conductance in a two-dimensional periodic potential*. Physical Review Letters **49.6**, 405–408 (cited in pages 32, 35).

Tjörnhammar, S., V. Maestroni, A. Zukauskas, T. K. Uždavinys, C. Canalias, F. Laurell and V. Pasiskevicius (2015). *Infrared absorption in KTP isomorphs induced with blue picosecond pulses*. Optical Materials Express **5.12**, 2951 (cited in page 45).

Tojo, S., M. Kitagawa, K. Enomoto, Y. Kato, Y. Takasu, M. Kumakura and Y. Takahashi (2006). *High-resolution photoassociation spectroscopy of ultracold ytterbium atoms by using the intercombination transition*. Physical Review Letters **96.15**, 153201 (cited in page 104).

Tomita, T., S. Nakajima, I. Danshita, Y. Takasu and Y. Takahashi (2017). *Observation of the Mott insulator to superfluid crossover of a driven-dissipative Bose-Hubbard system*. Science Advances **3.12**, e1701513 (cited in page 93).

Traverso, A., R. Chakraborty, Y. N. Martinez de Escobar, P. G. Mickelson, S. B. Nagel, M. Yan and T. C. Killian (2009). *Inelastic and elastic collision rates for triplet states of ultracold strontium*. Physical Review A **79.6**, 060702 (cited in pages 79, 91).

Truscott, A. G., K. E. Strecker, W. I. McAlexander, G. B. Partridge and R. G. Hulet (2001). *Observation of Fermi pressure in a gas of trapped atoms*. Science **291.5513**, 2570–2572 (cited in page 12).

Tsui, D. C., H. L. Stormer and A. C. Gossard (1982). *Two-dimensional magnetotransport in the extreme quantum limit*. Physical Review Letters **48.22**, 1559–1562 (cited in page 14).

Tung, S., V. Schweikhard and E. A. Cornell (2006). *Observation of vortex pinning in Bose-Einstein condensates*. Physical Review Letters **97.24** (cited in page 36).

Turchette, Q. A., C. J. Myatt, B. E. King, C. A. Sackett, D. Kielpinski, W. M. Itano, C. Monroe and D. J. Wineland (2000). *Decoherence and decay of motional quantum states of a trapped atom coupled to engineered reservoirs*. Physical Review A **62.5** (cited in page 12).

Vassen, W., C. Cohen-Tannoudji, M. Leduc, D. Boiron, C. I. Westbrook, A. Truscott, K. Baldwin, G. Birkl, P. Cancio and M. Trippenbach (2012). *Cold and trapped metastable noble gases*. Reviews of Modern Physics **84.1**, 175–210 (cited in page 15).

Verstraete, F., J. J. García-Ripoll and J. I. Cirac (2004). *Matrix product density operators: Simulation of finite-temperature and dissipative systems*. Physical Review Letters **93.20** (cited in page 125).

Ville, J. L., T. Bienaimé, R. Saint-Jalm, L. Corman, M. Aidelsburger et al. (2017). *Loading and compression of a single two-dimensional Bose gas in an optical accordion*. Physical Review A **95.1**, 013632 (cited in page 20).

von Klitzing, K. (1986). *The quantized Hall effect*. Reviews of Modern Physics **58.3**, 519–531 (cited in page 14).

Vuletić, V., C. Chin, A. J. Kerman and S. Chu (1998). *Degenerate Raman sideband cooling of trapped cesium atoms at very high atomic densities*. Physical Review Letters **81.26**, 5768–5771 (cited in page 133).

Vuletić, V., C. Chin, A. J. Kerman and S. Chu (1999). *Suppression of atomic radiative collisions by tuning the ground state scattering length*. Physical Review Letters **83**.**5**, 943–946 (cited in page 104).

Wang, P., Z.-Q. Yu, Z. Fu, J. Miao, L. Huang, S. Chai, H. Zhai and J. Zhang (2012). *Spin-orbit coupled degenerate Fermi gases*. Physical Review Letters **109**.**9** (cited in page 36).

Wannier, G. H. (1937). *The structure of electronic excitation levels in insulating crystals*. Physical Review **52**.**3**, 191–197 (cited in page 23).

Weimer, H., M. Müller, I. Lesanovsky, P. Zoller and H. P. Büchler (2010). *A Rydberg quantum simulator*. Nature Physics **6**.**5**, 382–388 (cited in page 11).

Westergaard, P. (2010). *Strontium optical lattice clock: In quest of the ultimate performance*. PhD Thesis. École nationale supérieure des télécommunications (cited in page 68).

White, S. R. and A. E. Feiguin (2004). *Real-time evolution using the density matrix renormalization group*. Physical Review Letters **93**.**7** (cited in page 125).

Will, S., T. Best, U. Schneider, L. Hackermüller, D.-S. Lühmann and I. Bloch (2010). *Time-resolved observation of coherent multi-body interactions in quantum phase revivals*. Nature **465**.**7295**, 197–201 (cited in page 64).

Wineland, D. J. and W. M. Itano (1979). *Laser cooling of atoms*. Physical Review A **20**.**4**, 1521–1540 (cited in pages 12, 132).

Wineland, D. J. (2013). *Nobel Lecture: Superposition, entanglement, and raising Schrödinger's cat*. Reviews of Modern Physics **85**.**3**, 1103–1114 (cited in page 12).

Yamaguchi, A., S. Uetake, S. Kato, H. Ito and Y. Takahashi (2010). *High-resolution laser spectroscopy of a Bose-Einstein condensate using the ultranarrow magnetic quadrupole transition*. New Journal of Physics **12**.**10**, 103001 (cited in pages 17, 53).

Zambelli, F., L. Pitaevskii, D. M. Stamper-Kurn and S. Stringari (2000). *Dynamic structure factor and momentum distribution of a trapped Bose gas*. Physical Review A **61**.**6**, 063608 (cited in page 71).

Zhu, B., B. Gadway, M. Foss-Feig, J. Schachenmayer, M. L. Wall et al. (2014). *Suppressing the loss of ultracold molecules via the continuous quantum Zeno effect*. Physical Review Letters **112**.**7**, 070404 (cited in page 91).

Zhu, B., J. Schachenmayer, M. Xu, F. Herrera, J. G. Restrepo, M. J. Holland and A. M. Rey (2015). *Synchronization of interacting quantum dipoles*. New Journal of Physics **17**.**8**, 083063 (cited in pages 18, 159).

Zupancic, P., P. M. Preiss, R. Ma, A. Lukin, M. E. Tai, M. Rispoli, R. Islam and M. Greiner (2016). *Ultra-precise holographic beam shaping for microscopic quantum control*. Optics Express **24**.**13**, 13881–13893 (cited in page 20).

Zurek, W. H. (2002). *Decoherence and the transition from quantum to classical – Revisited*. Los Alamos Science **27**, 86–109 (cited in page 12).

Zurek, W. H. (2003). *Decoherence, einselection, and the quantum origins of the classical*. Reviews of Modern Physics **75**.**3**, 715–775 (cited in page 12).

Zwerger, W. (2003). *Mott-Hubbard transition of cold atoms in optical lattices*. Journal of Optics B: Quantum and Semiclassical Optics **5**.**2**, S9 (cited in pages 25, 26, 61, 73).